EVALUATION OF THE FACTORS AFFECTING THE SURFACE RESISTIVITY OF FLY ASH

By

Prabhat Narayan Shukla

A DISSERTATION

Submitted to
Michigan State University
in partial fulfillment of the requirements
for the degree of

DOCTOR OF PHILOSOPHY

Department of Chemical Engineering

1980

ABSTRACT

EVALUATION OF THE FACTORS AFFECTING THE
SURFACE RESISTIVITY OF FLY ASH

By

Prabhat Narayan Shukla

Electrostatic precipitators are one of the more widely used high efficiency particulate control devices in coal fired power plants. The enactment of stringent emmissions standards has, in recent years, motivated a renewed research effort aimed at resolving some of the many interdisciplinary (engineering) problems, with the objective of improving the operating efficiency. One of the key factors that affects the operation of precipitators is the bulk electrical resistivity of the fly ash. An experimental procedure (point-plane technique) to determine the resistivity is proposed in this research.

The mode of charge conduction through a particulate layer is determined by the temperature regime of operation. Surface conductivity is predominant at the lower temperatures (less than 400^{o} F), and it is sensitive to the chemical composition. The surface conductivity (or resistivity) is modified by the addition of chemical conditioning agents. In general, this modification results in a lowering of the resistivity, and hence in the enhancement of the leakage current through the ash layer.

The total current through the ash layer is comprised of an electronic current and an ionic current. The behavior of the ionic

current is examined from the perspective of a theoretical model. This model incorporates the effects of two specific factors, viz., capillary condensation in the interparticle spaces and the variation of the axial field upon the particle surface. These factors are examined individually on the basis of the corresponding thermodynamic and electric contact theories.

The theory of capillary condensation is examined in light of the uncertainties associated with its applicability to small (molecular) volumes of the capillary condensate. Below a certain value of the relative saturation, the condensate is in tension (negative pressures). It is shown that, in this region, the isothermal susceptibility (χ_1) of the condensate decreases nonlinearly with its density. Under such conditions, the liquid ruptures for χ_1 equal to zero, and this constitutes the mechanical instability criterion for the capillary condensate. The other criterion for the vanishing of the condensate is the dimensional restriction, and it is shown that this feature predominates for the interparticle pore structure of the particulate bed.

The electric contact theory is used to determine the expression for the constriction resistance between two (spherical) particles in contact. This expression is utilized to evaluate the order of magnitude of the axial field strength at the neighborhood of the contact of two particles. Additionally, McLean's derivation for the surface resistance is used to secure an expression for the electric field, $E_s(\theta)$. The expressions for both of these fields predict an electrical breakdown near the contact.

The ionic (surface) transport flux due to the electrical gradient $E_s(\theta)$ is coupled with the molecular diffusion flux in the formulation of the differential equation for sodium ion migration. This equation is solved by the method of dominant balance which is applicable due to the specific location of the irregular singularities.

The results of the ion migration experiments are interpreted in terms of the MDB solution. The various model parameters are evaluated, and their interaction is discussed. It is concluded that the penetration distances for the experimental concentration profiles are inconsistent with the Nernst-Einstein equation. Such a conclusion follows from a study of the migration parameter $\bar{\alpha}$. This provides the basis for the speculation that surface (micropore) adsorption is important for an ionic current to exist.

The conclusion above is related to the (power plant) experimental observation that the surface resistivity is inversely related to the mositure content. This indicates the likelihood that one of the "functional" effects of chemical conditioning is demonstrated in the enhanced degree of surface adsorption.

DEDICATED TO

LSK

AND MY PARENTS

ACKNOWLEDGEMENTS

I would like to express my deep appreciation and indebtedness to my research advisor, Professor B.W. Wilkinson, for his patience, understanding and encouragement throughout this work. On numerous occasions I stood to benefit from his innovative approach and practical insight into the many experimental and theoretical problems that occured as this research developed.

I am grateful to the Office of the Vice President for Research and Graduate Studies, to the Department of Chemical Engineering and to the Division of Engineering Research for providing the financial support for this research.

Expressions of gratitude are also extended to the members of my doctoral committee, Dr. K. Jayaraman, Dr. M.L. Davis and Dr. J. Asmussen, Jr., for providing valuable assistance at various stages of this research. My thanks are due to Mr. J. Kavanaugh of Michigan State University power plant and to Mr. P.L. Thelen of the Board of Water and Light, Lansing, for giving me their assistance in the power plant (experimental) facilities. Helpful assistance was also received from Mr. J. Carrick with regard to nuclear activation analysis.

Finally, the excellent cooperation received from Mr. Robert Rose, Mr. Don Childs and Mr. Leo Szafranski is deeply appreciated. My thanks also go to Joanna Gruber, for her patience in typing the manuscript. The moral support received from my parents was indeed invaluable, and for this I am thankful.

TABLE OF CONTENTS

LIST OF TABLES

LIST OF FIGURES

INTRODUCTION

I.1 Motivation for the Research

This research problem was motivated by the high efficiency requirements for electrostatic precipitators in view of the stringent emissions standards of the revised Clean Air Act (of 1970). Precipitator technology still abounds in uncertainties, and these become more significant as the operating efficiency requirements increase.. Some of the major variables associated with these uncertainties are the gas flow pattern, electrical operating characteristics, internal configuration, rapping mechanism, flue gas characteristics, and the fly ash composition. This last variable has been a subject of some controversy and most investigations in this area have, at best, been empirical. Some installations now routinely use chemical additives (conditioning agents) in order to improve the efficiency of electrostatic precipitators. Sulfur trioxide and sodium compounds (NaCl) (W1) are two of the more popular conditioning agents.

These chemical conditioning agents act in a way so as to lower the bulk electrical resistivity of the fly ash by "modifying" its chemical composition. Their effectiveness is only limited to "cold" precipitators which operate at temperatures less than 400^{o} F. The electrical resistivity is one of the more important parameters and is taken into consideration during the design stage of an electrostatic precipitator.

Due to the lack of a standard procedure for the determination of resistivity, the need to develop a reliable experimental technique was recognized at the beginning of this research. This effort resulted in the development of the point-plane method.

The second part of this research was initiated by the controversy surrounding the effectiveness of sodium conditioning agents. It was proposed (B1) that an increase in the sodium content of the fly ash results in a lowering of the resistivity. This speculation was supported by similar observations on many glasses.

I.2 Review of Literature

The number of publications in the area of (chemical) compositional effects on resistivity of glasses are too numerous to mention. An excellent review of the research, until 1963, has been presented by Owen (02). The analogy, with regard to these effects, between the behaviors of glass and fly ash is presented by Bickelhaupt (B1, B2, B3). The basis of this comparison lies in the results of studies regarding ionic migration in glasses (under the influence of an externally applied electric field). Charles (C4) has published a fundamental study of the (alkali ion) migration in silicate glasses. A similar work by Doremus (D4) also needs to be mentioned in this context.

As mentioned in the previous section, there is a lack of literature regarding any theoretical investigation of the effects of chemical conditioning agents. The work of Dalmon and Tidy (D5) deals with a comparison of the effectiveness of chemical additives. Dismukes (D6) has published the results of his work with regard to

ammonia as a conditioning agent.

In comparison to the above, the effect of moisture upon the surface conductivity of oxides (and other solids) has been the subject of several (theoretical) investigations. The publications of Zettlemoyer and McCafferty (Z1, Z2) are pertinent to this area (of research). Furthermore, the interaction of water with silica surfaces is investigated by Young and Bursh (Y1). A study of the effect of water vapor on d.c. (surface) conductivity of solids has been conducted by Awakuni and Calderwood (A2). Martin and McLean (M8) have conducted a similar study of the effect of adsorbed gases.

There are many publications dealing with the studies of the behavior of fly ash in electrostatic precipitators. The principal papers referred to in this work were those of McLean (M1, M2 and M3) and Masuda (M5). The theoretical approach to the problem was suggested by the publications of Ditl and Coughlin (D1) and Melrose (M4). The latter dealt with the capillary condensation model.

Finally, a comprehensive review of the electrostatic precipitation of fly ash has been conducted by White (W3). Some of the basic features of fly ash characteristics are given in an earlier paper by the author (W5).

I.3. Significance of the Overall Problem

In a broad sense, the overall problem in this work deals with the migration of sodium ions on the surface of fly ash particulates (in a bed). The problem is approached on the basis of a theoretical model which consists of parameters that have a direct bearing upon

the bulk resistivity. For example, the effect of the average electric field (across the ash layer) is involved in a more complicated fashion than is suggested by the (relatively) straight forward power plant resistivity measurements of Chapter 1. The problem by itself, encompasses some of the major variables associated with fly ash conditioning. This aspect bears out its significance with regard to an operating electrostatic precipitator.

I.4 Description of the Research

As mentioned in Section I.1, the initial part of this research resulted in the development of the point plane technique. Very significant is the fact that the results from this result helps elucidate the relative effects of the variables involved.

The assumption of surface resistivity is carried through in all phases of the work. Surface resistivity implies that the leakage current (through the ash bed) flows along the surface of the particulates and it predominates over volume resistivity at the lower temperatures ($< 400^{o}$ F). The variation of surface resistivity with temperature is an important characteristic of the fly ash. This is shown in Figure I.1.

The second part of this work is devoted to a theoretical study of the factors which affect the alkali ion migration, and hence, the resistivity. This study is based on a mathematical model which recognizes the presence of two physical phenomena. These are:

i) Capillary condensation in the particulate bed

ii) The surface electric field due to the applied voltage gradient

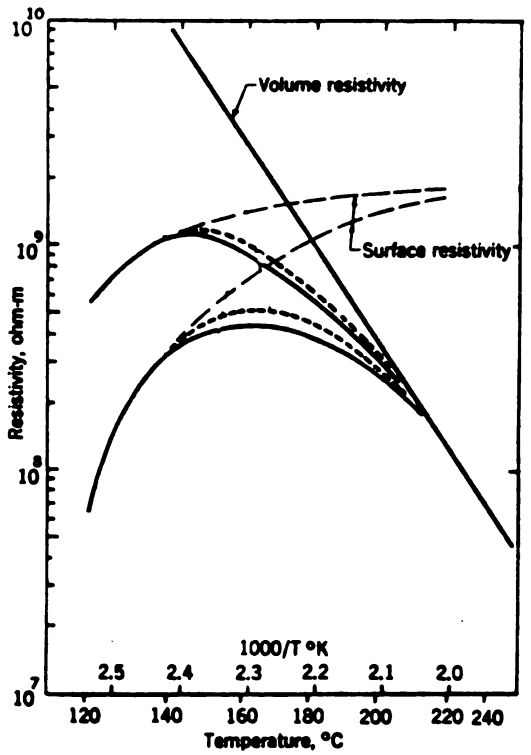

Figure I.1 The effect of temperature on the bulk resistivity of fly ash (M1).

The effects of these two phenomena are examined individually.

The conclusions are made on the basis of a comparison of the solution equation (to the mathematical model) to the results of the ion migration experiments conducted in the laboratory. The effects of the experimental parameters upon the ion migration are discussed. Finally, these conclusions are discussed in light of (water) conditioning experiments in the power plant.

CHAPTER 1

FLY ASH RESISTIVITY AND ITS INTERPRETATION

Overview

The influence of the bulk electrical resistivity of fly ash on the operating efficiency of electrostatic precipitators has mainly been understood in terms of its "post precipitation effects" only. The majority of the present resistivity problems stem from the high resistivity of the fly ash. Extremely large resistivity values ($>10^{11}$ ohm-cm) lead to a virtual breakdown in precipitator operation primarily due to the large fraction of the voltage between discharge wire and grounded electrode which is unavailable due to the high voltage drop across the deposited ash layer. Figures 1.1 and 1.2 illustrate this situation.

It is apparent that ΔV_d increases with an increase in the particulate resistivity, layer thickness, and the applied discharge (corona) voltage. However, this voltage cannot increase indefinitely and is limited by the sparkover voltage when the ash layer breaks down electrically and back corona* may set in. The reduction in this sparkover voltage in a negative

---

*Back corona is the phenomenon which occurs at or just beyond the electric breakdown of a resistive layer. Small holes are formed in the layer from which visible electrical flare discharges are produced and accompanied by a stream of positive ions flowing in opposition to the corona current. This phenomenon may be localized or may populate the entire layer. If the breakdown is localized it may cause a spark to propagate across the entire gap (W1).

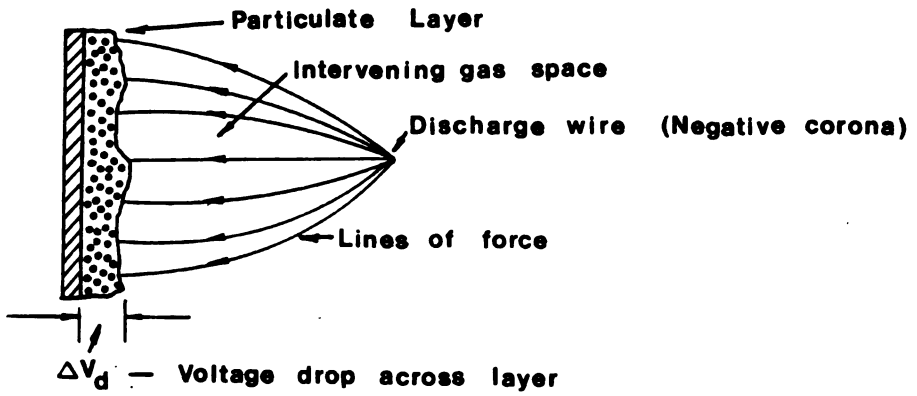

Figure 1.1. Schematic representation of a dust layer in a point-plane geometry.

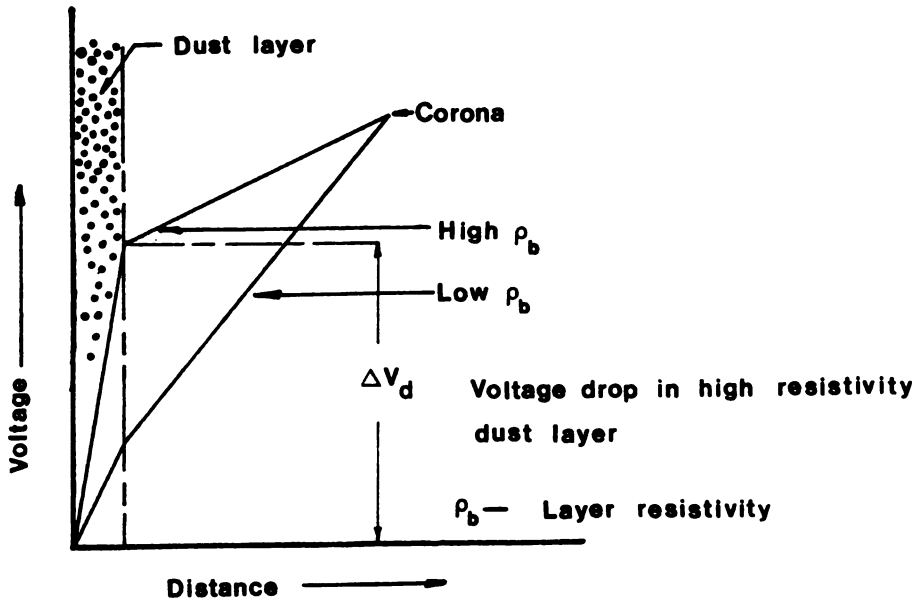

Figure 1.2. Relative voltage drops across high and low resistivity ashes.

point plane geometry due to the introduction of a porous dielectric was first observed by Walcott (W2) in 1918. An increase in the resistivity of the ash layer produced a decrease in the sparkover voltage by virtue of the high voltage gradient in the ash. In the extreme case the sparkover voltage would be so close to the corona initiation voltage that the precipitator would be inoperable even at the smallest corona currents. Besides interfering with the stable operation of a precipitator, the effects of an early onset of back corona are demonstrated by:

i) a lowering of the corona discharge voltage, and

ii) a reduction in the particle charging level

Both of these factors contribute, in conjunction, to a reduction in the operating efficiency of an electrostatic precipitator. As noted below, the efficiency is related to the particle migration velocity toward the collection electrode and is approximately proportional to the product of the particle charge and the applied voltage at the discharge wire.

Further, a highly resistive fly ash experiences strong cohesive forces within the deposited layer which lead to a decrease in the effectiveness of a rapper assembly. These forces are produced by the high electric fields which <u>also</u> act to reduce the resistivity at normal corona current densities ($\simeq 300\ \mu A/m^2$). This effect* arises due to the variation of bulk resistivity with the applied electric field. This is examined in this chapter as a result of resistivity experiments conducted in the inlet and outlet flues of operating precipitators in power plants.

*This effect is due to the high resistivity of the particulate bed which induces strong voltage gradients across it and which, in turn, reduces the operational resistivity that the precipitator "sees".

Recently Potter (P1) has discussed the effects of resistivity during the course of precipitation leading to the argument that this parameter should, in principle, be included in the theoretical efficiency equation. One form of this equation is given as (W3):

$$\eta = 1 - \int_0^\infty \exp(-kx)\, \gamma(x)\, dx$$

$$k = \frac{A}{v} \frac{\varepsilon_o E_c E_p}{\mu}$$

$$w = 2 \frac{\varepsilon_o E_c E_p a}{\mu}$$

$$q = 12\pi\varepsilon_o E_c a^2$$

where

$\gamma(x)$ - particle size - frequency distribution function

w - migration velocity [m-sec^{-1}]

q - particle charge [C]

A/v - specific collection area [m^2/m^3(gas)-sec^{-1}]

ε_o - permittivity constant, [8.85x10^{-12} A^2-sec^2/kg-m^3]

E_c, E_p - charging and precipitating field strengths respectively [V/m]

a - particle radius [m]

μ - gas viscosity [Kg/m-sec]

In the case of high resistivity dust, the voltage drop across the dust layer is not negligible, and hence any further collection occurs within a lower voltage drop (between corona wire and surface of ash layer). Bearing in mind that collection efficiency η, is directly related to the

square of the mean applied voltage ($\bar{V}^2$). This effect is, however, partially compensated for by the lowering of resistivity due to the increased field strength across the particulate layer.

1.1 Factors Affecting Resistivity

The bulk electrical resistivity of a compacted layer of particulates is a function of several variables, the more important of which are:

a. Particle size and size distribution

b. Mode of compaction of bed and applied pressure

c. Ambient gas temperature and composition

d. Electric field strengths ($\vec{E}$) within the ash layer

The volume and surface effective bulk resistivities vary directly with particle size (M1). Mode of compaction refers to the stacking arrangement of the particles in the layer and for a bone dry ash the effect is relatively minor (T1). The degree of compaction or the bulk density is not a major factor for the bone dry case and the variation with pressure is given as $1/(\text{Pressure})^{1/3}$.

The variation of resistivity with temperature is represented by the hump shaped curve (see Introduction) and the temperature regime determines whether the conduction is through the volume or along the surface (W4). The gas composition plays a significant role at the lower temperatures, where surface conduction is the dominant mode. The conditions of combustion and the time during which a coal particle undergoes transformation to a viscous melt followed by bubble nucleation when volatiles are evolved determine the shape and structure of the particle (F1,A1). The influence of chemical composition (alkali ions in particular) had been proposed by (Bickelhaupt (B1,B2,B3) and White (W1) based on similar

behaviour (under an imposed electric field) demonstrated by conventional glassy materials. McLean (M2) has theoretically investigated the effect of the electric field strength on the bulk resistivity and this analysis has been carried further based on Holm's (H1) theory of electric contacts.

This part of the work was motivated by the discrepancies between in-plant measurements of resistivity which are subject to the equipment used and the personnel involved. Inconsistency in results exists partly due to a lack of standard, recognized methods. Although the variation of resistivity with applied electric field was recognized, this fact was omitted in the most common experimental procedure adopted and it contributed to variations in the reported value of resistivity on the same ash sample. Hence, the objective of this work was three-fold:

i) Proposal of an experimental procedure (S1) and specification of proper experimental conditions.

ii) Identification of the physical significance of the reported value of the resistivity.

iii) Demonstration of the reproducibility of the resistivity within reasonable limits.

This work resulted in the proposal of a point plane technique of measuring in-situ resistivities. The details of this technique are presented in Appendix A.

1.2. Physical Significance of Results

All of the power plant tests involved the use of the SRI* resistivity probe (Figure A.3, Appendix A). The tests were conducted in the cold precipitator temperature region (300-360°F) where the surface conduction

*Southern Research Institute, Birmingham, Alabama.

mechanism is dominant. The point to plane probe best simulates the particulate collection mechanism in an electrostatic precipitator. Fly ash transported by the flue gas encounters the electric field between the negative corona and the grounded plane. All of the parameters needed to calculate the resistivity of the electrostatically deposited dust layer are measurable. It is generally agreed (W4,P1) that the reported value of the resistivity should be as close as possible to the threshold of electrical breakdown of the dust layer. This is a qualitative statement and therefore subject to the conditions of the experiment, However high field measurements are more realistic than the resistivity measurements made at low field strengths.

In principle one can calculate the bulk resistivity of a deposited ash layer if the leakage current corresponding to a given voltage drop across the layer is known. The effective resistivity is then given by:

$$\rho_b = \frac{(\Delta V)\ (A)}{(I)\ (d)} \qquad (1.1)$$

where

ρ_b = bulk resistivity, [ohm - cm].

ΔV = voltage drop, [volts].

I = leakage current [amperes].

d = thickness of particulate layer, [cm].

A = surface area normal to current flow [cm^2].

The proposed point-plane technique was determined to be physically meaningful and more reliable than the generally adopted disk method and the advantages of this technique are discussed in Appendix A.

Figure 1.3 shows the general shape of the experimental current-voltage (I-V) curves obtained by the point to plane method. The data used to obtain these plots are presented in Table 1.1. The figure is a computer generated plot obtained after fitting second order polynomials to the data points by the least squares method (see Appendices B-1,2). Essentially the same program as in Appendix B-1 was used to generate the fitting polynomial. The choice of the parabolic equation was made primarily because of its relative insensitivity to the data points near sparkover (breakdown) where the current readings are least stable. It was determined that a higher order polynomial with a relatively large negative coefficient for the x^3 term decreases in slope in this neighborhood and this is a physically invalid situation. A typical plot of the I-V relationship for the gas plus ash layer is shown in Figure 1.3. As the voltage approaches breakdown, the slope of the "dirty" plate curve increases to very large values. This was extended so as to make the slope equal to infinity at total sparkover. The plot routine draws a vertical line where the slope of the curve becomes infinity.

The disk plane technique yields direct evidence of the non-ohmic behaviour of both air and a particulate bed in that the rate of change of current with voltage increases with the applied voltage, thus the resistivity decreases. A linear I-V characteristic is indicated at the bottom of Figure 1.3 by the straight line representing a hypothetical situation of constant bulk resistivity. This is only valid at low average field strengths across the ash layer. The key to the shape of the non linear I-V characteristics (hence the decreasing resistivity) lies in the fact that the field strengths in the vicinity of the

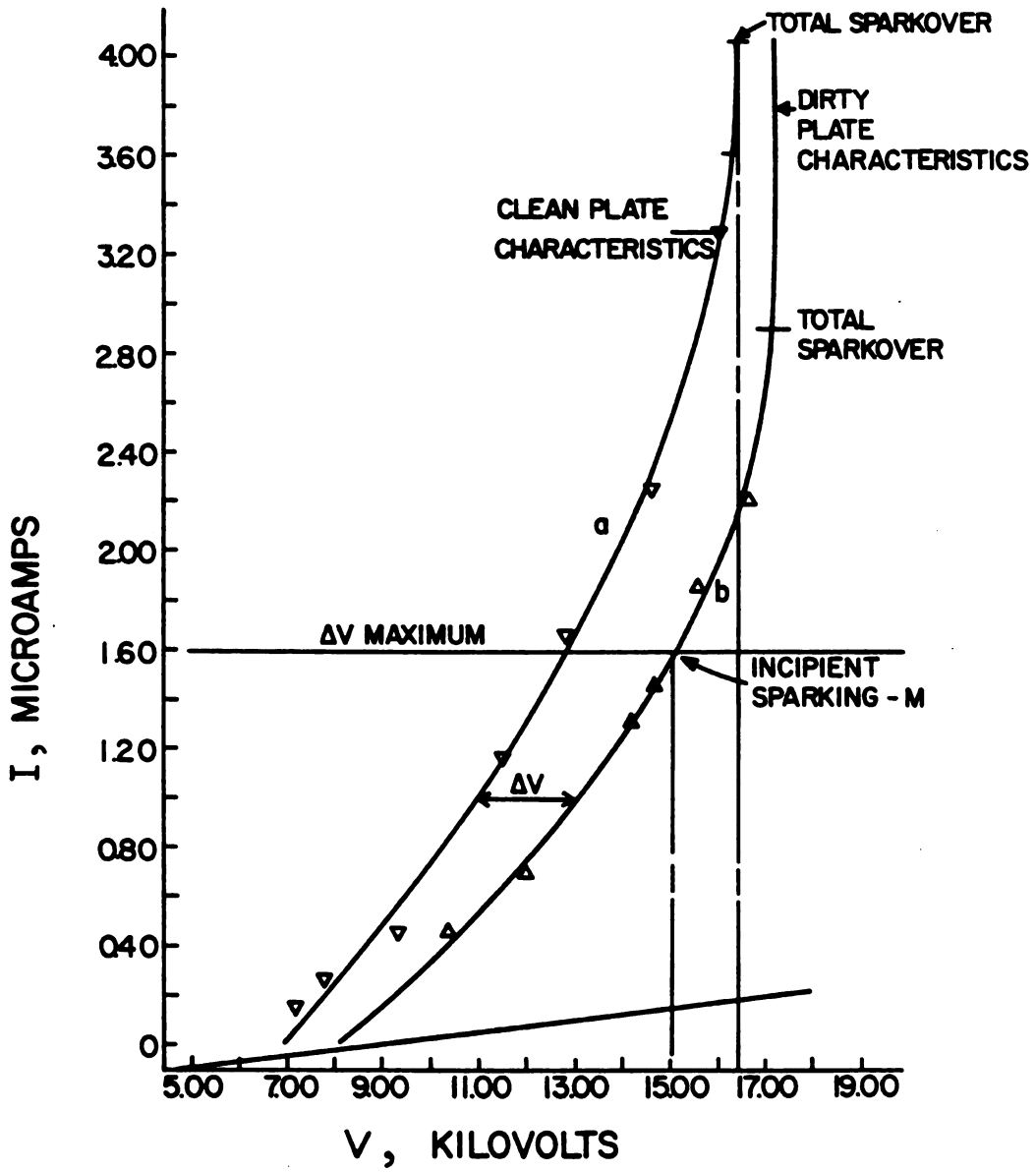

Figure 1.3. Plot showing the voltage - current characteristics of clean and dirty plates. Thickness of dust collected is 0.46 mm.

Table 1.1

A. Clean Plate (Flue Gas) Characteristic Data.

Corona Voltage (KV)	Measured Current (μA)
7.50	0.15
8.00	0.30
9.30	0.45
11.40	1.15
12.80	1.65
14.50	2.25
16.10	3.60

B. "Dirty" Plate Characteristic Data

Corona Voltage (KV)	Measured Current (μA)
10.40	0.45
12.00	0.70
14.20	1.30
14.60	1.45
15.50	1.85
16.50	2.20

C. Coefficients of Interpolating Polynomials.

$$V = Z(1) + Z(2)I + Z(3)I^2.$$

Coefficient	Clean Plate	Dirty Plate
Z(1)	6.905	8.088
Z(2)	4.612	5.957
Z(3)	-0.571	-0.995

interparticle contact are much higher than the average field strengths over the thickness of the layer. Hence, there is sustained an air gap discharge near the particle contact points due to localized breakdown of the gas in that region. An estimate of field strengths (assuming no breakdown) along the plane of contact and on the surface of the particles in the neighborhood of the contact has been presented in Chapter 3. The effective resistance in such a geometry arises due to the constriction of lines of current flow at the region of contact. It should be noted that this constriction resistance is expressed in terms of the material resistivity (H1). However, the bulk resistivity of the layer takes into account these points of contact in the particulate bed.

Upon generating the second order polynomial to fit the experimentally obtained data points, the point plane technique enables one to study the variation of resistivity with the applied corona voltage and with the average field strength across the layer as well (Figure 1.3). From the figure it is seen that the clean plate characteristic curve corresponds to a voltage drop between point and plane for the gas between them. The "dirty" plate characteristic curve is for the particulate layer deposited on the plane with the gas above it. For a given current level, the difference between the two values gives the voltage drop across the dust layer. In view of other measurement techniques (the disk method in particular) it should be noted that this voltage drop across the layer is inferred from the nature of the characteristic curves. The figure shows the variation of ΔV with increasing corona voltage along the curves. As the leakage current across the layer increases, the average field strength also increases; however, the current increase dominates so that

the net effect is a decrease in resistivity. As mentioned earlier, this effect is consistent with the presence of local fields which induce and sustain an air gap discharge, thus lowering the effective contact resistance and hence the overall resistivity. The characteristic curves separate and the horizontal distance between them, ΔV, continues to increase with applied voltage. When the threshold for back corona formation and local sparkover is reached, the layer exhibits a tendency for localized electrical breakdown. At such points, holes may be burned through the dust layer as was indicated by craters formed on the surface in some experiments. This is more severe in cases of high resistivity ash when the leakage current is so unstable that it is difficult to record a reading. Admitting, therefore, that the threshold corresponds to the first incidence of a local breakdown at some point on the dust layer (corresponding to current fluctuations about a mean value), the situation of total breakdown would correspond to an infinite current and a fairly high population of such "craters". It is relevant here to note that precipitators do often operate at levels close to the threshold of breakdown thus giving a definite spark rate (H2). The objective of such operation is to lower the operational resistivity as far as possible.

In theory, back corona and sparkover are separate but simultaneous phenomena. A stable back corona can occur for dust layers of extremely high resistivities when a large voltage drop is present across the layer. This is true even for corona voltages too low for sparkover. In Figure (1.3), the voltage drop increases at low voltages up to a maximum (in this case up to a current of 1.59 μA). This point M then represents the point of incipient sparking (threshold of breakdown) and is uniquely

defined for each set of characteristics obtained from a single experiment. Beyond this point, several sparks have jumped across the layer. The point of total sparkover is at the transition from the second order equation to the extended vertical tangent and occurs where the slope of the dust characteristic curve is infinite. This is calculated from the coefficients of the polynomials and shown in Table 1.1C. The reported value for the ash resistivity corresponds to the point M where the voltage drop in the ash layer is a maximum (in this case it is 2.249 kV). The variation of resistivity with ΔV across the deposited ash layer (which is proportional to the average field strength for a given bed thickness) is shown in Figure 1.4. The curve was fitted through the data points obtained from the computer output (see Table 1.2). In Figure 1.5 are presented results from another experiment (on the same day and location as the previous experiment) to demonstrate the consistency of the nature of the ρ_b - ΔV curve. The data used to generate Figure 1.3 are presented in Tables 1.3 and 1.4. In both cases, the resistivity decreases with increasing ΔV; however ΔV itself increases initially up to M after which it decreases due to localized breakdown in the ash layer. The reported resistivity in both cases is at incipient sparking. The circumstances which prevent an exact duplication of values (except experimental errors) are discussed in Appendix A.

The current fluctuations observed in the disk method* do indeed show that total breakdown (sparkover) does not occur suddenly at increasing

*In this method, the resistivity is measured by determining the leakage current across a dust layer sandwiched between a high voltage electrode and a plane grounded through a current meter.

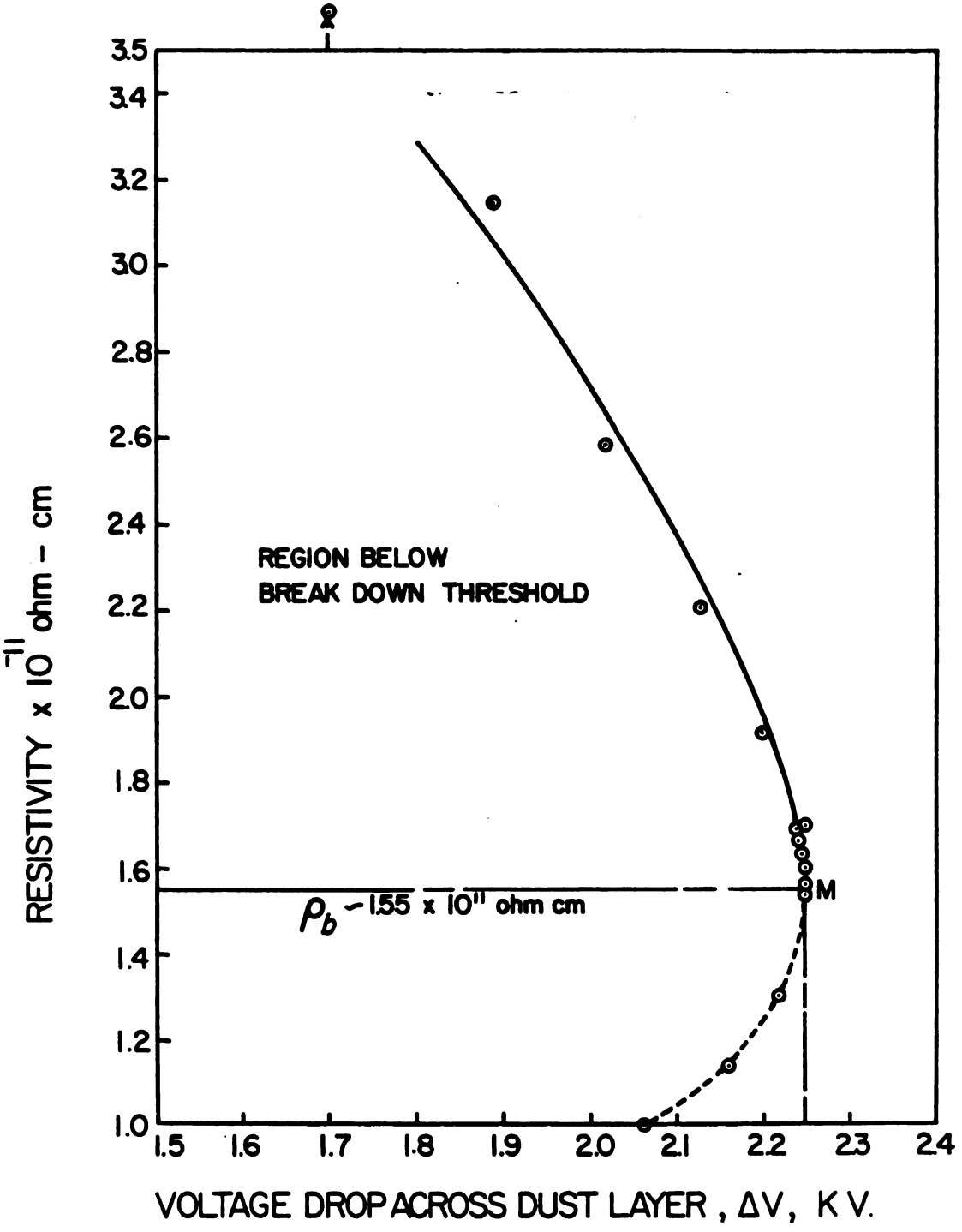

Figure 1.4. Resistivity - ΔV curve based on Figure 1.3.

Table 1.2 Resistivity Calculations Based on Figure 1.3

A.

ΔV (KV)	I (μA)	Resistivity (ohm - cm)	V (1)* (clean plate) (KV)	V (2)* (dust layer) (KV)
1.703	0.45	4.1127×10^{11}	8.86	10.57
1.878	0.65	3.1409×10^{11}	9.66	11.54
2.020	0.85	2.5830×10^{11}	10.41	12.43
2.128	1.05	2.2025×10^{11}	11.12	13.25
2.201	1.25	1.9143×10^{11}	11.78	13.98
2.241	1.45	1.6801×10^{11}	12.39	14.63
2.247	1.65	1.4803×10^{11}	12.96	15.21
2.219	1.85	1.3038×10^{11}	13.48	15.70
2.157	2.05	1.1437×10^{11}	13.96	16.12
2.061	2.25	9.9563×10^{10}	14.39	16.45
Data (for reduced current step size) near region of incipient sparking - point M on Figure 1.4				
2.240	1.44	1.6908×10^{11}	12.36	14.60
2.243	1.47	1.6588×10^{11}	12.45	14.69
2.246	1.50	1.6274×10^{11}	12.54	14.78
2.248	1.53	1.5968×10^{11}	12.62	14.87
2.249	1.56	1.5668×10^{11}	12.71	14.96
2.249	1.59	1.5374×10^{11}	12.79	15.04

B. Sparking Characteristics

Resistivity	Spark Voltage	$\rho_b d$	Layer Thickness	Temperature
1.5374×10^{11} ohm-cm	15.04 KV	7.0719×10^{9} ohm-cm^2	0.46 mm	286°F

Point - plane distance = 1.5 inches.

*V(1) and V(2) correspond to the corona voltages in Figure 1.3.

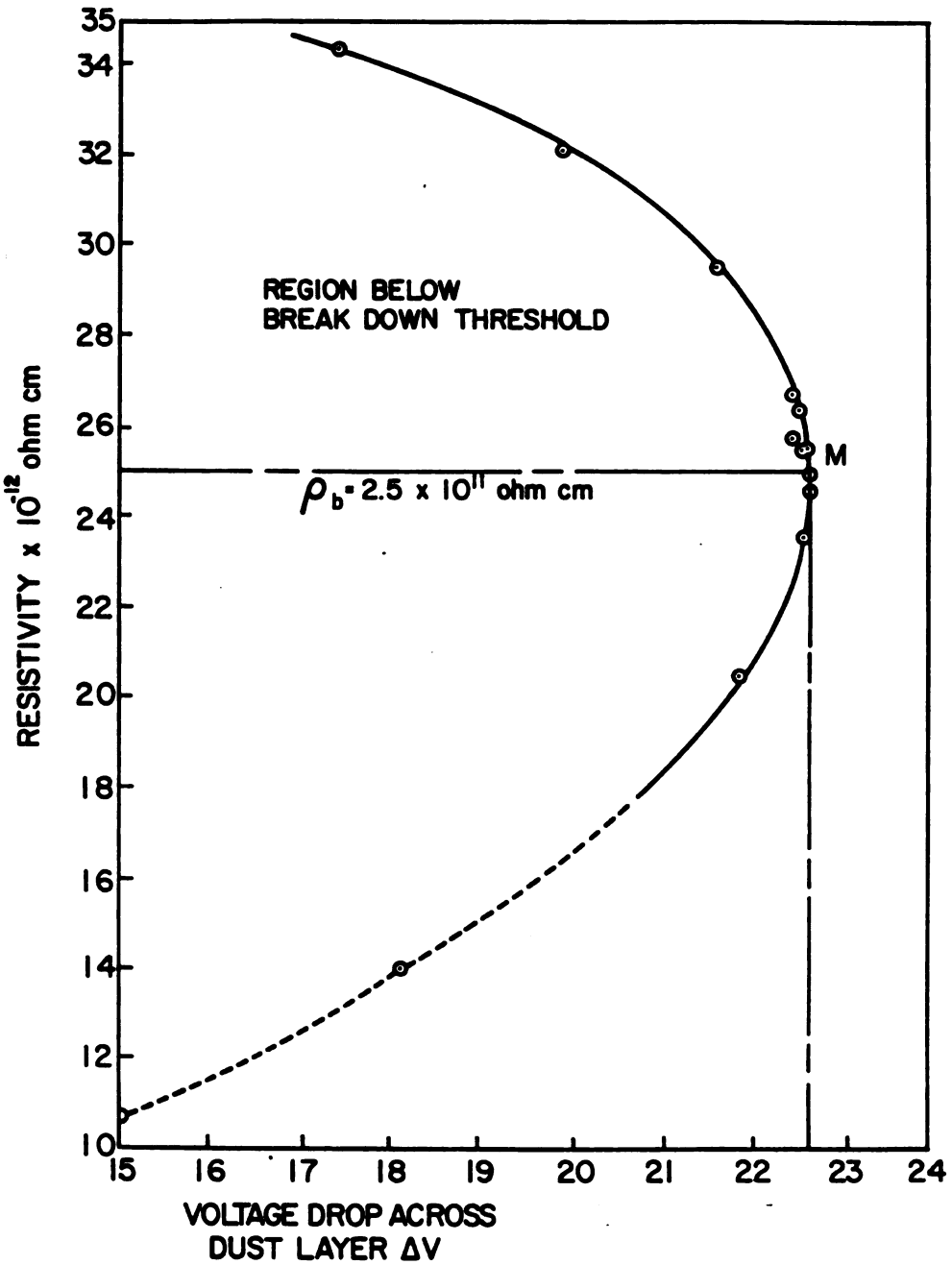

Figure 1.5. Resistivity - ΔV relationship for a typical fly ash layer.

Table 1.3 Resistivity - Voltage Data Used for Figure 1.5

A.

ΔV (KV)	I (μA)	Resistivity (ohm - cm)	V (1) (KV)	V (2) (KV)
1.734	0.90	3.4411×10^{11}	9.95	11.68
1.983	1.10	3.2192×10^{11}	10.63	12.62
2.153	1.30	2.9568×10^{11}	11.29	13.44
2.243	1.50	2.6699×10^{11}	11.91	14.16
2.254	1.70	2.3673×10^{11}	12.51	14.76
2.185	1.90	2.0539×10^{11}	13.07	15.25
2.038	2.10	1.7327×10^{11}	13.60	15.64
1.811	2.30	1.4059×10^{11}	14.10	15.91
1.505	2.50	1.0748×10^{11}	14.57	16.07
Data (for reduced current step size) near region of incipient sparking				
2.240	1.49	2.6847×10^{11}	11.88	14.12
2.247	1.52	2.6403×10^{11}	11.97	14.22
2.253	1.55	2.5955×10^{11}	12.07	14.32
2.257	1.58	2.5504×10^{11}	12.15	14.41
2.259	1.61	2.5050×10^{11}	12.24	14.50
2.259	1.64	2.4594×10^{11}	12.33	14.59

B. Sparking Characteristics

Resistivity	Spark Voltage	$(\rho_b d)$	Layer Thickness	Temperature
2.459×10^{11} ohm-cm	14.59 Kv	6.886×10^{9} ohm-cm^2	0.28 mm	280°F

Table 1.4 Experimental Current-Voltage Data Used to Generate Table 1.3

A. Clean Plate or Flue Gas Characteristic Data

Corona Voltage (kV)	Measured Current (μA)
6.00	0.10
8.00	0.35
10.00	0.80
11.40	1.15
12.40	1.50
13.30	2.00
14.20	2.45
16.00	3.60
17.20	4.65
18.40	5.30

B. Dust Layer Characteristic Data

Corona Voltage (kV)	Measured Current (μA)
11.70	0.90
13.00	1.20
14.50	1.60
16.00	2.40

C. Coefficients of Interpolating Polynomials.

$$V = Z(1) + Z(2)I + Z(3)\ I^2$$

Coefficient	Clean Plate	"Dirty" Plate
Z(1)	6.466	6.099
Z(2)	4.219	7.445
Z(3)	-0.392	-1.383

voltages. Rather, it is preceded by a gradual rise in the spark rate from the point where conditions are just right for the first spark to jump across the dust layer. In view of this fact and the observed ρ_b - ΔV relationship, it is proposed that M is the point of incipient sparking. The inverse relationship between ρ_b and ΔV is borne out by a porous particulate layer that has no localized points of breakdown. That this point M is unique clearly follows from the fact that the above relationship is upheld up to incipient sparking. The sections of the curves below the horizontal line in Figures 1.4 and 1.5 (corresponding to point M) are broken to indicate that they cannot be obtained by the disk method. Thus the point M obtained by a point-plane technique meets the following criteria:

a. It is unique.

b. It artificially defines the breakdown threshold of a porous dust layer.

c. The calculated value of M is consistent with the convention of reporting resistivity close to sparkover.

CHAPTER 2

CAPILLARY CONDENSATION WITHIN THE PARTICULATE LAYER

Overview

The bulk resistivity of a particulate layer of, say, fly ash particles under an externally imposed voltage gradient, is strongly dependent upon the (electrical) resistance that an electron or an ion encounters during its passage from one particle to another. At high temperatures (600° F or greater) such a migration occurs within the body and through the regions of contact of the particles. The resistivity under such conditions is called the volume resistivity. At lower temperatures (less than 400° F), the current carriers migrate along the particle surfaces and the bulk resistivity corresponding to these conditions is termed the surface resistivity.

In an electrostatic precipitator operating at the lower temperatures, the bed of fly ash particles is deposited on vertical grounded plate (collection electrode). The humid flue gas passes over the layer as it traverses the length of the precipitor. From a thermodynamic point of view, the particulates in the bed may be viewed as solid adsorbents for the water vapor in the flue gas. This then leads to a consideration of the adsorption of water vapor on the surface of the particles and in voids formed at the vicinity of the contact. The phenomena of adsorption in these voids (or macropores) is defined as

"capillary condensation" in a restricted sense, since the capillary pores on a particle surface are excluded in this terminology. The presence of this condensed phase modifies the path available for the (surface) migrating ions in the region of particle contact. As indicated later, the liquid condensate is retained in these macropores because of the effects of surface tension.

In this chapter, a thermodynamic analysis of the formation of condensate has been presented initially with the objective of determining the feasibility and extent of the condensation process. This analysis is based on the model developed by Melrose (M4). However, the conclusions based on the present analysis differ from those of the author. These conclusions, especially for the liquid phase behaviour and its physical properties, are discussed in Section 2.14, in light of the arguments presented in the Appendices (C,D and E) accompanying this chapter. The implications of the thermodynamic analyses in the Appendices are particularly relevant for small (molecular) volumes of the liquid condensate.

In Section 2.1 of this chapter, the experimental evidence of the occurence of capillary condensation is presented. The studies in this area were partly motivated by observations made by soil physicists (H5,F5), in the 1920's, on the pick up and retention of moisture in soils. The bulk of the publications appeared in the mid 1950's (C1,P2), however some of the conclusions were clouded by controversies and experimentation continued on through the mid 60's (H6). The present state of knowledge in this area is not complete, though the speculations

now have a stronger theoretical basis. Section 2.2 deals with the idealized particulate model. The necessary physical assumptions (stated in this chapter) are made in order to arrive at a thermodynamic relationship which characterizes the capillary condensation. The analysis of the model begins with Section 2.3 where the thermodynamic system is defined, and in Section 2.4 the various contributions to the total (Helmholtz) free energy change are specified. In Section 2.5, the Laplace and Young equations of capillarity (2.19, 2.20, 2.21), are developed by matching the coefficients of the thermodynamic equation in Section 2.4, and the hydrostatic balance equation for the capillary condensate. The application of the Laplace and Young equations to the specific gas and liquid phases requires that a reference state be defined. Departures from this reference state are measured in terms of liquid and gas chemical potentials. Sections 2.6 and 2.7 deal with the chemical potential changes for the gas, under the assumption that a (truncated) virial equation of state is valid for this phase. The potential changes for the liquid phase arise due to the generalization that the capillary condensate is compressible. These potential changes are evaluated in Sections 2.8 and 2.9. In Section 2.10, the sought after thermodynamic relationship (given at the end of Section 2.8) is discussed in light of the data generated, in this work, for water. The significances of some of the thermodynamic variables, with respect to departures from the state of reference, are presented in Section 2.11. This is followed by a specification of the geometry of the ideal structure, in Section 2.12, which consists of a capillary ring of condensate surrounding the spherical particles in contact. The

important dimensions of this ring are defined; and as outlined in the Summary (Section 2.13), these dimensions are completely specified by the known independent variables associated with this process. The work presented in this chapter is concluded with a discussion of the results in light of the assumptions made in the model as well as the specific arguments presented in the Appendices C, D and E.

2.1. Evidence and Significance of Capillary Condensation

The particulate bed of fly ash can be considered to be a porous system with adsorbate in thermodynamic equilibrium with water vapor contained in an inert carrier gas. Under such conditions, liquid condensate may be present in the crevices formed between solid particles in contact. For low temperature (cold) precipitators (where surface conduction is dominant), this effect needs to be considered because the capillary condensate provides conducting pathways for the current carriers. These current carriers are the electrons* and ions which migrate along the surface from one particle to another. Such a movement of the ions and electrons is therefore, facilitated relative to the case of high temperature (hot) precipitators which operate at temperatures in excess of 600° F and where the fly ash can be considered to be bone dry. On a qualitative basis, it would be expected that the bulk resistivity would be lowered with respect to the bone dry case. Hence the phenomena of capillary condensation needs to be incorporated into any model seeking to relate resistivity to the intrinsic parameters

*Some part of the current carried by the electrons may also be through the gas gap at the vicinity of contact betwen two particles if the fields in the region are high enough (see Chapter 1).

of the fly ash (shape, chemical composition, for example), and the conditions of the ambient environment.

The experimental evidence of the existence of liquid condensate was established by Carman, among others, in 1952 (C1,P2). Nonporous solids exhibit the familiar S-shaped adsorption isotherms. Deviations from this shape are attributable to the phenomenon of capillary condensation, since upon filling of the capillary the pore walls are no longer available for the growth of multilayer films and the isotherm flattens out (Figure 2.1).

This is easily visualized if the capillary filling process is accepted as occurring by one or more of the following two distinct processes.

i) condensate formation leading to a meniscus which bridges the pore walls

ii) growth of a multimolecular film on the capillary walls until the films coalesce to fill the space.

As an example, the adsorption isotherms of two samples of the same material were determined by Carman: one was a loose powder, and the other a compressed plug of porosity equal to 0.5. "If adsorption in the plug only took place by multilayer formation, the adsorption isotherm should lie below that for the powder, since restriction of the pore space limits the thickness of multilayer films. That the converse is true is strong evidence that an additional contribution is being made by capillary condensation" (C1).

Capillary condensation occurs due to the action of tensile forces on the curved surface of the liquid (at the liquid-vapor interface)

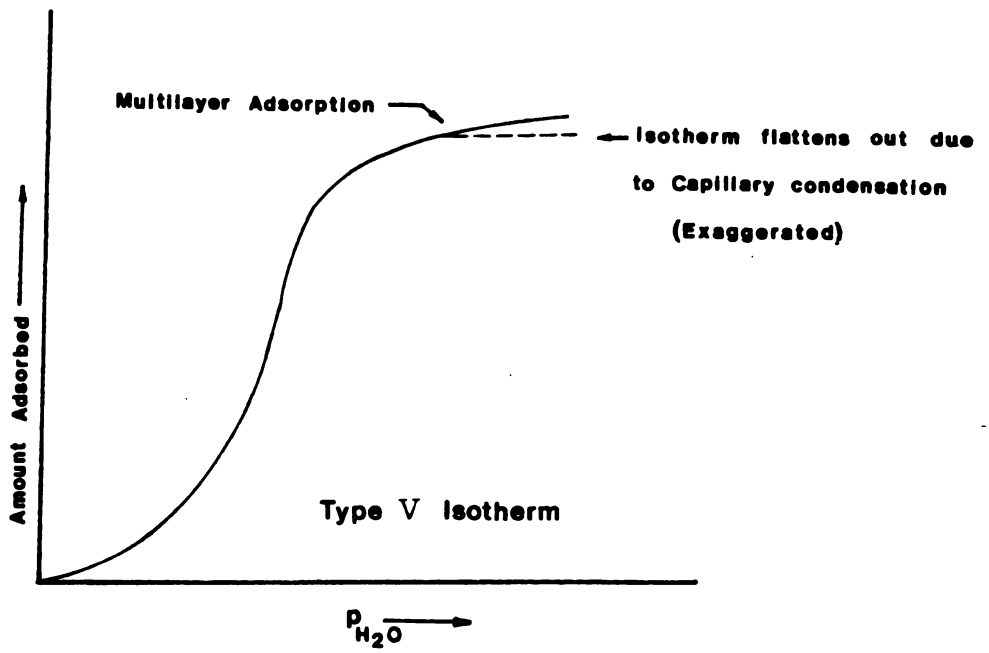

Figure 2.1. Representation of a type V adsorption isotherm illustrating the effect of capillary condensation (S2).

inside the macropore. The vapor pressure corresponding to the liquid in that state, at a given temperature, is lower than the normal vapor pressure (associated with an unconstrained, flat surface). The curvature of the liquid surface reflects the action of the surface tension along that surface as well as the difference in pressure between the two contiguous fluid phases in thermodynamic equilibrium. Hence it is possible to have liquids condensed in the pores and cracks of particles at temperatures above the dew point (C2). Under such conditions the liquid can exist in a state of tension if the pressure differential (between the vapor and the liquid phase) is great enough, and may exhibit physical properties that depart substantially from the values normally attributed to it (C1).

Ditl and Coughlin (D1) approached the problem of moisture conditioning by including the effect of condensation in their expression for the bulk resistivity. This expression contains the liquid phase conductivity as an adjustable parameter with values in the neighbourhood of 2.0×10^{-11} ohm^{-1} cm^{-1}. The work presented in this chapter was motivated by their approach, however it was felt that a detailed evaluation of the capillary condensation process was required before it could be incorporated into any particulate resistivity model.

This chapter attempts to define the physical extent of the capillary condensate by means of a thermodynamic equation (M4) as applied to a simple physical model. The more familiar Kelvin equation is a first approximation of this equation. The appropriate restrictions on the applicability of such an equation to small volumes of condensate (or, equivalently, to large curvatures in this system) are investigated.

A discussion of these restrictions has been presented in Appendix E. A quantitative description of this problem necessitates the specification of the structure of the particles constituting the bed, and of the bed itself.

A description of the idealized particulate resistivity model is given in the next section. The restrictions specified for the physical model apply to the thermodynamics of capillary condensation covered in this chapter. These assumptions also permit some mathematical simplifications of the electrical field equations in Chapter 3.

2.2. Description of the Idealized Model

The particulate bed of fly ash is assumed to be composed of monodisperse, non-rigid* spheres arranged in a regular cubic packing (Figure

*This characterization of elasticity is restrictive to the extent that the contact area between two spheres can be directly related to the cohesive pressure between them (M3). As far as capillary condensation is concerned, the particles are taken to be rigid. In a rigorous treatment, the presence of large tensile forces in the liquid phase would have to be considered in terms of dimensional changes in the solid phase. However, these tensile stresses act upon a small area of the solid. Furthermore, interparticle cohesive forces (electrostatic in origin) exist in such a bed and are due to the presence of strong electric fields in the vicinity of the contact (M3,D2). Since the particles are elastic, as assumed above, the area of contact increases with the interparticle force, and hence with an increase in the bulk resistivity (which induces the strong electric fields) (L1).

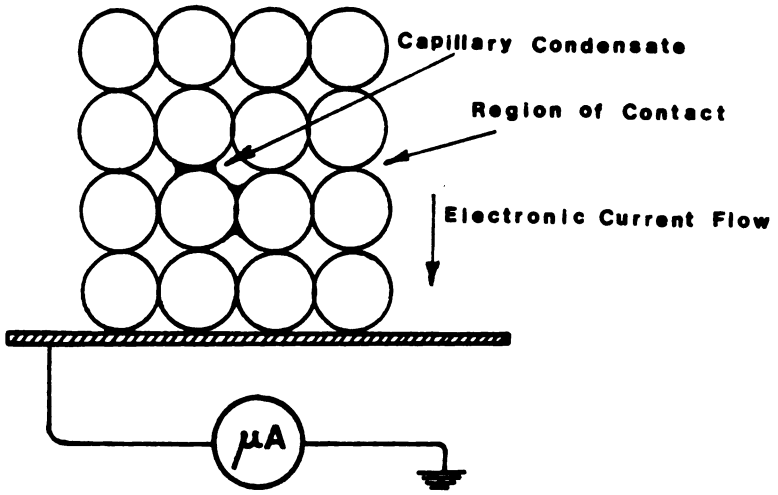

Figure 2.2. Arrangement of ideal spheres in a simple cubic packing.

2.2). The assumption of the spherical shape of the particles is justified by the fact that TEM** micrographs taken of typical fly ash samples reveal the predominance of spheres (Figure 2.3.).

Fisher, et al., (F1,F2,F3) have, in their studies on the chemistry and structure of the particulates, published micrographs that reveal the complex internal structure of the spheres. Eleven major morphological classes have been identified and are related qualitatively to their "probable" matrix compositions. In this classification scheme, these particles are labeled as cenospheres (hollow spheres) and plerospheres (spheres within spheres). A mechanism for their formation has been postulated by Fisher (F4).

The surface morphology, for the purposes of capillary condensate

---

** Transmission Electron Microscope

Figure 2.3. TEM micrographs of experimental fly ash samples.

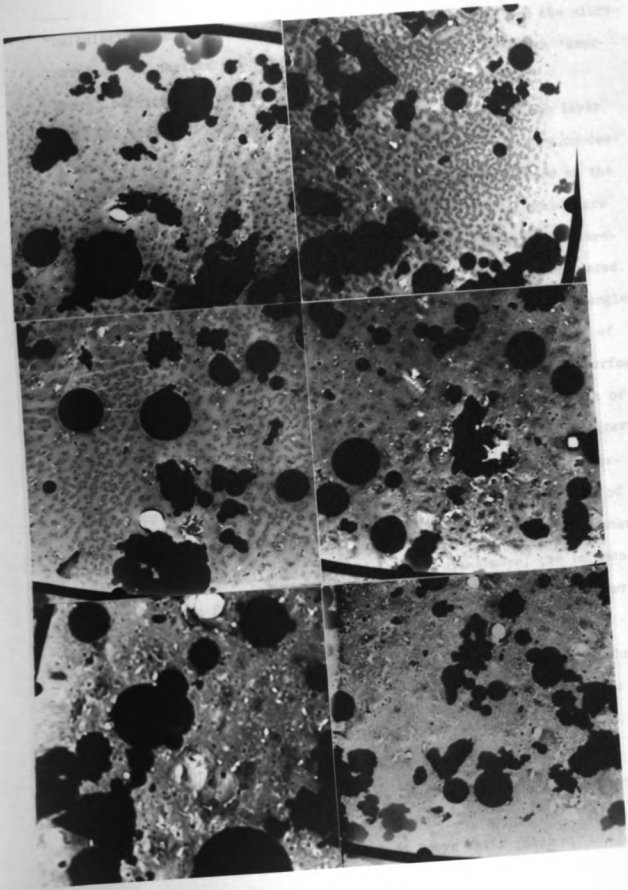

calculations in this chapter, is assumed to be identical, and the micropores on the surface which are invariably associated with such 'amorphous' particulates are neglected.

The influence of humidity of the ambient gas upon the ash layer surface resistivity is limited only to the extent of capillary condensation in the macropores. A macropore in this case is defined as the interparticle space between the ideal spheres. It may be noted here that formation of multilayers (adsorption on the surface) and condensation in the micropores (on the particle surface) are not considered. Water is assumed to wet the surface of particles and, hence, the angle of contact of the meniscus is assumed to be zero (C1). The angle of contact is measured between the tangents to the liquid and solid surfaces at the point of contact of these two phase interfaces. The effect of an externally applied voltage gradient (as also the magnetic and gravitational fields) upon the capillary condensate is excluded. (A formally complete thermodynamic balance would recognize the presence of an electric field, at least in the expression for the total free energy change for the solid-liquid-vapor system). Furthermore, the influence of the electric field upon such a surface phenomena with polar water molecules* is not included.

The temperature range of interest corresponds to the regime where the surface conduction mode is important ($<400^{o}$ F). Both electrons and ions can be visualized as migrating under an external electric field gradient along the spherical particle surface. This regime corresponds to the rising part of the hump shaped curve on the plot

---

*Pure water has a dipole moment of 1.84 Debye units (O1).

of resistivity versus temperature (see Introduction).

Finally, this problem is extended to the general case where both the liquid and vapor phases are assumed to be non-ideal. For the vapor phase a virial equation of state is assumed, and the departure from ideality is accounted for by the second virial coefficient. The liquid, (water in this case) is not assumed to be incompressible.* The study of the relative change of the isothermal susceptibility† with partial pressure of the water vapor is presented in Appendices C and E, and also discussed in Section 2.14 of this chapter.

In the next section, the analysis begins with a description of the thermodynamic system which is illustrated in Figure 2.4.

2.3. The Thermodynamic System

This section deals with a model, consistent with the restrictions imposed upon it, as described in Section 2.2, and with the aim of arriving at a thermodynamic relationship between the radius of curvature of the capillary condensate and the partial pressure (of water), at a fixed ambient temperature.

The non flow system is assumed to consist of two equal spheres in place with a ring of capillary condensate around the region of contact. The liquid is in (static) equilibrium with the surrounding vapor** and the three phase system is enclosed in a piston cylinder arrangement

---

*The assumption of ideality implies that the liquid is incompresible.

†Isothermal susceptibility is defined as $\partial P/\partial \rho_T$, where P is the liquid pressure, ρ is the density, and T is the temperature.

**The vapor phase is a mixture of noncondensible inert gases and water vapor.

which is isothermal. Figure 2.4 depicts the system.

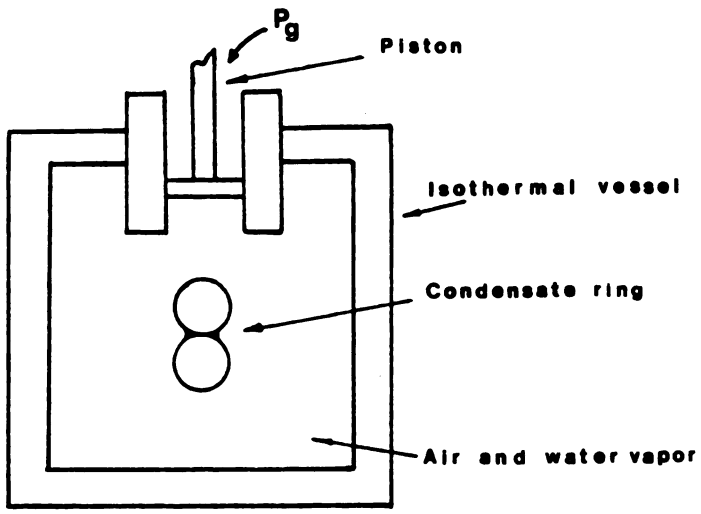

Figure 2.4. Arrangement of the Thermodynamic system.

The objective is to perturb the above system externally by moving the piston so that the total Helmholtz free energy changes by dA, and then examine how this total energy change is distributed between the three phases. The solid is assumed to be inert and a rigid (see footnote, Section 2.2) adsorbent. There are no free energy changes associated with the spherical particles due to lack of dimensional changes. This leaves the total external free energy change to be accounted for by chemical potential changes in the liquid and vapor phases only. Some of the foregoing assumptions (Section 2.2) need to be invoked at this stage in order to restrict the model system to the specific problem. Then, the free energy changes of the liquid and vapor phases can be equated to each other, leading to a simplified thermodynamic equation. The curvature parameter is introduced by examining the hydrostatic

balance of the system. A comparison of the coefficients of these two equations leads to the Laplace and Young equations of capillarity. The first of the two Laplace and Young equations relates the curvature to the pressure difference between the vapor and liquid, and is really a modified form of the thermodynamic equation (or the Kelvin equation).

The total Helmholtz free energy balance for the closed, thermodynamic system (illustrated by Figure 2.4) is given by equation (2.1) in the next section.

2.4. Helmholtz Free Energy Balance

For the closed, macroscopic*, system the total free energy change is given by

$$dA = -\Sigma PdV - SdT + \sigma_{sl}d\Omega_{sl} + \sigma_{lg}d\Omega_{lg} + \sigma_{sg}d\Omega_{sg} + \mu_s dn_s + \mu^{**}_{l/g}dn_{l/g} + \text{terms involving change of } \sigma_{lv} \qquad (2.1)$$

---

*The word macroscopic is used here to designate the amount of the condensate in the macropores. The free energy equation is valid only for large numbers of molecules in the liquid phase. As shown in Appendix E, this corresponds to the situation where the surface tension and the radius of curvature are invariant with the volume of the capillary condensate.

**Chemical potential for liquid and vapor phases are equal at equilibrium, that is, $\mu_l = \mu_v \equiv \mu_{l/v}$.

$$\Sigma PdV = P_s dV_s + P_l dV_l + P_g dV_g \qquad (2.2)$$

where,

A = Helmholtz free energy

P = pressure

V = volume

S = entropy

T = temperature

σ = interfacial tension

Ω = interfacial area between phases identified in subscripts

μ = chemical potential

n = number of moles

The subscripts are as follows:

s = solid, l = liquid, g = gas

l/g = liquid and gas phases, both included.

The sum of the interfacial areas is given in terms of the radius of sphere, R

$$\Omega_{sl} + \Omega_{sg} = 2\ (4\pi R^2) \qquad (2.3)$$

The total volume of the system, V, is given as

$$V = V_s + V_l + V_g \qquad (2.4)$$

It may be noted that the location of the surface of separation needs to be specified. For a one* component system (as in this case), the

location of the surface is mathematically specified by the distribution of that component among the phases (bulk volume) and the interfaces.

$$n_s = P_s V_s \tag{2.5a}$$

$$n_l = P_l V_l \tag{2.5b}$$

$$n_g = P_g V_g \tag{2.5c}$$

and,

$$n_{l/g} = n_l + n_g + \Gamma_{sl} + \Gamma_{sg} \tag{2.6}$$

where

ρ = bulk densities of the various phases

Γ = number of moles of water on the appropriate interface (solid-liquid, solid-gas)

For isothermal conditions, the assumption of an inert adsorbent in a closed system yields:

$$dT = dV_s = dn_s = dn_{l/g} = 0 \tag{2.7}$$

From equation (2.3) it follows

$$d\Omega_{sl} = -d\Omega s_g \tag{2.8}$$

and from equations (2.4) and (2.6), respectively,

---

*One component refers to the water vapor which alone participates in the condensation process.

$$dV = dV_g + dV_l \tag{2.9}$$

$$dn_g = - dn_l - d\Gamma_{sl} - d\Gamma_{sg} \tag{2.10}$$

Substituting relations (2.7) through (2.10) into equation (2.1)

$$dA = - P_l dV_l - P_g(dV-dV_l) + (\sigma_{sl}-\sigma_{sg})\, d\Omega_{sl} + \sigma_{lg} d\Omega_{lg}$$

or

$$dA = - P_g dV + (P_g-P_l)dV_l + (\sigma_{sl}-\sigma_{sg})\, d\Omega_{sl} + \sigma_{lg} d\Omega_{lg} \tag{2.11}$$

From equation (2.11) it is seen that the total change in the free energy is associated with pressure-volume work terms and with interfacial tensions. Referring to Figure 2.3, the change in the Helmholtz free energy of the system is effected by a movement of the piston, hence this total change is given by

$$dA_{total} = - P_g dV \tag{2.12}$$

for reversible, isothermal changes.

Decomposing dA_{total} into an external change dA_{ext}, and an internal change dA_{int}, yields

$$dA_{total} = dA_{ext}^{*} \tag{2.13}$$

---

*This follows from the first law of thermodynamics (for a closed system), and the defining expression for A.

and

$$dA_{int} = 0 \qquad (2.14)$$

The internal energy change is associated with changes in the capillary condensate; and from equation (2.11)

$$dA_{int} = \underbrace{(P_g - P_l)dV_l}_{\text{volume term}} + \underbrace{(\sigma_{sl} - \sigma_{sg})d\Omega_{sl} + \sigma_{lg}d\Omega_{lg}}_{\text{surface terms}} \qquad (2.15)$$

This equation suggests that any change in the volume term should be nullified by an equal and opposite change in the surface terms. This is valid for small changes in V_l, Ω_{sl}, and Ω_{sg} when V_l is not small, so that the coefficients of the terms on the right side of the equation do not change significantly.

The expression (2.15) for the Helmholtz free energy change is compared with the hydrostatic balance in Section 2.5. The Laplace and Young equations of capillarity are obtained upon equating the coefficients of similar terms in equations (2.15), and (2.18) given in the next section.

2.5. Laplace and Young Equations

The Laplace and Young equations are obtained by matching coefficients in equation (2.15) (which is derived from a thermodynamic balance), and the equation for the hydrostatic balance. To obtain this latter balance a mean curvature K, needs to be defined

$$K = \frac{1}{r_1} + \frac{1}{r_2} \qquad (2.16)$$

where r_1 and r_2 are the principal radii of curvature of the ring of

condensate in two mutually perpendicular planes. In this case, if r_1 corresponds to the curvature on the plane of the paper (Figure 2.5), then r_2 belongs in the direction perpendicular to the paper and centered at the point of contact of the spheres. Again, for small changes in V_1 (when V_1 is not small), K is invariant.

The contact angle θ_{sl} is zero (wetting of the solid surface is assumed) and hence, invariant as well. Furthermore, it is assumed that the liquid-vapor interface is spherical. With these assumptions, the following differential equation* holds:

$$KdV_1 + d\Omega_{lg} = \cos\theta_{sl}\, d\Omega_{sl} \qquad (2.17)$$

Multiplying through by the liquid-vapor interfacial tension σ_{lg},

$$\sigma_{lg}KdV_1 + \sigma_{lg}d\Omega_{lg} - \sigma_{lg}\cos\theta_{sl}d\Omega_{sl} = 0 \qquad (2.18)$$

On comparing equations (2.15) and (2.18) the appropriate coefficients are matched to give the Laplace and Young equations

$$P_g - P_l = \sigma_{lg}K \qquad (2.19)$$

and

$$\sigma_{sl} - \sigma_{sg} = \sigma_{lg}\cos\theta_{sl} \qquad (2.20)$$

for the general case of a non zero contact angle, and

---

*Equation (2.17) is easily verified for relatively simple cases, for example liquid in a cylinder. However, the derivation of this equation is non-trivial, and is obtained from differential geometry. In Appendix E the restriction to the use of this equation is discussed.

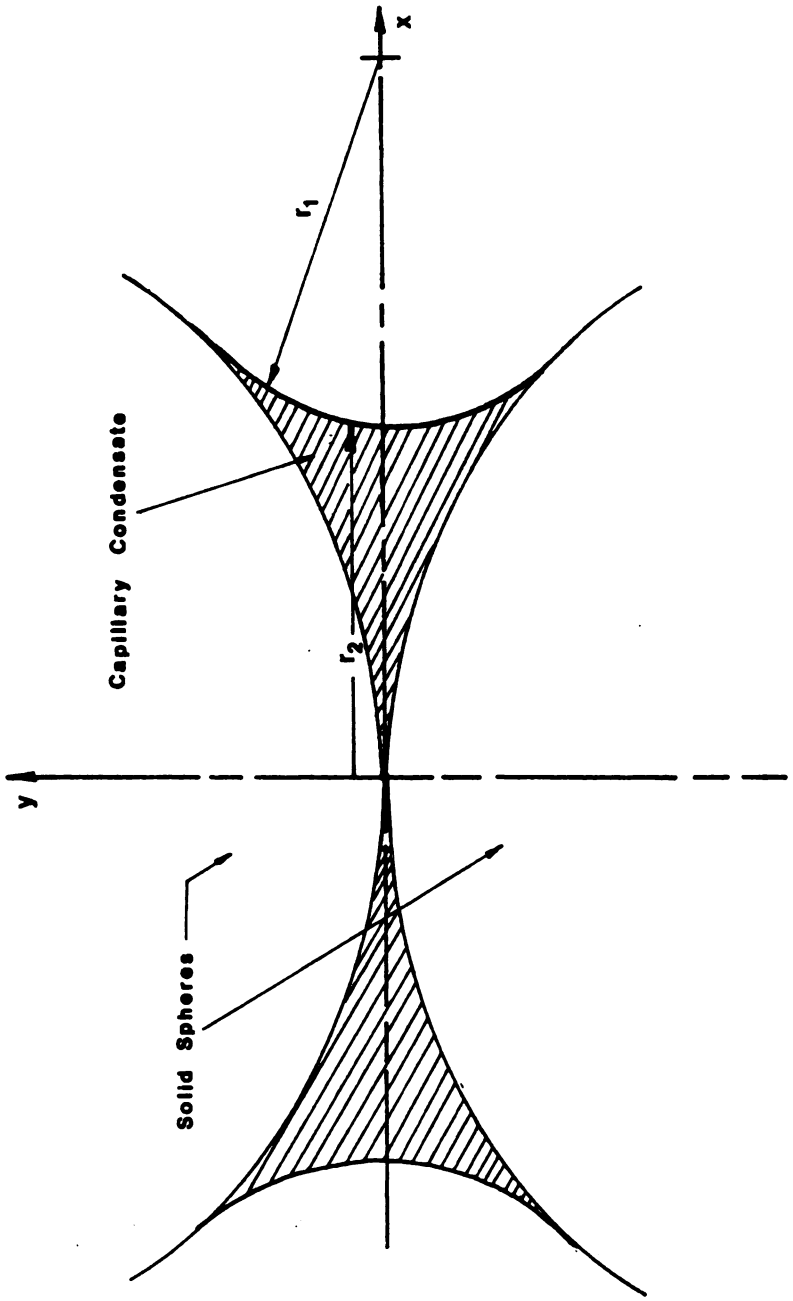

Figure 2.5. Illustration of the principal radii of curvature for the capillary condensate.

$$\sigma_{sl} - \sigma_{sg} = \sigma_{lg} \qquad (2.21)$$

for water, where the angle of contact is zero. An important conclusion follows from equation (2.19) in that the difference of pressures between the two fluid phases is directly proportional to the mean curvature K, provided that the surface tension is constant. As remarked earlier (see footnote, page 39) this is valid only for "macroscopic" volumes of condensate. This assumption fails to hold where the volume corresponds to linear dimensions of the order of molecular diameters.

The pressure P_g in equation (2.19) is related to the gas phase chemical potential term $\Delta\mu_g$ by means of the (truncated) second virial equation of state. This relationship is developed in the next section.

2.6. Chemical Potential Changes in the Gas Phase

As stated earlier since the solid has been assumed to be inert, the equilibrium between the gas and liquid phases need only be considered. The potential changes are measured with respect to a reference state which is given by equations (2.22) and (2.23).

$$K = 0 \qquad (2.22)$$

$$P_G = P_G^{o} \qquad (2.23)$$

This reference state therefore implies a liquid meniscus which is flat and in equilibrium with gas containing water vapor at its saturation pressure (P_G^{o}) for a given temperature. Further discussions regarding this reference state follow later in this chapter.

At equilibrium, (see footnote on page 39).

$$\mu_l = \mu_v \tag{2.24}$$

Denoting the departure of chemical potential from the reference state (identified by superscript ^{o}) by $\Delta\mu_g$ and $\Delta\mu_l$

$$\Delta\mu_g = \mu_g^o - \mu_g \tag{2.25}$$

$$\Delta\mu_l = \mu_l^o - \mu_l \tag{2.26}$$

Equation (2.27) holds when the departures from the reference state are induced reversibly so that the system is always at equilibrium

$$\Delta\mu_g = \Delta\mu_l \tag{2.27}$$

To calculate $\Delta\mu_G$, $\Delta\mu_l$, state relationships for the liquid and gas phases are required. For the gas, as mentioned earlier, a virial equation of state is assumed:

$$Z = \frac{P\tilde{V}_g}{RT} = 1 + B\rho_g + Cp_g^2 + ... \tag{2.28}$$

where

Z = compressibility factor

B,C = second and third virial coefficients respectively

R = universal gas constant

$\tilde{V}_g$ = molar volume of water vapor

ρ_g = molar density of water vapor

To a first approximation, equation (2.28) is truncated to give

$$P_g = \rho_g RT\ (1+B\rho_g) \tag{2.29}$$

The chemical potential is related to the fugacity (f) for a real gas as

$$\mu_g = \phi_1(T) + RT \ln f^* \tag{2.30}$$

where $\phi_1(T)$ is a function of the temperature only. For a real gas the fugacity is given (K1) in terms of the state (equation) variables by

$$\frac{\partial \ln(f/P_g)}{\partial P_g}_T = \frac{\tilde{V}_g}{RT} - \frac{\partial \ln P_g}{\partial P_g} \tag{2.31}$$

This is integrated to give

$$\ln f = \ln P_g + \int_0^P \left(\frac{1}{\rho_g RT} - \frac{1}{P_g}\right) dP_g \tag{2.32}$$

Substituting for P_g from (2.29)

$$\ln f = \ln [\rho_g RT(1+\rho_g B)] + \int_0^P \left[\frac{1}{\rho_g RT} - \frac{1}{\rho_g RT(1+B\rho_g)}\right] [RT+2BRT\rho_g] d\rho_g \tag{2.33}$$

The integral** is resolved to give the following expression

---

*The second term of this equation is really f/f^o; but the standard state is so chosen that $f^o = 1$.

**The standard integral $\int \frac{x\,dx}{a+bx} = \frac{x}{b} - \frac{a}{b^2} \ln (a+bx)$ is used.

$$\ln f = \ln P_g + 2B\rho_g - \ln (1+B\rho_g) \qquad (2.34)$$

The third term in equation (2.34) is approximated as

$$RT \ln (1+B\rho_g) \simeq RT\, B\rho_g \qquad (2.35)$$

Substituting the resulting expression for fugacity into (2.30) for the chemical potential

$$\mu_g = \phi_1(T) + RT \ln P_g + RT\, B\rho_g \qquad (2.36)$$

at the reference state $\mu_g = \mu_g^o$, $P_g = P_g^o$, hence

$$\mu_g^o = \phi_1(T) + RT \ln P_g^o + RT\, B\rho_g^o \qquad (2.37)$$

The departure from the reference state, $\Delta\mu_g$, is obtained from the difference between (2.37) and (2.36)

$$\Delta\mu_g = \mu_g^o - \mu_g = -RT \ln \alpha + BP_g^o (1-\alpha)^* \qquad (2.38)$$

---

*The second term $\Delta\mu_g^{(c)}$ in equation (2.38) is obtained as follows:

$$\rho_g RT \simeq P_g (1-B\rho_g+\ldots.) \qquad (2.38a)$$

$(B\rho_g)^2 << 1$

$$\Delta\mu_g^c = B\{RT(\rho_g^o-\rho_g)\} = B[P_g^o (1-B\rho_g^o+\ldots) - P_g(1-B\rho_g+\ldots)]$$

$$\simeq B(P_g^o-P_g)$$

$$= B\Delta P_g$$

$$\text{or } \Delta\mu_g^c = BP_g^o(1-\alpha) \qquad (2.38b)$$

$$\text{where } \Delta P_g = P_g^o(1-\alpha) \qquad (2.38c)$$

where α = relative saturation (P_g/P_g^{θ}) or

$$\Delta\mu_g = \Delta\mu_g^{id} - \Delta_{\mu g}^{c} \qquad (2.39)$$

where $\Delta\mu_g^{id}$ is the departure (from the reference state) for the ideal gas case

$$\Delta\mu_g^{id} = -RT \ln \alpha \qquad (2.40)$$

and $\Delta\mu_g^{c}$ is the correction term given in terms of the second virial coefficient

$$\Delta\mu_g^{c} = - BP_b^{0}(1-\alpha) \qquad (2.41)$$

It is seen that when $\alpha = 1$, $\Delta\mu_g^{c} = 0$ at the reference state.

The variation of B with temperature needs to be known before $\Delta\mu_g^{c}$ can be evaluated from equation (2.41). This is accomplished in the next section beginning with the virial equation of state for water vapor.

2.7 Estimation of the Second Virial Coefficient for Water Vapor

One method of evaluating the error introduced by truncating the virial equation beyond the second coefficient would be to determine the magnitude of this coefficient and the deviation from ideality that it implies. Generally, at low or moderate pressures the virial equation of state is a fairly good approximation (as indicated later). Such an equation is applicable for all uncharged (electrically neutral) molecules, polar or nonpolar, regardless of molecular complexity (P3).

For real gases, virial coefficients account for the presence of the intermolecular forces which are nonexistent in the ideal case. In the case of pure components, the coefficients are functions only of the temperature. The second virial coefficient takes into account deviations from ideality resulting from the collisions or interactions of two molecules. For pure, polar gases this is obtained from the empirical correlation of O'Connell and Prausnitz (01) in terms of the reduced second virial coefficient and the molecular polarity. The set of empirical equations, (2.42) through (2.48) are taken from reference (01).

For a single component

$$\frac{P_c B}{RT_c} = f^{(0)}_{BR}(T_R) + \omega_H f^{(1)}_{BR}(T_R) + f_{\nu R}(\nu_R, T_R) + \lambda f_{aR}(T_R) \qquad (2.42)$$

where,

Subscripts

c = critical

R = reduced

H = homomorph*

ν = dipole moment

a = association

$f^{(0)}_{BR}$ = reduced second virial coefficient for fluids with $\omega_H = 0$ (see equation 2.46)

---

*A homomorph of a polar molecule is a nonpolar molecule having approximately the same size and shape as those of a polar molecule.

$f^{(1)}_{BR}$ = correction function (see equation 2.47)

ω_H^* = acentric factor of the homomorph.

The function $f_{\nu R}$ is an empirical one and is a contribution due to the polarity of the molecule to the term on the left side of equation (2.42). It is given as

$$f_{\nu R} = -5.237220 + 5.665807 \ (\ln_{\nu R}) - 2.133816 \ (\ln\nu_R)^2 + 0.2525373 \ (\ln\nu_R)^3 + \frac{1}{T_R} \{\phi\nu_R\} \quad (2.43)$$

where

$$\phi_{\nu R} = 5.769770 - 6.181427 \ (\ln\nu_R) + 2.283270 \ (\ln\nu_R)^2 - 0.2649074 \ (\ln\nu_R)^3 \quad (2.44)$$

(valid for $\nu_R > 4$)

The contribution of the last term on the right side of equation (2.42) is due to the tendency for a component to associate with itself (dimerize, for example).

λ is the corresponding association constant, and for water it is equal to zero. The function f_{aR} is given by

$$f_{aR} = \exp [6.6 \ (0.70 - T_R)] \quad (2.45)$$

The functions $f^{(0)}_{BR}$ and $f^{(1)}_{BR}$ are as follows:

---

*This is a macrospic measure of the extent to which a force field around a molecule deviates from spherical symmetry. ω_H (spheres) ≈ 0.

$$f_{BR}^{(0)} = 0.1445 - \frac{0.330}{T_R} - \frac{0.1385}{T_R^2} - \frac{0.0121}{T_R^3} \qquad (2.46)$$

$$f_{BR}^{(1)} = 0.073 + \frac{0.460}{T_R} - \frac{0.50}{T_R^2} - \frac{0.097}{T_R^3} - \frac{0.0073}{T_R^8} \qquad (2.47)$$

As mentioned above, $f_{BR}^{(1)}$ is a correction function and its product with ω gives the effect of eccentricity on B.

Finally, the reduced dipole moment ν_R (in Debye units) is defined by equation (2.48)

$$\nu_R \equiv 10^5 \nu_{H_2O}^2 P_c/T_c^2 \qquad (2.48)$$

Substitution of the values for the above functions in (2.42) gives the second virial coefficient B at a specific temperature. For water, the following values are obtained for the reduced dipole moment, the association constant and the acentric factor

ν = 1.84 D

γ = 0.00

ω_H = 0.01

The reduced dipole moment is

$$\nu_R = \frac{10^5 (1.84)^2 (218.4)}{(374.15+273)^2} = 176.55$$

All of the laboratory sodium diffusion experiments were conducted in a temperature regime corresponding to the rising part of the resistivity-temperature curve between 150° F - 350° F (see Introduction). Hence

the values of B are required within this temperature range. A sample calculation for T = 290° F is shown.

$$T_R = T/T_c = 0.643;$$

$$f_{\nu R} = -0.8347;$$

$$f_{BR}^{(0)}(T_R) = 0.1445 - 0.330/(0.643) - 0.1385/(0.643)^2 - 0.0121/(0.643)^3$$

$$= -0.7486$$

$$f_{BR}^{(1)}(T_R) = 0.073 + 0.460/(0.643) - 0.50/(0.643)^2 - 0.097/(o.643)^3$$

$$- 0.0073/(0.643)^8 = -1.0334$$

R (gas constant) = 82.057 atm-cc/g mole - °K

Substituting these values in the expression for B (2.42) gives

$$\frac{P_c B}{T_c} = 82.057\ \{-0.7486 + (0.01)(-1.0334) - 0.8437 + 0.00\}$$

or

$$B = -387.485 \text{ cc/g mole}$$

The values of the functions $f_{\nu R}$, $f_{BR}^{(0)}$, $f_{BR}^{(1)}$ and the second virial coefficient were calculated at other experimental temperatures and these are shown in Table 2.1 below.

Table 2.1 Values of the second virial coefficient (B) at various temperatures.

Temperature °C	$f_{\nu R}$	$f_{BR}^{(0)}$	$f_{BR}^{(1)}$	B cc/g mole
65.56(150)*	-1.47108	-1.07740	-2.8576	-626.603
98.89(210)	-1.16494	-0.91280	-1.7650	-509.487
126.67(260)	-0.94981	-0.80430	-1.2497	-429.544
143.33(290)	-0.83470	-0.74860	-1.0334	-387.485
157.22(315)	-0.74520	-0.70645	-0.8879	-355.122
176.67(350)	-0.62960	-0.65340	-0.7243	-313.718

*The number in parenthesis is the temperature in degree F.

It is seen that the value of B increases with increasing temperature. However, the deviation from ideality decreases as the temperature rises. This deviation is given by the term $B\rho_g$ in equation 2.29).

Temperature (^oF)	$\lvert B\rho_g \rvert$	Deviation
150	2.256×10^{-2}	2.26%
350	8.507×10^{-3}	0.85%

It may be noted that the above correlation is only approximate, principally because information on the dipole moment is not complete. For example, the location of the dipole moment on the molecule needs to be known, in addition to its magnitude.

In view of the uncertainty involved in the above correlation, it was found necessary to compare values of B obtained by other methods. Black (B4) has used a van der Waals type equation containing an attraction coefficient ζ which is a function of temperature and pressure. The product of ζ with the van der Waals constant a is called the molal cohesive energy. Defining $\hat{B}$ as the negative of the residual volume, one obtains

$$\hat{B} = b - a\zeta/RT \qquad (2.49)$$

The underlying assumption is that, for the nonpolar components, the molal cohesive energy at zero pressure $a\zeta^o$ is a generalized function of the reduced temperature. For polar compounds, additional terms are required which contain empirical constants specific to each substance. The second virial coefficient is given by equation (2.49) and the value at zero pressure $\hat{B}_0$ is related to B in equation (2.42) as

$$B = \hat{B}_0/(1-\rho\hat{B}_0) \qquad (2.50)$$

In the case of water vapor, $\hat{B}$ is not sensitive to changes in pressure (at moderate pressures). Further, for gases with molecular weights $\simeq$ 29 (air, flue gas for example), $\rho\hat{B}_0 << 1$.

Therefore

$$B \simeq \hat{B}_0 \qquad (2.51)$$

Black has published values of $\hat{B}_0$ for water vapor and these have been plotted against temperature in Figure 2.6. The calculated values of B presented in Table 2.1 are shown in the same graph for purposes of comparison. It may be observed here that at the higher temperatures $|B_{calculated}|$ are greater than Black's values or, equivalently, that the O'Connell and Prausnitz correlation predicts relatively larger departures from ideality. However, both curves indicate the decreasing effect of the dipole moment with increasing temperatures as also shown by the magnitude of $f_{\nu R}$ in Table 2.1.

The choice of the O'Connell and Prausnitz method was made partly because of the uncertainty associated with the second virial coefficient (from a van der Waals type equation) at the higher temperatures where experimental data are lacking (see Figure 3, reference B4). The number of fitting parameters used in the first correlation are greater, also specific values are assigned to the individual (physical) variables listed below:

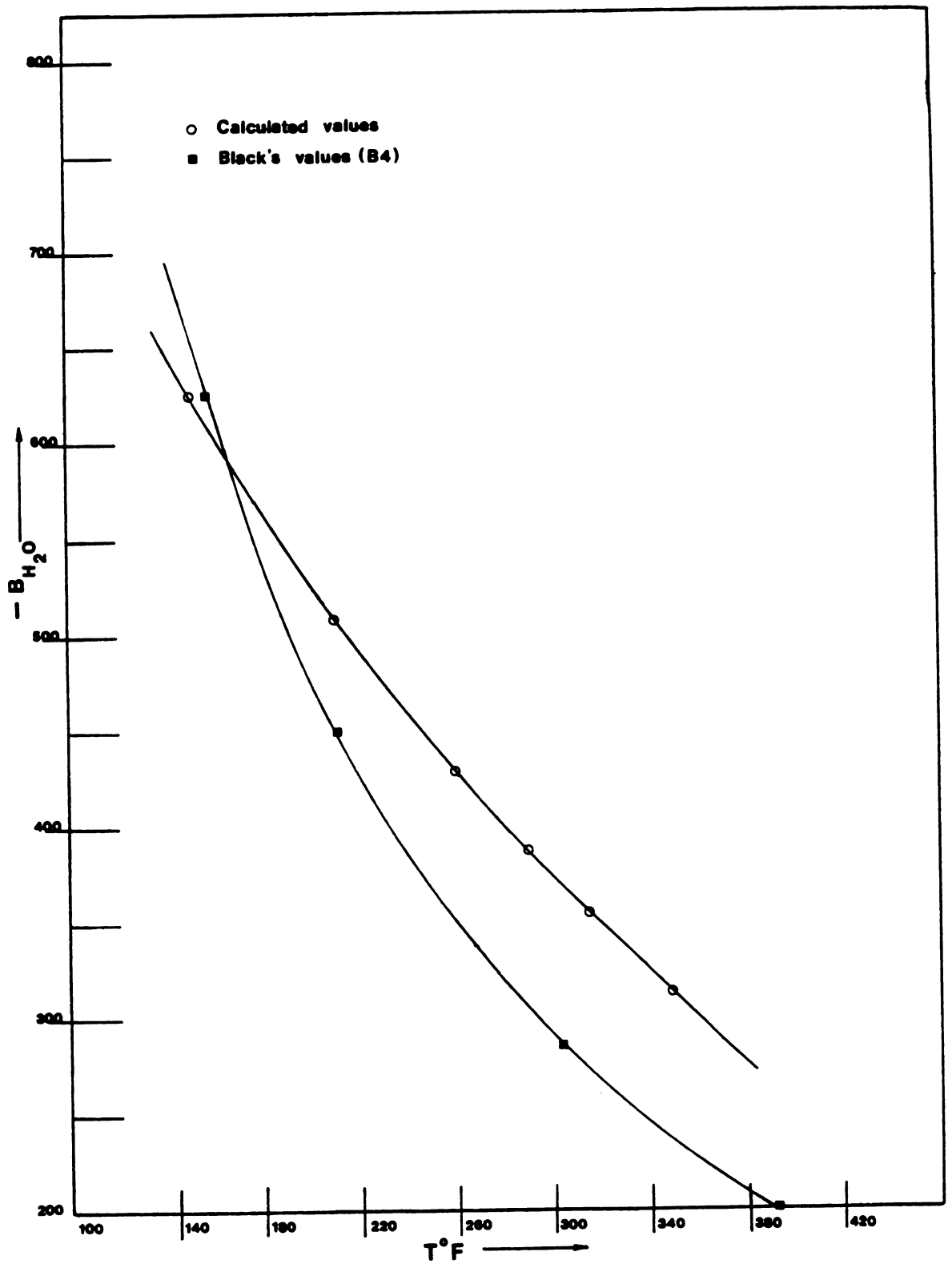

Figure 2.6. Variation of the second virial coefficient (B_{H_2O}) with temperature at moderate pressures.

i) Pitzer's acentric factor, ω_H

ii) dipole moment, ν

iii) association constant, γ

It is seen from Table 2.1 that the effect of acentricity [$f_{BR}^{(1)}$] (due to the noncentral intermolecular forces) on the second virial coefficient diminishes with increasing temperature, although numerically it is greater than both the moment and the association functions.

Section 2.8 deals with the chemical potential changes for the liquid phase. The generalization that the liquid state is compressible provides the basis for such potential changes associated with departures from the reference state.

2.8. Chemical Potential Change in the Liquid Phase

Referring to Figure 2.4 it is seen that fractional changes in the volume of the liquid (capillary condensate) are far more significant than those in the gas phase since the gas volume is much larger than the liquid. This fact, although obvious, is highlighted when one attempts to extend the range of the thermodynamic equation to extremely small volumes of condensate. As discussed in Section 2.14 the liquid is in a state of tension (negative pressure) when the relative saturation α decreases below a certain value α_o. The volume of the capillary condensate decreases with decreasing α (Section 2.11), and liquid behaviour for $\alpha < \alpha_o$ begins to deviate markedly from its behaviour in the positive pressure region. Hence, in contrast to the previous section, where an a priori assumption of an equation of state for a real gas is valid for the entire range, $P_g = P_g^0$ to $P_g = 0$, an equivalent assumption for the liquid phase becomes meaningless when the liquid

volumes are small. In addition, the Laplace and Young equations* do not apply very well and the equations (although intuitively correct), are essentially incomplete since they lack terms which are not negligible any longer in this extreme case (Appendix E and Section 2.14).

For "macroscopic" volumes of liquid, or equivalently, for relatively small departures of liquid (chemical) potential from the reference state (P_g not $<<$ P_g^0), a compressibility equation of state is assumed to hold

$$\chi_1 = \frac{1}{\rho_g \beta}** = \left(\frac{\partial P}{\partial \rho}\right)_T \qquad (2.52)$$

where χ_1 is the isothermal susceptibility. The non-ideality of the liquid is due to the finite isothermal susceptibility.

Defining relative density η_T* (at constant temperature) as

$$\eta_T = \rho_1/\rho_1^0 \qquad (2.53)$$

and using the general representation for $d\mu_T$† at constant temperature

$$d\mu_T = (\tilde{v}_1 dP)_T \qquad (2.54)$$

The change in the liquid phase chemical potential is given in terms of the isothermal susceptibility by equation (2.45)

---

*This is because the equations imply the invariance of surface tension with curvature, as mentioned earlier.

**β = compressibility coefficient = $-1/v\ (\partial v/\partial P)_T$

†Henceforth η_T and μ_T are designated by η and μ_1 respectively, understanding that the terms apply to isothermal conditions.

$$\Delta\mu_1 = \int_{\eta}^{1} \chi_1 d\ln \eta \qquad (2.55)^{\dagger}$$

Also the change in pressure in the liquid (departure from the saturation vapor pressure) is given as

$$\Delta P_1 = \rho \int_{\eta}^{1} \chi_1 d\eta \qquad (2.56)^{\dagger}$$

Generally, the relative density η does not vary drastically even within a wide range of liquid pressures (see Table D3, Appendix D). So for very large values of the isothermal susceptibility (in the ideal case this is infinite), the numerical values of the integrals in (2.55) and (2.56) are dominated by χ_1. Referring back to equation (2.54)*; for the "macroscopic" case:

$$\rho_1^{o} \Delta\mu_1 = \Delta P_1 + \rho_1^{o}\Delta\mu_1^{c} \qquad (2.58)$$

where now $\Delta\mu_1^{c}$ takes care of the deviation from ideality which arises due to the change in η with liquid pressures. It must be pointed out that though equation (2.58) (as written) is formally correct, it is valid for liquid states not too far removed from the reference state. The reason for this lies in the fact that the liquid phase pressure decreases for any departure from the reference state and the available empirical relationships between compressibility β and the liquid volumes exist in the range of low to high positive pressures. As is mentioned later, serious inconsistencies occurred with this approach which, in effect, amounts to the use of a non-deterministic expression (between χ_1 and η) over the entire range of liquid states (from one of

*$d\mu = (vdP)_T = dP/\rho_1$ where ρ_1 is the molar density.

†

Equations (2.55) and (2.56) are obtained as follows:

From (2.54), $$\Delta\mu_1 = \int_{P^o_1}^{P_1} \frac{dP_1}{\rho_1} \quad [\rho_1 = 1/v_1] \tag{2.57}$$

$$\Delta P_1 = \int_{P_1}^{P^o_1} dP_1 = \int_{\rho_1}^{\rho^o_1} \left(\frac{\partial P}{\partial \rho}\right)_T d\rho = \int_{\rho_1}^{\rho^o_1} \chi_1 d\rho$$

Substituting for $d\rho$ from (2.52)

$$\Delta P_1 = \rho^o_1 \int_{\eta}^{1} \chi_1 d\eta \tag{2.56}$$

now

$$\Delta\mu_1 = \rho^o_1 \int_1^{\eta} \frac{\chi_1 d\eta}{\rho^o_1 \eta}$$

from equations (2.53), (2.57) and (2.56)

$$\Delta\mu_1 = \int_1^{\eta} \chi_1 d\ln\ \eta \tag{2.55}$$

compression to one of tension). As stated in Section 2.1, the validity of such an approach is questionable (apart from the numerical inconsistencies)* in light of the fact that physical properties (of the capillary condensate) such as density, surface tension (H3), freezing point and the latent heat of vaporization are different from those for a bulk liquid.

An integral expression for $\Delta\mu_1^c$ is obtained from equation (2.58) upon substitution for $\Delta\mu_1$ and ΔP_1 from (2.55) and (2.56)

$$\Delta\mu_1^c = \int_\eta^1 \chi_1 \left(\frac{1}{\eta} - 1\right) d\eta \qquad (2.59)$$

or equivalently

$$\Delta\mu_1^c = \int_{P_1}^{P_1^o} \hat{v}_1 \, dP_1 - \hat{v}_1^o \int_{p_1}^{p_o} dp_. \qquad (2.60)$$

Where $\hat{v}_1^o$ is the molar volume of the liquid at the reference state.

Substitution of the values of $\Delta\mu_g$ (2.39) and $\Delta\mu_1$ (2.58) into equation (2.27) gives the expression for the change (from the reference state) in the liquid phase pressure ΔP_1:

$$\Delta P_1 = \rho_1^o [\Delta\mu_g^{id} - \Delta\mu_g^c - \Delta\mu_1^c] \qquad (2.61)$$

Recalling that $K = 0$ and $P_g = P_g^o$ at the reference state, equation (2.19) gives

$$\Delta P_g - \Delta P_1 = (P_g^o - P_g) - (P_1^o - P_1) = -\sigma_{1g}K$$

The final thermodynamic expression is obtained by substituting for ΔP_1

---

*See Appendices C and D.

from above into equation (2.61)

$$\sigma_{lg}K = \rho_l^o [\Delta\mu_g^{id} - \Delta\mu_g^c - \Delta\mu_l^c] - \Delta P_g \qquad (2.62)$$

Thus the curvature of the liquid meniscus is explicitly given in terms of the (chemical) potential changes of the liquid and the gas phases. The individual terms need to be (numerically) known in order to estimate the mean curvature K. The next section deals with the evaluation of the chemical potential changes for the liquid phase.

2.9. Evaluation of the Chemical Potential Changes in the Liquid Phase for Positive Pressures

A quantitative estimate for $\Delta\mu_l$ and $\Delta\mu_l^c$ at given conditions of gas phase temperature and pressure* presupposes an algebraic relationship between susceptibility χ_l, and the relative density of water η. As stated in Section 2.8, this information is available either as an empirical equation or as tabulated data for positive pressures. Kell and Whalley (K2) have formulated a nineteen parameter polynomial relating the specific volume of water to its pressure and temperature. This empirical equation of state is written as:

$$V_l\ (T,P_l)/V_l(T,1\ \text{atm}) = 1 + \sum_{k=0}^{5} \sum_{l=1}^{3} a_{kl} T^k\ (P_l - P_{lA})^l \qquad (2.63)$$

The coefficients a_{kl} of this equation are shown in Table 2.2.

The first few terms of this equation are:

---

*This refers to the partial pressure of water vapor (P_{H_2O}) At conditions other than those at the reference state; and the state of the liquid for $K \neq 0$ is sensitive to P_{H_2O}.

$$\frac{V_1\ (T,P_1)}{V_1(T,1\ \text{atm})} = 1 - 50.9769\text{x}10^{-6}\ (P_1-P_{1A}) + 8.2627 \times 10^{-9}\ (P_1-P_{1A})^2$$
$$- 9.109\text{x}10^{-13}\ (P_1-P_{1A})^3 + 3.7199 \times 10^{-6}\ (0.1T)\ (P_1-P_{1A})$$
$$- 1.3794\text{x}10^{-9}\ (0.1T)\ (P_1-P_{1A})^2 + ...$$

Table 2.2. Coefficients of the Kell-Whalley equation (2.63).
[T in deg. C., P_1 in bars, P_{1A} = 1 atm, V_1 in cc/gm]

Temperature	First term	Pressure coefficients		
	1	$10^{-6}\ (P_1-P_{1A})$	$10^{-9}\ (P_1-P_{1A})^2$	$10^{-13}\ (P_1-P_{1A})^3$
1	1	-50.97690	8.2626	-9.109
$10^{-1}T$		3.71999	-1.3794	2.626
$10^{-3}T^2$		-7.01760	3.4032	-8.913
$10^{-5}T^3$		6.00227	-3.6432	11.467
$10^{-7}T^4$		-3.09041	2.0836	-7.102
$10^{-10}T^5$		5.93416	-4.1744	14.841

To determine ($V_1(T,P_1)$ using equation (2.63), the specific volume of water at each of the experimental temperatures T and (1 atmosphere) pressure is required. The available data (K2) in this temperature range is presented in Table 2.4 and was plotted as shown in Figure 2.7. The required values of $V_1(T,1\ \text{atm})$ were obtained by interpolation. In Table 2.3 are shown the specific volumes and the saturation vapor pressures at each temperature. These specific volume values were obtained from the graph in Figure 2.7.

Table 2.3. Specific volumes of water at the laboratory experimental temperatures* and 1 atm. pressure

Temperature [°C (°F)]	p_g^o [atm]	p_g^o [bars]	$V_l(T,1atm)$ [cc/gm]
65.56(150)*	0.2530	0.2563	1.02130
98.89(210)	0.9616	0.9743	1.04261
126.67(260)	2.4107	2.4425	1.06670
143.33(290)	3.9176	3.9692	1.08351
157.22(315)	5.6821	5.7569	1.09856
176.67(350)	9.1617	9.2824	1.12340**

**This value obtained from Perry (P4), Table 2.29, page 371.

Table 2.4. Kell and Whalley Specific Volume - Temperature Data (K2).

Temperature [°C]	V_l(1 atm) [cc/gm]
80	1.029024
85	1.032398
90	1.035928
100	1.043450
110	1.051593
120	1.060363
130	1.069790
140	1.079900
150	1.090734

*These temperatures are for the experiments conducted in the present work.

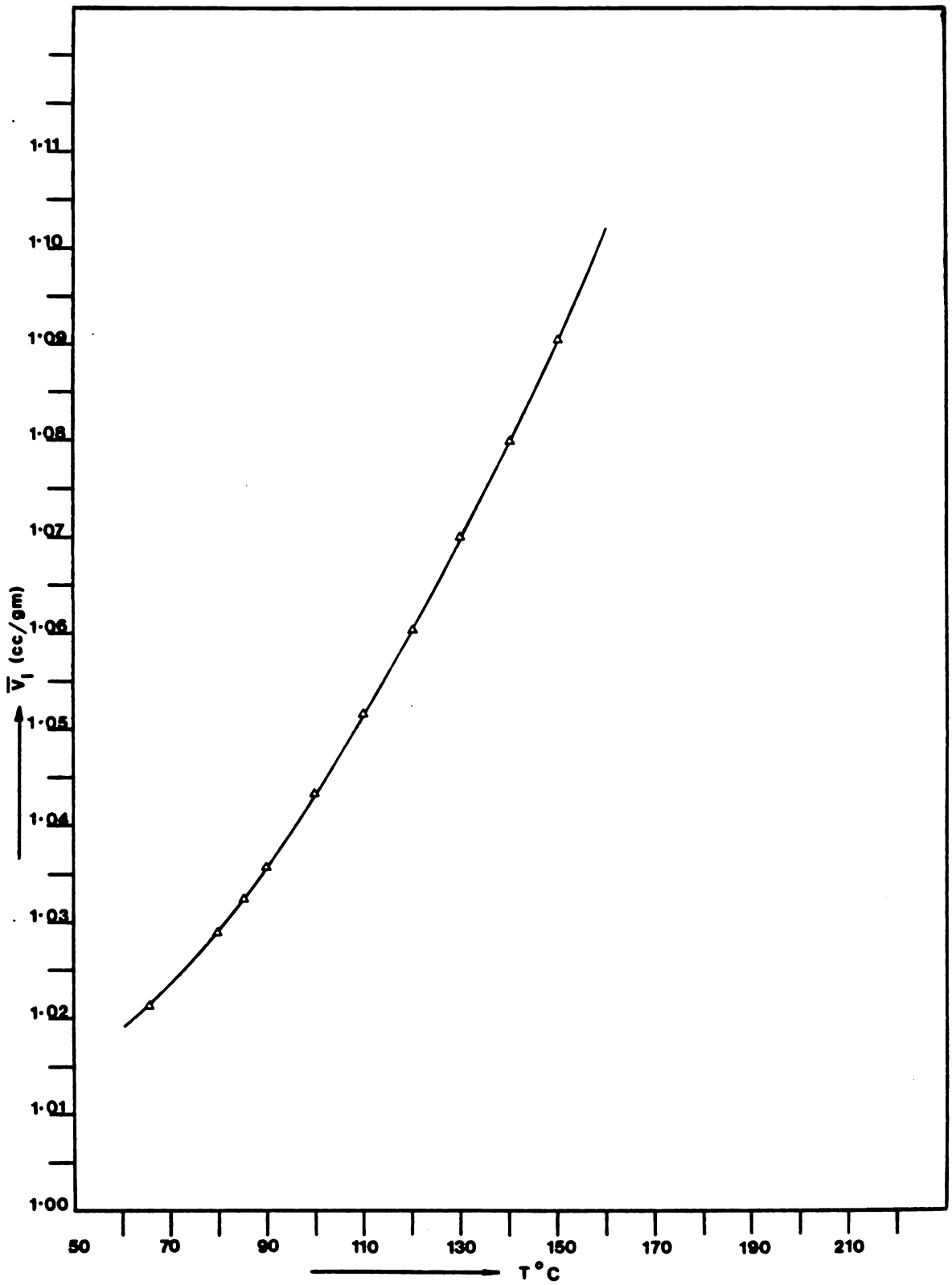

Figure 2.7. Variation of the specific volume of water with temperature at 1 atmosphere pressure.

Once the variation of specific volume with pressure* is known, all of the other physical properties needed to estimate $\Delta\mu_1$ are easily evaluated. Appendix F contains the listing for the computer program written for this purpose. A summary of the results for three of the temperatures 65.56° C, 126.67° C and 176.67° C is presented in Table 2.5. The columns of the output consist of temperature T, pressure P_1, specific (molar) volume $\tilde{v}_1$, molar density ρ_1, relative density (ρ_1/ρ_1°), the change in pressure from saturation (ΔP_1), isothermal susceptibility (χ_1) and the liquid phase potential change $(\Delta\mu_1)$. The suceptibility was calculated at each step simply as a ratio of the differences $(\Delta P/\Delta\rho)_T$. $\Delta\mu_1$ was obtained by subsequent integration of equation (2.55).

For each temperature the liquid pressure ranged, in arbitrary small steps, from the saturation vapor pressure (corresponding to K = 0) to a low value near zero. In this range the density is virtually invariant with pressure and the relative liquid phase density varies at most in the fifth decimal place. Also, the high values of χ_1 are fairly constant indicating correspondingly low liquid compressibilities. Thus, the capillary condensate can be considered to be an ideal liquid under these conditions between zero and ten atmospheres which corresponds to the (pressure) range of calculations yielding results listed in Table 2.5. The magnitudes of $\Delta\mu_1$ in each case are not large and the physical significance of these small numbers become apparent when compared with potential changes in the gas phase. This is discussed in Appendix D.

---

*The Kell-Whalley empirical equation was obtained for positive pressures only.

Table 2.5. Variation of chemical potential with pressure for the capillary condensate.

$T = 65.56^{o}$ C

Pressure (atm)	$V_{1(T,P)}$ (cc/gm)	ρ_1 (g-mole/cc)	η (dimensionless)	ΔP_1 (atm)	$\chi_1 (10^{-5})$ (cc-atm/g-mole)	$\Delta\mu_1$ (cc-atm/g-mole)
0.25297*	1.0213341	0.0543468	1.0000000	0.00	-	0.000
0.23297	1.0213350	0.0543467	0.9999991	0.02	4.050484	0.736
0.19297	1.0213368	0.0543466	0.9999973	0.06	4.050448	1.104
0.15297	1.0213387	0.0543465	0.9999955	0.10	4.050412	1.840
0.11297	1.0213405	0.0543464	0.9999936	0.14	4.050376	2.576
0.07297	1.0213424	0.0543463	0.9999918	0.18	4.050340	3.312
0.01297	1.0213452	0.0543462	0.9999891	0.24	4.050286	4.416

$T = 126.67^{o}$ C

2.41075*	1.0666159	0.0520396	1.0000000	0.00	-	0.0000
1.81075	1.0665130	0.0520378	0.9999668	0.60	3.4704022	11.530
1.21075	1.0666868	0.0520361	0.9999336	1.20	3.4697549	23.062

*The first entries in the pressure column are the saturation vapor pressures at that temperature.

Table 2.5 continued

Pressure (atm)	$V_{1(T,P)}$ (cc/gm)	ρ_1 (g-mole/cc)	η (dimensionless)	ΔP_1 (atm)	$\chi_1(10^{-5})$ (cc-atm/g-mole)	$\Delta\mu_1$ (cc-atm/g-mole)
0.91075	1.0667045	0.0520352	0.9999169	1.50	3.4694313	28.822
0.61075	1.0667222	0.0520344	0.9999003	1.80	3.4691077	34.592
0.01075	1.0667577	0.0520326	0.9998671	2.40	3.4684605	46.122
T = 176.67						
9.16173*	1.1227294	0.0494386	1.0000000	0.00	-	-
8.16173	1.1228112	0.0494350	0.9999271	1.00	2.7737870	20.227
7.16173	1.1228932	0.0494314	0.9998541	2.00	2.7726093	40.457
6.16173	1.1229751	0.0494278	0.9997812	3.00	2.7714321	60.697
5.16173	1.1230571	0.0494242	0.9997082	4.00	2.7702554	80.927
3.66173	1.1231802	0.0494188	0.9995986	5.50	2.7684914	111.257
2.16173	1.1233034	0.0494134	0.9994889	7.00	2.7667286	141.657
1.16173	1.1233856	0.0494098	0.9994158	8.00	2.7655541	161.857
0.16173	1.1234679	0.0494061	0.0003427	9.00	2.7643801	182.157

To determine $\Delta\mu_1^c$ from equation (2.59), a form of the relationship between χ_1 and η needs to be assumed. The relationship suggested by the values (of χ_1 and η) in Table 2.5 is a simple linear one

$$\chi_1 = K_1\eta - K_2 \qquad (2.64)$$

where

K_1, K_2 = empirical constants

The values of K_1 and K_2 were obtained by substituting for χ_1 and η at the ends of the range of pressure (in Table 2.5) and the validity of equation (2.64) checked by comparing the computed value of χ_1 with that obtained from the equation. This is shown in Table 2.6.

The integrated form of $\Delta\mu_1^c$ after substituting for χ_1 from above into equation (2.59) is

$$\Delta\mu_1^c = K_1\{0.5-\eta+0.5\eta^2\} + K_2\{1-\eta+\ln\eta\} \qquad (2.65)$$

To determine the order of magnitude of the correction term $\Delta\mu_1^c$, sample calculations were performed by substituting values for η into equation (2.65). The results of these computations are presented in Table 2.7.

The values of χ_1 in the last two columns of Table 2.6 compare reasonably well, hence the linear relationship given by equation (2.64) is a fairly good approximation. As a check the liquid phase pressures (ΔP_1) were evaluated from equation (2.56) on the assumption that the isothermal susceptibilities were invariant* in the range of pressures considered. Hence equation (2.56) can be written as:

---

*It is evident from Table 2.3 that this is an approximation.

Table 2.6. Comparison of values for the isothermal susceptibility. Verification of equation (2.64).

Temperature (^{o}C)	Pressure (atm)	η (dimensionless)	K_1	K_2	χ_1 computed (cc-atm/g-mole)	χ_1 (eqn (2.64)) (cc-atm/g-mole)
65.56	0.11297	0.9999936	1.98000×10^{6}	1.57495×10^{6}	4.0503765×10^{5}	4.0503755×10^{5}
126.67	0.91075	0.9999169	1.94789×10^{6}	1.60079×10^{6}	3.4694313×10^{5}	3.4694306×10^{5}
176.67	3.66173	0.9995986	1.61018×10^{6}	1.33268×10^{6}	2.7684914×10^{5}	2.7685006×10^{5}

Table 2.7. Typical values of $\Delta\mu_1^c$ for the capillary condensate for positive pressures.

Temperature (^{o}C)	Pressure (atm)	η (dimensionless	χ_1 (cc-atm/g-mole)	$\Delta\mu_1^c$ (cc-atm/g-mole)
65.56	0.1148	0.9999937	4.1037146×10^{5}	9.396×10^{-6}
126.67	1.2264	0.9999344	3.5154565×10^{5}	7.576×10^{-4}
176.67	5.7072	0.999748	2.8073740×10^{5}	8.920×10^{-3}

$$\Delta P_1 = \rho_1^0 \chi_1 (1-\eta) \qquad (2.66)$$

The values for ΔP_1 from equation (2.66) were compared with those from Tables 2.6 and 2.7*. Table 2.8 shows that the linear approximation is once again, justified. It may be noted that equation (2.66) follows from equation (2.58) on the assumption that $\Delta\mu_1^c$ is small compared to $\Delta\mu_1$**.

Table 2.8. Comparison of approximated liquid phase pressures with the exact (computed) values.

Temperature (°C)	η (dimensionless)	χ_1 (cc-atm/g-mole)	ΔP_1 computed (atm)	ΔP_1 from eqn. (2.66) (atm)
65.56	0.9999936	4.0503765×10^5	0.1400	0.1409
126.67	0. 169	3.4694313×10^5	1.5000	1.5000
176.67	0.9995986	2.7684914×10^5	5.500	5.494

Referring to the thermodynamic equation (2.62) it is seen that for a relatively small range of positive pressure for capillary condensed water, the $\Delta\mu_1^c$ correction term may be dropped resulting in

$$\sigma_{lg} K = \rho_1^o [\Delta\mu_g^{id} - \Delta\mu_g^c] - \Delta P_g \qquad (2.67)$$

Up to this point, all of the terms (with the exception of the curvature K)

---

*In the computer program which was used to obtain Tables 2.6 and 2.7, a step size for the liquid pressure was initiated to determine χ_1 and $\Delta\mu_1^c$.

**Actually both equations (2.64) and (2.66) are implied by the assumption that water is very nearly an incompressible liquid in this pressure range.

in an equation such as the above, can be calculated. The next section considers the evaluation of the radius of curvature of the liquid meniscus. The results are tabulated for each of the temperatures at which the laboratory experiments were conducted.

2.10. Application of the Thermodynamic Equation.

Once the second virial coefficient is known at the various temperatures, the chemical potential departure $\Delta\mu_g^{id}$ (from the reference state) and the correction term $\Delta\mu_g^c$ are readily evaluated. For values of the relative saturation, α, fairly close to unity and for high temperatures, the following approximations hold (see equations (2.38c), (2.40) and (2.41):

$$\Delta P_g \ll |RT \ln \alpha| \tag{2.68}$$

$$\Delta\mu_g^c \ll \Delta\mu_g^{id} \tag{2.69}$$

Equations (2.68) and (2.69) simplify equation (2.67) to the familiar form of the Kelvin Equation

$$K \simeq \frac{-RT \ln (P_g/P_g^0)}{\sigma_{lg}\tilde{v}_l} \tag{2.70}$$

where

$$\alpha = P_g/P_g^0$$

To evaluate equations (2.62) or (2.70) the surface tension, σ_{lg}, needs to be known as a function of temperature. This was obtained by interpolating data available for the air-water (Il) interfacial tension at various temperatures. The results of the interpolation are shown in Table 2.9.

Table 2.9 Temperature - Surface tension* Data

Temperature (^{o}C)	Surface tension (dynes/cm)
65.56	65.20
98.89	59.06
126.67	53.52
143.33	49.93
157.22	46.73
176.67	42.14

A sample calculation to evaluate the liquid meniscus curvature from equation (2.62) is shown below. This computation also demonstrates the relative contributions of the individual terms to the left side of the equation.

$$[K] = \frac{\text{atm}}{\text{dynes/cm}} \times \frac{1}{9.867\text{x}10^{-7}\ \text{atm}/\frac{\text{dynes}}{\text{cm}^2}}$$

*It should be noted that these values for σ_{lg} are substituted into equation (2.62) at all partial pressures (of water vapor) thus implying their invariance with curvature.

$T = 65.56^{o}$ C; $P_g = 0.23297$ atm; $P_g^{o} = 0.25297$ atm

$\bar{V}_1^{o} = 1.0213$ cc/gm; $B = -626.603$ cc/g-mole

and $\sigma_{lg} = 65.20$ dynes/cm

molar density $\rho^{o} = \dfrac{1}{\bar{V}_1^{o} \times 18.016} = 0.05435 \dfrac{\text{g-moles}}{\text{cc}}$

1. Relative saturation $\alpha = \dfrac{P_g}{P_g^{o}} = 0.92094$

2. Gas phase potential change $\Delta\mu_g^{id}$:

$$\Delta\mu_g^{id} = -RT^{l^{*}} \ln\alpha = 2289.18 \frac{\text{cc-atm}}{\text{g-mole}}$$

3. Correction due to the second virial coefficient:

$$\Delta\mu_g^{c} = -BP_g^{o}(1-\alpha)$$
$$= 12.532 \text{ cc - atm/g-mole}$$

4. Correction due to liquid phase nonideality:

$$\Delta\mu_l^{c} = \int_{\eta}^{1} x_1 (\eta^{-1}-1)\, d\eta$$
$$= 0 \{10^{-6}\}^{**} \text{ cc - atm/g-mole}$$

5. $\Delta P_g = 0.02$ atm

Substitution of these values into equation (2.62) for the mean curvature yields

---

*T^{l} is in degrees Kelvin.

**Order of magnitude.

$$K = 1.9227 \times 10^{6} \text{ cm}^{-1}$$

Mean radius of curvature $\bar{R} = \frac{2}{K} = 104.02$ Angstrom units.

As indicated by the value of α, the calculation above has been done for water vapor pressure close to saturation. The magnitude of the radius of curvature is high (compared to molecular dimensions), however the liquid meniscus is sharply concave when compared to a flat surface ($R = \infty$; the reference state). The gas phase chemical potential ($\Delta\mu_g$) is the dominant term on the right side of equation (2.62) and at low* temperatures and pressures close to saturation $\Delta\mu_l^c$ and ΔP_g are small. Since these terms are small the Kelvin equation applies for small departures from the reference state.

A computer program was written to evaluate the radius of curvature for all the experimental temperatures (Appendix F). The procedure followed was similar to the above calculation, however the liquid potential correction term $\Delta\mu_l^c$ was neglected all through the entire range of values of the relative saturation α**. A summary of the computation results for T equal to 65.56° C, 126.67° C and 176.67° C is presented in Tables 2.10-A,B and C respectively.

In each of the three tables, the gas phase chemical potential correction term $\Delta\mu_g^c$ is no more than a maximum of 8% of the ideal potential change $\Delta\mu_g^{id}$. Hence for relatively small changes of the liquid phase (potential) correction $\Delta\mu_l^c$ at moderate temperatures (so that ΔP_g is not significant):

$$K \propto -RT \ln \alpha$$

---

*Corresponding to cold precipitator temperatures.

**The validity of this assumption is discussed in Section 2.14 of this chapter.

Table 2.10-A. Summary of results of the program to evaluate radius of curvature from equation (2.62) for T = 65.56° C.

Saturation vapor pressure = 0.25297 atm

Pressure (atm)	α (dimensionless)	$\Delta\mu_g^{id}$ (cc-atm/g-mole	$\Delta\mu_g^{c}$ (cc-atm/g-mole)	ΔP_g (atm)	$\bar{R}$ (Angstroms)
0.25097	0.9921	2.206×10^2	1.253	0.002	1079.611
0.24897	0.9842	4.430×10^2	2.506	0.004	537.642
0.23297	0.9209	2.289×10^3	12.532	0.020	104.024
0.20297	0.8023	6.121×10^3	31.330	0.050	38.892
0.16697	0.6600	1.155×10^4	53.888	0.086	20.605
0.10497	0.4149	2.445×10^4	92.737	0.148	9.723
0.07097	0.2805	3.533×10^4	114.040	0.182	6.725
0.04697	0.1857	4.680×10^4	129.080	0.206	5.074
0.01897	0.0750	7.200×10^4	146.630	0.234	3.296
0.01097	0.0434	8.723×10^4	151.640	0.242	2.719
0.00497	0.0196	1.092×10^5	155.400	0.248	2.171
0.00297	0.0117	1.236×10^5	156.650	0.250	1.919
0.00097	0.0038	1.547×10^5	157.900	0.252	1.532
0.000465	0.00184*	1.750×10^5	157.770	0.252505	1.363

*Extrapolated value

Table 2.10-B. Summary of results of the program to evaluate radius of curvature from equation (2.62)

Table 2.10-B. Summary of results of the program to evaluate radius of curvature from equation (2.62) for T = 126.67° C.

Saturation vapor pressure = 2.41075 atm

Pressure (atm)	α (dimensionless)	$\Delta\mu_g^{id}$ (cc-atm/g-mole)	$\Delta\mu_g^{c}$ (cc-atm/g-mole)	ΔP_g (atm)	$\overline{R}$ (Angstroms)
2.40075	0.9959	1.364×10^2	4.295	0.010	1539.083
2.38075	0.9876	4.108×10^2	12.886	0.030	510.816
2.33075	0.9668	1.107×10^3	34.364	0.080	189.470
2.18075	0.9046	3.289×10^3	98.795	0.230	63.703
1.86075	0.7719	8.496×10^3	236.250	0.550	24.607
1.52075	0.6308	1.512×10^4	382.290	0.890	13.793
1.27075	0.5271	2.101×10^4	489.680	1.140	9.903
1.10075	0.4566	2.572×10^4	562.700	1.310	8.077
0.98075	0.4068	2.951×10^4	614.250	1.430	7.032
0.88075	0.3653	3.304×10^4	657.200	1.530	6.275
0.74075	0.3073	3.872×10^4	717.340	1.670	5.347
0.55075	0.2285	4.844×10^4	798.950	1.860	4.264
0.32075	0.1330	6.618×10^4	897.750	2.090	3.112
0.15075	0.0625	9.095×10^4	970.770	2.260	2.257
0.04075	0.0169	1.339×10^5	1018.000	2.370	1.529
0.03075	0.0128	1.431×10^6	1022.300	2.380	1.429

Table 2.10-C. Summary of results of the program to evaluate radius of curvature from equation (2.62) for T = 176.67° C.

Saturation vapor pressure = 9.16173 atm

Pressure (atm)	α (dimensionless)	$\Delta\mu_g^{id}$ (cc-atm/g-mole)	$\Delta\mu_g^{c}$ (cc-atm/g-mole)	ΔP_g (atm)	$\bar{R}$ (Angstroms)
9.14173	0.9978	8.067×10^{1}	6.274	0.020	2273.848
9.08173	0.9913	3.237×10^{2}	25.097	0.080	566.427
8.94173	0.9760	8.972×10^{2}	69.018	0.220	204.242
8.80173	0.9607	1.480×10^{3}	112.940	0.360	123.753
8.64173	0.9432	2.157×10^{3}	163.130	0.520	84.831
8.32173	0.9083	3.549×10^{3}	263.520	0.840	51.462
8.04173	0.8778	4.813×10^{3}	351.360	1.120	37.900
7.60173	0.8297	6.890×10^{3}	489.400	1.560	26.415
7.04173	0.7686	9.715×10^{3}	665.080	2.120	18.679
5.90173	0.6442	1.623×10^{4}	1022.700	3.260	11.109
4.72173	0.5154	2.447×10^{4}	1392.900	4.440	7.320
2.98173	0.3255	4.144×10^{4}	1938.800	6.180	4.273
1.14173	0.1246	7.687×10^{4}	2516.000	8.020	2.268
0.58173	0.0635	1.018×10^{5}	2619.700	8.580	1.701
0.46173	0.0504	1.103×10^{5}	2729.300	8.700	1.567
0.34173	0.0373	1.214×10^{5}	2767.000	8.820	1.420
0.30173	0.0329	1.260×10^{5}	2779.500	8.860	1.367

so that

$$\alpha \propto \exp\left[-\frac{K}{RT}\right] \qquad (2.71)$$

The variation of the radius of curvature $\bar{R}$ (in the last columns of Tables 2.10-A,B and C) is significant in that it decreases over many orders of magnitude over a small fraction of the change in the relative saturation α. As discussed later, this observation is particularly relevant when simultaneous changes in the liquid potential $\Delta\mu_1$ and its correction term $\Delta\mu_1^c$ are compared with such non uniform changes in $\bar{R}$. Table 2.10 shows the variations in $\bar{R}$ for all of the experimental temperatures. The range of α spans the partial pressure of water vapor (P_{H_2O}) from zero atmospheres to the saturation pressure. It might be noted that the radius of curvature decreases very rapidly with small departures from saturation. Table 2.10 shows values of α at which the radius of curvature has decreased from infinity (at saturation) to 100 Angstrom units.

Table 2.11 Relative saturation α at experimental temperatures corresponding to the decrease in $\bar{R}$ from infinity to 100 A^o.

Temperature (^oC)	P_{H_2O} at which $\bar{R} \cong 100\ A^o$ (atm)	α (Pg/Pg^o)
65.56	0.233	0.9209
98.89	0.890	0.9271
126.67	2.260	0.9378
143.33	3.690	0.9413
157.22	5.380	0.9472
176.67	8.720	0.9520

The variations of $\Delta\mu_g^{id}$ and $\bar{R}$ with α are illustrated by the curves in Figure 2.8. In agreement with the above, it is seen that a change of $10A^o$ unit in $\bar{R}$ at about $10A^o$ radius requires a change of 30000 cc-atm/g-mole in $\Delta\mu_g^{id}$, as opposed to 160 cc-atm/g-mole required to go from an $\bar{R}$ of 110 A^o to 100 A^o. Since $\Delta\mu_g^c$ is comparatively small, changes as large as this in the chemical potential below about 20 A^o (see Figure 2.8) reflect on comparable changes in the liquid phase potential by virtue of the two phase equilibrium condition expressed by equation (2.27). Such an effect on the small volumes of liquid leads to a speculation upon the invariance of the physical properties of the capillary condensate.

Since the Kelvin equation (2.70) is so widely used to determine the meniscus curvature under such conditions, it is appropriate to compare results with the more exact equation (2.62). It may be noted here that differences between the two are only due to the additional terms $\Delta\mu_g^c$ and ΔP_g, since $\Delta\mu_l^c$ has been omitted in the calculations leading to the results in Tables 2.10-A, B and C. A comparison of the values of the radius of curvature $\bar{R}$ obtained by the two equations is shown in Table 2.12.

In regard to Table 2.12 the following specific observations may be made:

i) In each case, the deviation decreases with α since this decreases the magnitude of ΔP_g (equal to $P_g^o - P_g$) and $\Delta\mu_g^c$; both terms being positive and the Kelvin equation better approximates the more rigorous equation (2.62). Similarly the deviation is greater for the same relative saturation

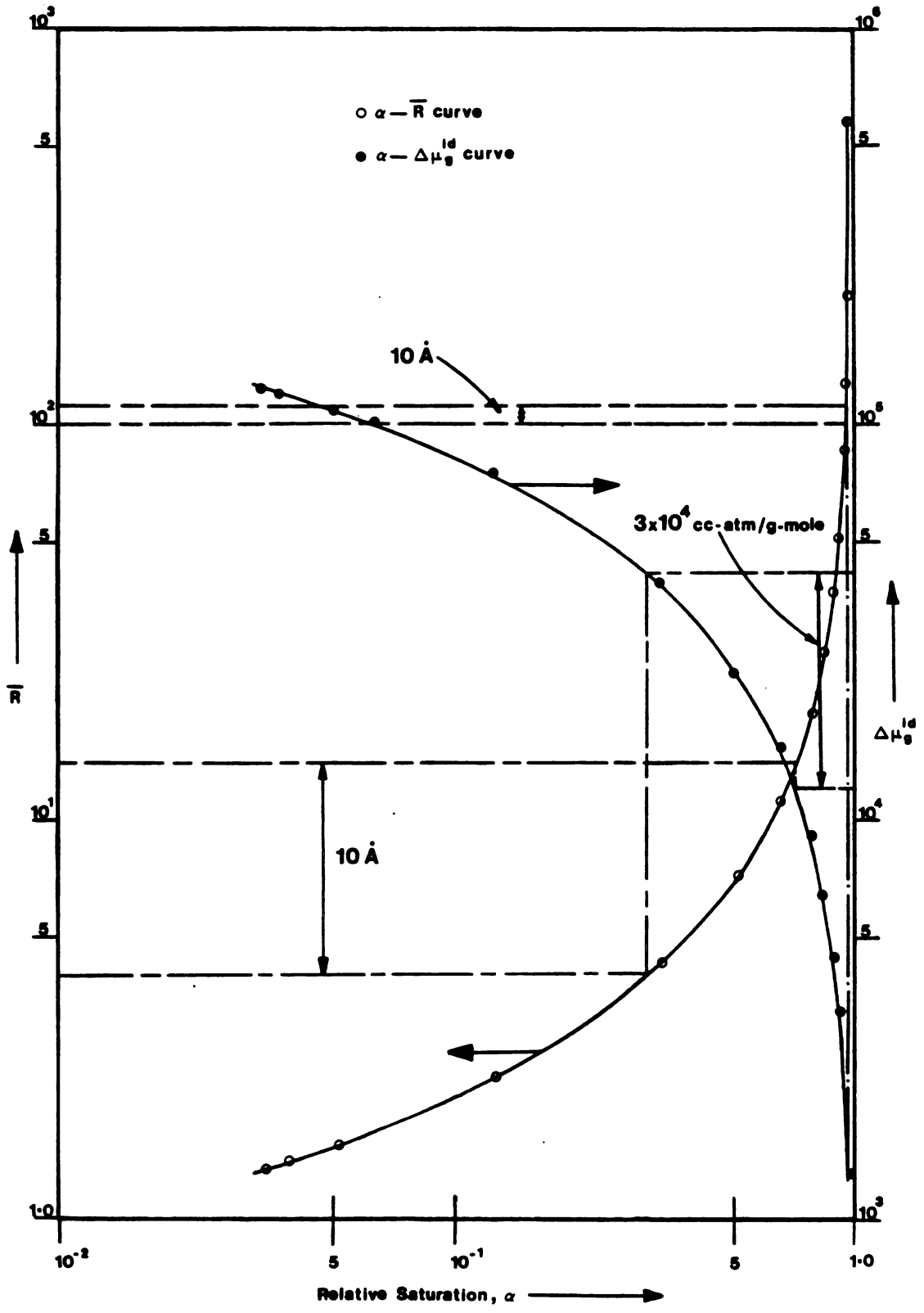

Figure 2.8. Variation of gas phase chemical potential ($\Delta\mu_g^{id}$) and radius of curvature with the relative saturation.

Table 2.12 Comparison of results from equation (2.62) and (2.70).

1	2	3	4	5	6
Temperature (°C)	Pressure (atm)	α (P_g/P_g^{o})	$\bar{R}$ [Kelvin] (A^{o})	$\bar{R}$ [Rigorous] (A^{o})	% Deviation from column 5
65.56	0.23297	0.9209	103.382	104.025	0.62
	0.17297	0.6838	22.413	22.520	0.48
	0.09297	0.3675	8.510	8.543	0.38
	0.03297	0.1303	4.180	4.191	0.27
98.89	0.94163	0.9792	341.215	346.962	1.66
	0.80163	0.8336	39.407	40.020	1.53
	0.64163	0.6672	17.724	17.972	1.38
	0.50163	0.5216	11.020	11.158	1.24
	0.36163	0.3761	7.334	7.412	1.05
	0.24163	0.2513	5.193	5.240	0.89
	0.14163	0.1473	3.745	3.772	0.73
	0.02163	0.0225	1.890	1.898	0.43
126.67	2.11075	0.8756	46.577	48.039	3.04
	1.51075	0.6267	13.241	13.597	2.62
	0.61075	0.2533	4.506	4.589	1.80
	0.01075	0.0045	1.145	1.150	0.44

Table 2.12 (cont'd)

1	2	3	4	5	6
Temperature (^{o}C)	Pressure (atm)	α (P_g/P_g^{o})	$\bar{R}$ [Kelvin] (A^{o})	$\bar{R}$ [Rigorous] (A^{o})	% Deviation from column 5
143.33	3.61760	0.9234	70.631	73.958	4.50
	2.71760	0.6937	15.391	16.014	3.90
	1.51760	0.3874	5.936	6.119	2.99
	0.31760	0.0811	2.241	2.279	1.68
157.22	5.38206	0.9472	95.292	101.206	5.84
	4.18206	0.7360	16.864	17.783	5.17
	2.98206	0.5248	8.017	8.388	4.42
	1.78206	0.3136	4.458	4.621	3.54
	0.28206	0.1024	2.268	2.323	2.37
176.67	8.66173	0.9454	81.226	88.335	8.05
	7.16173	0.7817	18.518	19.974	7.29
	5.66173	0.6180	9.477	10.137	6.51
	3.66173	0.3997	4.973	5.255	5.37
	1.16173	0.1268	2.208	2.287	3.45

at the higher temperatures.

ii) At a given temperature, the radius of curvature of the liquid meniscus increases as the vapor pressure approaches saturation. The volume of the condensate is sensitive to changes in the partial pressure of water vapor (see also Figure 2.8) and decreases relatively slowly with a rise in temperature. Furthermore, it is evident that decreasing partial pressure will cause the curved meniscus to recede leading to a decreasing radius of curvature and liquid volume owing to the restriction of tangency (contact angle of zero) at the circles of contact between liquid and the solid spheres (Figure 2.7).

This section concludes the thermodynamic analysis which led to the results presented in Tables 2.10-A, B and C. It must be recognized, however, that this analysis is not complete in as much as restriction of liquid phase ideality needs to be investigated*. In recognition of this fact, it is necessary to identify the physical (and numerical) significance of the variables that are pertinent to the liquid phase. The next section deals with this aspect in connection with the reference state.

2.11. The Reference State

From Tables 2.5 and 2.10 it follows that, corresponding to a partial pressure P_g, there exists a unique set of values for the parameters

*An extension of the thermodynamic analysis, pertaining to this assumption, has been presented in Appendices C, D and E.

that characterize the gas and the liquid states. A given set of conditions for the capillary condensate is defined for this system by any one of the following inter-related parameters for the liquid phase.

i) The chemical potential departure $\Delta\mu_1$ or the pressure specified by ΔP_1

ii) The isothermal susceptibility χ_1

iii) The curvature of the liquid meniscus K

iv) The liquid density ρ_1 incorporated in the definition for η.

As mentioned above, all of these properties relate to a unique value of α for the thermodynamic system. For purposes of computation the liquid and gas states are related by equation (2.27)

$$\Delta\mu_g = \Delta\mu_1$$

or

$$\Delta\mu_g^{id} - \Delta\mu_g^{c} = \Delta\mu_1$$

$$\therefore \quad BP_g^o (1-\alpha) - RT \ln\alpha = \int_{\eta}^{1} x_1 \, d\ln \eta \qquad (2.72)$$

It is seen that α equal to 1 corresponds to the lower limit of the right hand integral $\eta = 1$. This defines the reference state for the liquid phase in terms of the gas phase:

$$K = 0; \; P_g = P_g^0; \quad \eta = 1, \; (\rho_1 = \rho_1^0)$$

Hence the reference state liquid density belongs to a capillary condensate with infinite radius of curvature in thermodynamic equilibrium with its vapor at the saturation pressure for a given temperature.

A unique value of α for each η is obtained by solving equation

(2.72) after evaluating the right hand integral.

In the context of the objective of the work presented in this chapter, it is necessary to ascertain the fraction of the particle surface that is in contact with the capillary condensate. This problem is dealt with in the next section, where the geometry of the model, depicted earlier in Figure 2.4, is specified.

2.12. Estimation of the Dimensions of the Capillary Ring

A complete quantitative description of the extent of capillary condensation requires that the dimensions (volume for example) of the circular ring of liquid surrounding the area of contact of two particles be specified (Figure 2.4). The general problem for the cases where the contact angle is not zero (M4), and where the liquid gas interface is not spherical (F5), results in solutions for the liquid volume involving the iterative computation of incomplete integrals (M4). The geometry is greatly simplified by imposing the following three restrictions:

i) The interface (liquid - vapor) is spherical.

ii) The angle of contact θ is zero.

iii) The mean curvature K (of the liquid meniscus) corresponds to a mean radius of curvature $\bar{R}$ given by 2/K and which by definition is the same in both planes of the capillary ring (Figure 2.5).

Figure 2.9 shows the co-ordinates for the capillary ring around the point of contact specified by (0,0). The dimension x_0 corresponds to the lower limit below which condensation cannot occur. This limit is specified by two physical restrictions and these have been

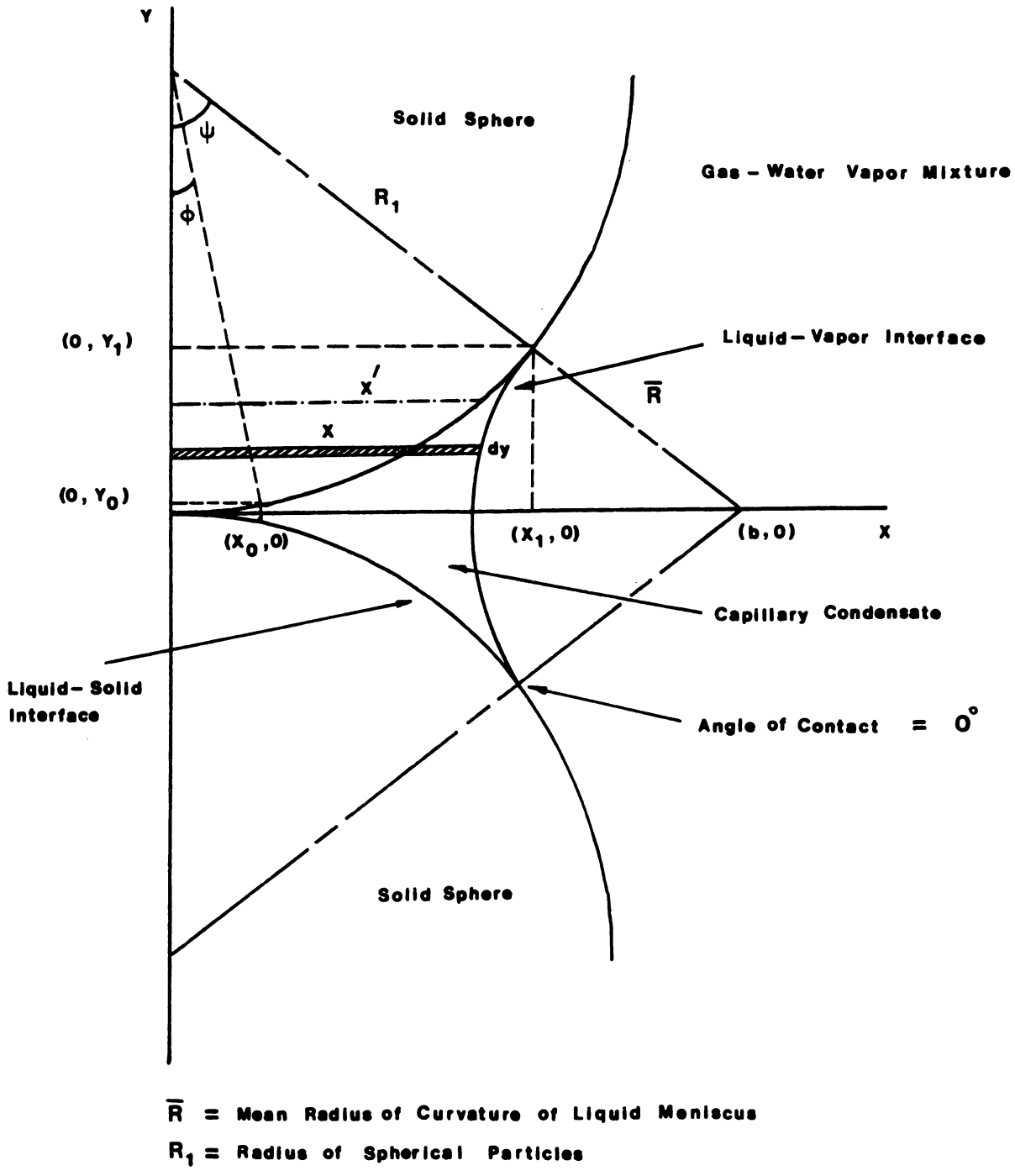

Figure 2.9. Geometry of the capillary ring around the solid spheres.

discussed in Section 2.14.

The volume of the capillary condensate (V_l) is determined by rotating the circular interface profile around the y axis and subtracting the volume of the solid spheres included in the process (V_s)

$$V_m = 2 \int_{y_0}^{y_1} \pi x^2 dy \tag{2.73}$$

where

V_m = volume obtained by rotation of the meniscus

For a spherical profile y is known explicitly as a function of x;

$$y = \sqrt{\bar{R}^2 - (x-b)^2} \tag{2.74}$$

Substituting for y into (2.73)

$$V_m = -2\pi \int_{x_0}^{x_1} \frac{x^2(x-b)dx}{\bar{R}^2-(x-b)^2} \tag{2.75}$$

where

$x_1 = R_1 \sin\psi$

$y_1 = R_1 (1-\cos\psi)$

also

$$y_1 = \bar{R} \sin (\tfrac{\pi}{2} - \psi) \tag{2.76}$$

$$\therefore \quad \psi = \cos^{-1} (R_1/\bar{R}+R_1) \tag{2.77}$$

and

$$x_1 = R_1 \sin \{\cos^{-1} (R_1/\bar{R}+R_1)\} \tag{2.78}$$

$$\phi = \cos^{-1}\left\{\frac{R_1 - y_0}{R_1}\right\} \tag{2.79}$$

y_0 is the coordinate corresponding to the lower limit.

$$\text{and} \qquad x_0 = R_1 \sin\left\{\cos^{-1}\left(\frac{R_1 - y_0}{R_1}\right)\right\} \tag{2.80}$$

Expression (2.73) for V_m can be resolved by means of the standard integral tables (T2) to give the following result for the indefinite integral* I.

$$I = \left[\left\{\frac{2}{3}ab + \left(\frac{3-5b}{6}\right)(3b^2 + a)\right\}\sin^{-1}\left(\frac{b-x}{R}\right) - \left\{\frac{x^2}{3} - \left(\frac{3-5b}{6}\right)(x+3b) + \frac{2a}{3}\right\}\sqrt{B}\right] \tag{2.81}$$

---

*The solution for the general indefinite integral is given as

$$\int\frac{x^m dx}{\sqrt{B^n}} = \frac{1}{(m-n+1)c}\left[\frac{x^{m-1}}{\sqrt{B^{n-2}}} - \frac{(2m-n)b}{2}\int\frac{x^{m-1}}{\sqrt{B^n}}dx - (m-1)a\int\frac{x^{m-2}}{\sqrt{B^n}}dx\right] \tag{2.82}$$

where

$B = a + b_1 x + cx^2$ (quadratic term in the denominator of integral)

$a = R^2 - b^2$, $b_1 = 2b$, $c = -1$ (<0)

and

$$\int\frac{dx}{\sqrt{B}} = \frac{-1}{\sqrt{-c}}\sin^{-1}\frac{\lambda_1}{\sqrt{-\lambda_2}} \tag{2.83}$$

where

$$\lambda_1 = dB/dx \qquad \lambda_2 = 4ac - b_1^2 < 0$$

$$I = \int_{x_0}^{x_1}\frac{x^2(x-b)dx}{\sqrt{R^2-(x-b)^2}} \tag{2.84}$$

and

$$V_m = 2\pi |I| \Big|_{x_0}^{x_1} \tag{2.85}$$

The volume of the spheres included in the above integration is

$$V_s = 2 \int_{y_0}^{y_1} \pi x^{1^2} dy \tag{2.86}$$

Let λ^1 be the running variable from 0 to ψ then

$$x^1 = R_1 \sin \psi^1$$

for a spherical solid surface

$$dy = \tan \psi^1 \, dx$$

$$= R_1 \sin \psi^1 d\psi$$

Substituting into (2.85)

$$V_s = 2\pi \int_0^{\psi} R_1^3 (\sin^2 \psi^1) \sin \psi^1 \, d\psi$$

$$= 2\pi R_1^3 \{\tfrac{2}{3} - \cos \psi + \tfrac{1}{3} \cos^3 \psi\} \tag{2.87}$$

The abbreviated expression (2.85) for V_m also contains volume of the solid spheres included in the rotation. The liquid volume V_1 is then given by (2.88).

Volume of capillary condensate V_l

$$V_l = V_m - V_s \tag{2.88}$$

Equations (2.76) through (2.80) and (2.88) yield the parameters needed to determine the extent of condensation. It may be observed that all of these parameters are given in terms of the known quantities $\bar{R}$ and R_1. As mentioned earlier in this section the three assumptions of spherical interface, contact angle of zero and mean curvature K simplify the problem considerably. In general, for a non zero angle of contact θ, the normals to the solid-liquid and liquid-vapor interfaces are not collinear so that the radius $\bar{R}$ (Figure 2.7) makes an angle $\theta + \psi$ with the y axis. The resulting elliptic integrals required to solve for the condensate volume have a modulus and an amplitude which are functions of

i) The filling angle ψ

ii) The modular angle θ'*

iii) The mean curvature K

In view of the overall resistivity model and the restrictions imposed upon it as discussed in general in Chapters 2 and 3, and in particular in Chapter 4; not all of the features of the condensate ring are needed. Specifically, the linear dimensions of the ring given by the coordinates x_1, y_1, and x_0, y_0 are required to calculate the extent of coverage of the particle surface. This enables one to determine the fractional "dry surface" length over the circumference of the particle and along the externally imposed voltage gradient.

---

*The modular angle $\theta' \equiv \pi/2 - (\theta+\psi)$

Furthermore, the migrating ion encounters a larger "effective" contact area between two particles due to the presence of a ring of liquid. As a result of these two effects the overall particulate layer resistivity is modified.

2.13 Summary

The physical model for capillary condensation described has been assumed to be fairly ideal and has gone through several stages of development with the objective of determining the size of the liquid ring around the region of contact. As such it is appropriate at this stage to recapitulate the procedure used and identify the dependent and independent variables.

The closed, isothermal and reversible thermodynamic system was defined with all of the attendant assumptions, and the total (Helmholtz) free energy change dA was expressed in terms of the individual bulk phase and interfacial free energy changes. For the case of an inert, adsorbent solid; dA was given in terms of the liquid and gas phase properties only. The simplified equation was compared to the hydrostatic equation (2.17) containing the mean curvature term, and this resulted in the Laplace and Young equations. The changes in pressure from a reference state for the real gas (water vapor) and liquid phases were related to their chemical potential departures also from the same reference state. Substitution of these latter relationships into the first of the Laplace and Young equations gave the sought after thermodynamic equation relating liquid meniscus curvature to the gas and liquid chemical potentials.

The ideal phase chemical potential terms as well as the terms

arising due to nonideality were determined from the virial equation of state for the gas and the compressibility equation of state for the capillary condensate. The magnitudes of each of these terms were computed for the range of temperatures at which the laboratory (alkali) ion migration experiments were conducted. The significance of each of these terms was briefly mentioned, and, particularly, the importance of the liquid phase chemical potential correction term $\Delta\mu_1^c$, for small liquid volumes, was underscored. It was also noted that, in such cases, the assumption of constant (bulk) liquid phase properties was not rigorously valid.

For a given equilibrium state specified by the relative saturation α, equation (2.72) related the gas and liquid chemical potentials and permitted the simultaneous estimation of the individual phase properties. Based on this the reference state was defined. The physical significance of decreasing α was indicated in that the radius of curvature of the meniscus decreased as it receded back into the "macropore".

Finally, under the assumptions of spherical geometry for the liquid-gas and liquid-solid interfaces it was shown that the dimensions of the condensate ring could be estimated from known quantities $\overline{R}$ and R_1. These dimensions need to be known in order to determine the "effective" particulate layer resistivity. The radius of curvature $\overline{R}$ is obtained from the thermodynamic equation (2.62). The terms on the right side of this equation are functions of the relative saturation and the ambient temperature. It follows, therefore, that the temperature and the partial pressure of water vapor are the independent variables. The total gas phase pressure is also an independent

variable and is reflected in the Kell-Whalley empirical equation (2.63) for liquid volume $\overline{V}_l$ which is given as a function of pressure and temperature. However all of the laboratory experiments were conducted at approximately one atmosphere pressure and the errors arising due to this, in the evaluation of $\overline{V}_l$, are negligible. The particle size* R_l is a controlled variable which together with intermediate dependent variable $\overline{R}$ gives the required dimensions x_l and y_l respectively.

The thermodynamic analysis presented in this chapter is discussed in the next section. The discussion is primarily confined to the extension of this analysis to molecular volumes of condensate.

2.14. Discussion

The model assumptions that have been made in the course of development of the thermodynamic relationship [equation (2.62)] need to be examined in the light of the results that have been tabulated in Tables 2.10-A, B and C. The basis of such an examination lies in the correspondence between the numerical values of the relative saturation α, and the chemical potential departures (from the reference state) for the liquid ($\Delta\mu_l$) and the vapor phase ($\Delta\mu_g$) respectively. As shown later (and discussed in Appendices C, D and E as well), a simultaneous comparison of these three quantities brings forth several important features of the capillary condensation process. These features help determine the extent of the feasibility of the calculations which lead, ultimately, to the values for the mean radius

*The mass median diameter of a well mixed sample of the fly ash was used as the mean particle size.

of curvature of the meniscus of the capillary condensate.

A key characteristic of the development of the thermodynamic model presented in this chapter is the formulation of the concise set of equations (2.19) and (2.20) and equation (2.21) for water. These relationships, generally known as the Laplace and Young equations of capillarity are not unique to this development -- indeed, more general derivations have been recognized prior to the publication of Melrose (M4, 1966).

$$P_g - P_l = \sigma_{lg} K \tag{2.19}$$

$$\sigma_{sl} - \sigma_{sg} = \sigma_{lg} \cos \theta \tag{2.20}$$

$$\sigma_{sl} - \sigma_{sg} = \sigma_{lg} \tag{2.21}$$

Equation (2.19), in particular, relates the pressure differential between the two contiguous fluid phases directly to the liquid surface tension and meniscus curvature.

The system (illustrated by Figure 2.4) is considered to be isothermal, reversible and closed. The total Helmholtz free energy in Section 2.4 was shown to split into internal and external free energy changes. These changes are associated with the thermodynamic work done within and without the boundaries of the system respectively,

$$dA_{total} = dA_{external} + dA_{internal} \tag{2.89}$$

The net internal free energy change was shown to be zero for such a system, and $dA_{internal}$ in turn was decomposed as follows:

$$dA_{internal} = dA_{\substack{liquid \\ volume}} + dA_{surface} = 0 \tag{2.90}$$

hence

$$\left|dA_{\substack{liquid \\ volume}}\right| = \left|dA_{surface}\right| \tag{2.91}$$

Thus the change in free energy due to a decrease or increase of condensate volume is exactly counterbalanced by an equivalent change in the surface free energy. This argument assumes that no part of the solid moves* such that an energy exchange takes place with the surroundings as a result of changes in the condensate volume. It may be noted at this stage that the surface energy contribution to the internal free energy change is shown in equation (2.15) to be associated with the change in the interfacial areas only.

Perhaps one of the more important implications of the thermodynamic analysis of the earlier sections results from its extension to molecular volumes of the capillary condensate within the macropore. The state variables that specify a liquid state (and some of its physical properties**) are ascertained reliably by such an analysis (beginning with Section 2.4) which, owing to its very nature, is valid for macroscopic volumes of condensate. However, when statiscally large numbers of liquid molecules are not present, the foregoing analysis must be

---

*The solid is assumed to be incompressible (rigid) for the capillary condensation process only.

**The liquid surface tension, for example, is given as a function of the curvature (Appendix E).

subject to refinements (or modifications); indeed, the question whether the condensate can really exist needs to be resolved. This question becomes increasingly important as the water vapor partial pressure decreases, and this results in smaller liquid volumes as noted at the end of Section 2.10.

There are two independent features that predict the existence of a lower limit below which capillary condensation cannot occur. The first of these results directly from the dimensions of the macropore. By moving into the pore from its open end (Figure 2.9), it is seen that when the pore dimension (in the y direction) equals the molecular size of the liquid, no further condensation can occur. This is visualized in analogy with the fact that the condensate meniscus recedes into the pore as the relative saturation α decreases. Hence this limit is specified by the radius of curvature $\overline{R}$ when it corresponds to the molecular diameter of water.

The second feature which predicts the lower limit (of capillary condensation) results from the fact that the isothermal susceptibility (χ_1) is a function of the liquid relative density η^*. A linear form of this relationship, valid for values of α (P_g/P_g^o) close to unity, is indicated by equation 2.64. For a general case (as also for lower α) this relationship is nonlinear, however χ_1 and η still vary in the same direction as α. Hence, as the partial pressure of water vapor decreases (decreasing α), χ_1 decreases, and ultimately a value of α is reached where χ_1 vanishes. The liquid becomes mechanically unstable

---

*This is shown in Table 2.3 where η varies with the liquid pressure, and hence χ_1 changes as well.

at this value of α and this point is identified as the point of rupture of the liquid. This has been discussed in detail in Appendices C and D where this point is associated with the limit of metastability (Figure C.1) on the van der Waals isotherm.

The partial results of the computations for the liquid phase are presented in Table 2.3. For each temperature, the value of ΔP_1 (equal to $P_g^o - P_1$) does not exceed the corresponding saturation pressure P_g^o, hence for the range of results in this table the liquid pressure is always positive. When ΔP_1 equals or exceeds P_g^o, it follows that the liquid pressure is zero or negative, respectively, and the value of α corresponding to this state of liquid-vapor equilibrium is given by equation 2.72 as

$$BP_g^o (1-\alpha) - RT \ln\alpha = \int_{\eta}^{1} \chi_1 \, d \ln \eta \qquad (2.72)$$

The right hand side of this term is equal to $\Delta\mu_1$, and for the range of pressures in Table 2.5, it is seen from the results in Table 2.7 that

$$\Delta\mu_1^c << \Delta\mu_1$$

so that the following holds (see equation 2.56)

$$BP_g^o (1-\alpha) - RT \ln\alpha \simeq \Delta\mu_1^{id} \qquad (2.92)$$

$$\simeq \Delta P_1/\rho^o{}_1$$

The relative saturation α and the liquid phase pressure ΔP_1 are plotted against $\Delta\mu_1$ in Figure 2.10. The ΔP_1 - $\Delta\mu_1$ values were taken

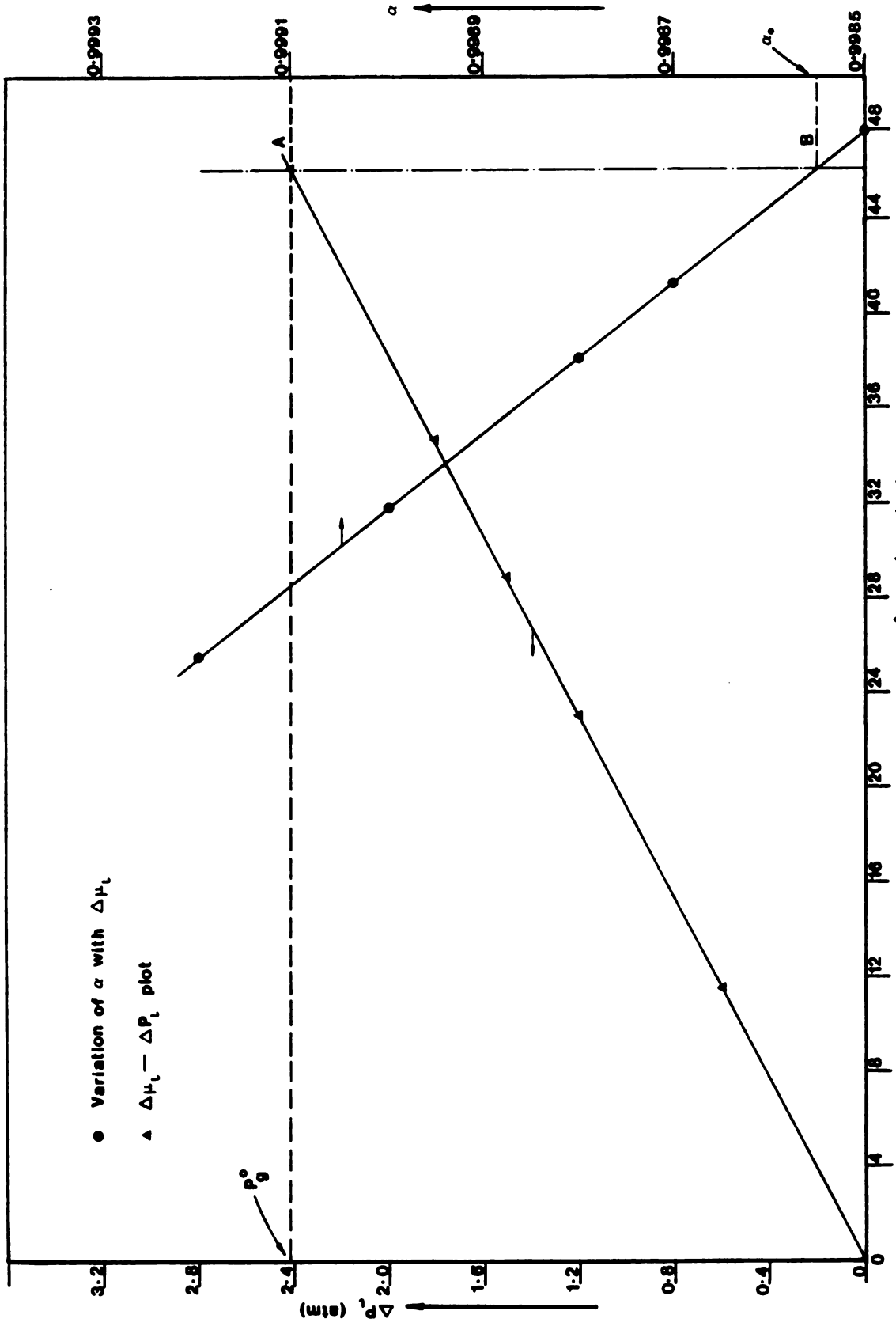

Figure 2.10. Plot for the capillary condensate illustrating the variation of ΔP_l and the relative saturation α with $\Delta\mu_l$ for small departures. Points A and B for the two lines correspond to values of ΔP_l and α respectively where $P_l = 0$.

from Table 2.5 (for a temperature of 126.67° C). The point A on the plot identifies the value of $\Delta\mu_1$ for which $\Delta P_1 = P_g^o$ or, equivalently, $P_1 = 0$. Equation (2.92) is solved for $\Delta\mu_1^{id}$ for various values of α and the results are plotted on the graph to give the point B which corresponds to the value of α at which $P_1 = 0$. Hence at this fairly high value of α_0 (=0.99855) the liquid phase does not experience any compressive stress due to the adjoining gas. It follows from this, that for any $\alpha < \alpha_0$, the capillary condensate is in a state of tension.

Although there is no abrupt transition from a state of compression (positive pressures) to one of tension within the liquid, a decreasing relative saturation induces increasing tensile stresses in the condensate. As a result, some of the physical properties of the liquid deviate from the values normally ascribed to the bulk phase (C1). Furthermore, the increase in liquid tension is limited to the tensile strength† (at a given temperature) at which point the liquid becomes mechanically unstable.

Melrose (M4)*, in his calculations, has arrived at values for $\Delta\mu_1$ by extrapolating the linear relationship (2.64) (established for a state of compression) to high tensile states within the liquid. The liquid ruptures when $\chi_1 = 0$, and from equation (2.64) the value of η, at this point, is given by

$$\eta = \eta_0 = |K_2/K_1|$$

---

†This is the maximum theoretical tension a liquid can withstand before rupturing.

*The author has used argon and an inert solid as the absorbate - absorbent system (M4).

Program Liquid (listed in Appendix F) was modified to calculate $\Delta\mu_1$ for values of η up to η_0. The results obtained, however, were inconsistent with the expectation that χ_1 vanish when η decreases to its final value of η_0*. A typical set of results, for a temperature of 65.56° C is presented in Table 2.13.

Table 2.13. Parameters for the liquid phase H_2O near its estimated point of rupture [calculated from equation (2.64)].

P_L (atm)	$\bar{V}_1$ ($\frac{cc}{gm}$)	$\frac{\eta}{\rho_1}$ ($\frac{}{\rho_1^o}$)	ΔP_1 (atm)	χ_1 ($\frac{cc\text{-}atm}{g\text{-}mole}$)	$\Delta\mu_1$ ($\frac{cc\text{-}atm}{g\text{-}mole}$)
∿-3275	1.2855	0.7945	3275	2.376×10^5	8.089×10^2

$$\eta_0 = K_2/K_1 = 0.7954$$

It is evident from the results in the table above that χ_1 is far from zero at η close to η_0. Also, $\Delta\mu_1$** is smaller than would normally be expected for a volume of liquid that has undergone a large pressure variation from about 0.25 atmospheres (P_g^o) to minus 3275 atmospheres (tension). The immediate conclusion to be drawn here is that an empirical relation such as (2.64), upon which η_0 is based, is far too simplistic and is valid, at best, for a limited region of partial

---

*It may be noted here that the empirical constants K_1 and K_2 are obtained for the range of positive pressures only (see Table 2.6)

**$\Delta\mu_1$ is zero when $\eta = 1$ ($P_1 = P_g^o$) at the reference state.

pressures (beginning with P_g^o).

$$\chi_1 = K_1\eta - K_2 \tag{2.64}$$

A linear interpolation between χ_1 values was also not possible when empirical constants K_1 and K_2 were based on the entire range $\alpha = 1$ to $\alpha = \alpha_0$. This kind of an interpolation assumes, of course, that the computation procedure (leading to numbers such as those in Table 2.13) is appropriate, in particular, that the $\Delta\mu_1$ values are correct.

In view of the above, the overall problem mentioned here appears to stem from the compressibility equation of state for the liquid. A modified form* of this equation, stated earlier, is as follows:

$$\Delta P_1 = \rho_1^o \int_\eta^1 \chi_1 \, d\eta \tag{2.56}$$

An analytical evaluation of an integral such as the above [see expression (2.55) for $\Delta\mu_1$] presupposes a relationship between the isothermal susceptibility χ_1, and the relative density η. Quite obviously this is not known, and the process of determining this for the region of (liquid) tension is equivalent to searching for another equation of state which is valid for this region. In effect, this amounts to substituting an "empirically fitted" compressibility equation (of state), which is obtained from the pressure-volume (constant temperature) data generated by the foregoing alternative equation of state.

*This is obtained from the generally recognized form:

$$\chi_1 = -1/\rho_g \beta = (\partial P/\partial \rho)_T \tag{2.52}$$

The isothermal susceptibility (or compressibility) of a liquid can be determined from an empirical relation typically given as follows (V1)*:

$$\rho_1 = c_1 + c_2 P_1 - c_3 P_1^2 \tag{2.93}$$

where c_1, c_2, and c_3 are given as functions of temperature. Normally $c_1 >> c_2 >> c_3$ and 0 (M) of $\{c_2^2\} = c_3$

The empirical equation for susceptibility $[\chi_1 = (\partial P_1/\partial \rho_1)_T]$ is obtained from (2.93) and given as,

$$(\frac{\partial P_1}{\partial \rho_1})_T^{**} = 1/(c_2 - 2c_3 P_1) \tag{2.94}$$

Substituting the quadratic solution for the liquid pressure P_1 [from equation (2.93)] into (2.94) gives

$$\chi_1 = 1/[c_2 - 2c_3 \{c_2 \pm \sqrt{c_2^2 + 4c_3 (c_1 - \rho_1)/2c_3}\}] \tag{2.95}$$

Although (2.95) is derived from an empirical relationship (2.93), the nonlinearity between χ_1 and ρ_1 (and, hence, also $\eta = \rho_1/\rho_1^0$) is evident from the above equation. This may be viewed in contrast to equation (2.64) over the range of η*** in light of the fact that the region of extrapolation (or tension) is not insignificant when compared with the positive (liquid) pressure region for which the empirical

*Type of equation used by Melrose (M4) to extrapolate to lower values of pressure and susceptibility.

**Subscript T implies constant temperature.

***The range of the relative density η extends from 1.00 to η_0, which includes states of (liquid) tension.

coefficients c_1, c_2 and c_3 are established.

An alternative, simpler, expression for χ_1 may be derived from equation (2.93)† and is given as

$$\chi_1 = \left(\frac{\partial P_1}{\partial \rho_1}\right) = \frac{P_1}{(\rho_1 - c_1) - c_3 P_1^2} \qquad (2.97)$$

Hence $\chi_1 \to 0$ if

i) $P_1 \to 0$ (2.98)

or ii) $|c_3 P_1^2| >> P_1$ (2.99)

This latter condition assumes, of course, that $|c_3 P_1^2| >> (\rho_1 - c_1)$ and c_3 is negative. Both conditions (i) and (ii) are unrealistic, since in the first case P_1 tends to increasing negative values (tension), and in the second case P_1 would have to be extremely large (far greater than the tensile strength of water). The tensile strength is discussed and evaluated for various temperatures in Appendix C.

In view of physical property changes of the liquid associated with its tensile state and the foregoing incompatibility between state

† $$\frac{\rho_1}{P_1} = \frac{c_1}{P_1} + c_2 - c_3 P_1 \qquad (2.96)$$

$$\left(\frac{\rho_1 - c_1}{P_1}\right) - c_3 P_1 = c_2 - 2c_3 P_1$$

From equation (2.94)

$$\chi_1 = \frac{\partial P_1}{\partial \rho_1} = P_1 / \{(\rho_1 - c_1) - c_3 P_1^2\} \qquad (2.97)$$

relationships valid for the regions of compression and tension, an expression such as (2.93) for η_0 is suspect. The use of this expression or the compressibility equation (2.56) amounts to drawing a physical* conclusion from an extrapolation of an empirical relation, valid in a region of positive liquid pressures, to one of high (liquid) tension. This fact necessitates the adoption of another equation of state that approximates liquid behaviour for negative pressures. The work of Benson and Guerjoy (B5), published in 1949, shows that the simple van der Waals equation can be used to approximate the liquid behaviour under such conditions. This is examined in detail in Appendices C and D.

As mentioned in the beginning of this discussion, the key to the validity of the thermodynamic analysis, presented in this chapter, lies in the correspondence between the simultaneous values of α, $\Delta\mu g$, and $\Delta\mu_l$. Both $\Delta\mu_g$ and $\Delta\mu_l$ are given by similar equations as follows,

$$\Delta\mu_g = \Delta\mu_g^{\text{ideal}} - \Delta\mu_g^{\text{correction}} \qquad (2.39)$$

$$\Delta\mu_l = \Delta\mu_l^{\text{ideal}} + \Delta\mu_l^{\text{correction}} \qquad (2.100)$$

From equations (2.40), (2.41) and (2.58)

$$\Delta\mu_g = -RT \ln\alpha + BP_g^{o}(1-\alpha) \qquad (2.101)$$

$$\Delta\mu_l = \frac{\Delta P_l}{\rho_l^{o}} + \Delta\mu_l^{c} \qquad (2.102)$$

---

*That the capillary condensate cannot sustain itself due to mechanical instability.

At equilibrium between the liquid and gas phases, the chemical potentials for the two phases, for any α, must be equal, so that

$$- RT \ln\alpha + BP_g^o (1-\alpha) = \frac{\Delta P_1}{\rho_1^o} + \Delta\mu_1^c \qquad (2.103)$$

For α equal to say 0.4 and T = 126.67° C, the left hand side ($\Delta\mu_g$) is equal to 2.94×10^4 $\frac{\text{cc-atm}}{\text{g mole}}$. Assuming, therefore, that $\Delta\mu_1^c$ is small compared with $\Delta\mu_1^{id*}$, the value of ΔP_1 would have to be very large so that equation (2.103) holds. Added to this unreasonably large value is the fact that both equations (2.56) and (2.64), predict $\Delta\mu_1^c << \Delta\mu_1^{id}$ even at the tensile strength of the liquid at that temperature.

The above inequality stipulates that the liquid is ideal at large (negative) pressures corresponding to the tensile strength of the liquid, at a fixed temperature. Recalling that the liquid volume decreases with the relative saturation α (increasing tension), deviation from ideality of the liquid is much more likely to occur. The implications of the compressibility equation regarding the magnitudes of $\Delta\mu_1$ and χ_1 are not self consistent. This aspect of the argument (against the use of the compressibility equation) is covered in Appendix D.

In contrast to the compressibility equation, it has been shown in Appendix E that the van der Waals equation does indeed imply large deviations from ideality for the liquid phase, when molecular volumes

---

*Which indeed the compressibility equation predicts (see Appendix D).

of the capillary condensate are involved. Furthermore, the van der Waals equation also allows the estimation of the tensile strengths of liquids, for fixed temperatures. These have been tabulated in Table (C.2) in Appendix C.

The liquid potential change (from the reference state) was given earlier [equation (2.102)] by an ideal term $\Delta\mu_1^{id}$, and a correction term to account for the fact that the liquid is not truly incompressible.

$$\Delta\mu_1 = \frac{\Delta P_1}{\rho_1^o} + \Delta\mu_1^c \qquad (2.102)$$

An order of magnitude calculation of the terms in the above equation for T = 126.67° C and $\alpha = 0.4$, yields the following results:

$$\Delta\mu_1 = \Delta\mu_g = 2.94 \times 10^4 \text{ cc - atm/g-mole}$$

Tensile strength (at 126.67° C) of water, (from Table C.2, Appendix C) = 500 atm.

$$|\Delta P_1| \simeq 500 + 2.4 = 502.4 \text{ atm}$$

$$\rho_1^o \text{ (from Table 2.3)} \simeq 0.052 \text{ g-moles/cc}$$

$$\Delta\mu_1^c \simeq 1.97 \times 10^4 \text{ cc - atm/g-mole}$$

Hence, $\Delta\mu_1$ at $\alpha = 0.4$ exceeds the maximum* value of $\Delta P / \rho_1^o$ so that even $\Delta\mu_1^c$ exceeds the ideal term contribution. Consequently, the utility of an equation such as (2.102) where the correction term exceeds the magnitude of what should be the dominant term ($\Delta\mu_g^{id}$), is

*$\Delta P_1/\rho_1^o$ is computed at the tensile strength of the liquid to illustrate the point being made here.

limited to a fairly small range of α. It may be noted here that the potential changes given by (2.102) are associated with free energy changes given by pressure - volume type work terms. This observation is especially pertinent when considered in light of the fact that smaller volumes of the capillary condensate are present at the lower partial pressures (of water vapor). Furthermore, varying interfacial tensions and the resulting surface free energies involved at the liquid-solid and liquid vapor interfaces assume increasing importance*.

The variation of surface tension with curvature has been investigated by several workers (H4, for example) and one form of the dependence of σ_{lg} upon K is shown and discussed in Section E-2, Appendix E. This fact does away with the assumption of the invariance of surface tension used to formulate the Laplace and Young equations (Section 2.5), which are intermediate in the development of the final thermodynamic expression for the radius of curvature.

Referring back to equation (2.11), the modified expression of total (system) free energy change becomes

$$dA = -P_g\, dV + (P_g - P_l)\, dV_l + (\sigma_{sl} - \sigma_{sg})\, d\Omega_{sl} + \Omega_{sl}\, (d\sigma_{sl} - d\sigma_{sg}) + \sigma_{lg} d\Omega_{lg} + \Omega_{lg} d\sigma_{lg} \qquad (2.104)$$

The above expression takes into account the change in the interfacial tensions, and equation (2.15) for the internal free energy change is rewritten in a similar manner as

---

*See Appendix E.

$$dA_{int} = (P_g - P_l)\, dV_l + (\sigma_{sl} - \sigma_{sg})\, d\Omega_{sl} + \Omega_{sl}\, (d\sigma_{sl} - d\sigma_{sg}) + \sigma_{lg}\, d\Omega_{lg} + \Omega_{lg} d\sigma_{lg} \qquad (2.105)$$

It should be emphasized here that equations (2.104) and (2.105) may not be complete in themselves as far as the inclusion of all contributing (free energy) terms are concerned. However, even a qualitative approach to the extension of such a system of thermodynamic and hydrostatic equations to meniscus curvatures corresponding to molecular sizes necessitates the inclusion of the curvature effect on the spreading pressure,* and a modified hydrostatic equation [Appendix E, equation (E.8)]. In light of this, the first of the Laplace and Young equations (2.19) for the molecular (liquid volume) region should be of the following form:

$$P_g - P_l - \phi_l\, (\sigma_{lg} K) = 0 \qquad (2.106)$$

where ϕ, is an explicit or implicit function given by

$$\phi_l = \phi_2\, \{\sigma_{lg}, \sigma_{sg}, \Omega_{lg}, K\} \qquad (2.107)$$

The calculation procedure, shown earlier, to evaluate $\Delta\mu_l^c$ involved, first, an estimation of $\Delta\mu_g$. This is because the gas phase potential change is explicitly given, once the temperature and the relative saturation are fixed. This was then equated to the right hand side of equation (2.102) which consisted of two terms involving pressure-volume free energy changes only. It was then concluded that $\Delta\mu_l^{id}$ was

---

*Surface tension

low enough so that $\Delta\mu_1^c$ dominated and the liquid was therefore non-ideal. This tentative conclusion is implied by the van der Waals equation (Appendix E). However, in light of equations (2.104), (2.105) and (2.106), it is logical to deduce that the total liquid potential change ($\Delta\mu_1$) is also associated with the surface free energy contributions, in addition to the P-V terms. These contributions become important at small liquid volumes and this, perhaps, is suggested by the (relatively) low value of $\Delta P_1/\rho_1^o$ ($\Delta\mu_1^{id}$) itself which, as seen earlier, cannot numerically account for the magnitude of $\Delta\mu_g$ (equal to $\Delta\mu_1$) outside of a small range of α.

Assuming
$$|BP_g(1-\alpha)| \ll |RT\ln\alpha| \qquad (2.108)$$

a threshold value of α, equal to α_1 is defined as

$$\alpha_1 \simeq \exp[-\Delta\mu_1/RT] \qquad (2.109)$$

The significance of α_1 is that it is the lower limit to the range (mentioned above) of the relative saturation over which equation (2.102) holds. The criterion here is that below $\alpha = \alpha_1, \Delta\mu_1^c$ is acceptably small* such that it is low compared to $\Delta P_1/\rho_c^o$. Below $\alpha = \alpha_1$, therefore equation (2.102) is essentially incomplete, and must at least include thermodynamic potentials associated with changes in σ_{lg} and Ω_{sg} (solid-liquid contact area).

---

*In the context of this discussion this is arbitrary.

Thus

$$\Delta\mu_1 = \frac{\Delta P_1}{\rho_1^o} + f(\sigma_{sl}, \Omega_{sg}, K) + \Delta\mu_{11}^c \qquad (2.110)$$

where

f = a function of the variables indicated

$\Delta\mu_{11}^c$ = modified correction term.

The significance of $\Delta\mu_{11}^c$ is evident in equation (2.110). However, it is important to recognize that now

$$\Delta\mu_{11}^c < \Delta\mu_1^c \qquad (2.111)$$

so that the capillary condensate may not be as non-ideal as stated earlier, and as the van der Waals equation purports it to be (Appendix E).

It was stated, earlier in this section, that there are two physical limits that need to be examined to assure the existence of the capillary condensate. These two limits relate to the dimensional restriction of the pore and the mechanical instability of the liquid. It is important to determine whether the values of the relative saturation α at these limits are only marginally different or that one prevails over the other. The results of the calculations to this end are presented in Table 2.11 for the six experimental temperatures in this work.

The pore dimensional restriction was estimated on the premise that one molecule of water can fit at the point in question (inside the pore), such that the linear dimension along the y axis (Figure

Table 2.14. Values of the Liquid (or Gas)* Chemical Potential Departures (from reference state) at the Two Limits of Capillary Condensation.

Temperature (^{o}C)	P_g^{o} (saturation) (atm)	α_{DR} (P_g/P_g^{o})	$\Delta\mu_{l,DR}$ (cc-atm/g-mole)	$\Delta\mu_{l,MI}$ (cc-atm/g-mole)
65.56	0.253	0.00184	1.577×10^5	$>10^7$
98.89	0.962	0.00519	1.601×10^5	$>10^7$
126.67	2.411	0.01046	1.486×10^5	1.111×10^7
143.33	3.918	0.01541	1.411×10^5	6.152×10^6
157.22	5.682	0.02129	1.340×10^5	4.285×10^6
176.67	9.162	0.03256	1.236×10^5	2.873×10^6

DR = Dimensional restriction

MI = Mechanical Instability restriction

α_{DR} = Relative Saturation corresponding to Dimensional restriction

*At equilibrium, $\Delta\mu_l = \Delta\mu_g$.

2.9) from one point of liquid-solid contact to another is equal to the molecular diameter ($2.725A^{o}$)*.

The entries in the fifth column for $\Delta\mu_l$ are obtained from Table D.2 in Appendix D. In each case, $\Delta\mu_l$ corresponding to the mechanical instability limit (of the liquid) exceeds the value in column 4 by at least one order of magnitude. Since α decreases as $\Delta\mu_l$ (or $\Delta\mu_g$) increases, it is evident from the results in the table that a receding liquid meniscus encounters the dimensional limit before the instability criterion can be met. Hence the sizes of the molecule and the pore are relatively more important than a consideration of the tensile strength of the liquid.

The emphasis of the previous paragraph is not so much on the numerical accuracy of the values of the liquid potential; instead the main focus is on the fact that the molecular and macropore dimensional restriction prevails over the limit imposed by the rupture of the liquid. As mentioned in Appendix E, the objective of the work presented in this chapter was not to arrive at a thermodynamically complete model of the capillary condensation process. Such a model would at least begin with a formally complete expression for the total (Helmholtz) free energy change for the closed system as well as a generalized hydrostatic balance. The problem would, as a result, become more involved particularly if the variation of surface tension with curvature were included.

---

*The molecular diameter in this case is taken to be one of the force constants (collision diameter) for water vapor and this value is calculated from a modified Stockmayer potential equation (H3).

The uncertainties involved in the use of the van der Waals equation to approximate liquid behaviour (in the tensile region) have been discussed in Appendices D and E. Additionally, the expressions for the surface tension in terms of curvature include the assumption that the liquid is incompressible. Hence, a quantitatively precise expression for σ_{lg} as a function of K (without the restriction of liquid incompressibility) changes the structure of this problem to an implicit one* since K is then known in terms of an equation of state which is precisely what the Kelvin equation seeks to determine in a modified form.

The purpose of Chapter 2 ties into the overall objective of the work in so far as the (particle) surface coverage by condensate can be estimated from the known variables. This coverage can be calculated if the radius of curvature of the meniscus and the solid particle diameter are known. In this context, it may be noted that the uncertainties involving equation (2.102) do not reflect on the accuracy of the values of curvature calculated from equation (2.62). This is true as long as $\Delta\mu_{11}^{c} < \Delta\mu_{g}$**. Such an assumption is not far fetched in light of the discussion related to equation (2.110). The correction to the liquid phase chemical potential $\Delta\mu_{11}^{c}$ (which arises due to compressibility) is therefore assumed to be small enough compared to

---

*In contrast to equation (2.67), which is an explicit expression for the radius of curvature.

**$\Delta\mu_{11}^{c}$ should be, at worst, small enough relative to $\Delta\mu_{g}$ so that it doesn't affect the magnitude of K significantly.

$\Delta\mu_g$ so that the thermodynamic equation [2.67] is accepted as being valid.

The principal objective of evaluating liquid chemical potentials at low values of α was to be able to arrive at the foregoing conclusion regarding the physical limitations upon the existence of the capillary condensate. Hence, the partial results presented in Tables 2.8-A, B and C for the three temperatures (65.56° C, 126.67° C and 176.67° C) cover the range of the relative saturation that is accepted as being theoretically feasible.

CHAPTER THREE

EXAMINATION OF THE ELECTRIC FIELD IN THE VICINITY OF THE INTERPARTICLE CONTACT

Overview

The phenomenon of capillary condensation of water in the macropores of a particulate layer was examined in Chapter 2. The presence of liquid (condensate) affects the bulk surface resistivity, and therefore it was determined necessary to evaluate the extent of the condensation for a given temperature, hu idity and pressure. In this chapter, the other important aspect of high field strengths in the macropore* is investigated. The physical significance of this feature is highlighted by the non-linear current-voltage (I-V) curve of particulate layers of fly ash as indicated by the results of Chapter 1.

In the context of the overall problem** this chapter provides the necessary continuity in the sense that the "electrical behaviour" near the contact (or macropore) is investigated. In Chapter 2, the "thermodynamic behaviour" (of the system), at the macropore, was examined. For the purposes of this work, only these two aspects of the particulate layer are considered. The thermodynamic and electrical considerations provide a physical (and mathematical) basis for the overall problem. In addition to this, the resistances that are encountered by a migrating charge carrier (ion or electron on the particle surface) are

---

*This constitutes the vicinity of the contact.

**Of characterizing the bulk surface resistivity of a layer of particulates.

visualized.* This is schematically illustrated by Figure 3.1.

It is generally recognized that the non-ohmic behaviour of a particulate layer of fly ash, under normal operating conditions in an electrostatic precipitator, partly results from the high field strengths in the vicinity of the contact between particles (M3). These field strengths may be high enough to sustain a charge emission across the gap. This implies a "region of breakdown" in the vicinity of the contact, and it is therefore (at least) qualitatively apparent that the resistivity is modified as a result.

In order to substantiate the phenomenon of electrical breakdown, one needs to know the variation of the relevant fields with respect to position in the gap. These are the field strength at the line** of the interparticle contact $\vec{E}_1$, and the field on the particle surface $\vec{E}_s(\theta)$. The derivation of the expressions for $\vec{E}_1$ and $\vec{E}_s(\theta)$ are independent of each other, however a unique feature of this problem is the contact or the constriction resistance. Since electrostatic forces are roughly proportional to the square of the electric field (W4, M3), the presence of high gap field strengths gives rise to appreciable cohesive forces within the particulate layer (L1). This is discussed in Section 3.1 where the interparticle contact spot is described.

*The resistance due to the capillary condensate, in the macropore, is not considered in this chapter.

**Although the interparticle contact forms a plane, this is visualized in the figures in this chapter as a line. The "line of contact" goes symmetrically through the plane of contact and the term is used in the following text as a matter of convenience (see Figure 3.1).

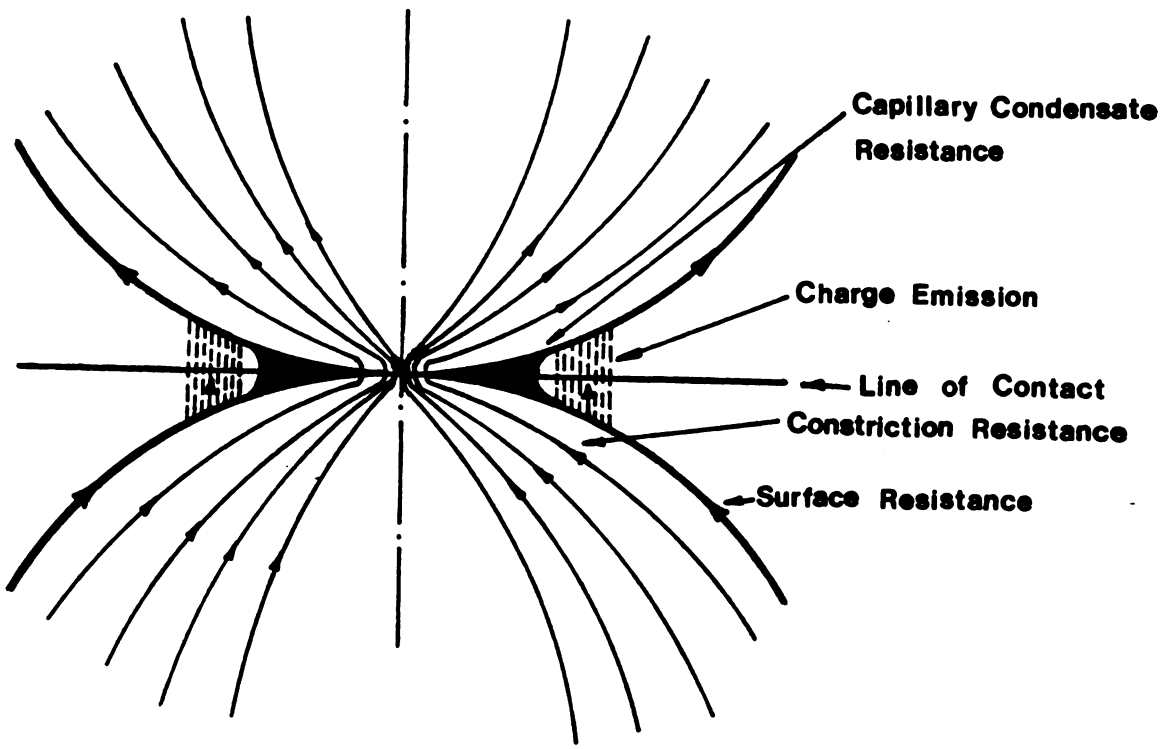

Figure 3.1 Schematic illustration of the resistances near the interparticle contact.

The contact resistance is introduced in Section 3.2, where it is shown that this is the resistance between equipotential surfaces (inside a spherical particle) that are normal to the lines of force "radiating" from the actual contact (or constriction). A simple expression due to Holm (H1), illustrating this feature, is derived in this section.

A more formal approach than the above (suggested by Smythe, S4) is required* for the case where the objective (as in this chapter) is to ascertain and compare the magnitudes of the field strengths $\vec{E}_1$ and $\vec{E}_s$ (θ). This is presented in Section 3.3 where the analysis leading to the expression for the contact resistance begins with a general representation of the (oblate hemispheroidal) equipotential surfaces. The Laplace equation is used to arrive at a second order differential equation for the potential (of an equipotential surface) in terms of Cartesian coordinates and a characteristic distance parameter μ. This leads to a general (integral) solution, equation (3.27). The spatial derivative of the potential gives the field strength at an equipotential surface. For the contact resistance problem, one needs to know the capacitance between two equipotentials in terms of the parameter μ. Since capacitance G is directly related to the charge (on a surface), the relationship between field strength** and the surface charge density must be established. This is accomplished by means of the Gauss law for $\vec{E}$ field (Appendix H).

Once the capacitance (between a charged surface and an equipotential in this case) is known as a function of μ, the foregoing problem is

*For the determination of the contact resistance.

**Which is given in terms of μ now.

transformed to a (geometrically similar) current or resistance problem. The current density is given in terms of the potential gradient. Since the electrical resistance and capacitance are both related to the potential difference, the contact resistance is easily obtained, after some manipulation, as a function of μ only [equation (3.67)].

The final expression for the contact resistance can now be used to determine the potential and potential gradients (field strength) on the particle and in the gap near the contact. This is done in Section 3.4 where the axial* field strength, $\vec{E}_1$, on the line of contact, is given in terms of the dimensionless distance from the contact. In Section 3.5 the expression for the axial (particle) surface field strength $\vec{E}_s$ (θ) is derived. The significance of $\vec{E}_s(\theta)$ is based upon the fact that it is this field strength that a migrating charge carrier (ion or electron) experiences on the surface of the particle.

The methods used to determine the fields $\vec{E}_1$ and $\vec{E}_s$ (θ) was suggested by McLean (M2, M3), however the final expressions differ from those of the author. The differences between the corresponding results are discussed in Sections 3.4 and 3.8, in light of the physics of the problem. In Section 3.6, the field strengths $\vec{E}_1$ and $\vec{E}_s$ (θ) are numerically evaluated, and it is shown that both these fields can achieve the breakdown value. This fact establishes the phenomenon of charge emission across the gap. From this information, a region of breakdown can be defined in terms of the particle surface area.

The procedure leading to the results in Section 3.6 is recapitulated in Section 3.7. The foregoing material is reviewed, in this section,

---

*In the direction of the external voltage gradient.

additional resistance due to the constriction, and is caused by the narrowing of the lines of current flow at the contact spots (for both surface and volume conduction). This resistance depends upon the size and shape of the contact spot. In the absence of any interparticle forces (electrical or otherwise)*, the contact is theoretically a point where two neighbouring spheres meet. However, as mentioned in Section 2.2, where the idealized model is described, a resistive body of particulates experiences cohesive forces when under the influence of an externally imposed electric field. A theoretical expression for the "electrical" component of the cohesive force can be derived for the idealized layer (M3). As described in the Introduction, the magnitude of the cohesive forces within an electrostatic precipitator partly determine the effectiveness of the (vibrating or impulse) rapper that dislodges particles deposited on the collection electrode.

The interparticle cohesive force induces a contact of a certain area between two particles. This area is related to the force F between two particles by means of the Hertz equation** (M1):

$$a = \left[\frac{0.75\ \mathbf{S}\ (1-v^2)\ F}{Y}\right]^{1/3} \qquad (3.1)$$

where

a = radius of common contact between particles

S = particle radius

v = Poisson's ratio

Y = Young's modulus

---

*See reference D2.

**See also reference M5.

from the perspective of the overall problem of characterizing the bulk surface resistivity of a particulate layer. This is followed by a discussion of the procedure and results, of this chapter, in Section 3.8.

3.1 The Interparticle Contact Spot

The non-ohmic behaviour of a particulate bed of fly ash, under normal operating conditions in an industrial electrostatic precipitator, results from the high electric field strengths in the vicinity of the contact. Such a behaviour was illustrated by the current-voltage characteristics of the type shown in Figure 1.3, Chapter 1. It was also pointed out in Section 1.2 that the presence of strong fields* ($\vec{E}$), near the contact of two adjoining particles, explains the phenomenon of an air (or gas) gap discharge between the particles.

Referring to Figure 2.2 (Chapter 2), it is seen that an ion or electron, migrating along the surface or through the body of any spherical particle, encounters a constriction at the point of contact. This physical constriction of the lines of current flow across the layer, is associated with an electrical resistance defined as the constriction resistance.** This type of a resistance is a common feature of the theory of electrical contacts (H1).

The constriction resistance, according to Holm (H1), is an

---

*It is shown later in this chapter (Sections 3.3, 3.4), that the magnitudes of the field strengths, in the immediate neighborhood of the contact, is equal to the breakdown value.

**The constriction resistance is described, in more detail in Appendix G.

It may be recalled here that the particles were considered to be rigid as far as capillary condensation was concerned (Section 2.2, Chapter 2; and Section E.2, Appendix E). This restriction is removed in the present context partly because a well defined deformation resulting in a (plane) circular contact area can be mathematically related to a compressive force F as shown in equation (3.1). It is a plausible assumption at this stage, that the magnitude of this area affects the constriction resistance since it directly determines the degree of the constriction of the lines of current flow. It can, therefore, be expected that the size of contact will also influence the overall bulk resistivity (of the layer).

The above generalization of particle compressibility implies the existence of two separate but distinct phenomena:

i) The cohesive forces within a layer

ii) The interparticle contact spots, and their effect on the layer resistivity.

In as much as particle elasticity is taken to be a generalization, it has been stipulated above that the resulting contact spots are circular with a well defined radius. Such a stipulation is a restriction which simplifies the mathematics of the problem (Section 3.3). One method of determining a simplified general expression for the contact resistance between two resistive bodies involves the representation of the contact spot by a (relatively) small conducting sphere, and this is presented in the next section. In the context of the analysis in Section 3.2 (and in subsequent sections as well) it may be borne in mind that electrical breakdown* of the air or gas, in the vicinity

*Hence, also an air gap discharge.

of the contact, is not mentioned (nor assumed) until it is first established.

3.2 The Contact Resistance - A Simplified Analysis

The electrical resistance of two bodies in contact always implies a constriction resistance. This is a consequence of the current flow being localized through the small conducting spot. The main part of the constriction resistance is localized in the immediate vicinity of the contact area.

A simplified analysis of this problem consists in representing the contact spot by a conducting sphere, of radius r, joining two plates as shown in Figure 3.2*. The radial lines of electronic current flow are normal to the hemispherical equipotential surfaces, which are symmetric with respect to the spherical contact.

Consider the resistance in the lower contact member. The resistance between two equipotential surfaces B and C, separated by a distance dr, is given by

$$dR^{1} = \rho\, dr/2\pi r^{2**} \qquad (3.2)$$

---

*The analysis, in this section, is restricted to the extent that the equipotential surfaces are considered to hemispheres (as shown in Figure 3.2). The generalized analysis is presented in the next section. Furthermore, in the present section, only a crude representation of the contact resistance is sought, with the immediate objective of characterizing the resistance due to the constriction only.

**The resistance due to a volume current is given by

$$R = \rho\, L/A$$

where R = resistance, ρ = material resistivity, L = length of current flow, A = cross sectional area normal to current flow.

where

dR^1 = differential resistance, ohm.

ρ = resistivity of the monolothic material of the contact members, ohm - cm.

r = radius of hemisphere C, cm.

The constriction (or contact) resistance for one contact member, is obtained by integrating this expression (3.2) from $r = r_1$ to $r = \infty$, where r_1 is the radius of the spherical contact. The contribution to the resistance, due to an increase in r, decreases as $1/r^2$; hence the inclusion of more distant hemispherical equipotentials contributes relatively little to the integral below. The value $r = \infty$, therefore, may be chosen as the upper limit of integration in (3.3).

$$R^1 = \frac{\rho}{2\pi} \int_{r_1}^{\infty} \frac{dr}{r^2} \tag{3.3}$$

$$\therefore R^1 = \rho/2\pi r_1 \tag{3.4}$$

Thus the total constriction resistance R^1_T (due to both contact members) is given as

$$R^1_T = \rho/\pi r_1 \tag{3.5}$$

This expression is true only for the idealized case above, however, the dependence of the contact resistance upon the size of the contact (r_1) is indicated by (3.5).

As stated in the overview of this chapter, the objective of the work in this chapter is to be able to arrive at formal expressions for the directional variations of the field strength in the vicinity of the

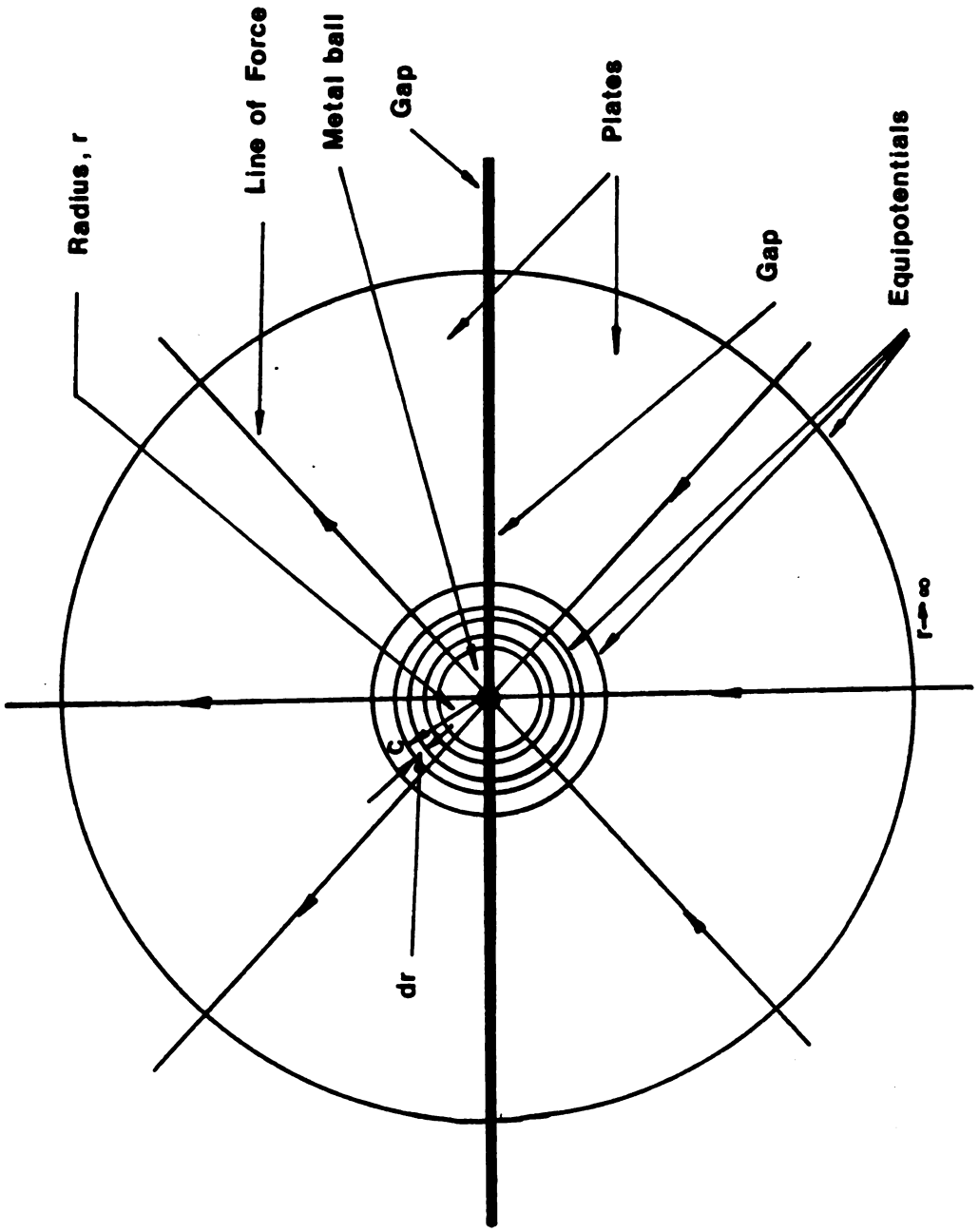

Figure 3.2 Simplified representation of the contact resistance.

contact. These, then, can be incorporated into a resistivity model for the bulk particulate layer. For this purpose, the problem of determining the constriction resistance requires a generalized approach, and this is presented in the next section.

3.3 Generalized Representation of the Contact Resistance.

This section deals with a formal approach to the problem of determining the resistance due to one contact between two spherical particles in the idealized model. The idealized model was described earlier in Section 2.2, Chapter 2. A rigorous analysis would begin by defining the surface of the contact spot as an equipotential surface which has the (generalized) contour of a conicoid and is confocal with similar equipotential surfaces in the vicinity. The immediate problem is one of electrostatics, where it is required to determine the capacitance between a surface A_c containing some surface charge, and another equipotential surface A_1 at a distance away from it (Figure 3.3).

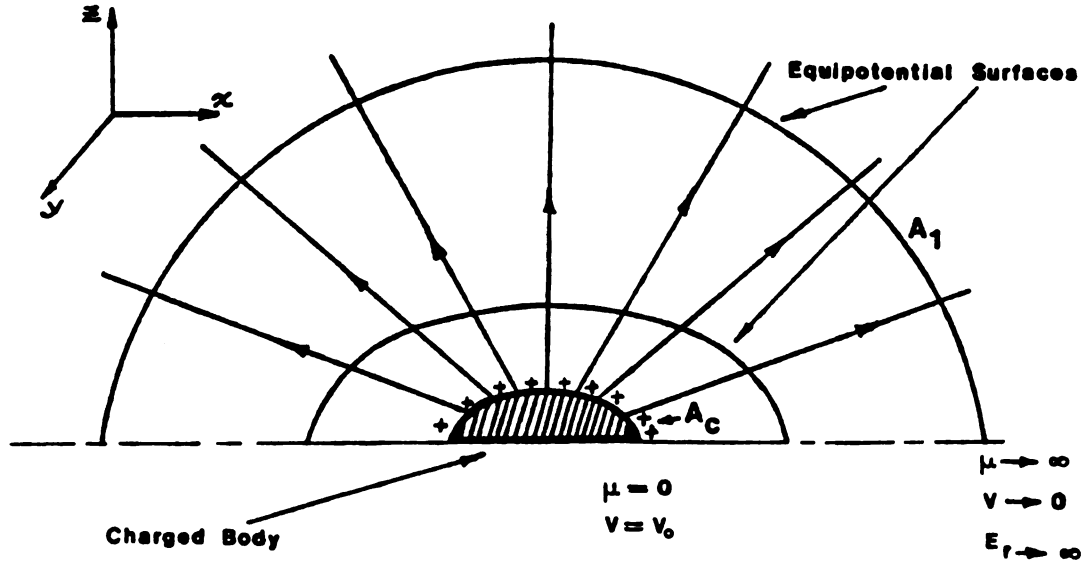

Figure 3.3 Schematic representation of equipotentials and field lines of force from a charged semi-ellipsoid.

The equipotential surfaces, as shown in Figures 3.2 and 3.3 are a set of non-intersecting surfaces (or lines in a two dimensional plane) in space; and to each value of the potential function V there corresponds a single value $\overline{C}$ (S4):

$$\text{Let } V = f(\overline{C}) \tag{3.6}$$

where $\overline{C}$ is some function of the three dimensional co-ordinates,

$$\overline{C} = \psi(x,y,z) \tag{3.7}$$

V being harmonic* satisfies Laplace's equation,

$$\nabla^2 V = 0 \tag{3.8}$$

From equation (3.6) the first and second derivatives are as follows:

$$\frac{\partial V}{\partial x} = f'(\overline{C}) \frac{\partial \overline{C}}{\partial x} \tag{3.9}$$

and

---

*Harmonic functions satisfy Laplace's equation. If two families of curves V (x,y) and U (x,y) intersect each other orthogonally, and if one of them, say V, is called the potential function, then U is known as the stream function. In this case if V represents the set of equipotentials then U represents the lines of force. The potential and stream functions are conjugate and analytic and hence satisfy the Cauchy-Riemann equations:

$$\frac{\partial V}{\partial x} = -\frac{\partial U}{\partial y}\ ;\ \frac{\partial V}{\partial y} = \frac{\partial U}{\partial x}$$

if

$$W = U + iV$$

The magnitude of the electric field strength (voltage gradient) is given by

$$\left|\frac{dW}{dz}\right| = \frac{\partial V}{\partial n}$$

where

$$z = x + iy$$

and dn is the length in the direction of the maximum increase of potential.

$$\frac{\partial^2 V}{\partial x^2} = f''(\bar{C}) \left(\frac{\partial \bar{C}}{\partial x}\right)^2 + f'(\bar{C}) \left(\frac{\partial^2 \bar{C}}{\partial x^2}\right) \tag{3.10}$$

Substituting (3.9) and (3.10) into Laplace's equation for one dimension only

$$f''(\nabla \bar{C})^2 + f'(\nabla^2 \bar{C}) = 0 \tag{3.11}$$

$$\therefore \quad \frac{\nabla^2 \bar{C}}{(\nabla \bar{C})^2} = -\frac{f''(\bar{C})}{f'(\bar{C})} = \bar{f}(\bar{C}) \tag{3.12}$$

Since the right hand side of equation (3.12) is a function of C only, C is unique and corresponds to a non-intersecting equipotential surface. Equation (3.11) can be solved if two boundary conditions are known.

As mentioned earlier in this section, the most general form for an equipotential surface is one of the three sets of non intersecting confocal conicoids:

$$\frac{x^2}{a^2+\mu} + \frac{y^2}{b^2+\mu} + \frac{z^2}{c^2+\mu} = 1 \tag{3.13}$$

where

a,b,c = conicoid semi-axes in the three directions x, y and z respectively

μ = a parameter with features relevant to the physical problem.*

*For example, $\mu = -a^2$ represents an ellipsoid flattened to a disk on the y - z plane.

Let

$$M_n \equiv \frac{x^2}{(a^2+\mu)^n} + \frac{y^2}{(b^2+\mu)^n} + \frac{z^2}{(c^2+\mu)^n} \qquad (3.14)$$

be the generalized representation of a conicoid.

Also define N such that

$$N \equiv \frac{1}{(a^2+\mu)} + \frac{1}{(b^2+\mu)} + \frac{1}{(c^2+\mu)} \qquad (3.15)$$

Equation (3.13) above becomes

$$M_1 = 1 \qquad (3.16)$$

The total derivative of M_1 (in one dimension) is:

$$dM_1 = \frac{d}{dx}\left(\frac{x^2}{a^2+\mu}\right) dx = \frac{d}{d\mu}\left(\frac{x^2}{a^2+\mu}\right) d\mu = 0$$

or

$$\frac{2x}{a^2+\mu} = M_2 \frac{d\mu}{dx} \qquad (3.17)$$

where M_2 (in terms of x coordinate only) is suggested by definition (3.14)

$$M_2 = x^2/(a^2+\mu)^2 \qquad (3.18)$$

The parameter μ here is analogous to $\overline{C}$ in equation (3.11). Since now the equipotential surface has been specified by equation (3.13), a solution to the differential equation (3.12) is sought in terms of μ, after making the appropriate substitutions as shown.

$$(\nabla\mu)^2 = (\frac{\partial\mu}{\partial x})^2 + (\frac{\partial\mu}{\partial y})^2 + (\frac{\partial\mu}{\partial z})^2 \qquad (3.19)$$

Substituting for each of terms on the right side of equation (3.19) using equation (3.17)

$$(\nabla\mu)^2 = \frac{4}{M_2^2}\left[\frac{x^2}{(a^2+\mu)^2} + \frac{y^2}{(b^2+\mu)^2} + \frac{z^2}{(c^2+\mu)^2}\right] = 4/M_2 \qquad (3.20)$$

The second derivative of μ with respect to x is obtained from (3.17)

$$\frac{\partial^2\mu}{\partial x^2} = \frac{2}{M_2(a^2+\mu)} - \frac{2x}{M_2(a^2+\mu)^2}\frac{\partial\mu}{\partial x} - \frac{2x}{(a^2+\mu)}\frac{1}{M_2^2}\left[\frac{2x}{(a^2+\mu)^2} + 2M_3\frac{\partial\mu}{\partial x}\right]$$

$$= \frac{2N}{M_2} - \frac{8M_3}{M_2^2} + \frac{8M_2M_3}{M_2^3}$$

$$\therefore \quad \nabla^2\mu = 2N/M_2 \qquad (3.21)$$

Substitution of the derivatives, $\nabla\mu$ and $\nabla^2\mu$, into the Laplace's equation yields a second order differential equation of type (3.12). It may be noted that this results in a function $\overline{f}(\mu)$ shown below, that is given

in terms of the variable μ only*.

$$\frac{\nabla^2\mu}{(\nabla\mu)^2} = \frac{2N}{M_2} \cdot \frac{M_2}{4} = \frac{N}{2}$$

$$= \bar{f}(\mu) \qquad (3.22)$$

where now

$$\bar{f}(\mu) \equiv \tfrac{1}{2}\left(\frac{1}{(a^2+\mu)} + \frac{1}{(b^2+\mu)} + \frac{1}{\mu}\right) \qquad (3.23)$$

from the definition for N in equation (3.15). In equation (3.23) the z axis parameter c is dropped so that the set of equipotentials is characterized, along this direction, by μ only. The general solution to (3.22) is straight forward, and is obtained by substituting $\bar{f}(u)$ into the solution for equation (3.12) as shown below.

$$\int \bar{f}\,(\bar{C})\, d\,\bar{C} = -\int^{\bar{C}} \frac{f''(\bar{C})}{f'(\bar{C})}\, d\bar{C} \qquad (3.24)$$

$$\therefore -V' = f(\bar{C}) = A \int^{\bar{C}} \exp\left[-\int \bar{f}(\bar{C})\, d\bar{C}\right] + B \qquad (3.25)$$

from equation (3.6). A and B are integration constants. Replacing $\bar{f}(\bar{C})$ by $\bar{f}(\mu)$ which is now defined, one gets:

$$V = A \int^{\mu} \exp\left[-\int \tfrac{1}{2}\left\{\frac{1}{(a^2+\mu)} + \frac{1}{(b^2+\mu)} + \frac{1}{\mu}\right\} d\mu\right] d\mu + B \qquad (3.26)$$

---

*a, b and c are the constants (semi-axes) of the conicoid.

where V may be viewed as the electric potential corresponding to an equipotential surface for a fixed value of μ. The potential, then, is given by the right hand side of (3.26).

The inner integral simplifies to:

$$-\tfrac{1}{2} \ln \{(a^2+\mu)\ (b^2+\mu)\mu\}$$

hence,

$$V = f(\mu) = A \int_{\mu}^{\infty} [(a^2+\mu)(b^2+\mu)\mu]^{-\frac{1}{2}}\, d\mu + B \qquad (3.27)$$

It may be recognized that the expression for V is given in terms of an elliptic integral. The general solution (3.27) for the potential V may now be applied to the present problem by setting boundary conditions. This is depicted in Figure 3.3, where semiellipsoidal ($c^2 = 0 < \mu$) equipotential surfaces are located symmetrically, and at increasing distances away from a charged surface which is at a potential V_o. These distances, along the z axis, are given by the parameter μ. It is assumed that the potential is zero at a point far removed from the surface charge. Hence the two boundary conditions are,

$$V = V_o \text{ at } \mu = 0 \qquad (3.28)$$

$$V = 0 \text{ at } \mu = \infty \qquad (3.29)$$

Using boundary conditions (3.28) and (3.29), in that order, gives

$$B = 0 \tag{3.30}$$

and

$$V_o = - A \int_o^\infty [(a^2+\mu)\ (b^2+\mu)\mu]^{-\frac{1}{2}}\, d\mu \tag{3.31}$$

So that the integration constant A is given as

$$A = - V_o \{ \int_o^\infty [(a^2+\mu)\ (b^2+\mu)\mu]^{-\frac{1}{2}}\, d\mu\}^{-1} \tag{3.32}$$

The electric field strength (voltage gradient) at very large distances* due to the charged ellipsoid is evaluated as follows:

As $\mu \to \infty$

$$x^2 + y^2 + z^2 = r^2, \quad \text{where } \mu \simeq r^2 \tag{3.33}$$

so that at infinity the equipotential surfaces are approximated by hemispheroids of radius r (equal to $\sqrt{\mu}$).

$$\frac{\partial \mu}{\partial r}\Big|_{r \to \infty} = 2r \tag{3.34}$$

$$\vec{E}_r\Big|_{r\to\infty} = \frac{\partial V}{\partial r}\Big|_{r\to\infty} = \frac{\partial V}{\partial \mu} \cdot \frac{\partial \mu}{\partial r} = \frac{\partial V}{\partial \mu} \cdot 2r \tag{3.35}$$

---

*Relative to the dimensions of the body containing the surface charge.

For large values of μ: $\mu \geq a^2$, $\mu \geq b^2$; equation (3.27) simplifies to

$$V = A \int_0^{\infty} (\mu^3)^{-\frac{1}{2}} \, d\mu \tag{3.36}$$

yielding upon the substitution $\mu \simeq r^2$ [into (3.36)]*

$$\vec{E}_r \Big|_{r \to \infty} = -\frac{\partial V}{\partial r}$$

$$= -\frac{2A}{r^2} \tag{3.37}$$

Equation (3.37) gives the field strength at very large distances from the charged ellipsoid. This field strength is given in terms of the two semi axes of the ellipsoid; its potential due to charge, and the distance from it to the point where the field is to be determined. It may be noted from (3.37) that $\vec{E}_r$ decreases as r (or $\sqrt{\mu}$) increases.

Having determined the field strength at large distances from the surface charge, it is now necessary to relate it to the electric charge. The objective here, is to arrive at an expression for the capacitance between two equipotential surfaces. To accomplish this, two established relationships are required.

---

*$\vec{E}_r = -\partial V/\partial r = -\left(\frac{\partial V}{\partial \mu} \cdot \frac{\partial \mu}{\partial r}\right) = -\left\{\frac{A}{r^3} \cdot 2r\right\} = -\frac{2A}{r^2}$

1) Maxwell's first equation of electrostatics*

$$\nabla \cdot \vec{E}_r = \frac{\overline{\rho}}{\varepsilon}(\vec{r}) \tag{3.38}$$

where

$\vec{E}_r$ = electric field strength (function of $\vec{r}$)

$\overline{\rho}$ = volume charge density

ε = permittivity of medium†

Hence, the divergence of an electrostatic field is directly related to the (free) charge density of an isolated body which is the source of that field.

2) The divergence theorem. Mathematically, this simply relates the surface integral of a vector (over a closed surface) to the volume integral of its divergence.

$$\int_{\hat{V}} \nabla \cdot \vec{E} \, d\hat{V} = \int_S \hat{n} \cdot \vec{E} \, dS \tag{3.39}$$

where

$\hat{V}$ = volume of body

$\hat{n}$ = unit outward (normal) vector on closed surface S.

---

*This has been derived in Appendix H. The familiar Poisson equation follows from this:

$$\nabla^2 \phi(r) = -\overline{\rho}(\vec{r})/\varepsilon$$

where ϕ is the potential and is related to $\vec{E}$ by means of $\vec{E} = -\nabla\phi$.

†The medium is not a dielectric.

From equation (3.38)

$$\int \nabla \cdot \vec{E}\, d\hat{V} = \frac{1}{\varepsilon} \int_{\hat{V}} \bar{\rho}(\vec{r})\, d\hat{V} \qquad (3.40)$$

$$= \frac{1}{\varepsilon} \int_{\hat{V}} \sigma(\vec{r})\, dS \qquad (3.41)$$

Equation (3.41) applies to a pure surface charge only*, where σ is the surface charge density. From equation (3.39) one gets

$$\int_S \hat{n} \cdot \vec{E}\, dS = \frac{1}{\varepsilon} Q \qquad (3.42)$$

Equation (3.42) is the Gauss law for $\vec{E}$ field. Q is the total surface (or volume) charge.

For the condition that,

$$\mu \simeq r^2 \geq a^2$$
$$\geq b^2$$

the equipotential surfaces can be considered to be hemispherical. Hence the integral in (3.42) resolves to

$$\vec{E}(\vec{r}) = \hat{r} E_r = \hat{r} \frac{Q}{2\Pi\varepsilon r^2} \qquad (3.43)$$

where E_r is the scalar component in the $\hat{r}$ (which in this case is identical to the unit vector $\hat{n}$) direction.

---

*It may be noted that the quantities inside the integrals in (3.40) and (3.41) are both differential (electric) charges.

$$\therefore E_r = Q/2\Pi\epsilon r^2 \tag{3.44}$$

Expression (3.44) gives the field strength, far removed from the charged surface, in terms of the charge Q and the distance r. The field strength $\vec{E}$ decreases as $1/r^2$.

From equations (3.37) and (3.44)

$$-\frac{2A}{r^2} = \frac{Q}{2\Pi\epsilon r^2} \tag{3.45}$$

As described earlier the equipotential surfaces are normal to the lines of force, and situated symmetrically (confocal) with respect to the charged ellipsoid. This is illustrated by Figure 3.3 below.

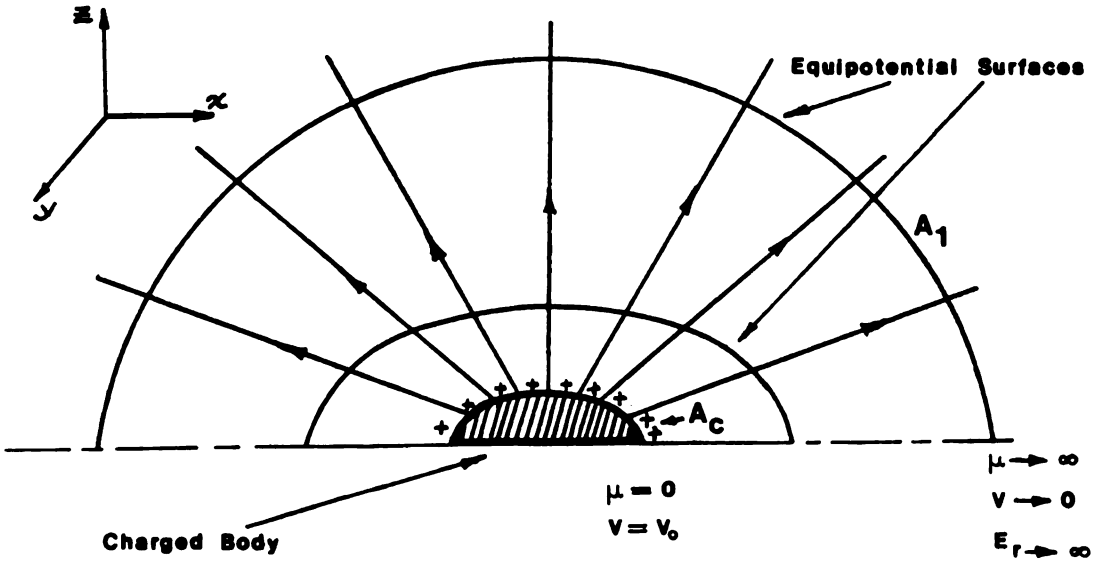

Figure 3.3 Schematic representation of equipotentials and field lines of force from a charged semi-ellipsoid. (repeated)

The capacitance C is, by definition, equal to Q/V_o. Substitution of Q from (3.45) gives

$$C = Q/V_o = \frac{-4\Pi\epsilon A}{V_o} \tag{3.46}$$

The surface potential V_o is substituted above from equation (3.31) to give

$$C = 4\pi\epsilon[\int_o^\infty \{(a^2+\mu)\ (b^2+\mu)\ \mu d\mu\}^{-\frac{1}{2}}]^{-1} \tag{3.47}$$

Equation (3.47) is the formal expression for the capacitance of the charged surface, with the restriction that c = 0. This is an elliptic integral of the first kind and is numerically solved by the use of tables.

The surface charge density σ is given by [see equation (3.44)]

$$\sigma = \epsilon E = -\epsilon \nabla V|_{\mu=0} \tag{3.48}$$

$$= -\epsilon\{\frac{\partial V}{\partial \mu} \cdot |\nabla \mu|\}|_{\mu=0} \tag{3.49}$$

To determine $\frac{\partial V}{\partial \mu}|_{\mu=0}$, the originally complete equation, where spheroidal z axis parameter $c \neq 0$, is required. This equation is of the form (3.26) as shown (see Footnote)*.

---

*The derivative $\frac{\partial V}{\partial \mu}$ cannot be determined by the modified equation (3.27) since

$$\frac{\partial V}{\partial \mu}|_{\mu=0} = A\ [(a^2+\mu)\ (b^2+\mu)\mu]^{-\frac{1}{2}} = 0$$

$$V = A \int^{\mu} \exp\left[-\int^{\mu} \tfrac{1}{2}\left\{\frac{1}{(a^2+\mu)} + \frac{1}{(b^2+\mu)} + \frac{1}{(c^2+\mu)}\right\} d\mu\right] d\mu \quad (3.50)$$

This equation simplifies to a form given by (3.27) with $c \neq 0$.

Differentiation of (3.50) with respect to μ, and setting $\mu = 0$, gives

$$\left.\frac{\partial V}{\partial \mu}\right|_{\mu=0} = \frac{A}{abc} \quad (3.51)$$

also

$$|\nabla \mu| = \frac{2}{\sqrt{M_2}} \quad \text{from (3.20)}$$

where M_2 is given by the general definition (3.14). From equation (3.45),

$$-\varepsilon A = \frac{Q}{4\pi} \quad (3.52)$$

Substituting for $\left.\frac{\partial V}{\partial \mu}\right|_{\mu=0}$, $|\nabla \mu|$ and using (3.52), the expression (3.49) for the surface charge density is:

$$\sigma = \frac{Q}{4\pi abc}\left[\frac{x^2}{a^4} + \frac{y^2}{b^4} + \frac{z^2}{c^4}\right]^{-\frac{1}{2}} \quad (3.53)$$

For the special case where the charged surface is an elliptic disk on the x-y plane (so that $c = 0$), equation (3.53) may be written in the following form

$$\sigma = \frac{Q}{4\pi ab}\left[\frac{c^2x^2}{a^4} + \frac{c^2y^2}{b^4} + \frac{z^2}{c^2}\right]^{-\frac{1}{2}} \qquad (3.54)$$

The first two terms in parethesis vanish for c = 0 in this last expression. The third term is indeterminate (as given) since both z, c → 0 as the charged ellipsoid of Figure 3.3 is flattened to a disk. This term, z^2/c^2, is however, given by the general equation (3.13) for $\mu = 0$.

hence $$\frac{z^2}{c^2} = 1 - \frac{x^2}{a^2} - \frac{y^2}{b^2}$$

Substitution of z^2/c^2 into (3.54) gives the final expression for the surface charge density of an elliptic disk*.

$$\sigma = \frac{Q}{4\pi ab}\left[1 - \frac{x^2}{a^2} - \frac{y^2}{b^2}\right]^{-\frac{1}{2}} \qquad (3.55)$$

Up to this point the problem depicted by Figure 3.3 has been solved in terms of the following:

i) The equipotentials are defined.

ii) The capacitance and the surface charge density is determined.

The problem, thus far, is one of electrostatics and has been completely determined, except for the resistance between two equipotentials. To determine this latter quantity, the flow of current (or current density) along the lines of force needs to be assumed. As will be shown later, the particular arrangement of the equipotential surfaces and radiating lines of force** is of the same form as that in an

*To obtain the charge density for a circular disk, a similar procedure is adopted with a = b and c = 0.

**As shown in Figure 3.3.

interparticle contact, which is symbolized by the charged surface.

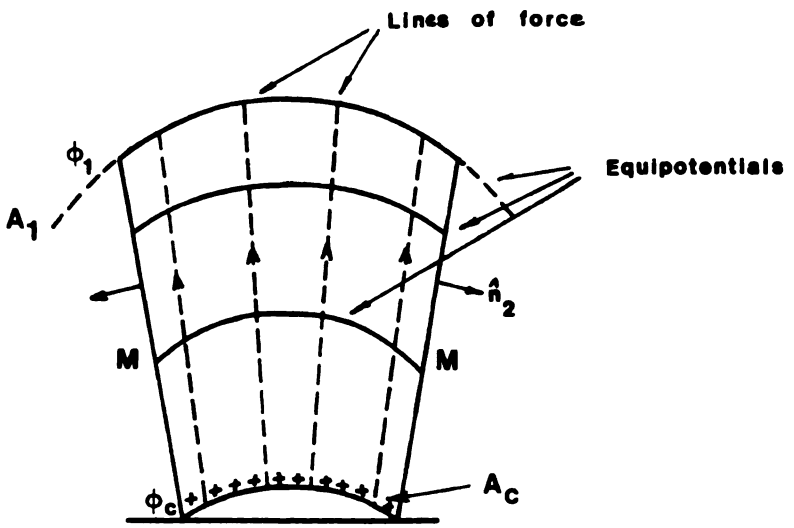

Figure 3.4 Equipotentials in the current flow problem.

The determination of the contact resistance requires the expression for the capacitance C derived earlier [equation (3.47)]. To begin with, Figure 3.4 shows a slightly lossy* medium which is interposed between a current source A_c and sink A_1. For this (electric) current problem, the region between A_c and A_1 is free of any sources or sinks; furthermore, the following boundary condition is satisfied at the boundaries M:

$$\left.\frac{\partial \phi}{\partial \hat{n}_2}\right|_M = 0 \qquad (3.56)$$

*This term implies that the material (dielectric) medium is highly resistive so that only a leakage current flows through it.

where

ϕ = potential function

$\hat{n}_2$ = unit vector as shown in Figure 3.4.

The potential function satisfies Laplace's equation (3.8), also, the Gauss law applies* [equation 3.42] for the electrostatic case. Hence,

$$\int_S \hat{n} \cdot \vec{E}\, dS = \frac{Q}{\varepsilon} \tag{3.42}$$

where Q is the total charge, and S refers to A_c.

The capacitance C of the medium between equipotentials ϕ_c and ϕ, is

$$C = \frac{Q}{|\phi_c - \phi_1|} \tag{3.57}$$

and the current density $\vec{J}$ is formally expressed as

$$\vec{J} = \frac{1}{\rho} \left|\frac{\vec{\partial\phi}}{\partial n}\right| \tag{3.58}$$

where ρ = monolithic material resistivity

n = unit vector directed normal to A_c.

The total (leakage) current is therefore, given by

---

*The $\vec{E}$ field in all three directions, except the one shown in Figure 3.4 is zero, so that the divergence theorem is valid.

$$\vec{I} = \int_{A_c} \vec{J} \cdot dA_c$$

$$= \frac{1}{\rho} \int_{A_c} \left|\frac{\vec{\partial\phi}}{\partial n}\right| dA_c \qquad (3.59)$$

from (3.58)

Referring to Figure 3.4, the resistance R_{c1} from A_c to A_1 is by definition;

$$R_{c1} = \frac{|\phi_c - \phi_1|}{I} \qquad (3.60)$$

From equations (3.57) and (3.59)

$$R_{c1} = \frac{Q/\epsilon}{\frac{1}{\rho}\int_{A_c} \left|\frac{\vec{\partial\phi}}{\partial n}\right| dA_c} \qquad (3.61)$$

It is appropriate to recall, at this stage, the characteristic feature of the contact resistance, namely, that it is a surplus resistance arising due to the constriction of the lines of current flow at the point of contact. The shape of the contact is assumed to be either that of a elliptical or circular disk. Figure 3.5 illustrates this situation. In Figure 3.6 an enlarged view of the region of contact is shown.

Both of these figures indicate the lines of current flow which are normal to the equipotentials at the points of intersection.* As mentioned earlier, both of these are harmonic in the region shown

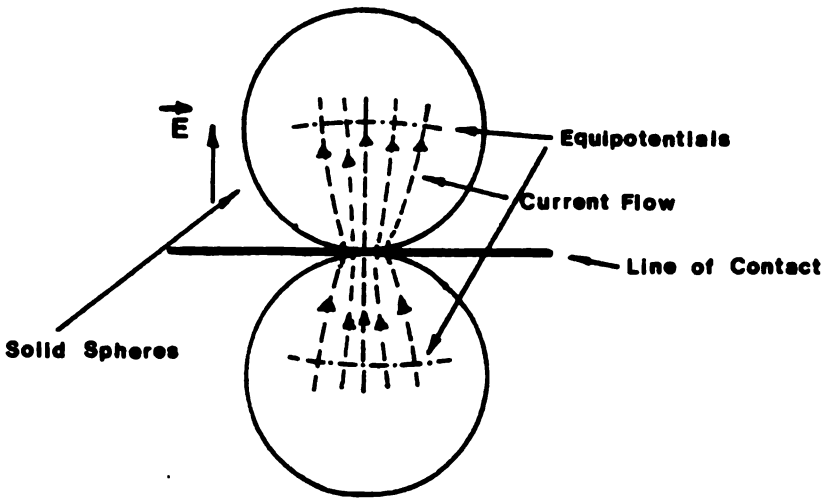

Figure 3.5. Volume conduction across solid spherical dielectrics.

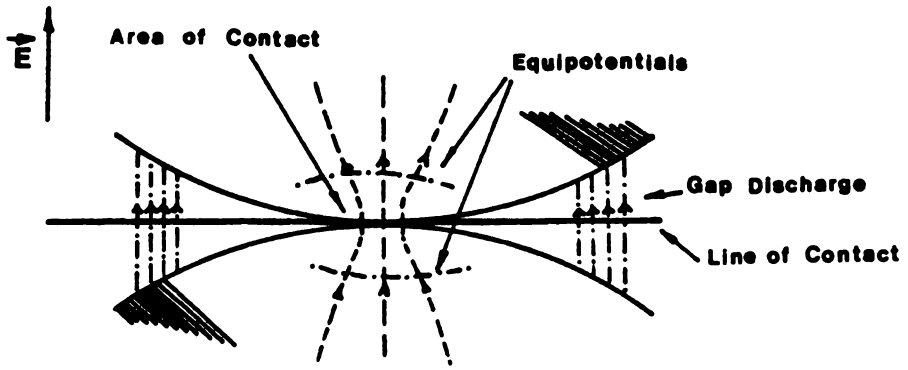

Figure 3.6. Detail of region of contact showing equipotentials and charge transfer (discharge) across gap.

and are conjugate to each other. Before proceeding with the determination of the constriction resistance, it is worthwhile to note the geometrical similarity of this current flow problem in a dielectric and the electrostatic problem of Figure 3.3.

In accordance with equation (3.13), the equipotential surfaces in the contact members**, for c = 0, are given by

$$\frac{x^2}{a^2+\mu} + \frac{y^2}{b^2+\mu} + \frac{z^2}{\mu} = 1 \qquad (3.62)$$

where the magnitude of μ locates the equipotential and $\sqrt{a^2+\mu}$, $\sqrt{b^2+\mu}$ are the semiaxes on the x-y plane. The equipotentials are oblate hemispheroids.

The capacitance from A_c to an equipotential ϕ [see equation (3.47)]

$$C = 4\pi\varepsilon \left[\int_0^{\sqrt{\mu}} \frac{d\mu}{\sqrt{(a^2+\mu)\ (b^2+\mu)\mu}}\right]^{-1} \qquad (3.63)$$

Substituting for Q from (3.42) into expression (3.47) for the contact resistance $R_{c\phi}$ (between A_c and equipotential ϕ)

$$R_{c\phi} = \frac{\frac{\varepsilon}{c}\int_{A_c} \hat{n}\ \left|\frac{\overrightarrow{\partial\phi}}{\partial n}\right|\ dA_c}{\frac{1}{\rho}\int_{A_c} \left|\frac{\vec{\partial\phi}}{\partial n}\right|\ dA_c} \qquad (3.64)$$

where

---

*Within the solid particles.

**The contact members are isotropic, homogeneous dielectrics.

$$\vec{E} = d\vec{\phi}/dn$$

$$R_{c\phi} = \rho\varepsilon/C \tag{3.65}$$

The capacitance C is given by equation (3.63). Hence

$$R_{c\phi} = \frac{\rho}{4\pi} \int^{\sqrt{\mu}} \frac{d\mu}{\sqrt{(a^2+\mu)(b^2+\mu)\mu}} \tag{3.66}$$

for a general elliptic disk contact.

In the context of the objective of this chapter and the overall resistivity model, the simpler case of a circular interparticle contact is assumed. In such case, then, a = b in equation (3.66) and the contact resistance R_μ simplifies to:

$$R_{c\phi} = \frac{\rho}{4\pi} \int_0^{\sqrt{\mu}} \frac{d\mu}{(a^2+\mu)\sqrt{\mu}} \tag{3.67}$$

Integrating (3.67), and recalling that $R_{c\phi}$ is the resistance between the contact and an equipotential ϕ in one contact member only, the total contact resistance R_μ is

$$R_\mu = 2R_{c\phi} \tag{3.68a}$$

Hence,

$$R_\mu = \frac{\rho}{\pi a} \tan^{-1} \frac{\sqrt{\mu}}{a}^{*} \tag{3.68b}$$

---

*See reference M2.

The inverse relationship between the contact resistance R_μ and the contact parameter(s), given above by the circle radius a, may be viewed in analogy with the similar (but crude) expression [equation (3.5)] derived in Section 3.2. Thus the resistance between two spherical particles in (circular) contact is given in terms of the equipotential surface coordinate μ, the material resistivity ρ and the contact radius a. Furthermore, it should be noted that the inclusion of the μ coordinate is in terms of the trigonometric term in equation (3.68b). The additional contributions, due to the increase in this coordinate*, decrease in magnitude.

Having established the expression for the contact resistance, it is now necessary to determine the electric field intensity at the vicinity of the interparticle contact. This is examined in the next section.

3.4 The Electric Field Strengths at the Plane of the Contact

In Chapter 1, it was mentioned that the particulate layer of fly ash demonstrated non-ohmic behaviour leading to nonlinear current-voltage characteristics of the type shown in Figure 1.3. This was partly due to the high electric field strengths near the interparticle contact. McLean (M2) has discussed the variation of the electric field strength along the contact plane, under the prior assumption that the air or gas gap can sustain field strengths greater than the breakdown value. Upon establishing this phenomenon of breakdown in

---

*In other words, the equipotentials further away from the contact are included, for the purpose of determining the contact resistance.

the immediate vicinity of the contact, he concludes that a gap discharge does indeed occur. In this section, the expressions for the gap field strengths, perpendicular to and coplanar with the plane of an idealized circular contact, are derived.

For a current I, the voltage drop between an equipotential surface of coordinate μ and the line of contact is given by the potential ϕ [from equations (3.67)] as:

$$\phi = \frac{I\rho}{a\pi a} \tan^{-1} \frac{\sqrt{\mu}}{a} \qquad (3.69)$$

In the following, all distances are normalized with respect to the contact circle radius a^*, so that a distance variable r (along the x axis) is given by

$$r = \lambda a \qquad (3.70)$$

where

λ = normalized distance parameter, ($\lambda \geq 1.0$).

It should be noted here that the equation for the hemispheroidal equipotentials (3.62) consists of parameters a and b. Thus, while a and b are the semiaxes of the plane elliptical (or circular, in which case a = b) contact : $\sqrt{a^2+\mu}$ and $\sqrt{b^2+\mu}$ are similar semiaxes of the equipotential surface. Hence a point along the surface of contact corresponding to an equipotential specified by $\sqrt{\mu}$, and located beyond the area of contact (along the x axis) is at a distance r, where*

*See Figure 3.3. It may be recalled here that while the contact area is a plane circle on the x-z plane, the equipotentials are oblate hemispheroids.

$$r = \sqrt{a^2+\mu} \tag{3.71}$$

Substitution for μ from (3.71) into equation (3.69) for the potential gives

$$\phi = \frac{I\rho}{2\pi a} \tan^{-1}\sqrt{\lambda^2-1} \tag{3.72}$$

in terms of the normalized distance λ from (3.70), $\lambda = 0$ at the center of the contact circle.

Equation (3.71) for ϕ, then gives the electrostatic potential of an equipotential with respect to the (circular) surface of contact. In order to evaluate the electric field strength at any point near the vicinity of the contact, the potential must be known as a function of the distance along the vector joining the contact perimeter and the point in question. In view of the perspective of the problem* in this section it is logical to determine the field strength along the z axis (Figure 3.3), i.e., in the same direction as the externally applied field. Prior to doing this, however, it is necessary to establish certain geometrical features of this problem.

The illustration in Figure 3.7 depicts a metal sphere in contact with the surface of an insulating slab. If the metal sphere is considered to be a perfect conductor, then it is easily established from electrostatics that the lines of force are incident normally at the sphere

---

*That of determining the order of magnitude of the field strength, and of the variation of $\vec{E}$ along the line of contact.

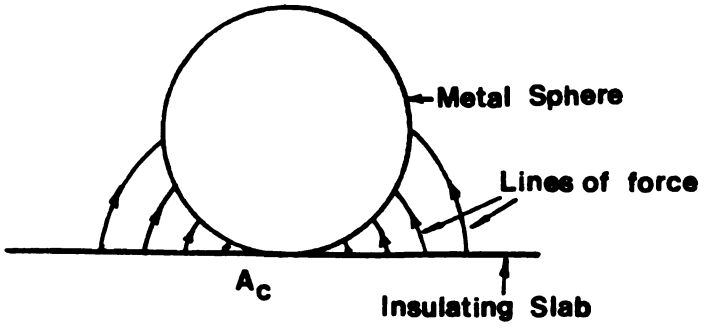

Figure 3.7 Representation of the equipotential surfaces and the lines of force in the gap between an interparticle contact.

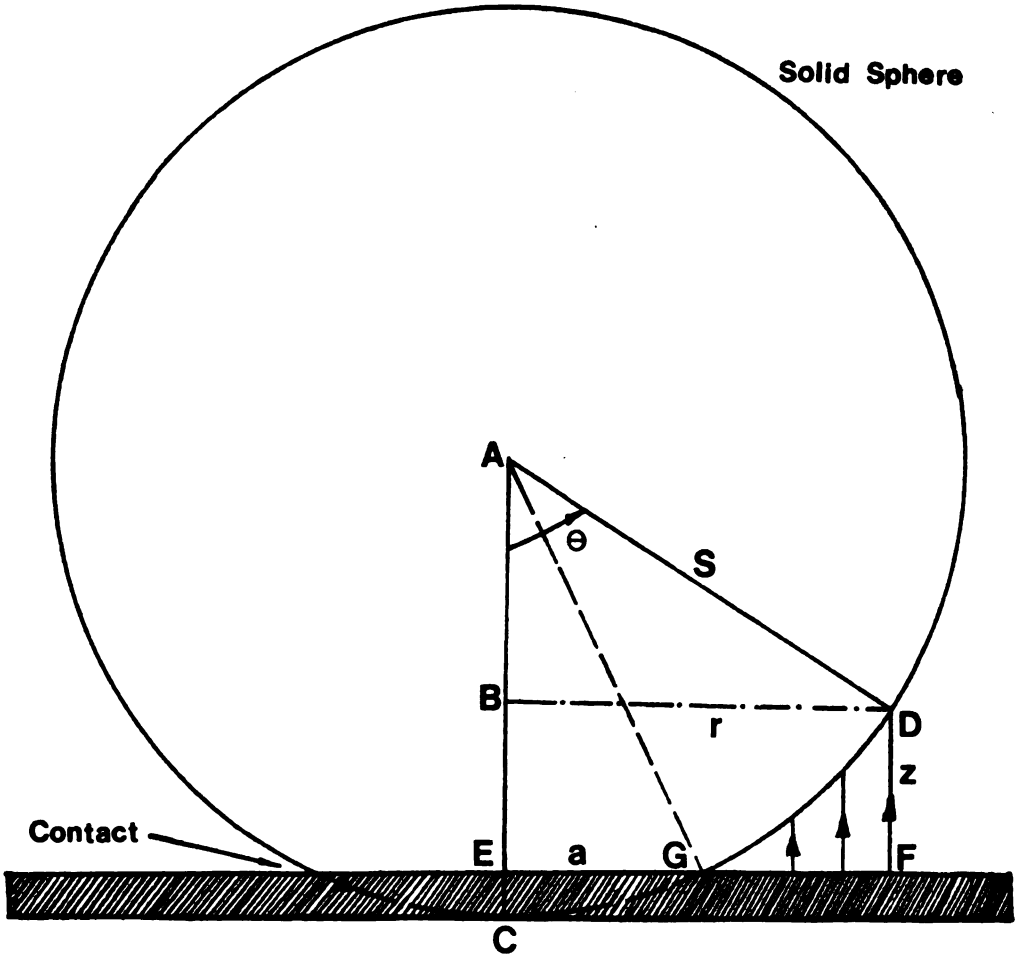

Figure 3.8. Detail of one contact showing the simplified geometry (exaggerated).

boundary.* In the case of a material that is not a perfect conductor (fly ash particles), the lines of force are not as curved as shown, and align themselves more toward the z axis. Hence, in order to simplify the geometry, shown in Figure 3.8, the line of force FD is taken to be straight**.

The solid sphere in Figure 3.8 represents a particle pressed against the slab which results in a circular contact of radius a. The straight line of force meets the sphere surface at D, and the radius AD forms an angle θ with the vertical line AC.

Thus,

$$\bar{AE} = \sqrt{S^2 - a^2} \qquad (3.73a)$$

where S = particle radius

---

†The metal ball models the equipotential surface between two particles and the insulating slab models the contact.

*See, for example, reference S4. In contrast to the situation in Figures 3.5 and 3.6, the lines of force shown here are through the gap in the vicinity of the contact. The reason only these are shown is due to the anticipation (to be confirmed subsequently) that strong fields exist in the interparticle spaces, as indicated by the non ohmic behaviour mentioned in connection with the fly ash resistivity measurements (Chapter 4).

**In reality this is slightly curved toward the spherical surface, and the angle of incidence at the particle surface is determined by the dielectric constant.

$$\overline{AB} = \sqrt{S^2 - r^2} \tag{3.73b}$$

$$\therefore z = \overline{AE} - \overline{AB}$$

$$= S[1-(\frac{a}{S})^2]^{\frac{1}{2}} - S[1-(\frac{r}{S})^2]^{\frac{1}{2}}$$

Since S >> a, the foregoing simplifies to

$$z = S[\frac{1}{2}\frac{r^2-a^2}{S^2}] \tag{3.73c}$$

Substituting for r above, from equation (3.56)

$$z = \frac{a^2(z^2-1)}{2S} \tag{3.73d}$$

The potential drop ϕ, between F and D, is given by expression (3.72). Hence the field strength $\vec{E}_1$, assuming this to be linear in the short distance $\overrightarrow{FD}$, is given by

$$\vec{E}_1 = \frac{\phi}{z} = \frac{I\rho}{2\pi a} \frac{\tan^{-1}\sqrt{\lambda^2-1}}{a^2(\lambda^2-1)} \cdot 2S \tag{3.74}$$

From equation (3.67),

$$\rho = 2\pi a R_{c\phi}/\tan^{-1}(\lambda^2-1)^{\frac{1}{2}} \tag{3.75}$$

Substituting for ρ into (3.74) one gets

$$E_1 = 2\frac{V}{a}\frac{S}{a}\frac{1}{(\lambda^2-1)}, \quad \lambda \geq 1.0 \tag{3.76}$$

where V is the voltage drop (equal to $IR_{c\phi}$) due to a single contact.

Equation (3.76) is the final expression for the electric field strength, in the interparticle gap, along the direction of the externally applied field. It is seen that $\vec{E}_1$ decreases with an increase in the contact area ($\vec{E}_1 \propto a^2$), hence for a given particle radius S, the intensity of the electric field is quite sensitive to the contact area which is represented by a^2. The term $\frac{S}{a}$ is ratio of the particle radius to the contact radius; this ratio, therefore, can be taken to represent the degree of the constriction (Figures 3.5 and 3.6, and Figure G.2 in Appendix G). The larger the ratio $\frac{S}{a}$, the longer* the constriction and vice versa.

McLean, in his analysis (M2), has used the equation

$$R_{c\phi} = \rho/4\ a \quad ** \qquad (3.77)$$

to substitute for ρ into equation (3.74) for $\vec{E}_1$. This leads to the expression for the field strength as follows:

$$\vec{E}_1 = \frac{4}{\pi} \frac{V}{a} \frac{S}{a} \frac{\tan^{-1}\sqrt{\lambda^2-1}}{(\lambda^2-1)} \qquad (3.78)$$

In light of the disagreement between equations (3.76) and (3.78), it may be recalled that one half of the total contact resistance R_μ was given earlier by equations (3.68a) and (3.68b) as follows:

---

*By a long constriction is meant that the lines of current flow are less constricted when compared with a short constriction. Long and short constrictions are discussed in Appendix G.

**This equation has been derived by Holm (H1).

$$R_{c\phi} = \frac{\rho}{2\pi a} \tan^{-1} \sqrt{\lambda^2-1} \qquad (3.79)$$

where μ is replaced by the dimensionless distance parameter λ from equations (3.70) and (3.71). As $\lambda \to \infty$, the following approximation holds,

$$R_{c\phi} \simeq \frac{\rho}{2\pi a} \tan^{-1} \lambda \qquad (3.80)$$

$$\simeq (0.2499) \frac{\rho}{a}$$

$$\simeq \frac{\rho}{4a}$$

Thus equation (3.77), and hence (3.78) as well, are applicable in the situation where λ is large. Since $R_{c\phi}$ is the resistance measured between an equipotential (within the solid) surface and the plane of the contact, and $\sqrt{\mu} = a\sqrt{\lambda^2-1}$, the above implies the equipotential is far removed from the contact. Hence the contact resistance $R_{c\phi}$, from (3.77) is that of a long constriction. This criteria constitutes an assumption, which is implicit here, and is valid for the case where the contact area between two large spheres is relatively small*. In view of this

*Furthermore, equation (3.77) is associated with two identical cylinders in contact, where the constriction is long, and where the lines of current flow are straight immediately outside the constriction volume (Appendix G). The boundary of the constriction volume is not as readily apparent for spherical bodies, where the differences in curvature of the lines of force (or current flow) due to the constriction and due to the particle shape are not as marked. See also Section 3.8.

restriction, Equation (3.76) for the field strength is accepted as being general, and is used for the evaluation of $\vec{E}_1$ in the vicinity of the contact.

In addition to $\vec{E}_1$, the field strength along the line of contact* can also be evaluated from equation (3.72). Differentiating the potential ϕ with respect to r, where $r = \lambda a$ (3.79)

$$\vec{E}_g = \frac{d\phi}{ad\lambda}^{**} \tag{3.81}$$

Differentiation of equation (3.72) with respect to λ gives:

$$\frac{d\phi}{d\lambda} = \frac{\rho I}{2\pi a} \frac{1}{\lambda(\lambda^2-1)^{\frac{1}{2}}} \tag{3.82}$$

Substituting for ρ from equation (3.75), where $V = I R_{c\phi}$

$$\frac{d\phi}{d\lambda} = V/(\lambda\sqrt{\lambda^2-1} \tan^{-1} \sqrt{\lambda^2-1})$$

Hence, from (3.81)

$$\vec{E}_g = \frac{V}{a} \cdot \frac{1}{\lambda\sqrt{\lambda^2-1} \tan^{-1} \sqrt{\lambda^2-1}} \tag{3.83}$$

If instead of (3.75), the expression for ρ in (3.77) is substituted into (3.81), one gets

*The line of contact (as shown in Figures 3.5 and 3.6) is the line that goes symmetrically through the contact. In this context it is the same as the plane of contact.

**This equation applies to near the circumference of the contact circle.

$$\vec{E}_g = \frac{2V}{a} \frac{1}{\pi\lambda\sqrt{\lambda^2-1}} \tag{3.84}$$

Equations (3.83) and (3.84) are equivalent for large values of λ so that

$$\frac{1}{\tan^{-1}\sqrt{\lambda^2-1}} \simeq \frac{2}{\pi}$$

and hence, again as in the case of $\vec{E}_1$, equation (3.84) is valid for relatively large constriction volumes (Appendix G), i.e., for long constrictions. This equation gives $\vec{E}_g$ as a function of λ, where λ is the distance parameter along the surface or line of contact, and $\vec{E}_g$ is also directed along the same line. Hence the variation of the electric field strength is known as a function of the distance along the line of contact. Again, $\vec{E}_g$ decreases with increase of λ, and for large λ ($\lambda^2 >> 1$); this inverse dependence is second order with respect to λ.

The derivation of the general expressions for the electric field strengths in the vicinity of an interparticle gap has been accomplished in this section. These expressions for $\vec{E}_1$ and $\vec{E}_g$ are given by (3.76) and (3.83) respectively. A representative calculation leading to a value for $\vec{E}_1$ is presented in Section 3.6. The objective of such a calculation is to establish the phenomenon of the electrical breakdown at the gap.

In the next section (3.5), the electric field strength $\vec{E}_s(\theta)$, at the particle surface is derived. The significance of $\vec{E}_s(\theta)$ lies in the fact that it influences the surface migration of ions and electrons. This has a direct bearing upon the present work, where (as stated in

Section 2.1, Chapter 2) the objective is to characterize the overall electrical resistivity of a particulate layer within the temperature regime (<400^{o} F) of "cold" precipitators.

3.5 Electric Field Strength at a (Spherical) Particle Surface

This section deals with the variation of the electric field strength along the surface of a single idealized (spherical) particle in contact with an identical particle. The contact formed is a circle of radius a, as in the previous section, and is identical to the other contacts in the idealized cubic packing of spherical particles (Figure 2.2). The evaluation of the (particle) surface field strength, near the contact, is independent of the procedure of Section 3.4. This, then, provides a consistency check on the magnitudes of the field strength at the line of contact, $\vec{E}_1$ at F on Figure 3.8, and the field strength on the particle surface at D on the same figure. For a line of force FD sufficiently close to the circumference of contact, these two field strengths, although not equal, should be of a comparable order of magnitude.

The resistance to (ionic and electronic) current flow is, in the case of surface conduction, explicitly recognized to occur as a result of the following:

a) constriction of the lines of current flow at the contact spots.

b) resistance to current flow along the surface of a particle.*

---

*In addition to a) and b) above, resistance may also be encountered due to the capillary condensate. This aspect is not considered here.

The model assumed, in this analysis, is consistent with the description given in Section 2.2 (Chapter 2). In the present case, only two particles in contact need to be considered. Figure 3.9 below shows the parameters that are involved in the analysis.

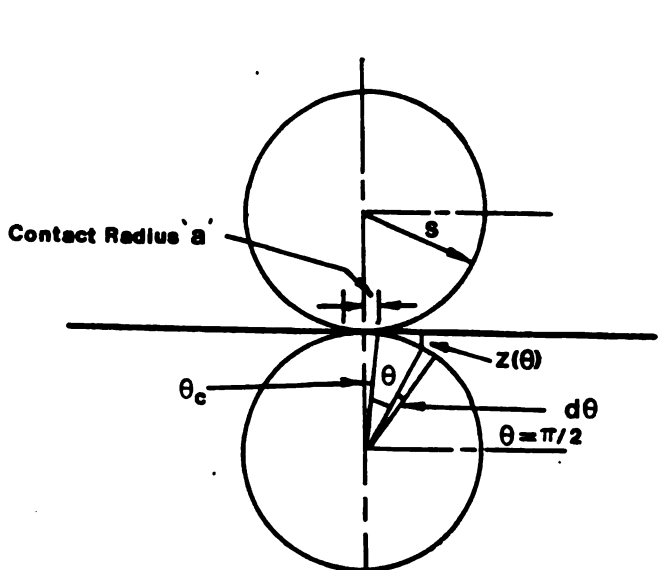

Figure 3.9. Geometrical parameters for two particles in contact.

The figure shows two identical spheres of radius S forming a circle of contact of radius a. The location on the particle surface is specified either by the polar angle θ or the vertical distance, $z(\theta)$, to the line of contact. It may be recalled from Section 3.4 (Figure 3.8) that $z(\theta)$ represents a line of force. As indicated on the diagram, θ_c is half the angle projected by the actual contact to the spherical center. The length of the current pathway that is relevant to the surface resistance problem corresponds to the range

of θ, $\theta_c < \theta < \pi/2$*.

The resistance from θ to θ_c is obtained from Ohm's law applied to a surface current,

$$\vec{E} = \vec{K} \cdot \rho_s \tag{3.85}$$

where

$\vec{E}$ = electric field strength (Volts/cm)

$\vec{K}$ = surface current density (amp/cm)

ρ_s = surface resistivity (ohm).

For any surface current I flowing along a rectangular lamina of length l, the Ohm's law applies as follows:

$$\frac{V}{I} = \frac{I}{b} \rho_s \tag{3.86}$$

where

V = voltage across length l

b = width, ($\perp$ to current flow).

From (3.85) and (3.86),

$$\vec{E} = \frac{V}{l}; \quad K = \frac{I}{b}$$

Equation (3.86) is rewritten to give a relationship between the resistance and the surface resistivity. If the resistance R = V/I, then

---

*The other lengths of the current path on the surfaces of particles are obtained from symmetry.

$$R = \frac{1}{b}\frac{(\parallel \text{ to current flow})}{(\perp \text{ to current flow})} \cdot \rho_s \qquad (3.87)$$

By analogy with (3.87), the resistance over a differential angle $d\theta$ in Figure 3.9 is given by

$$dR(\theta) = \rho_s \cdot \frac{2d\theta}{2\pi S \sin\theta}$$

Integration of the above from $\theta = \theta$ to $\theta = \theta_c$ gives the total resistance $R(\theta)$ for the length of the current path mentioned earlier.

$$R(\theta) = \rho_s \int_{\theta_c}^{\theta} \frac{S\, d\theta}{2\pi S \sin\theta} \qquad (3.88)$$

$$\therefore R(\theta) = \rho_s \ln\left[\frac{\tan\theta/2}{\tan\theta_c/2}\right] \qquad (3.89)$$

From equation (3.89) the approximate value of the surface potential θ, with respect to the point along the line of force on contact plane, can be estimated. Let $\vec{E}_a$ be the average field strength of a particulate layer which is given by the voltage drop across it divided by its thickness. Then assuming $\theta_c << \pi/2$, the approximate potential difference between $\theta = \pi/2$ (on the particle surface) and the corresponding point on the line of contact is given by:

$$V(\theta) = R(\theta)\, S\, E_a / R\left(\frac{\pi}{2}\right) \qquad (3.90)$$

Substituting for $R(\theta)$ from (3.89)

$$V(\theta) = S \vec{E}_a \left[\ln \left(\tan \frac{\theta}{2} / \tan \frac{\theta_c}{2}\right) / \ln \left(1/\tan \theta_c/_2\right)\right] \quad (3.91)$$

where the value of R ($\pi/2$) is obtained by the appropriate substitution into (3.89).

As mentioned earlier, the voltage $V(\theta)$ given by equation (3.91) is the potential of the point (S,θ) on the surface with respect to the point along the line of force where it meets the contact plane. The length of this line of force $z(\theta)$ is given as,

$$z(\theta) = S (\cos \theta_c - \cos \theta) \quad (3.92)$$

Assuming that the electric field $\vec{E}_s$ at (S,θ) is predominantly axial*, the magnitude of $\vec{E}_s$ at this local point is given by:

$$E_s(\theta) = d V(\theta)/dz(\theta) \quad (3.93)$$

where,

$$\frac{dV(\theta)}{dz(\theta)} = \frac{dV(\theta)}{d\theta} \cdot \frac{d\theta}{dz(\theta)} \quad (3.94)$$

The derivative in equation (3.93) is

$$\frac{dV(\theta)}{dz(\theta)} = \frac{\vec{E}_a \{d \ln \left(\tan \frac{\theta}{2} / \tan \frac{\theta_c}{2}\right) / \ln \left(1/\tan \frac{\theta_c}{2}\right)\}}{d \{\cos \theta_c - \cos \theta\}} \quad (3.95)$$

The expression on the right hand side simplifies to**:

Footnote

*That is, in the same direction as the externally applied field $\vec{E}_a$ (across the particulate layer). Also, it may be noted that if $\vec{z}(\theta)$ is the running distance variable along a vertical line from the line of the interparticle contact to the point on the particle surface then the true field strength on the particle surface is given by

$$\vec{E}_s(\theta)\big|_z = \frac{dV(\vec{z})}{d\bar{z}}\Big|_{\bar{z}=z}$$

where z is not a variable as indicated in equation (3.93). Instead, it is now the maximum value of $\bar{z}$. The above equation is more rigorous than equation (3.93) due to the fact that a non linear variation of $\vec{E}_s(\theta)$ with $\bar{z}$ is implicitly recognized here. This is discussed in more detail in Section 3.8.

**

$$\frac{d\{V(\theta)\}}{d\{z(\theta)\}} = \frac{E_a\, d\{(\ln\tan\frac{\theta}{2} - \ln\tan\frac{\theta_c}{2}) / -\ln\tan\frac{\theta_c}{2}\}}{-d\cos\theta}$$

Numerator

$$\text{Let } \beta = -\ln\tan\frac{\theta_c}{2}$$

$$\therefore E_a\, d\{(\ln\tan\tfrac{\theta}{2}/\beta) + 1\} = \frac{E_a}{\beta}\frac{1}{\tan\frac{\theta}{2}}\, d(\tan\tfrac{\theta}{2})$$

$$= \frac{E_a}{\beta\tan\frac{\theta}{2}} \cdot \frac{d\theta}{2\cos^2\frac{\theta}{2}}$$

Footnote continued

$$= \frac{E_a \, d\theta}{2\beta \cdot \sin\frac{\theta}{2} \cdot \cos\frac{\theta}{2}}$$

$$d\{V(\theta)\} = \frac{E_a \, d\theta}{\beta \sin\theta}^{*}$$

Denominator

$$d\{z(\theta)\} = -d\cos\theta = \sin\theta \, d\theta^{*}$$

$$\therefore \frac{\{d\,V(\theta)\}}{\{d\,z(\theta)\}} = E_a/\beta \sin^2\theta$$

or

$$\vec{E}_s(\theta) = E_a/-\{\ln \tan\frac{\theta_c}{2}\}\{\sin^2\theta\} \qquad (3.96)$$

*The radius S is dropped from the numerator and denominator.

$$\vec{E}_s(\theta) = \vec{E}_a / -\{\ln \tan \frac{\theta_c}{2}\}\{\sin^2 \theta\} \qquad (3.96)$$

If, in Figure 3.8, θ_c is small, then,

$$\theta_c \simeq \tan \theta_c = \frac{a}{S}$$

$$\therefore \theta_c/2 = a/2S \qquad (3.97)$$

Substitution of (3.97) into the denominator of (3.96) above, gives

$$\vec{E}_s(\theta) = \vec{E}_a / -\{\ln \frac{a}{2S}\}\{\sin^2 \theta\} \qquad (3.98)$$

Hence equation (3.98) gives the expression for the (axially directed) field strength $\vec{E}_s(\theta)$ in terms of the average layer field strength $\vec{E}_a$ and the polar coordinate θ. It may be noted that since $a/S < 1.0$, the magnitude of $\vec{E}_s(\theta)$ decreases when a/S decreases. This is in contrast to the expression (3.76) for the field strength at the line of contact, which indicates an inverse dependence between $\vec{E}_1$ and the contact area 'a' (or, equivalently, the dimensionless ratio a/S). The (particle) surface field strength is, therefore, higher for a long constriction* than for a short constriction. However, as indicated in the discussion (Section 3.8), the degree of dependence of $\vec{E}_s(\theta)$ on the constriction ratio S/a in equation (3.98) is not as strong as that

---

* $\frac{a}{S}$ (short constriction) > $\frac{a}{S}$ (long constriction)

of $\vec{E}_1$ in equation (3.76). Furthermore, $\vec{E}_s(\theta)$ decreases as θ increases up to $\theta = \pi/2$ which corresponds to the point on the surface most distant from the contact.

Having established the expressions for the field strengths $\vec{E}_1$ (equation 3.76) and $\vec{E}_s(\theta)$ (equation 3.98), it is now necessary to determine the magnitudes of these terms, and their variation with position along the contact vicinity. This is presented in the next section which begins with a representative calculation showing the typical orders of magnitudes of the terms involved.

3.6 Magnitudes and Variation of the Electric Fields in the Vicinity of the Contact

The interparticle gap field strength along the line of contact is given by equation (3.76) as

$$\vec{E}_1 = 2 \frac{V}{a} \frac{S}{a} \frac{1}{\lambda^2 - 1}, \quad \lambda \geq 1.0 \qquad (3.76)$$

It may be recalled that the term V above is the voltage drop per contact. If it is assumed that the major portion of the resistance for two particles, in contact, is due to the constriction*, then the bulk of the voltage drop V should occur in the vicinity of the contact. The vicinity of the contact may be visualized as the axial** dimension of the constriction volume. This corresponds (roughly) to the linear dimension+ between

*This is mentioned at the beginning of Section 3.2.

**Along the direction of the externally imposed field (across the layer). Refer to Figure G.2, Appendix G.

+This dimension is for half the contact as, for example, depicted in Figure 3.8.

the line of contact and the equipotential beyond which the curvature of the current flow lines are no longer due to the constriction. Assuming that this dimension is of the same order of magnitude as the contact, the electric field strength in its vicinity should be approximately given by $\frac{V}{2a}$. For an order of magnitude estimate of $\vec{E}_1$ the following typical values are assumed:

1. D (particle diameter = 20 μm
2. S/a (constriction ratio, reference M2) = 100
3. H (bed thickness) = 0.32 cm*
4. ΔV (voltage drop across bed) = 2 Kv

$\therefore$ Radius of contact = 0.10 μ

Number of particles in the cubic packing (along one vertical stack)

$$= \frac{0.32 \times 10^{-2}}{20 \times 10^{-6}} = 160$$

Voltage drop per contact $\simeq \frac{2000}{160} \simeq 12.5$ V

$$\therefore \frac{V}{2a} \left(\frac{\text{volts}}{\text{meter}}\right) = \frac{12.5}{2\ (0.1 \times 10^{-6})} = 6.25 \times 10^7$$

$$\therefore O(M) \quad \text{of } \vec{E}_1 = 10^7 \text{ to } 10^8 \text{ V/m}$$

The high value of the gap field strength above is sufficient to support a charge emission across the air (or gas) gap (M2). This constitutes the phenomenon of electrical breakdown in the neighborhood of the contact, and when this occurs the procedures leading to the

*This value for H is the particulate layer thickness in the laboratory experiments conducted in this work.

expressions for $\vec{E}_1$ and $\vec{E}_s(\theta)$, equations (3.76) and (3.98), do not apply.

The axial field $\vec{E}_1$ along the line of contact, given by equation (3.76), is plotted against the dimensionless parameter λ in Figure 3.10. The numerical values of the voltage per contact V/a and the constriction ratio S/a are the same as in the sample calculation above*.

Figure 3.10 illustrates the non linear variation of $\vec{E}_1$ with the distance (along the line of contact) parameter. The field strength rises sharply with decreasing distance from the contact. If, as indicated on the figure, the value of 5×10^7 volts/meter is assumed to be the (approximate) value of the breakdown field strength, than a gap charge emission is sustained for $\lambda \leq 22$. Again, it may be recalled here, that $\vec{E}_1$ is the field strength at the center line of contact between the two particles. Hence, electrical breakdown of the medium (gas or air), in the immediate vicinity of the contact is established.

The variation of the surface field strength $\vec{E}_s(\theta)$ with the polar angle θ is shown in Figure 3.11. As mentioned earlier, the angle θ locates a circle on the particle surface at which the axial field strength is $\vec{E}_s(\theta)$. $\vec{E}_s(\theta)$ is obtained (as a function of θ) from equation (3.98). The value of $\frac{a}{S}$ is the same as in Figure 3.10, and equal to 0.01. This value corresponds to half the contact angle Θ_c.

$$\Theta_c = \text{arc tan } 0.01$$
$$= 0.573^o \text{ (34.4 minutes)}$$

---

*The particle diameter D and the bed thickness are approximately equal to that used in the laboratory experiments.

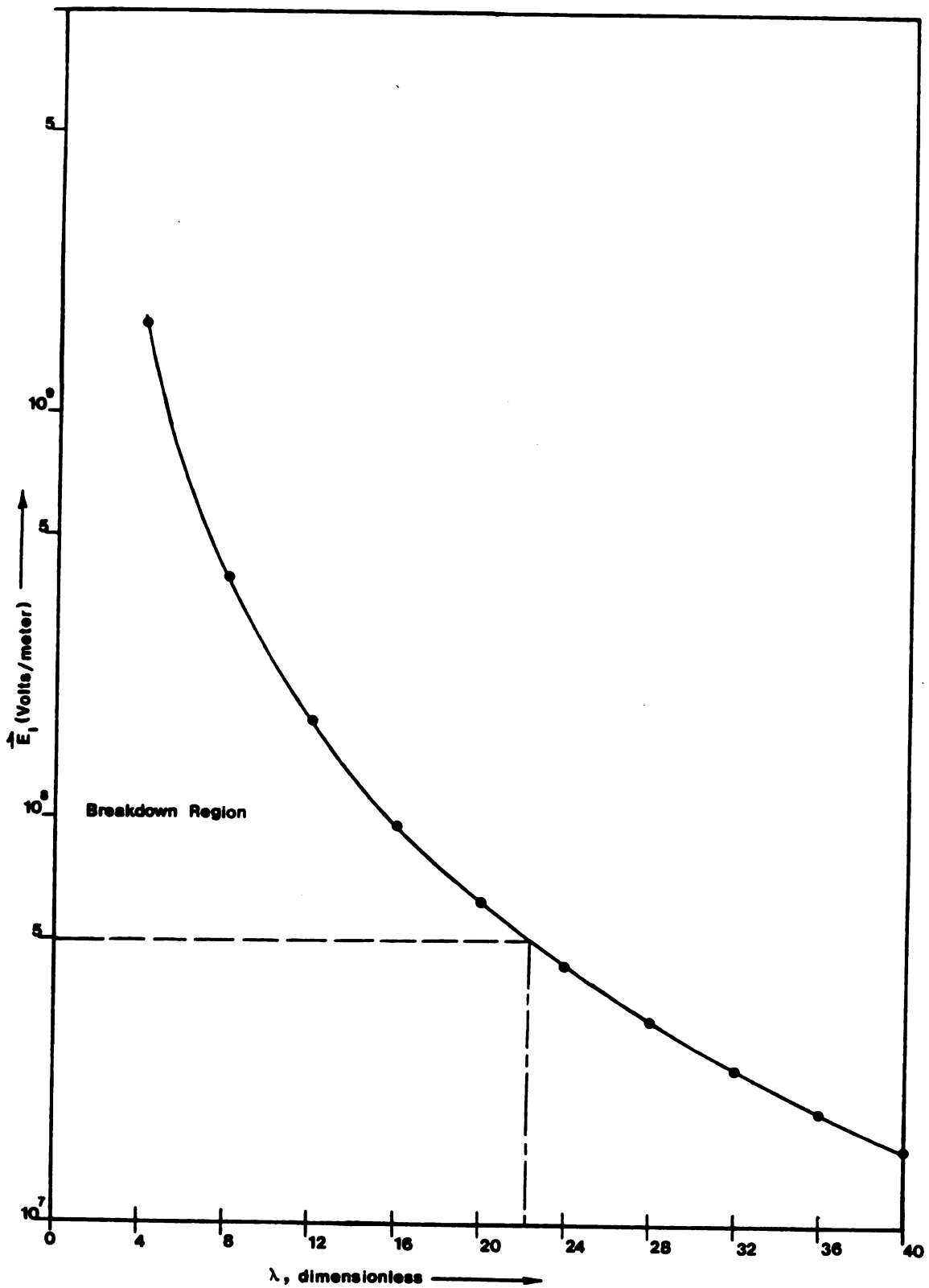

Figure 3.10. Variation of the gap field strength $\vec{E}_1$ along the line of contact.

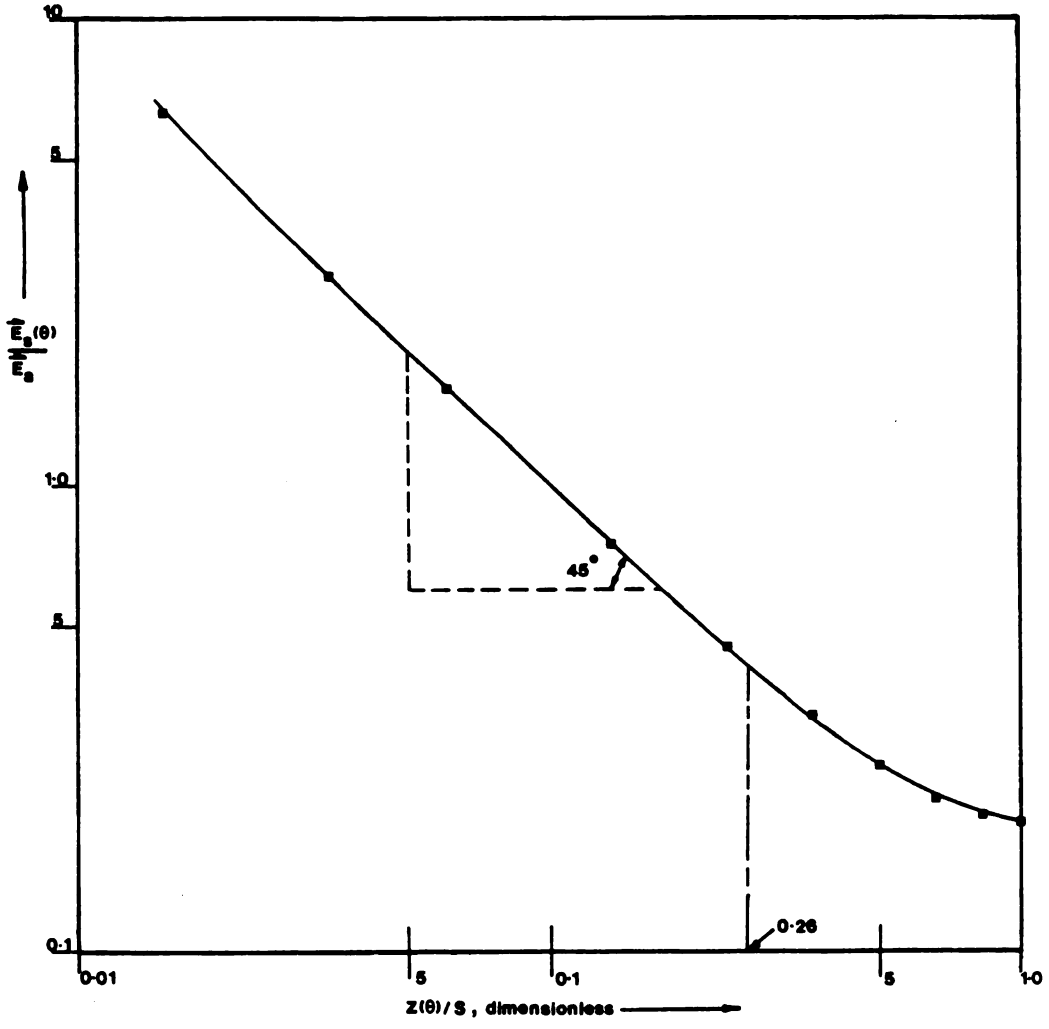

Figure 3.11. Variation of the (dimensionless) surface field strength with position on particle surface.

Both of the variables in Figure 3.11 are dimensionless, and the surface field $\vec{E}_s(\theta)$ is normalized with respect to the layer average field $\vec{E}_a$ which is given as follows:

$$\vec{E}_a = \Delta V/H$$

$$= 2000/0.0032, \text{ from page}$$

$$= 6.25 \times 10^5 \text{ Volts/meter}$$

The numerical values of the normalized variables are tabulated in Table 3.1. The table has some entries for $\theta < 10^o$, whereas the figure (3.11) covers the range of $z(\theta)/S$ corresponding to $10^o < \theta < 90^o$.

Table 3.1 Axial field strength at the particle surface [from equation (3.98)].

θ (degrees)	$z(\theta)/S$ (dimensionless)	$\vec{E}_s(\theta)$ (Volts/meter)
1	0.00015	3.873×10^8
3	0.0014	4.307×10^7
5	0.0038	1.553×10^7
7	0.0075	7.942×10^6
10	0.0152	3.911×10^6
20	0.0603	1.008×10^6
30	0.1340	4.719×10^5
40	0.2340	2.856×10^5
50	0.3572	2.013×10^5
60	0.5000	1.575×10^5
70	0.6580	1.338×10^5
80	0.8264	1.219×10^5
90	1.0000	1.181×10^5

Once again, as in the earlier case, if the approximate breakdown value of $\vec{E}_s(\theta)$ is 5.0×10^7 V/m then Table 3.1 shows that a gap emission is sustained on the particle surface at a value of θ slightly less than 3 degrees. The surface field strength at $\theta = \pi/2$, i.e., at the equator of the sphere, is 1.181×10^5 V/m. This value (also obtained from Figure 3.11) is the magnitude of the weakest field intensity on the surface of the spherical particle. Furthermore, it is seen from Figure 3.11 that the rate of change of $\vec{E}_s(\theta)$ increases with decrease in θ (and hence also $z(\theta)/S$). This increase stabilizes somewhat at $z(\theta)/S$ equal to 0.26 ($\theta \simeq 42^o$), which is approximately half way along the circumference (from $\theta = \pi/2$) to the edge of the contact circle.

The figures (3.10) and (3.11), in this section, do indeed show that the magnitudes of $\vec{E}_1$ and $\vec{E}_s(\theta)$ are high enough in the contact vicinity so that the electrical breakdown of the air (or flue gas) is feasible. When breakdown sets in, the calculations (in this section) for $\vec{E}^*$ greater than $\vec{E}_b$ ** are not valid. The graph in Figure 3.10, and the values for $\vec{E}_s(\theta)$ ($\theta \leq 3^o$) in Table 3.1, are presented beyond the breakdown value under the "hypothetical" assumption that the air (or gas) in this contact region does not permit a charge emission at these field strengths (about 5×10^7 Volts/meter). In effect, the pre-breakdown calculations have been extended to the region where "$\vec{E} \geq \vec{E}_b$", and the very "existence" of such a region indicates the theoretical feasibility of a charge emission. Once this is established, the above assumption is removed since the field strength in the foregoing region is uniformly equal to the breakdown value.

---

* $\vec{E}$ = any one of two fields, $\vec{E}_1$ or $\vec{E}_s(\theta)$.

** $\vec{E}_b$ = breakdown field strength.

This concludes the analysis of the problem in the present section, and, at this stage, it is desirable to review the procedure that led to the formulation of the expressions for the fields $\vec{E}_1$ and $\vec{E}_s(\theta)$ [equations (3.76) and (3.98)]. A summary of the preceding Sections, 3.1 through 3.6, is presented in Section 3.7.

3.7 Summary

It was stated in the overview to this chapter that one of the more important aspects of the overall resistivity problem * involves the study of the electrical behaviour in the neighbourhood of an inter-particle contact. An important feature that characterizes an electrical contact is the constriction resistance, and this was introduced in Section 3.1. (The constriction resistance is explained in more detail in Appendix G). The fact that (electrical) cohesive forces are present in a resistive particulate bed was mentioned in brief. The orgin of the cohesive force is traceable, ultimately, to the size of the constriction, one form of which is expressed by the dimensionless constriction ratio S/a**. This is discussed in the next section (3.8) where an expression for the attractive force between two particles is given. In addition, a simplified representation for the contact resistance was presented. The objective here was to show the inverse dependence between the contact resistance R_T^1 and the radius r_1 of the spheroidal contact [equation (3.5)]. The actual contact in this

*Characterization of the bulk surface resistivity of a particulate layer.

**For spherical particles in contact, where S is the particle radius and 'a' is the radius of the contact circle.

case is modeled by a conducting spherical ball. Also, this section introduces, in Figure 3.2, the arrangement of the lines of current flow and the equipotential surfaces with respect to the spherical contact. The more rigorous procedure, leading to a generalized representation of the contact resistance, is dealt with in Section 3.3. This section begins with a discussion of the mathematical criterion for an equipotential to be unique. This criterion leads to the formulation of a second order differential equation (3.12) for a parameter $\overline{C}$ (unique for each equipotential surface), which is given in terms of the three dimensional coordinates. Equation (3.12) can be solved for the potential $V = f(\overline{C})$. A functional representation of $\overline{C}$ requires that the equipotential surfaces be given algebraically. This is done in equation (3.13) where an equipotential surface is defined as a general non-intersecting conicoid. (The key variable here is the distance μ which uniquely specifies an equipotential). Some algebraic manipulation follows, yielding an expression $[\overline{f}(\mu)]$ which replaces $\overline{f}(\overline{C})$ in the solution for (3.12). The solution (3.27) then gives an explicit expression for the potential V in terms of μ and a pair of integration constants. These two integration constants are obtained from the boundary conditions for the physical problem. In the problem, a charged surface is situated symmetric to (confocal) oblate hemispheroids which represent the equipotential surfaces. The assumption that the equipotentials can be considered to be hemispheres, at large distances from the circumference of the contact, leads to a simple expression for the field strength (voltage gradient at $\mu \to \infty$) in equation (3.37). This field strength needs to be related to the total charge, and this is accomplished by using the Gauss law for $\vec{E}$ field

[equation (3.42), which is obtained from Maxwell's first equation and the divergence theorem, Appendix H]. The objective is to obtain an expression for the capacitance (between the charged surface and an equipotential). Since capacitance is given in terms of the charge which is related to the $\vec{E}$ field using Gauss's law, the final expression for the capacitance is obtained solely in terms of μ as shown in equation (3.47). Although not directly related to the problem (of determining the contact resistance), it is shown that the surface charge density σ at $\mu = 0$, can also be obtained by means of the relationships established up to this point.

The electrostatic problem is now transformed to a current flow problem, although the geometry of the charged surface (now a current source) and the equipotentials is retained in this transformation. The current density vector (3.58) $\vec{J}$ and the resistance (3.61) R_{c_1} are defined for this case. The capacitance C for the resistive material here is given by equation (3.47) derived earlier. Using the Gauss law in combination with the expressions for $\vec{J}$, R_{c1} and C gives the general expression for the contact resistance $R_{c\phi}$ in the integral form of equation (3.66). The resistance $R_{c\phi}$ pertains to the region (of the material) from the current source A_c to an equipotential (ϕ) which is specified by the length of its semi-axes $\sqrt{\mu}$. For the simpler case where the contact is a circle of radius 'a' the total contact resistance is given by equation (3.68b). The contact (or constriction) resistance is taken to mean the resistance, of the constriction volume, along the direction of the externally applied voltage. The constriction volume is the volume (of the material) enclosed by the "end" equipotentials due to the constriction at the contact. This is described in

Appendix G.

In order to establish the phenomenon of electrical breakdown in the vicinity of an interparticle contact, one first needs to determine the expressions of the electric field strengths in that region. This is examined in Section 3.4 where the potential at a particular equipotential surface is simply given by the product of the current and the contact resistance (derived in the previous section). From this the field strength $\vec{E}_1$ at the line of contact, and at a known distance from the periphery of the contact, is known [equation (3.76)]. Furthermore, the field strength along the line of contact $\vec{E}_g$ is also known [equation (3.83)]. In Section 3.5, the expression for the axially directed* field strength on the surface of a spherical particle $\vec{E}_s(\theta)$ is derived [equation (3.98)]. The approach to the development of this latter expression is independent of the previous section, in fact, the contact resistance does not figure in this case. However, the relevance of $\vec{E}_s(\theta)$ to the overall problem lies in the fact that it is this field intensity that a migrating charge carrier encounters on the dielectric particle surface.

The expressions for the field strengths $\vec{E}_1$ and $\vec{E}_s(\theta)$ are numerically evaluated in Section 3.6. Typical values of the parameters involved in these expressions are assumed in a representative calculation presented in this section. The order of magnitudes of the numbers for $\vec{E}_1$ and $\vec{E}_s(\theta)$ in the gap, in the immediate neighbourhood of the contact, show that electrical breakdown is feasible in this region. This supports a charge emission across the gap, from the surface of

---

*In the direction of the externally imposed voltage across the layer.

one particle to another. Further, the variations of $\vec{E}_1$ and $\vec{E}_s(\theta)$, with distance (λ) and position (given by θ) respectively, are presented in Figures 3.10 and 3.11. In both cases, as expected, it is seen that the field strength increases as the contact is approached.

The theory of electric contacts as presented in this chapter, and the numerical results that follow from it, are discussed in the next section (3.8).

3.8 Discussion

It was shown in Section 3.6 that the phenomenon of electrical breakdown in the interparticle space is conclusively supported by the result of the sample calculation and the magnitudes of the surface field strength (Table 3.1). The procedures used to determine the expressions for $\vec{E}_s(\theta)$ and $\vec{E}_1$ [in this case beginning with the equation for the contact resistance R_μ, equation (3.68b)] was essentially similar to that adopted by McLean (M2, M3). However, as indicated in Section 3.4, the end result of the procedure (in Section 3.3) for $\vec{E}_1$ given by equation (3.76) is different from that obtained by the author. The two equations for $\vec{E}_1$ are:

$$\vec{E}_1 \text{ (this work)} = 2 \frac{V}{a} \frac{S}{a} \frac{1}{(\lambda^2-1)} \qquad (3.76)$$

$$\vec{E}_1 \text{ (McLean)}^* = \frac{4}{\pi} \frac{V}{a} \frac{S}{a} \frac{\tan^{-1} \sqrt{\lambda^2-1}}{(\lambda^2-1)} \qquad (3.78)$$

These two expressions are equivalent for the condition that λ is large, since

---

*See reference M2.

$$\frac{4}{\pi} \tan^{-1} \sqrt{\lambda^2-1} \rightarrow 2$$

as $\lambda \rightarrow \infty$

In the example calculation of Section 3.6 the maximum value of λ is approximately 100 (S/a = 100). This λ maximum corresponds to the point along the line of contact (Figure 3.9) which is collinear with the equatorial points on the surfaces of the contacting spheres ($\theta = \pi/2$). At this value of $\lambda = \lambda$ max,

$$\frac{4}{\pi} \tan^{-1} \sqrt{\lambda^2-1} = 1.987$$

and the two values of $\vec{E}_1$ from the equations above differ by a small margin of 0.65%. The discrepancy between the two equations increases as λ decreases, i.e., as the circumference of the contact circle is approached. For example at $\lambda = 6$ (at a distance of six times the radius of contact),

$$\frac{4}{\pi} \tan^{-1} \sqrt{\lambda^2-1} = 1.787$$

This number differs from the factor 2 in equation (3.76) by about 10.7%.

The underlying assumption of a long* constriction, which is implicit in the expression for $R_{c\phi}$, equation (3.77) [and hence equation (3.78)

*See Appendix G

as well], is discussed in Section 3.4. In the case where the constriction is not long, equation (3.76) is valid for the situation where λ is large. It must be remembered that $\vec{E}_1$ is the field strength obtained by dividing the potential ϕ by a distance FD which represents half the line of force from one particle to another (see Figure 3.8). The distance GF is given by λ, and the value of ϕ is the potential of D with respect to F. Hence D is the end point (on the particle surface) of an equipotential surface whose relative* potential is given by ϕ. Thus, in as much as a large value of λ means that F is distant from G, it alos implies that D (and hence the corresponding equipotential) is equivalently further away from F. This statement is exactly true under the assumption, of course, that the lines of force are straight**.

In contrast to the above, the general equation for resistivity is used to obtain the expression (3.76) for $\vec{E}_1$. This equation incorporates no assumptions of the type mentioned in the previous paragraph, and is therefore valid for short or long constrictions, and for small or large values of the dimensionless distance λ.

It may be noted that the mathematical procedure that led to the formulation of the expression (3.76) for $\vec{E}_1$ does not refer to any lines of current flow or lines of force on the particle surface. Indeed, the figures, 3.2 through 3.5, depict equipotentials which are inside the sphere, and lines of force that go through the volume of the particle. In the context of the final objective (of this work) of characterizing the bulk surface resistivity of a particulate layer, the relevance of the above procedure lies in the fact that, irrespective of the dominant

---

*Relative to the plane of contact.

**This is an approximation, as mentioned in Section 3.4.

mode of conduction of the charge carriers*, the lines of force and equipotentials exist by virtue of the externally applied voltage. If these equipotentials are known, then the potentials on the particle surface are also known, so that the average voltage gradients along a "straight" line of force, joining two particles, can be evaluated. Furthermore, an important aspect of the algebra presented in Section 3.3 is that it helps elicit the concept of the contact resistance. An important significance of this is that it is this electrical feature of the contact that accounts for the high electric field intensities in the interparticle gap, as evidenced by the magnitude of $\vec{E}_1$. The fact that this field strength, as indicated earlier, may exceed the breakdown value (thus sustaining a charge emission across the gap) then, partially bears out the observed non ohmic behaviour of a layer of particulate fly ash.

In addition to the above, it is shown later that a comparison of $\vec{E}_1$ and the surface field strength $\vec{E}_s(\theta)$ can be used to define a "region of breakdown". The procedure leading to the expression for $\vec{E}_s(\theta)$, equation (3.98), does not recognize the presence of equipotentials inside the spheres. Hence it has no bearing on the contact resistance R_μ [equation (3.68b)]. However, as stated in Section 3.5, equation (3.98) does include the effect of the size of the constriction which, in this case, is given by the constriction ratio S/a.

$$\vec{E}_s(\theta) = \vec{E}_a / - \{\ln \frac{a}{2S}\} \{\sin^2\theta\} \qquad (3.98)$$

---

*Surface or volume conduction.

It was stated in Section 3.5 that $\vec{E}_s(\theta)$ decreases with the dimensionless ratio a/S, in contrast to the relationship between $\vec{E}_1$ and a/S in equation (3.76). However, this preliminary observation, which is based on the equations (3.76 and 3.98) alone, needs to be quantitatively investigated on the basis of the variations of $\vec{E}_1$ and $\vec{E}_s(\theta)$ with respect to the parameters in the two equations. Table 3.2 shows that field strengths at different values of S/a and λ.

Table 3.2 Magnitudes of $\vec{E}_1$ and $\vec{E}_s(\theta)$ at different constriction ratios [from equations (3.76) and (3.98)].

Constriction Ratio S/a	λ	$\vec{E}_1$ (Volts/meter)	$\vec{E}_s(\theta)$ $\{\theta=9.1^o\}$ (Volts/meter)
100	16	9.80×10^7	4.72×10^6
1000	160	9.77×10^7	3.29×10^6

The results in this table are obtained from the data used in the calculations for $\vec{E}_1$ and $\vec{E}_s(\theta)$ in Section 3.6. The different values of λ correspond to the two constriction ratios for which the field strengths have been estimated. The field strengths $\vec{E}_1$ and $\vec{E}_s$ (θ) are along the same line of force*, corresponding to an angle θ equal to 9.1^o. The difference in the two rows of figures in the table is only due to the contact areas which differ by a factor of 100.

It is seen from Table 3.2 that $\vec{E}_1$ is relatively invariant with the constriction ratio. This invariance occurs when the line of force is fixed i.e., the absolute distance from the circumference of contact is constant. Hence if r is fixed in equation 3.70,

---

*For example, line FD on Figure 3.7. $\vec{E}_s(\theta)$ is the field at D while $\vec{E}_1$ is at F (on the line of contact).

$$\lambda \propto \frac{1}{a} \tag{3.99}$$

and it is readily apparent that $\vec{E}_1$ [equation (3.76)] does not change as a result of this. If, instead, the field strength $\vec{E}_1$ is calculated at the same value of λ, when S/a = 1000, the result is an order of magnitude several times higher than 9.80×10^7 Volts/meter. In this case $\vec{E}_1$ is given as:

$$\vec{E}_1\ (\lambda_2=16) \simeq \vec{E}_1\ (\lambda_1=160) \cdot \{\lambda_1^2/\lambda_2^2\}$$

$$= 9.77 \times 10^9 \text{ Volts/meter.}$$

This result is consistent with the remark made in Section 3.4, that is,

$$\vec{E}_1 \propto 1/a^2$$

As expected, the variation of the surface field strength $\vec{E}_s(\theta)$ is in the same direction as a/S. The degree of dependence of $\vec{E}_s(\theta)$ on the constriction ratio S/a is not as strong as $\vec{E}_1$ (for the case of constant λ, as shown above). This dependence $\{\vec{E}_s(\theta) = f\ (a/S)\}$ increases as θ decreases, i.e., as the point of contact is approached. It is evident from the expression for $\vec{E}_s(\theta)$ (shown below) that its minimum value occurs at $\theta = \pi/2$. This is also intuitively obvious since the equatorial circle is furtherst from the contact.

From the perspective of an idealized particulate layer model, it

is important to note here that lateral* interparticulate contacts do not modify the electric field distribution. It may be recalled that the physical model consists of a well ordered, homogeneous, and monodisperse spherical particles arranged in a cubical packing (Section 2.2, Chapter 2). No voltage gradients exist in a direction that is transverse with respect to the externally applied voltage, and therefore there are no lines of force (or current flow) that go through the lateral contacts. Hence the distribution of $\vec{E}_s(\theta)$ (on the surface of a spherical particle), as calculated from equation (3.98), applies to this model. A similar argument may be invoked in the case of capillary condensation, where the condensate formed at these (lateral) macropores is really extraneous to any consideration of layer resistivity modification (due to capillary condensation). Since there is no electronic or ionic current flow perpendicular to the applied voltage, the presence of capillary condensate in these macropores does not affect the bulk resistivity of the layer.

The pair of equations (3.91) and (3.92), from which $\vec{E}_s(\theta)$ is determined in Section 3.5, may be used to obtain an average field strength $\vec{E}_z(\theta)$ in the gap and along a line of force. Assuming that the line of force is short so that the voltage varies linearly with distance along it, $\vec{E}_z(\theta)$ is obtained simply as,

*The electrical contacts formed in a vertical stack of particles, such as the one shown in Figure 3.9, are considered to be longitudinal contacts. Lateral contacts are formed in a transverse direction. Thus a plane which goes through the centers of circles of lateral contact, is perpendicular to the applied voltage gradient.

$$\vec{E}_z(\theta) = V(\theta)/z(\theta)$$

$$= \frac{E_a \left[\ln \left(\tan \frac{\theta}{2} / \tan \frac{\theta_c}{2}\right) / \ln \left(1/\tan \frac{\theta_c}{2}\right]\right.}{[\cos \theta_c - \cos \theta]} \qquad (3.100)$$

where $V(\theta)$ is the potential difference between the points (on the surfaces of two contacting spheres) that form the ends of an axial line of force of length $z(\theta)$. The similarity between $\vec{E}_z(\theta)$ and $\vec{E}_1$ may be noted here; thus, while $\vec{E}_1$ is estimated from the voltage drop between symmetric* equipotentials, $\vec{E}_z(\theta)$ is based on the voltage difference between two points on the particle surface due to the surface resistivity (ρ_s).

Under the assumption that the electric field is predominantly axial across the entire gap, McLean (M3) has defined a cohesive force F_z between two particles. The electrostatic cohesive force is proportional to the square of the field strength, hence the dominant contribution to F_z would be due to the high electric field in the air gap. The force F_z is given below as,**

$$F_z = \int^A \frac{\epsilon_o}{2} E_z(\theta)^2 \, dA \qquad (3.101)$$

where F_z is in the same direction as $E_z(\theta)$ and dA is the annular differential area on the contact plane. The total cohesive force for a layer is obtained by summing F_z over all the contacts in the layer.

---

*Symmetric (equidistant) to the plane of contact.

**See reference M3.

The "region of breakdown" mentioned earlier in this section, is obtained by comparing the magnitudes of $\vec{E}_1$ and $\vec{E}_s(\theta)$. Table 3.3 below shows the values of these two field strengths at different locations in the interparticle gap.

Table 3.3. Variation of $\vec{E}_1$ and $\vec{E}_s(\theta)$ with position in the interparticle gap.

θ (degrees)	λ (dimensionless)	$\vec{E}_1$ (Volts/meter)	$\vec{E}_s(\theta)$ (Volts/meter)
1	1.745	1.222×10^{10}	3.873×10^{8}
5	8.749	3.309×10^{8}	1.553×10^{7}
10	17.633	8.067×10^{7}	3.912×10^{6}
15	26.795	3.487×10^{7}	1.761×10^{6}
20	36.397	1.889×10^{7}	1.008×10^{6}
25	46.631	1.150×10^{7}	6.605×10^{5}
30	57.735	7.502×10^{6}	4.719×10^{5}
35	70.021	5.100×10^{6}	3.586×10^{5}
40	83.910	3.551×10^{6}	2.855×10^{5}
45	100.000	2.500×10^{6}	2.359×10^{5}

The variation of $\vec{E}_1$ and $\vec{E}_s(\theta)$ with the polar angle θ in the foregoing table is illustrated by the plots in Figure 3.12. The plots span the range $0^o < \theta < 45^o$. It is seen that E_1 always exceeds the surface field strength $\vec{E}_s(\theta)$. When θ exceeds 45^o the corresponding value of λ is greater than 100, and the field strength $\vec{E}_1$ in this region is due to the neighbouring longitudinal contact. Also $\vec{E}_s(\theta)$, for $\theta > 45^o$, is the field strength on the hemispherical surface due the other (longitudinal)

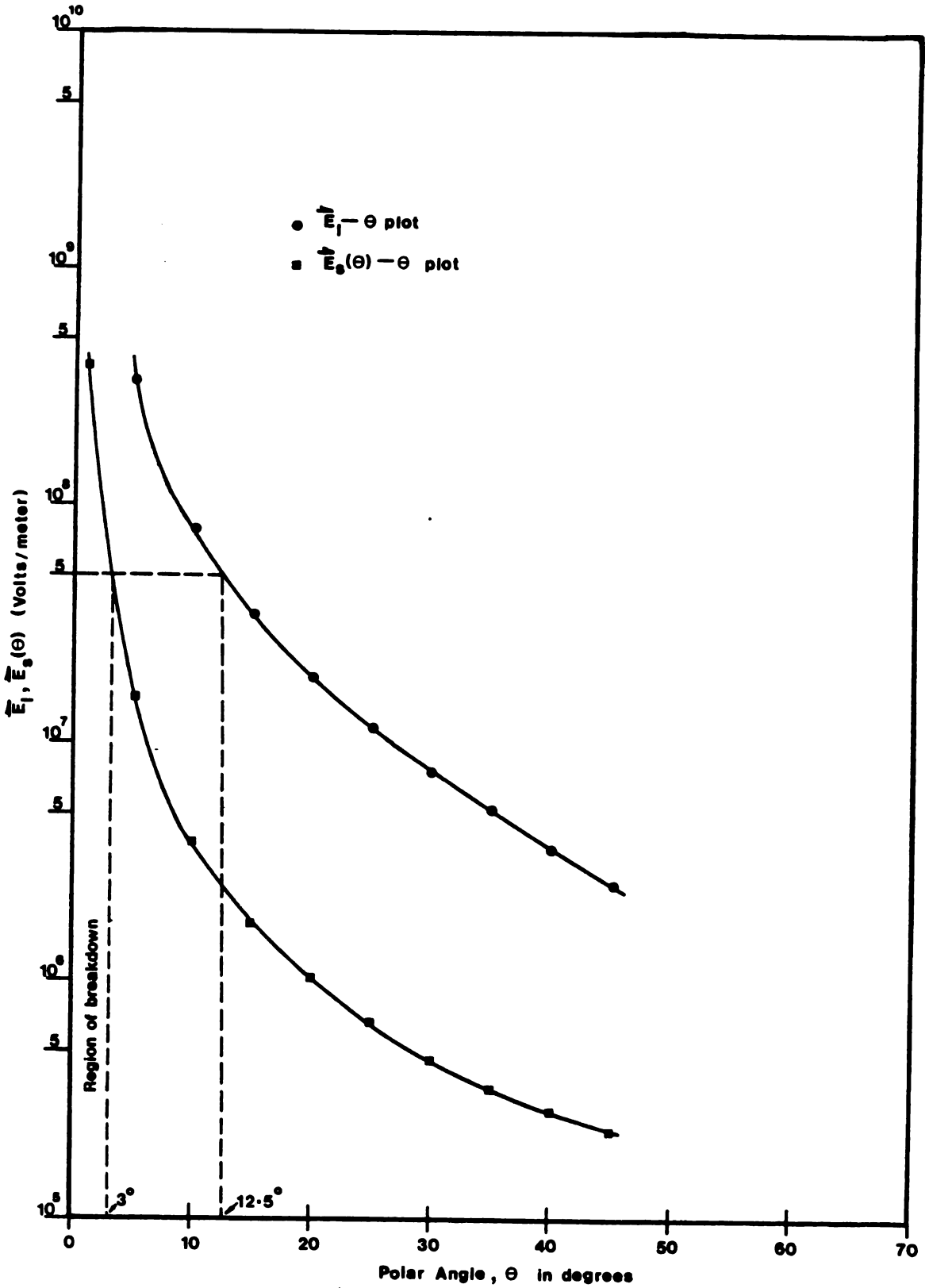

Figure 3.12. Variation of $\vec{E}_1$ and $\vec{E}_s(\theta)$ with polar angle θ.

contact of the particle. The graph shows that while the $\vec{E}_1$ curve predicts breakdown at θ equal to 12.5^o, the surface field $\vec{E}_s(\theta)$ assumes that magnitude at $\theta = 3^o$. Hence the "region of breakdown", based upon $\vec{E}_s(\theta)$, corresponds to the portion of the spherical surface (excluding the contact) that subtends a solid angle of 6^o at the center.

The figure (3.12) is based on the parameter values of Section 3.6; however this example shows that the $\vec{E}_1$ plot predicts the larger breakdown region. If it is considered that a charge emission can occur from the surface of one particle to another, then this may be initiated by the field strength $\vec{E}_s(\theta)$ if it equals the breakdown value. Thus, it is assumed here that the criterion of charge emission is that the surface field strength $\vec{E}_s(\theta) = \vec{E}_b$. Hence the region of breakdown is given as indicated in Figure 3.12, i.e., the region for which $\vec{E}_s(\theta) \geq \vec{E}_b$.

This region may also be estimated in terms of the spherical surface area over which charge emission occurs. From equation (3.92) if $\theta = \theta_b = 3^o$

$$z(\theta_b)/S = \cos \theta_c - \cos \theta_b$$

$$= 0.0013$$

where

$$\Theta_c = \tan^{-1} \frac{a}{S}$$

$$A_b = 4\pi\,(0.0013)S^2 - \pi(.0013)^2\, S^2 - A_c$$

where,

A_b = surface area over which breakdown occurs

A_c = area of contact

Hence, the fractional breakdown surface area (on one side) is given by

$$A_{bf} = 0.0013 - \frac{\pi}{4}(0.0013)^2 - \frac{1}{4}\left(\frac{a}{S}\right)^2$$

$$\simeq 0.0013$$

Hence, in this example, the total breakdown surface area (for both contacts) is approximately 0.26% of the sphere area. It may be remarked that this figure is not necessarily typical, for the surface area evaluated by this procedure is an implicit function of the bed geometry, the constriction ratio, the applied voltage and the field strengths $\vec{E}_1$ and $\vec{E}_s(\theta)$. However, it might be observed that even though A_{bf} is not large, it is quite significant in view of the fact that I-V plot of such a particulate layer is decidedly nonlinear (if this is the cause of non-linearity).

The equation (3.100) for $\vec{E}_z(\theta)$ recognizes it as being the average field strength along a line of force specified by θ. In the strict sense, the field may be assumed to vary and the modified expression for $\vec{E}_z(\theta)$ is then given as

$$\vec{E}_{\bar{z}}(\theta)\Big|_z = dV(\bar{z})/d\bar{z} \qquad (3.102)$$

where $\bar{z}$ is the running variable defined in Section 3.5 [see footnote

to equation (3.93)].

Hence,

$$\vec{E}_s(\theta)\big|_z = \vec{E}_{\bar{z}}(\theta)\big|_{\bar{z}=z}$$

Thus the surface field strength $\vec{E}_s(\theta)$ is (rigorously) given by the value of $\vec{E}_{\bar{z}}(\theta)$ at the surface. By way of comparison, it may be noted that equation (3.93) for $\vec{E}_s(\theta)$ is given as the ratio of $dV(\theta)$ and $dz(\theta)$ which are the differential changes of those variables (for a differential change in the polar angle,(θ) on the particle surface.

The expressions for $\vec{E}_1$ and $\vec{E}_s(\theta)$ both involve approximations that are associated with the assumptions used to arrive at the two equations (3.76) and (3.98). The approximation for $\vec{E}_1$ involved the assumption that the gap lines of force are straight, as shown in Figure 3.8. In the case of equation (3.98) for $\vec{E}_s(\theta)$, the voltage drop per contact was assumed to uniform throughout the layer. It is apparent that in the realistic case (of an operating electrostatic precipitator) that is not true. However, from the perspective of characterization of the bulk surface resistivity, this latter assumption is valid for the specifically chosen idealized model as shown in Figure 2.2 (Chapter 2).

CHAPTER FOUR

FORMULATION OF THE MATHEMATICAL PROBLEM TO DESCRIBE SURFACE (ALKALI) ION TRANSPORT AND ITS SOLUTION.

Overview

The material presented earlier in Chapter 2 and 3 was restricted to an investigation of two important physical features of the model depicted in Figure 2.2 (Chapter 2). The phenomenon of capillary condensation (in a humid environment) within the macropores of an idealized particulate bed was discussed in Chapter 2. As indicated in Figure 3.1, the presence of liquid water in the interparticle spaces modifies the (resistance) path of a migrating sodium ion. This migration of a singly charged ion occurs in the presence of two forces, namely a concentration driving force and an electric driving force. While the "concentration (transport) flux" is accountable by molecular diffusion, the "electrical" flux is dependent upon the local voltage gradient on the particle surface. Thus the variation of voltage gradient with position on the particle surface is required, and this was evaluated in Chapter 3 along with an examination of the various electric fields within the bed in the presence of an externally applied voltage gradient.

The mathematical description of the ion migration problem is straightforward once the model parameters specific to the ambient condition, as outlined in Chapters 2 and 3, are obtained. In effect one seeks to arrive at alkali (sodium) ion concentration profiles on the particulate bed for fixed values of these parameters.

In this chapter the migration problem is illustrated in Section 4.1. This is followed by a mathematical formulation of the problem in Section 4.2, in terms of an ordinary, linear differential equation (4.10). The technique adopted to solve this equation is called the "method of dominant balance" (B7). Briefly, this technique helps determine asymptotic approximations to the exact solution in the neighborhood of the irregular singularities of the differential equation. This is presented in Section 4.3 along with a formal solution to the equation (4.10). Finally, this chapter is concluded with a discussion of the "appropriateness" of the solution and of some of its relevant features.

4.1 The Physical Problem

The physics of the ion transport problem is visualized for the simple case of contact of two identical spherical particles. This is shown in Figure 4.1. The average electric field strength across the bed is given by $\vec{E}_s(\theta)$ which, as shown in Chapter 3 [equation (3.98)], is a function of θ. For a particle of a given radius S the extent of capillary condensation is completely determined by the angles θ_o and θ_c. As shown in the next chapter* these values are easily determined once the radius of curvature of the capillary condensate is specified.

As depicted in Figure 4.1 there exists a "pool" of sodium ions in the capillary condensate at the bottom end of the lower particle (between θ_c and θ_o). For this problem the sodium ion concentration on the surfaces of the two particles outside of this region is relatively small and hence neglected. The spherical path of migration on the

---

*See also equations (2.77) and (2.79) in Chapter 2. Here the angles ψ and ϕ correspond to θ_c and θ_o respectively.

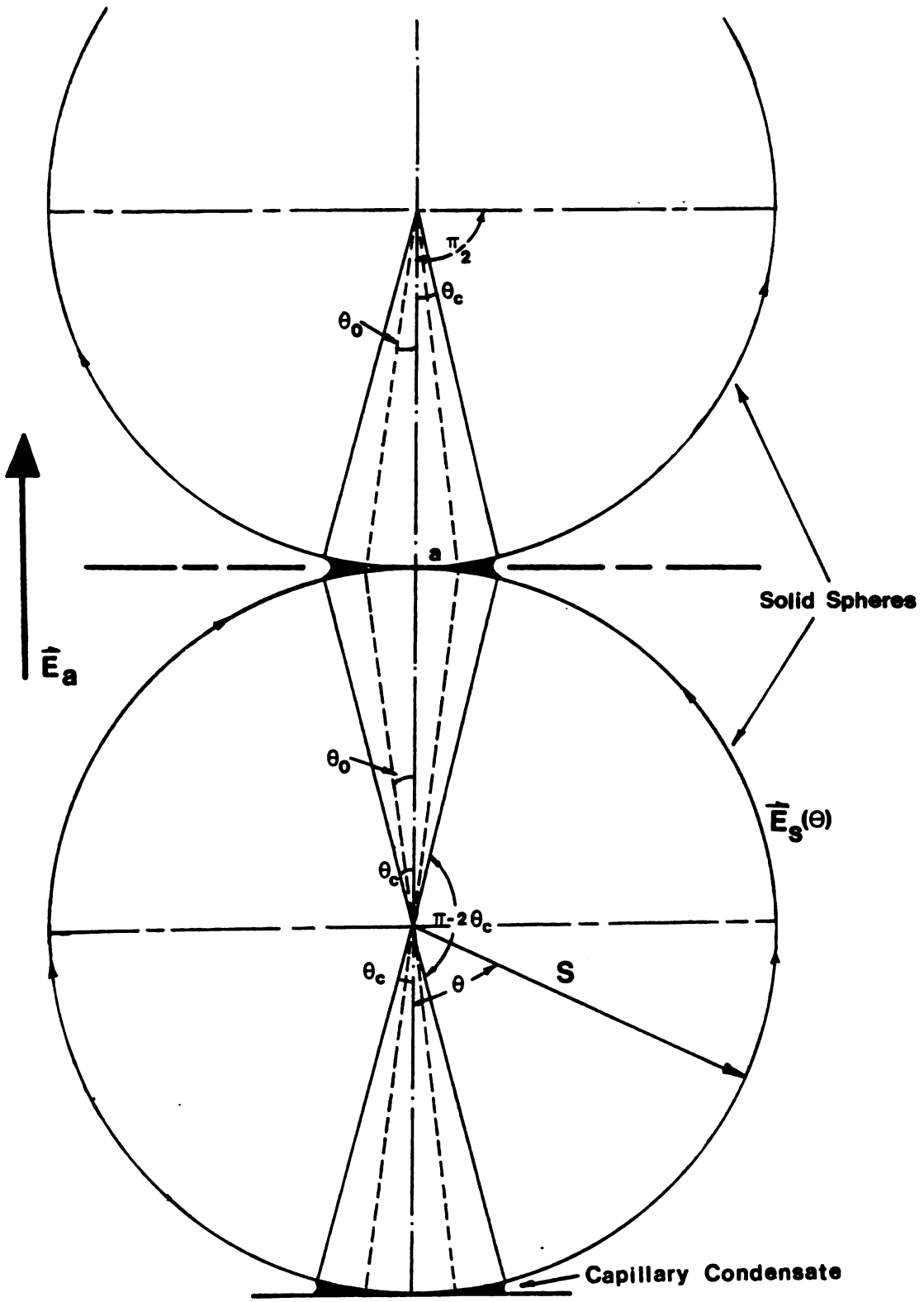

Figure 4.1. Illustration of ion transport problem.

surface of a single particle is given by the region $\theta_c < \theta < \pi - 2\theta_c$. It is assumed that the electrical resistance of the condensate is negligibly small relative to the particle surface resistance. Furthermore, the volume of the condensate is small enough so that no concentration gradients persist within it; in effect the sodium ion concentration is uniform in the region $0 \leq \theta \leq \theta_c$.

In the ideal situation the two particles are perfect identical spheres which contact each other at a point. However it was mentioned in Chapter 3 [equation (3.101)]* that a resistive particulate bed experiences a cohesive force when an external voltage gradient is applied across it. This cohesive force then determines the area of contact between the two spheres, or the radius of contact 'a' in Figure 4.1 (M3, M5).

Finally, as revealed by the current-time data for the experiments conducted in the laboratory (Chapter 5), it was determined that the (solid state) rate of surface transport of sodium ions was small enough so that the diffusion was essentially at steady state. This follows from the fact that the variation of current, after an initial period of stabilization, was negligible for the duration of the experiments.

Having specified the physical structure of the problem, it is now necessary to transform it to a mathematical expression to describe the 'electrical' and 'concentration' fluxes. In the next section a second order differential equation is derived to describe the steady state ion diffusion for the problem of Figure 4.1.

---

*See Section 3.1, Chapter 3.

4.2 The Ion Transport Equation

A general form of the continuity equation for a constant density binary system is given as (B8):

$$\frac{\partial c}{\partial t} + \nabla \cdot cv = \nabla \cdot (D\nabla c) + R \qquad (4.1)$$

where

c = surface concentration

v = velocity of the ionic species

D = mass diffusivity

R = rate of reaction

For the condition of steady state and no reaction equation (4.1) becomes

$$D\nabla^2 c - \nabla \cdot cv = 0 \qquad (4.2)$$

Transformation of this equation into spherical coordinates (with no ion concentration gradients in either the r or ϕ directions)* yields:

$$\frac{D}{S^2}\left(\frac{\partial^2 c}{\partial \theta^2} + \cot\theta \frac{\partial c}{\partial \theta}\right) - \nabla \cdot cv = 0 \qquad (4.3)$$

The velocity v in the second term of the above equation arises due to the interaction of the single positive charge on the sodium ion and the local electric field $\vec{E}_s(\theta)$. Under these conditions it is related to the mobility μ as:

*r and ϕ are the usual spherical notations for the radius and transverse angle. See reference B8, page 740.

$$\mu = \frac{v}{\vec{E}_s(\theta)} \quad * \tag{4.4}$$

If the diffusivity is assumed to be a constant then the electrical mobility may be considered to be a function of temperature only so that the variations in the velocity v is reflected by the corresponding changes in $\vec{E}_s(\theta)$. Substituting (4.4) into the second term of equation (4.3),

$$\nabla \cdot cv = \nabla \cdot c\mu\vec{E}_s \quad **$$

$$= c\,(\nabla\cdot\mu\vec{E}_s) + (\mu\vec{E}_s\cdot\nabla c) \tag{4.5}$$

now

$$c(\nabla\cdot\mu\vec{E}_s) = \frac{c}{S \sin\theta} = \frac{\partial}{\partial\theta}(\mu\vec{E}_s \sin\theta) \tag{4.6}$$

From equation (3.98), Chapter 3, the surface field strength $\vec{E}_s$ is given as,

$$\vec{E}_s = \vec{E}_a/- \ln K \cdot \sin^2\theta \tag{3.98}$$

where

$$K = a/2S$$

---

*This is analogous to the hydrodynamical mobility (see reference B.8, page 513).

**The θ notation is dropped for convenience.

Substitution of (3.98) into equation (4.6) and subsequent simplification gives

$$c\,(\nabla\cdot\mu\vec{E}_s) = \frac{\mu\vec{E}_a c}{S\ln K}\,\frac{\cos\theta}{\sin^3\theta} \tag{4.7}$$

The second term of equation (4.5) is written as

$$\mu\vec{E}_s\cdot\nabla c = \frac{-\mu\vec{E}_a}{S\ln K\cdot\sin^2\theta}\,\frac{\partial c}{\partial\theta} \tag{4.8}$$

Incorporating the substitutions (4.7) and (4.8) into equation (4.3) one gets the ordinary differential equation

$$\frac{D}{S^2}\frac{\partial^2 c}{\partial\theta^2} + \frac{D}{S^2}\frac{\cos\theta}{\sin\theta}\frac{\partial c}{\partial\theta} - \frac{\mu\vec{E}_a c}{S\ln k}\frac{\cos\theta}{\sin^3\theta} + \frac{\mu\vec{E}_a}{S\ln K\sin^2\theta}\frac{\partial c}{\partial\theta} = 0 \tag{4.9}$$

Equation (4.9) can be divided by D/S^2 and the term $\mu SE_a/_D \ln K$ set equal to $\bar{\alpha}$ to give a simplified form as follows:

$$c'' + (\cot\theta + \bar{\alpha}\csc^2\theta)\,c' - \bar{\alpha}\,c\cot\theta\csc^2\theta = 0^* \tag{4.10}$$

Equation (4.10) is the mathematical representation of the ion migration problem described in the previous section. This equation is valid for isothermal, steady state diffusion for which the parameter $\bar{\alpha}$ is assumed to be a constant.

*Double and single primes correspond to the usual notations of second and first derivatives respectively.

The method of dominant balance approach is used to obtain a solution to the foregoing differential equation (B7). A general solution to (4.10) is initially sought prior to applying the boundary condition appropriate to the problem. This is presented in the next section.

4.3 Solution by the Method of Dominant Balance

It is known that a Taylor series solution to a differential equation, about a point $x = x_o$, must be analytic in the neighborhood of x_o and at x_o. A Frobenius series solution is constructed if x_o is a regular singular point (H7). However at an irregular singular point all solutions to a linear differential equation cannot have a Frobenius series representation; i.e., at least one solution has no Frobenius form. Hence, to begin with a solution, it is first necessary to identify the singular points in the differential equation (4.10).

It is seen that the coefficients of c' and c in equation (4.10) are not analytic at $\theta = 0$. Further, as shown subsequently, $\theta = 0$ is not a regular singular point.

The series solution obtained by the method of dominant balance is valid in the neighborhood of the singular point and the controlling factor in the leading behavior of such an asymptotic series is the same as that of the exact solution. The controlling factor is usually in the form of an exponential (B7), hence a substitution of the form $c(\theta) = \exp\{s(\theta)\}$ is appropriate. Using this substitution in equation (4.10) gives

$$e^s \{s'' + (s')^2\} + \{\cot\theta + \bar{\alpha}\csc^2\theta\}e^s \cdot s' - e^s \cdot \bar{\alpha}\cot\theta\csc^2\theta = 0 \qquad (4.11)$$

If $\theta = 0$ is an irregular singular point it is usually true that (B7)

$$s'' << (s')^2, \quad \theta \to 0 \tag{4.12}$$

Working with this assumption (to be verified subsequently), one gets the following asymptotic equality

$$(s')^2 \simeq -\{\cot\theta + \bar{\alpha}\csc^2\theta\}\, s' + \bar{\alpha}\cot\theta\csc^2\theta \tag{4.13}$$
$$\theta \to 0$$

It is apparent that the second order differential equation (4.11) has been reduced to first order by means of the inequality (4.12), and is valid in the neighborhood of the singularity.

Solving for the asymptotic relationship (4.13), which is a quadratic in s', gives

$$s' \simeq -\tfrac{1}{2}(\cot\theta + \bar{\alpha}\csc^2\theta) \pm \tfrac{1}{2}\{(\cot\theta + \bar{\alpha}\csc^2\theta)^2 + 4\bar{\alpha}\cot\theta\csc^2\theta\}^{\frac{1}{2}} \tag{4.14}$$

Some algebraic manipulation of the above yields

$$s' \simeq -\tfrac{1}{2}(\cot\theta + \bar{\alpha}\csc^2\theta) \pm \tfrac{1}{2}\bar{\alpha}\csc^2\theta\left\{1 + \underbrace{\frac{\cot^2\theta}{\alpha^{-4}\csc^4\theta}}_{\theta \to 0} + \underbrace{\frac{6\bar{\alpha}\cot\theta\csc^2\theta}{\bar{\alpha}\csc^4\theta}}_{\text{II}}\right\}^{\frac{1}{2}} \tag{4.15}$$
$$\theta \to 0 \qquad\qquad \text{I}$$

If

$$x = \frac{\cot^2\theta}{\bar{\alpha}^4 \csc^4\theta} + \frac{6\,\bar{\alpha}\cot\theta\csc^2\theta}{\bar{\alpha}^2\csc^4\theta}$$

then as $\theta \to 0$ $\quad x^2 << 1$

Hence the term within the second parenthesis in (4.15) can be expanded to give

$$(1+x)^{\frac{1}{2}} = 1 + \tfrac{1}{2}\left\{\frac{\cot^2\theta}{\bar{\alpha}^2\csc^4\theta} + \frac{6}{\bar{\alpha}}\frac{\cot\theta}{\csc^2\theta}\right\} - \frac{1}{8}\left\{\frac{\cot^4\theta}{\bar{\alpha}^4\csc^4\theta} + \frac{6}{\bar{\alpha}}\frac{\cot\theta}{\csc^2\theta}\right\} + \ldots. \qquad (4.16)$$

$$\theta \to 0$$

Integration of (4.15), term by term, to determine s gives

$$\text{Integral I} = -\tfrac{1}{2}\int(\bar{\alpha}\csc^2\theta + \cot\theta)d\theta$$

$$= \frac{\bar{\alpha}}{2}\cot\theta - \tfrac{1}{2}\ln\sin\theta$$

$$\text{Integral II} = \pm\tfrac{1}{2}\int\bar{\alpha}\csc^2\theta\left\{1 + \tfrac{1}{2}\left(\frac{\cot\theta}{\bar{\alpha}^2\csc^4\theta} + \frac{6}{\bar{\alpha}}\frac{\cot\theta}{\csc^2\theta}\right) - \frac{1}{8}\left(\frac{\cot^4\theta}{\bar{\alpha}^4\csc^8\theta} + \frac{36}{\bar{\alpha}^2}\frac{\cot^2\theta}{\csc^4\theta} + \frac{12}{\bar{\alpha}^3}\frac{\cot^3\theta}{\csc^6\theta}\right) + \ldots\right\}d\theta$$

It is evident that as $\theta \to 0$ the magnitude of the subsequent terms decrease rapidly, relative to the first term. Hence only the first two terms in the expansion (4.16) are considered.

Solving integral II above gives

$$\text{Integral II} = \pm \tfrac{1}{2} \{-\frac{\bar{\alpha}}{2} \cot \theta + \frac{1}{4\bar{\alpha}} (\frac{\sin 2\theta}{4} + \frac{\theta}{2}) + \frac{3}{2} \ln \sin \theta\}$$

Addition of integrals I and II gives the two solutions, s_1, and s_2, to the quadratic (4.13).

$$s_1 \simeq \bar{\alpha} \cot \theta + 2 \ln \csc \theta - \frac{1}{4\bar{\alpha}} (\frac{\sin 2\theta}{4} + \frac{\theta}{2}) \tag{4.17}$$

and

$$s_2 \simeq \ln \sin \theta + \frac{1}{4\bar{\alpha}} (\frac{\sin 2\theta}{4} + \frac{\theta}{2}) \tag{4.18}$$

$$\theta \to 0$$

As stated earlier it is essential that the controlling factors be such that both roots s_1 and s_2 satisfy inequality (4.12). Examining s_2 first, one obtains upon differentiation of (4.18) and squaring,

$$(s_2')^2 \simeq \cot^2 \theta + \frac{1}{4\bar{\alpha}^2} \frac{\cot^4 \theta}{\csc^4 \theta} + \frac{1}{2\bar{\alpha}} \frac{\cot^3 \theta}{\csc^2 \theta}$$

and

$$s_2'' \simeq -\csc^2 \theta - \frac{\cos \theta \sin \theta}{2\bar{\alpha}}$$

$$\theta \to 0$$

As $\theta \to 0$ it is seen that indeed $(s_2')^2 >> s_2''$, since

$$|(s_2')^2| - |s_2''| \simeq \frac{1}{2\bar{\alpha}} \cot \theta$$

$$\cot^2 \theta \simeq \csc^2 \theta \quad : \quad \theta \to 0$$

Similarly for the first root s_1, one obtains

$$s_1' \simeq -\bar{\alpha} \cos^2 \theta - 2 \cot \theta - \frac{1}{4\bar{\alpha}} \cos^2 \theta$$

$$\theta \to 0$$

Thus one gets for the root s_1

$$(s_1')^2 \simeq \bar{\alpha}^2 \csc^4 \theta \quad , \qquad \theta \to 0$$

and

$$s_1'' \simeq 2 \bar{\alpha} \csc^2 \theta \cot \theta + 2 \csc^2 \theta + \frac{2 \cos \theta \sin \theta}{4 \bar{\alpha}}$$

so that

$$s_1'' \simeq 2 \bar{\alpha} \cot^3 \theta, \qquad \theta \to 0$$

Since $\cot^2 \theta \to \csc^2 \theta$ as $\theta \to 0$, it is seen again that inequality (4.12) holds for this solution. In view of the fact that both roots s_1 and s_2 satisfy this approximation for $\theta \to 0$, it is concluded that $\theta = 0$ is

an irregular singular point. Hence s_1 and s_2 are valid roots of equation (4.13).

The leading behavior is determined by just those contributions to $s(\theta)$ which do not vanish as θ approaches the irregular singularity. Hence the two solutions are:

$$s_1 \simeq \bar{\alpha} \cot \theta + \ln \csc^2 \theta, \text{ and} \tag{4.19}$$

$$s_2 \simeq \ln \sin \theta, \ \theta \to 0 \tag{4.20}$$

The solution to the differential equation (4.10) corresponding to s_1 can be improved by estimating an integrating function $f_1(\theta)$ such that

$$s_1 = \bar{\alpha} \cot + \ln \csc^2 \theta + f_1(\theta)$$

where

$$f_1(\theta) << \bar{\alpha} \cot \theta + \ln \csc^2 \theta, \ \theta \to 0$$

Substitution of $s_1(\theta)$ into equation (4.13) yields a differential equation in terms of $f_1(\theta)$,

$$s_1' \simeq - \bar{\alpha} \csc^2 - 2 \cot \theta + f_1'(\theta) \text{ and}$$

$$s_1'' \simeq 2\bar{\alpha} \csc^2 \theta \cot \theta + 2 \csc^2 \theta + f_1''(\theta)$$

$$f_1'' + (f_1')^2 \simeq (\bar{\alpha} \csc^2 \theta + 3 \cot\ ) f_1' - 2 \bar{\alpha} \csc^2 \theta \cot \theta$$

$$- 2 (\csc^2 \theta + \cot^2 \theta) \quad (4.21)$$

This equation may be approximated by an asymptotic differential equation f_1 using the criterion stated earlier, i.e.,

$$f_1 << \bar{\alpha} \cot \theta + \ln \csc^2 \theta, \ \theta \to 0 \quad (4.22)$$

Using (4.22) the following approximations may be obtained

$$\bar{\alpha} \cot \theta >> \ln \csc^2 \theta$$

$$\therefore |\bar{\alpha} \csc^2 \theta| >> f_1'(\theta) \quad] \ \theta \to 0$$

$$|2 \bar{\alpha} \csc^2 \theta \cot \theta| >> f_1''(\theta) \quad (4.23)$$

Hence, if $f_1'(\theta) << \bar{\alpha} \csc^2 \theta$, then

$$(f_1')^2 << \bar{\alpha} f_1' \csc^2 \theta, \quad \theta \to 0 \quad (4.24)$$

Inequalities (4.23) and (4.24) may be used to reduce the order of equation (4.21) giving

$$(\bar{\alpha} \csc^2 \theta + 3 \cot \theta) f_1' \simeq 2 \bar{\alpha} \csc^2 \theta \cot \theta + 2 (\csc^2 \theta + \cot \theta) \quad \theta \to 0$$

Solving for f_1' gives

$$f_1' \simeq \frac{2\,\bar{\alpha}\cot\theta + 2\,(1 + \cot^2\theta/\csc^2\theta)}{\bar{\alpha} + 3\cot\theta/\csc^2\theta}$$

since

$$\frac{\cot\theta}{\csc^2\theta} \to 0, \quad \frac{\cot^2\theta}{\csc^2\theta} \to 1$$

and

$$\int \cot\theta\, d\theta >> \frac{4}{\bar{\alpha}}\theta^{*} \text{ as } \theta \to 0$$

one gets

$$f_1 \simeq 2 \ln \sin\theta \tag{4.25}$$

Substituting for $f_1(\theta)$ in the solution for the root s_1, the following is obtained:

$$s_1(\theta) \simeq \bar{\alpha}\cot\theta$$

It may be verified that $f_1(\theta) << s_1(\theta)$ $\theta \to 0$. Further it may be seen that the effect of including $f_1(\theta)$ eliminates the less dominant term in the leading behavior $\ln \sin^2\theta$.

The addition of integration functions like $f_1(\theta)$ to the original root $s_1(\theta)$ can be continued indefinitely to yield better estimates of the exact solution to the differential equation (4.10). These functions

---

*The right hand side of this inequality goes to zero as $\theta \to 0$.

satisfy the criterion

$$f_1(\theta) >> f_2(\theta) >> f_3(\theta)... \quad , \theta \to 0$$

Instead of the above the solution is conveniently represented in the following form

$$c(\theta) \simeq c_1 \exp(\bar{\alpha} \cot \theta)\, \omega(\theta) \tag{4.26}$$

where

$$\omega(\theta) = 1 + \varepsilon(\theta) \tag{4.27}$$

and

$$\varepsilon(\theta) \to 0;\ \theta \to 0$$

c_1 is a constant determined by the boundary condition of the problem.

The function $\omega(\theta)$ in the solution (4.26) asymptotically behaves like a constant. The determination of $\omega(\theta)$ involves the substitution of $c(\theta)$ from the above into the original equation (4.10) so that, in effect, the leading behaviour in (4.26) is "peeled off". This results in a differential equation for ω which still exhibits the same irregular singularity as equation (4.10).

$$\omega'' \simeq \bar{\alpha} \csc^2 \theta \, \omega' - \omega' \cot \theta, \; \theta \to 0$$

Substitution for $\omega(\theta)$ from (4.27) into the above gives

$$\varepsilon'' \simeq (\bar{\alpha} \csc^2 \theta + \cot \theta)\varepsilon', \quad \theta \to 0 \tag{4.28}$$

This differential equation may be simplified by using one of three of the following approximations:

I $\quad \varepsilon'' >> \bar{\alpha} \csc^2 \theta \, \varepsilon', \quad \theta \to 0$

II $\quad \varepsilon'' \simeq (\bar{\alpha} \csc^2 \theta + \cot \theta)\varepsilon', \quad \theta \to 0$

III $\quad \varepsilon'' << (\bar{\alpha} \csc^2 \theta + \cot \theta)\varepsilon', \quad \theta \to 0$

Since it is anticipated that $\varepsilon(\theta)$ is decaying function as $\theta \to 0$ it is verified that only in equality III is valid*. Hence equation (4.28) simplifies to

$$(\bar{\alpha} \csc^2 \theta + \cot \theta)\varepsilon' \simeq 0, \; \theta \to 0 \tag{4.29}$$

In order to satisfy $\varepsilon(\theta) \to 0, \theta \to 0$, it is seen that $\varepsilon(\theta)$ is at least of the order of $1/\csc^3 \theta$. One way in which this may be expressed is

---

*Approximations I and II lead to an unbounded increase in $\varepsilon(\theta)$ as $\theta \to 0$.

$$\varepsilon' \simeq -\beta^2/\bar{\alpha}\ \csc^3\theta$$

$$\cot\theta << \csc^2\theta,\ \theta \to 0 \qquad (4.30)$$

where β^2 is a constant and the negative sign is chosen for convenience. Since $\sin\theta \to \theta$, $\theta \to 0$ the following substitution may be made,

$$\varepsilon' \simeq (-\beta^2/\bar{\alpha})\theta^3$$

or

$$\varepsilon \simeq -\frac{\beta^2}{4\bar{\alpha}}\theta^4,\ \theta \to 0 \qquad (4.30)$$

As would be expected for a decaying function ($\theta \to 0$), equation (4.30) suggests that $\varepsilon(\theta)$ is a series in θ beginning with the lowest power of four. To determine this series it is assumed that $\omega(\theta) \simeq \sum_{n=0}^{\infty} a_n \theta^{\mu+n}$.

Before substituting for $\omega(\theta)$ into the differential equation for ω it is necessary to modify equation (4.28) slightly in view of (4.30). The reconstructed equation for ε is

$$\varepsilon' \simeq \varepsilon'(\bar{\alpha}\csc^2\theta + \cot\theta) + \beta^2,\ \theta \to 0$$

Since $\omega = 1 + \varepsilon$, $\omega' = \varepsilon'$ and $\omega'' = \varepsilon''$, one gets

$$\omega'' - \omega'(\bar{\alpha}\csc^2\theta + \cot\theta) \simeq +\beta^2\omega,\ \theta \to 0 \qquad (4.31)$$

since $\beta^2\varepsilon \ll \beta^2$, $\theta \to 0(\varepsilon \to 0)$

Substituting the series expansion for $\omega(\theta)$ into the equation (4.31), one obtains

$$a_n \sum_{n=0}^{\infty} (\mu+n)(\mu+n-1)\theta^{n+\mu-2} - \bar{\alpha} a_n \sum_{n=0}^{\infty} (\mu+n)\theta^{n+\mu-3}$$

$$- \bar{\alpha} a_n \sum_{n=0}^{\infty} (\mu+n)\theta^{n+\mu-2} + \beta^2 a_n \sum_{n=0}^{\infty} \theta^{\mu+n} = 0$$

The indices are shifted to equalize the powers of θ and the resulting coefficients are matched to give

$$\mu = 0;\ a_1 = 0,\ a_2 = 0,\ a_3 = 0 \text{ and}$$

$$a_4 = \frac{-\beta^2}{4\bar{\alpha}} a_0^{*}$$

For the general case the following recursive relation is obtained

$$a_{k+4} = \frac{\{(k+4)(k+2) - \bar{\alpha}(k+3)\} a_{k+3} - \beta^2 a_k}{\bar{\alpha}(k+4)}$$

$$k = 0, 1, 2, \ldots.$$

---

*$a_0 = 1$, since the first term in the power series expansion for $\omega(\theta)$ is 1.

This yields a general expression for a_{k+4} and the resulting series for the $\omega(\theta)$ is:

$$\omega(\theta) \simeq 1 - \beta^2 \left[\sum_{k=0}^{3} \frac{\Gamma(k+2)}{(k+4)\bar{\alpha}^{k+1}} + \sum_{K=4}^{\infty} \frac{1}{(k+4)} \left\{\frac{\Gamma(k+2)}{\bar{\alpha}^{k+1}} - \frac{\beta^2 \Gamma(k-2)}{k\bar{\alpha}^{k-2}}\right] \theta^{k+4}\right.$$

If

$$\psi_k = 1/(k+4)\bar{\alpha}^{k+1} \quad \text{and} \quad \phi_k = \frac{1}{k+4}\left\{\frac{\Gamma(k+2)}{\bar{\alpha}^{k+1}} - \beta^2 \frac{\Gamma(k-2)}{\bar{\alpha}^{k-2}}\right\}$$

then

$$\omega(\theta) \simeq 1 - a_0\beta^2 \left[\sum_{k=0}^{3} \psi_k \Gamma(k+2) + \sum_{k=4}^{\infty} \phi_k\right] \theta^{k+4} \qquad (4.32)$$

$$\theta \to 0$$

Substituting this expression for $\omega(\theta)$ into equation (4.26) one obtains the full local behavior of this solution as follows, .

$$c(\theta) \simeq c_1 \exp(\bar{\alpha} \cot \theta) \left\{1 - a_0\beta^2 \left[\sum_{k=0}^{3} \psi_k \Gamma(k+2) + \sum_{k=4}^{\infty} \phi_k\right] \theta^{k+4}\right\}$$

$$\Theta \to 0 \qquad (4.33)$$

The expression (4.33) for c (θ) is the approximate solution corresponding to the root s_1 for the original differential equation (4.10). The complete solution would entail the inclusion of the leading behavior due to the second root s_2 of the quadratic equation (4.13). This root was earlier given as

$$s_2 \simeq \ln \sin \theta, \ \theta \to 0 \tag{4.20}$$

The leading behavior of the solution corresponding to this root is obtained in a similar fashion as the foregoing procedure. A better estimate of the leading behavior may be made by adding an integration function g_1 (θ) to the above so that

$$s_2 (\theta) = \ln \sin \theta + g_1 (\theta) \tag{4.34}$$

and

$$g_1 (\theta) << \ln \sin \theta, \ \theta \to 0 \tag{4.35}$$

Substituting (4.34) into the differential equation (4.13) for s' one gets

$$s_2' = \cot \theta + g_1'$$
$$s_2'' = -\csc^2 \theta + g_1'', \text{ and}$$

$$g_1'' + (g_1')^2 \simeq -(3 \cot \theta + \bar{\alpha} \csc^2 \theta) g_1' - 2 \cot^2 \theta + \csc^2 \theta$$

$$\theta \to 0 \tag{4.36}$$

Again, from criterion (4.35) the following approximations are valid

$$g_1' \ll \cot\theta$$
$$g_1'' \ll \csc^2\theta \text{ and}$$
$$(g_1')^2 \ll g_1' \cot\theta,\ \theta \to 0$$

Equation (4.36) for g_1 is reduced by this set of approximations to a first order differential equation.

$$g_1' \simeq \frac{\csc^2\theta - 2\cot^2\theta}{\bar{\alpha}\csc^2\theta + 3\cot\theta}$$

or

$$g_1' \simeq \frac{1 - 2\cot^2\theta/\csc^2\theta}{\bar{\alpha} + 3\cot\theta/\csc^2\theta},\ \theta \to 0 \qquad (4.37)$$

or

$$g_1'(\theta) \simeq -\frac{1}{\bar{\alpha}}^{*} \qquad (4.38)$$

hence

$$g_1(\theta) \simeq -\frac{\theta}{\bar{\alpha}} \qquad (4.39)$$

---

*The integration of (4.37) above may be performed slightly more rigorously as follows:

$$g_1' \simeq \frac{1 - 2\cos^2\theta}{\bar{\alpha} + 3\cos\theta\sin\theta}$$

(footnote continued)

or

$$g_1 \simeq -\frac{1}{\bar{\alpha}} \int \frac{\cos 2\theta \, d\theta}{1 + \frac{3}{2\bar{\alpha}} \sin 2\theta}$$

$$\simeq -\frac{1}{\bar{\alpha}} \{\ln (1 + \frac{3}{2\bar{\alpha}} \sin 2\theta)\} / \frac{3}{\bar{\alpha}}$$

$$\simeq -\frac{1}{3} \ln (1 + 3/2\, \bar{\alpha} \cdot \sin 2\theta)$$

$\theta \to 0$; $\bar{\alpha}$ (minimum) $\simeq 25$, from Chapter 5.

This is approximately equal to the simpler expression (4.39) as θ approaches the irregular singularity. Furthermore, it may be noted that this expression, like (4.39), also goes to zero as θ approaches zero.

It is seen that the inequality (4.35) holds in this case for $g_1(\theta)$. However it may be noted that $g_1(\theta)$ is not nonvanishing as θ approaches the irregular singularity. This is relevant in light of the statement made earlier with regard to the terms that can be included in the leading behaviour. The terms in the full local behavior of an asymptotic solution that vanish (as $\theta \to 0$, in this case) are lumped in a series such as $\omega(\theta)$ in equation (4.26). Let an analogous series for the present case be given by $\mu(\theta)$ so that the complete solution for the original differential equation (4.10) is given as a linear sum of the solutions for the two roots. Hence the concentration $c(\theta)$ is given by

$$c(\theta) \simeq c_1 \exp(\bar{\alpha} \cot \theta) \{1 - a_0 \beta^2 [\sum_{k=0}^{3} \psi_k \Gamma(k+2)\theta^{k+4} + \sum_{k=4}^{\infty} \phi_k \theta^{k+4}]\} + c_2 \sin\theta . \mu(\theta) \qquad (4.40)$$

where $\mu(\theta) = 1 + e(\theta)$ and $e(\theta) \to 0$, $\theta \to 0$, so that $\mu(\theta)$ asymptotically behaves like a constant. The constant c_2 in (4.40) corresponds to the second solution (the root s_2) and both c_1 and c_2 are determined from the boundary conditions. The boundary condition for the determination of the particular solution (to this problem) is presented in the next chapter.

Equation (4.40) is now a formally complete asymptotic approximation to the solution of the ion transport equation (4.10). It represents the alkali ion concentration profile (c as a function of θ) over the

particle when the migration occurs in the presence of an electric field $\vec{E}_s$ on the surface. This concentration profile is formally valid in the neighborhood of the irregular singularity ($\theta = 0$). A discussion of its validity outside of this neighborhood and of some of its important features is presented in Section 4.4 as well as in Chapter 5.

4.4 Discussion

The method of dominant balance approach used to arrive at the concentration profile over the particle surface yields a solution near the irregular singular point of the differential equation. The component of the leading behavior that varies most rapidly is called the controlling factor. The controlling factors for the two solutions in Section 4.3 (corresponding to the two roots s_1 and s_2) are $\exp(\bar{\alpha} \cot \theta)$ and $\sin \theta$ respectively. The several approximations made in this section are subsequently verified in each case so that the solution is consistent with the assumptions. Furthermore, once the controlling factor is determined all subsequent additions to the roots have progressively decreasing magnitudes near the point of singularity.

The key term in the solution for the concentration $c(\theta)$, equation (4.40), is the controlling factor corresponding to the first root (s_1), $\exp(\bar{\alpha} \cot \theta)$. Hence the solution function, then, exhibits an essential singularity* at $\theta = 0$. The degree of variation also depends upon the

---

*A function $f(\theta)$ has an essential singularity at $\theta = a$, say, if $\theta = a$ is an isolated singular point and if the first derivative does not exist (at $\theta = a$), and there is no integer n for which $\frac{d}{d\theta}[(\theta - a)^n f(\theta)]$ exists at $\theta = a$.

magnitude of the (parameter) constant $\bar{\alpha}^{*}$ into which is lumped the average layer field strength $\vec{E}_a$, particle size(s), diffusion coefficient D, the electric mobility μ, and the constriction ratio a/s**. As will be seen later this dimensionless parameter $\bar{\alpha}$ has an important bearing upon the extent of ion migration and ultimately upon the electrical response of a (sodium ion) chemically conditioned fly ash to an external voltage gradient in terms of its bulk surface resistivity.

A comparison of the solutions in expression (4.40), for the two roots s_1 and s_2, indicates that

$$e^{s_1}\,\omega(\theta) \;>>\; e^{s_2}\,\mu(\theta), \quad \theta \to 0 \tag{4.41}$$

Additionally, it is evident that as θ decreases, exp $s_1\{.\,\omega(\theta)\}$ increases while exp $s_2\{.\,\mu(\theta)\}$ decreases. In view of this fact the boundary condition at the bottom end of the lower particle (Figure 4.1) corresponds almost completely to the solution due to the first root (s_1). In this respect this boundary condition appropriately applies at a region for which the differential equation (4.10) has been solved. Thus the constant c_1 of equation (4.40), evaluated at this boundary† is at least as accurate as the approximate solution itself. The second constant c_2 is determined if information concerning the concentration at any other

---

*A discussion of the dependence of the concentration $c(\theta)$ upon the (experimental) parameter $\bar{\alpha}$ is postponed until Chapter 5.

**See Chapter 3, equation (3.76).

†This boundary condition refers to the 'initial' concentration of sodium ions in the capillary condensate (between θ_0 and θ_c). See Section 4.1.

point of the particle is known*. This, of course, entails the inherent approximation involved in evaluating a (solution) constant from a boundary condition which extends beyond the neighborhood of the essential singularity of the differential equation (4.10).

One of the important features of the solution obtained by the dominant balance approach is that it is an asymptotic approximation. In contrast to a local series about an ordinary or a regular singular point, the behavior of a solution near an irregular singular point "may be relatively, but not approximately, equal to the exact solution" (B7). The reason for this is that the absolute value of the slope approaches a maximum as $\theta \to 0$; hence the concentration changes very rapidly in this region. However, most importantly, the controlling factor in the leading behavior of this solution is the same as that of the exact solution. This is true when the equation obtained after 'peeling off' the dominant balance solution has a solution that does not vary as rapidly as the dominant balance solution. The significance of this lies in the fact that the rate of change of concentration is largely determined by the controlling factor and that this rate of change determines how "good" the asymptotic approximation is.

Referring to the original equation (4.10) for the surface ion

---

*Alternatively, as evidenced by the experimental results of Chapter 5 the following criterion may be used, with some loss of accuracy, to evaluate c_2:

$$\int_{\theta_0}^{\pi-2\theta_0} c(\theta)\, dA(\theta) \simeq W,$$

where $dA(\theta)$ is the differential (spherical) surface area, and W is the total amount of ions participating in the diffusion process.

concentration it is seen that $\theta = \pi$ is also an irregular singular point. Since the independent variable θ occurs in the differential equation as trigonometric (periodic) functions, the solution behavior (not the magnitude) is similar to the above ($\theta \to 0$) near the end of second quadrant ($\theta \to \pi$)*. The behavior of $\cot^2 \theta$ and $\csc^2 \theta$ are identical to each other at

$$0 < \theta \leq \theta + \varepsilon$$

$$\pi - \varepsilon \leq \theta < \pi, \quad \varepsilon \to 0$$

As a result the binomial expansion in equation (4.16) is valid and the (order reduction) approximation:

$$s'' << (s')^2 \tag{4.12}$$

is also justified near the irregular singularity $\theta = \pi$. Hence a first estimate of the two roots is the same as in the case $\theta \to 0$.

$$s_1 \simeq \bar{\alpha} \cot \theta + \ln \csc^2 \tag{4.19}$$

$$s_2 \simeq \ln \sin \theta \tag{4.20}$$

The estimate integration $f_1(\theta)$ also satisfies the same criterion:

$$f_1(\theta) << \bar{\alpha} \cot \theta, \quad \theta \to 0$$

*This refers to the top end of the lower particle in Figure 4.1.

so that the dominant balance solution corresponding to the first root is the same as given earlier. The asymptotic series approximation, however, is different in this case since $\sin\theta, \tan\theta \to \theta$, $\theta \to \pi$ [equation (4.30)]. Upon examing the coefficients of equation (4.10) the following observation may be made with regard to the series in the leading behaviour

$$\sin^2\theta \ \{\theta \to 0\} \to \theta \ = \ \sin^3\theta \to \pi - \theta \ \{\theta \to \pi\}$$

and

$$\tan\theta \ \{\theta \to 0\} \to \theta \ = \ -\tan\theta \to \pi - \theta \ \{\theta \to \pi\}$$

This series also (asymptotically) goes to a constant as before. A replacement of this series (not evaluated) by just the one term for $\varepsilon(\theta)$, given by the coefficient a_4, yields a similar formal solution corresponding to the root s_1:

$$c(\theta)\ \{s_1\} \ \simeq \ c_1 \exp(\bar{\alpha}\cot\theta)\ \{1 - \frac{\beta^2}{4\bar{\alpha}}(\pi-\theta)\} \qquad (4.42)$$

By a similar procedure it is determined that the leading behavior due to the second root ($\theta \to \pi$) is the same as derived earlier. Once again the asymptotic series $\mu_\pi(\pi-\theta)$ for this case is given about the term $(\pi - \theta)$. Hence a formally complete solution for this case would be given by

$$c(\theta) \ \simeq \ c_1 \exp(\bar{\alpha}\cot\theta)\ \{1 - \frac{\beta^2}{4\bar{\alpha}}(\pi-\theta)\} \ + \ c_2 \sin\theta\ \mu_\pi(\pi-\theta) \qquad (4.43)$$
$$\theta \to \pi$$

Hence the general solution to the differential equation (4.10) is valid near the region of both irregular singularities of the particle. Beyond $\theta = \pi/2$ it is seen from both equations (4.33) and (4.43) that the second solution grows (relative to the first one) in magnitude, and depending upon the value of $\bar{\alpha}$ it may be dominating. This feature is discussed in Chapter 5.

In conclusion, it may be observed that the validity of the general solution near the two ends of the particle enables the determination of an approximate concentration profile. It is expected that the deviation from the exact solution will increase as the MDB* solution is extended beyond the regions $\theta \to 0, \pi$, toward the center of the particle. However, as seen in the next chapter, this does not detract from the objective of estimation of the parameters of the migration process.

*Method of dominant balance.

CHAPTER 5

INTERPRETATION OF THE RESULTS OF THE ION MIGRATION EXPERIMENTS

Overview

The phenomenon of capillary condensation within the macropores of an ash layer and the effects of an externally applied electric field have been discussed in Chapters 2 and 3 respectively. In Chapter 4 these two factors are incorporated into a mathematical model which is developed in order to explain the observations made in connection with the alkali ion migration experiments. This chapter begins with a description of the (laboratory) apparatus and the procedure used with regard to these experiments (Section 5.1). One of the objectives of the experiments was to determine the extent of the migration of sodium ions into a (particulate) fly ash bed. The ash layer itself is supported on the plane of the resistivity probe which was modified for this purpose. The experimental arrangement and the equipment used are illustrated by the figures in this section.

The material of Chapters 2 and 3 is used to determine the experimental parameters associated with the fly ash bed. This is presented in Section 5.2 where the effects of capillary condensation and the applied electric field are quantitatively evaluated. The results of this evaluation are essentially presented in Tables 5.4, 5.7 and 5.8. The importance of the current-time data (for the laboratory experiments) is indicated and these data are presented as plots in Figures 5.6,

5.7, 5.8, and tabulated in Appendix K as well.

The physical significance of the experimental parameters and the assumptions involved in their evaluation are also stated in Section 5.2. These assumptions need to be consistent with those made earlier and have a bearing upon the interpretation of the ion concentration profiles obtained from the laboratory experiments.

The experimental concentration profiles are presented in Section 5.3 and the "extent" of migration is discussed in terms of the penetration thickness, δ_{2p}. The effect of the capillary ring angle is also discussed in terms of $\delta_2 p$. In Section 5.4, the nature of the experimental plots is discussed in light of the solution (4.40) to the mathematical model. The Nernst-Einstein equation is introduced at this stage. It is seen that the values of the migration parameter $\bar{\alpha}$ predicted by this equation are far too high. This analysis is done in view of the controversy surrounding the mechanism of ionic migration. Following this the more realistic values of $\bar{\alpha}_{max}$ are evaluated and its relationship with the capillary ring angle is underscored.

Finally, the implications of this result are discussed in a broader sense in Section 5.5. The appropriateness of the particular theoretical model of Chapter 4 is viewed in light of the physical phenomena associated with this problem.

5.1 The Experimental Unit and Procedure

The experimental arrangement used to study the ion migration problem consists of the resistivity probe with a (high voltage) corona point at a fixed distance from the plane. The plane is grounded through a micro-ammeter. The probe was used in connection with fly ash resistivity measurements described in Chapter 1 and is shown in Figures A.2 and A.3 (Appendix A).

For the purposes of the present experiments the resistivity probe was modified to accomodate a stable layer of fly ash over the plane. This was accomplished by inserting a teflon cylinder with the same inside diameter as the plane. One end of this teflon cylinder has a protruding lip which fits snugly in the gap between the guard ring and the collecting plane.* Figure 5.1 shows this modification of the probe along with a schematic of the entire experimental set up. Metered air (through a rotameter) is bubbled through water impingers in a temperature controlled water bath. This moist air is then led via an insulated tube through a flask in order to prevent any condensate carry over to the heating chamber of the probe. This section of the probe (Figure 5.2) is enclosed by a protective casing and is maintained isothermal by means of a heating tape wrapped around the casing. Variations in temperature in the probe chamber and the (electrically) heated water bath, which occur due to line voltage fluctuations, are minimized by the use of voltage stabilizers.

A 20 Kv DC power supply is used with the probe to obtain the required corona voltage. The leakage current across the ash bed is monitored by

---

*See also Figure A.1.

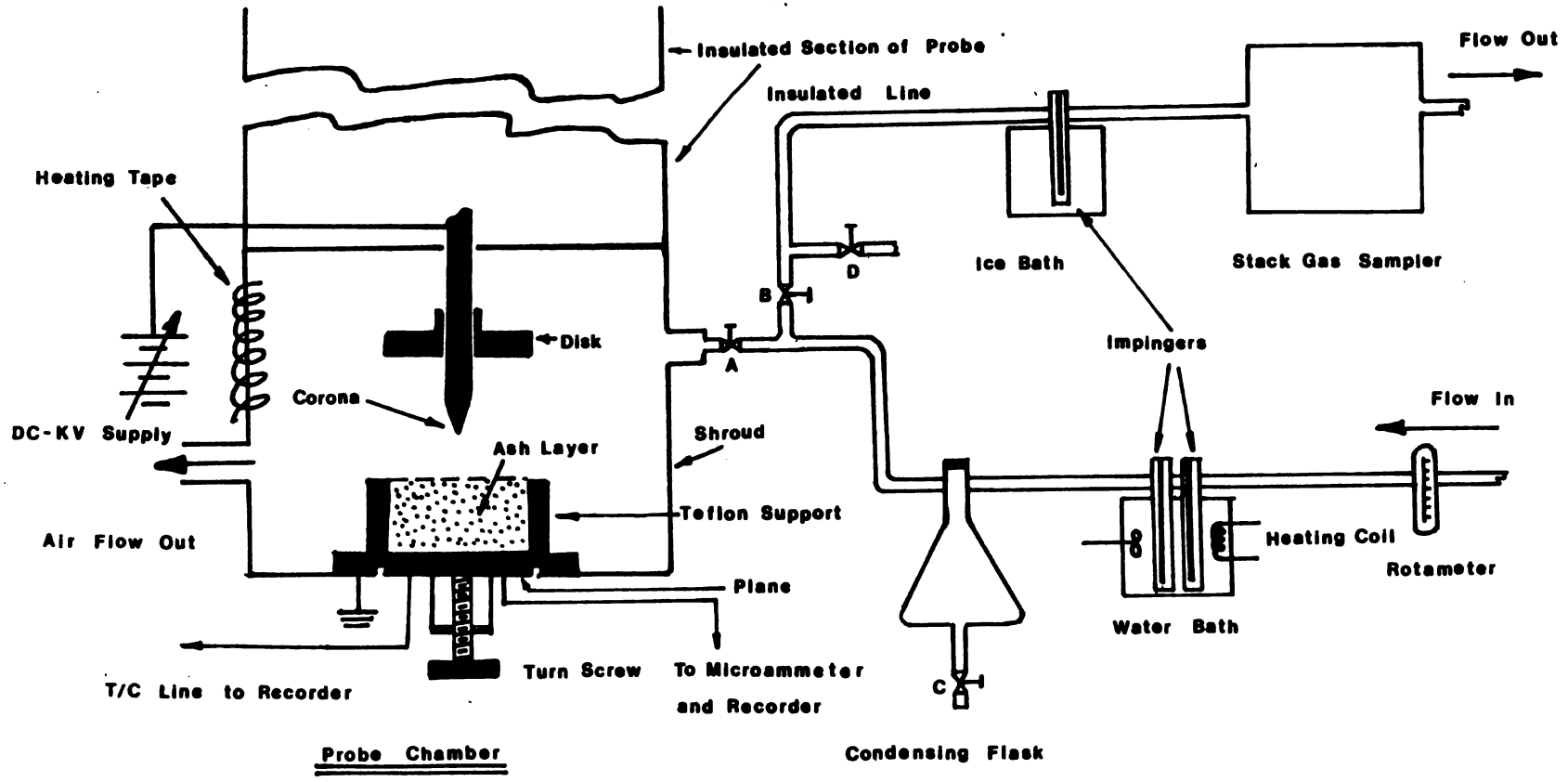

Figure 5.1. Schematic illustration of experimental apparatus.

Figure 5.2. Modified point-plane configuration in the probe chamber.

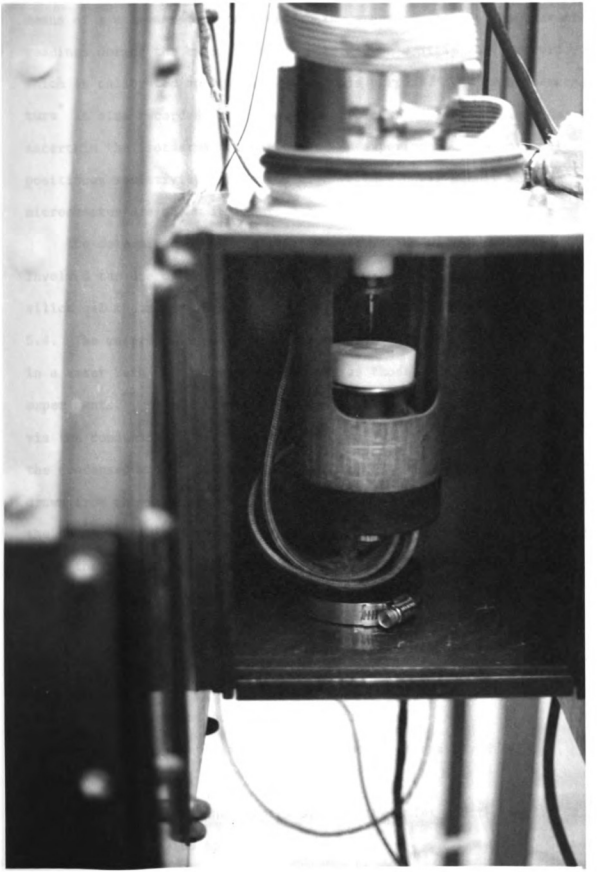

means of a microammeter connected to the grounded plane. The current readings during the experiment are recorded on a strip chart recorder which is calibrated appropriately for this purpose. The probe temperature* is also recorded on a separate strip chart (recorder) in order to ascertain the isothermal conditions of an experiment. The vertically positioned resistivity probe, the high voltage power supply and the microammeter are shown in Figure 5.3.

The determination of the relative saturation of the moist air involved the use of a standard stack gas sampler (Appendix I) and silica gel impingers in an ice bath. The sampler is shown in Figure 5.4. The metered air is bubbled through glass (water filled) impingers in a water bath at the same temperatures as those in the ion migration experiments.** The moist air is then led through an insulated tube, via the condensing flask, to the (ice bath) silica gel impinger where the condensed water adds to the weight of the impinger. The dry air is drawn from the impinger outlet to the stack gas sampler which measures the total volume and temperature of the air sampled through the impinger.† Since the air line is under vacuum all of the joints and connections are checked for leaks before each experiment.

In order to be able to analyse the fly ash for sodium it is necessary to separate the ash bed into thin layers. This is accomplished

---

*Which is the same as that of the fly ash bed.

**These (humidity) experiments were conducted separately from the migration experiments.

†This equipment gives the temperatures at the inlet and the outlet of the sampler (see also Appendix I).

Figure 5.3. High voltage power supply and microammeter.

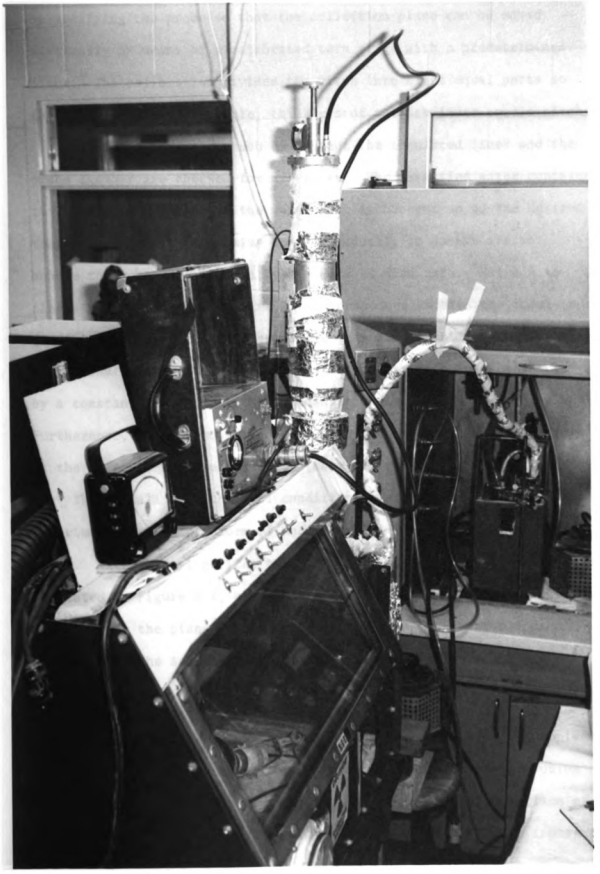

by modifying the probe so that the collection plane can be moved vertically by means of a calibrated turn screw with a predetermined pitch. The calibration divides the pitch into eight equal parts so that the minimum (measurable) thickness of the ash layer equals pitch/8.*

At the beginning of each experiment the insulated lines and the probe chamber are checked for air leaks. The distilled water contained in the glass impingers in the water bath is brought up to the desired temperature and the air valve opened gradually to permit air to bubble through the impingers at a specified flow rate. Valve A is closed and D open at this time. This procedure enables the insulated (air) line to the probe chamber to be thermally stabilized before the corona voltage is turned on. This stabilization is ascertained by a constant rate of moisture condensation in the condensing flask. Furthermore, this is confirmed by a constant air temperature reading at the inlet to the probe chamber (near valve A).

The (alkali ion) chemical conditioning agent selected for these experiments was in the form of sodium hydroxide solution (1.824 g/lit NaOH). With the cylindrical teflon support removed** from the position indicated in Figure 5.1, a measured amount of NaOH solution is carefully deposited on the plane with a pipette. The handling of the sodium hydroxide in the solution form, at this stage, enables a uniform

---

*Equal to 0.009922 cm.

**The support is inserted in place only after the solution is completely evaporated from the plane in order to ensure that there is no sodium hydroxide on its inside surface. As is evident from the direction of sodium ion diffusion (toward the negative corona), this is an important precaution. (See also Section 5.3, Chapter 5).

deposition upon the plane. This is subsequently evaporated under an infra-red lamp.

The cylindrical support is inserted in place and the plane is raised (with the turn screw) so that it is flush with the top surface of the support. The plane is now lowered to a predetermined position and the corresponding number of turns of the screw noted. This gives the thickness of the fly ash layer. The ash is carefully placed into the hollow space thus formed, and the upper surface aligned with the top edge of the support (Figure 5.1).

The probe chamber is now closed and valve A opened to let the humidified air into the chamber*. The probe heater is turned on and a sufficient** amount of time is allowed for the ash bed to equilibrate with the (humid) ambient environment. The bed temperature is monitored on the temperature recorder.

The current (strip chart) recorder and the DC power supply are now turned on simultaneously, and the latter adjusted to give the predetermined corona voltage. This gives the initial leakage currents through the ash layer (for a given applied voltage).

The experimental unit is left on for the duration of the experiment (90 - 120 hours) and the system variables (temperatures, air flow rate, voltage) periodically checked to assure constant

---

*The line leading to the ice bath and sampler is isolated at this time.

**For the present set of ion migration experiments the system above was left on for about 4 hours in each case before the corona voltage was applied. (See also Section 5.4).

conditions. The condensate in the flask is also drained periodically to prevent any moisture carry over to the probe chamber.

After the experiment time has elapsed, the system is turned off and the probe allowed to cool. The probe chamber is opened by removing the shroud. The ash bed is now separated into layers of a predetermined thickness by rotating the turn screw so that the plane moves upward by a given number of divisions.* The (amounts of) ash corresponding to these layers are then carefully removed from the top and collected in weighed plastic vials. These vials are irradiated in a nuclear reactor** and the resulting ash samples analyzed for the sodium ion concentration. This is determined by the standard neutron activation analysis procedure by obtaining the gamma ray peak areas for the Na^{24} isotope.***

Finally, after the completion of an ion migration experiment the (water bath) temperature and air flow conditions are reproduced in order to determine the humidity. Valves A and D are closed and the air is led through the (ice bath) silica-gel impinger before it enters the stack gas sampler (for volume measurement). As described in Appendix I the moisture content is obtained simply from the increase in the weight of the impinger and the volume of air sampled. The moisture content

---

*As stated earlier these (eight) divisions are etched on the bottom of the screw head.

**Michigan State University Triga reactor. The ash samples were irradiated at a flux of 10^{12} neutrons/sq cm/sec for about 15 minutes.

***The equipment used for this analysis consists of a standard Ge-Li detector (15% relative efficiency) coupled with a signal amplifier and interfaced with a computer based multichannel analyzer (CANBERRA SERIES -80).

Figure 5.4. Standard stack (flue) gas sampler.

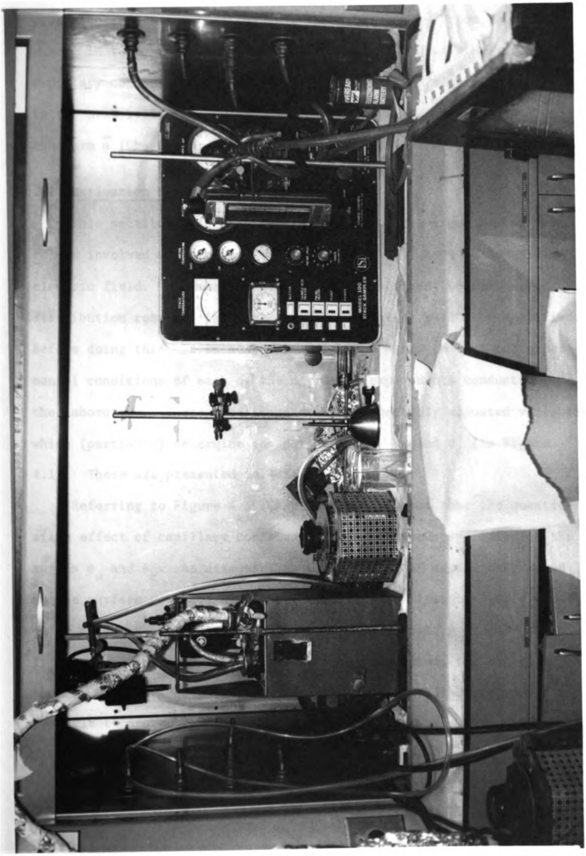

EVEREADY
STACK TEMPERATURE
METER TEMPERATURE
MODEL 100
STACK SAMPLER

gives the relative saturation (α) of the air in the probe chamber which, in turn, is used to estimate the radius of curvature of the capillary condensate by the method of Chapter 2. This is presented in the next section where also the other model parameters lumped in the term $\bar{\alpha}$ (Chapter 4) are calculated.

5.2 Estimation of Model Parameters

This section deals with the estimation of the experimental parameters involved with the ion transport in the presence of an applied electric field. A numerical evaluation of the (ion) concentration distribution requires that the term $\bar{\alpha}$ in equation (4.10) be specified. Before doing this, it is appropriate at this stage to list the experimental conditions of each of the migration experiments conducted in the laboratory. These conditions are the externally adjusted variables which (partially) determine the parameters $\bar{\alpha}$, θ_c and θ_o (in Figure 4.1). These are presented in Table 5.1.

Referring to Figure 4.1 (Chapter 4) it is seen that the quantitative effect of capillary condensation is completely specified by the angles θ_o and θ_c. As discussed in Chapter 2 these angles correspond to the surface coverage of a particulate sphere* (Figure 2.9). The value of θ_c is given directly by the calculated radius of curvature. It is seen from Figure 4.1 that this value determines the length of the "dry" resistance path on the spherical surface from one end of the particle to another.† Without making any presumptions regarding the

*θ_o and θ_c are the same as ϕ and ψ respectively (Figure 2.9).

Table 5.1. Laboratory (experimental) conditions for the ionic migration experiments.

Experiment No.	Corona Voltage (Kv)	Probe Temperature (^{o} F)	Bath Temperature (^{o} F)	Air Flow Rate† (cu. in/min)	Duration (Hrs)*
1	9.40	296.00	116.00	100	134
2	10.00	346.44	147.50	142	96
3	9.50	310.00	156.35	140	103
4	9.00	315.00	160.00	139	121
5	9.50	314.00	175.00	137	121
6	9.00	211.00	142.50	143	95
7	9.00	260.00	165.00	135	121
8	7.50	150.00	132.00	127	96
9	8.00	150.00	110.00	129	103

*Approximate time in hours for an experimental run.

†Nominal air flow rate.

variation of the surface electric field strength (with θ), it is seen that θ_c is a significant parameter in the determination of the concentration distribution.

The evaluation of θ_o (and θ_c) is relatively straight forward once the radius of curvature of the capillary condensate and the particle size are known [equations (2.77) and (2.79)]. To determine the radius of curvature $\bar{R}$ one needs to know the moisture content of the air (B_{wo}). The procedure and formulas involved with this computation is presented in Appendix I.**

The moisture content is determined from the humidity experiments by the foregoing procedure. The results of the calculations are presented in Table 5.2. The values of the relative saturation α are also shown in this table. This is obtained directly as,

$$\alpha = \frac{B_{wo}}{(100)P_{sat}}$$

---

† It was mentioned earlier (Chapter 2) that the effect of surface (multilayer) adsorption is not considered in this model. Hence the region of the particle surface subtended by the angle $\pi - 2\theta_c$ is "dry" relative to the ring of capillary condensate.

** The method used to evaluate the (air) moisture content is part of a standard procedure for conducting a stack gas analysis (B9). This method conveniently applies where a stack gas sampler is used (as in this case, Appendix I).

Table 5.2. Values of the volumetric moisture content (of air) and relative saturation (α) for the laboratory experiments.

Expermiment* No.	Probe Temp. (^{o}F)	Bath Temp. (^{o}F)	Relative Saturation α	P_g^{o}†† (atm)	B_{wo} (%)
8**	150.00	132.00	0.1774	0.2530	4.489
9**	150.00	110.00	0.1630	0.2530	4.123
6	211.00	142.50	0.0522	0.9808	5.119
7	260.00	165.00	0.0473	2.4107	11.387
1†	296.00	116.00	0.0184	4.2930	7.901
3	310.00	156.35	0.0121	5.2870	6.409
4	315.00	160.00	0.0143	5.6821	8.140
5	314.00	175.00	0.0317	5.6010	17.735
2	346.44	146.00	0.0070	9.0380	6.349

*Experiment numbers are arranged in order of increasing probe temperatures.

**These values extrapolated from Figure 5.5.

†The air flow rate in this case was lower than in the other experiment (100 cu.in/min).

††$P_g^{o} = P_{sat}$

where B_{wo} is volume percent moisture in the air and P_{sat} is the saturation vapor pressure corresponding to the ash bed temperature (equal to the probe temperature). The total pressure inside the probe chamber is assumed to be equal to 1 atmosphere. The variation of the moisture content with water bath temperature is shown in Figure 5.5. The moisture content $\overline{B}_{wo}$ in this particular case is equal to the volumetric ratio of water vapor to dry air (expressed as %). The plot itself is specific to the actual configuration of the experimental set up*, however the nature of the variation is as expected, i.e., the value of $\overline{B}_{wo}$ (or $B_{w\theta}$) declines with water bath temperature. The relatively steep increase of B_{wo} at the higher temperatures is reflected by the fact that P_{sat} also rises with temperature at an increasing rate.

The values of the relative saturation α shown in Table 5.2 are now substituted into the modified Kelvin equation (2.67) in Chapter 2.

$$\sigma_{lg} K = \rho_l^{o} [\Delta\mu_g^{id} - \Delta\mu_g^{c}] - \Delta p_g \qquad (2.67)$$

All of the other terms are known (at a single temperature), hence the curvature K can be calculated by means of this equation. The mean radius of curvature of the capillary condensate is given by $\overline{R}$, where**

---

*In other words, the actual $\overline{B}_{wo}$ values (in Figure 5.5) depend upon the rates of condensation within the insulated lines and in the condensing flask, and upon the degree of saturation at the outlet of the impinger(s) in the water bath as well (see Figure 5.1).

**See Section 2.12, Chapter 2.

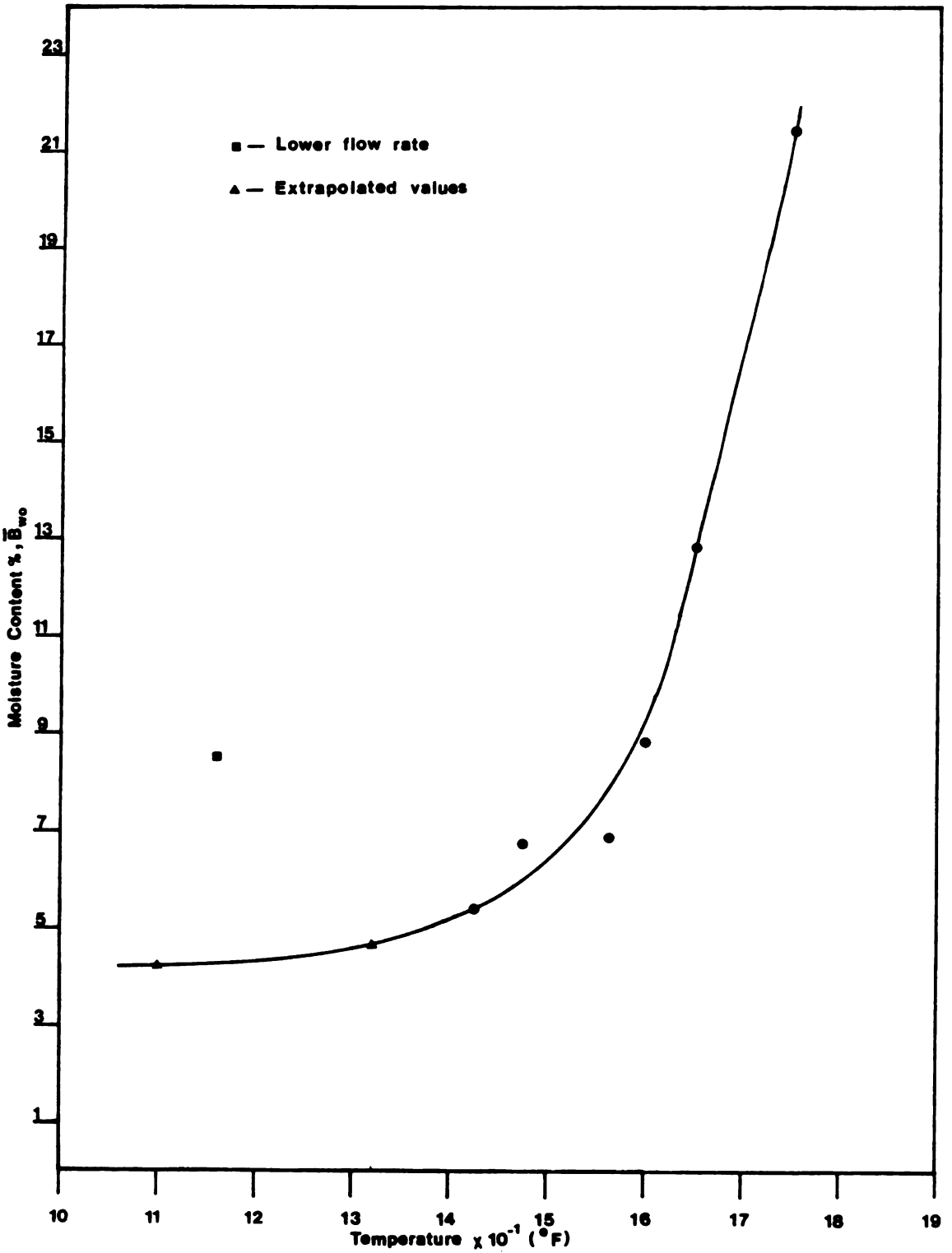

Figure 5.5. Variation of $\bar{B}_{wo}$ (vol. H_2O vapor/vol. dry air) with water bath temperature.

$$\overline{R} = \frac{2}{K}$$

The numerical values of each of the individual terms in equation (2.67) are presented in Table 5.3. The last column of this table shows the values of $\overline{R}$ for each of the experimental temperatures.

It may be observed from the table that the underscored values of $\overline{R}$ (cases 2, 3, 4) are lower than that corresponding to the assumed molecular size* of 2.725A^{o} ($\overline{R}$ = 1.363A^{o}). This is a simple dimensional restriction which implies that the pore size is not large enough to accomodate a water molecule. This assertion is made purely on the basis of the results generated in Table 5.3 and must be viewed in light of the uncertainty associated with the use of an equation such as (2.67) in such cases. The applicability of this equation (and the Kelvin equation as well) in the region of "dimensional restriction" has been discussed in detail in Section 2.14 (Chapter 2) and in Appendices C, D and E.

As mentioned earlier in this section the angles θ_c and θ_o can be calculated once the radius of curvature $\overline{R}$ is known. For the perfect** geometry of Figure 2.9 the following relationships hold,

$$\theta_c = \theta_{cc} = \text{arc cos } (S/\overline{R} + S)^{\dagger} \qquad (2.77)$$

---

*See Section 2.14, Chapter 2.

**This means that the spheres are perfect and meet each other at a single point of contact.

†The particle radius S is equal to R_1 in Chapter 2.

Table 5.3. Thermodynamic variables and the radius of curvature at the experimental temperatures.

Expermiment No.	ρ_1^{o*} (g mole/cc)	α (P_g/p_g^o)	T (^oC)	P_g^o (atm)	$\sigma_{lg}^{\dagger}$ (dynes/cm)	$\Delta\mu_g^{id}$ (cc-atm/g mole)	$\Delta\mu_g^{c**}$ (cc-atm/g mole)	Δp_g (atm)	$\bar{R}$ (A^o)
1	0.05109	0.0184	146.67	4.2930	49.18	1.376×10^5	1.601×10^3	4.214	1.398
2	0.04956	0.0070	174.69	9.0380	42.59	1.823×10^5	2.849×10^3	8.975	0.946
3	0.05068	0.0121	154.44	5.2870	47.39	1.549×10^5	1.901×10^3	5.223	1.207
4	0.05054	0.0143	157.22	5.6821	46.73	1.500×10^5	1.989×10^3	5.601	1.234
5	0.05058	0.0317	156.67	5.6010	47.00	1.217×10^5	1.939×10^3	5.423	1.533
6	0.05324	0.0522	99.44	0.9808	59.10	9.028×10^4	4.722×10^2	0.9296	2.440
7	0.05204	0.0473	126.67	2.4107	53.52	1.001×10^5	9.865×10^2	2.297	2.048
8	0.05435	0.1774	65.56	0.2530	65.20	4.807×10^4	1.304×10^2	0.2081	4.939
9	0.05435	0.1630	65.56	0.2530	65.20	5.042×10^4	1.327×10^2	0.2118	4.709

*Values of ρ_1^o are obtained from Figure 2.7.

†The variation of σ_{lg} with temperature is indicated in Table 2.7 (Chapter 2).

**The second virial coefficient B (required to calculate $\Delta\mu_g^c$) is obtained from Figure 2.6.

and

$$\theta_o = \theta_{co} = \text{arc cos } (S-1.363)/S \qquad (2.79)$$

where θ_{cc} and θ_{co} are the angles due to the capillary condensate ring. For the more realistic case where the interparticle contact is not at a point* the ring may be visualized to be "pushed" further out of the macropore so that in general $\theta_c > \theta_{cc}$ and $\theta_o > \theta_{co}$. θ_{cc} is referred to as the capillary ring angle in order to distinguish it from θ_c.

The values of θ_{cc} obtained from the foregoing equations are shown in Table 5.4 for all of the nine different experiments. As remarked earlier the thermodynamic equation (2.67) predicts no capillary ring for the cases 2, 3, and 4. Hence, for these cases, one would expect that the surface (ionic) migration is not assisted by capillary condensate formation i.e., the entire path of migration is "dry".**

The angle θ_{co} of the capillary ring corresponds to the lower limit imposed by the dimensional (molecular size) restriction. Since this depends only upon the particule radius S (equal to 9.575 $x10^{-4}$ cm]+

---

*It was stated in Chapter 3 that the actual contact is specified by an area (of contact). In the simplest case this is assumed to be a circle of radius a.

**The effect of surface (micropore) adsorption is not considered.

+The bulk properties of the fly ash used in the laboratory experiments (BET specific surface area, size analysis, etc) were determined separately. These are presented in Appendix J.

Table 5.4. Estimation of the capillary ring angle from equation (2.77).

Experiment No.	T (^{o}C)	α (P_g/P_g^{o})	$\bar{R}$ (A^{o})	θ_{cc} (degrees)
1	146.67	0.0184	1.398	0.310
2	174.69	0.0070	0.946	--
3	154.44	0.0121	1.207	--
4	157.22	0.0143	1.234	--
5	156.67	0.0317	1.533	0.324
6	98.89	0.0522	2.440	0.409
7	126.67	0.0473	2.048	0.375
8	65.56	0.1774	4.939	0.582
9	65.56	0.1630	4.709	0.568

the value of θ_{co} is constant and equal to 0.306^{o} [from equation (2.79)].

Thus, as mentioned earlier, the results of Table 5.4 (θ_{cc} and $\bar{R}$ in particular) completely specify the extent of the capillary ring for a given particle geometry. The next step is to evaluate the average electric field strength $\vec{E}_a$ for the ash layer. It may be recalled from Chapter 4 that this term is contained in the exponential parameter $\bar{\alpha}^*$ in the solution equation (4.33) where

$$\bar{\alpha} = \mu S E_a / D \cdot \ln K \qquad (5.1)$$

where

μ = electric mobility, m^2/V-hr.

S = particle radius, m.

E_a = average electric field strength within the fly ash layer, V/m

D = diffusivity, m^2/hr.

K = dimensionless constriction ratio equal to a/2S (Section 3.4, Chapter 3) where

a = radius of the circular contact between two spherical particles.

It should be noted here that the term E_a denotes both a time average as well as a distance average** electric field strength. A consideration of a time average value of E_a is necessitated by the nature of the current-

---

*Henceforth $\bar{\alpha}$ is also referred to as the migration parameter.

**This implies that E_a is a representative value of the field strength along the length of ash bed in the direction of the applied voltage gradient (See Figure 5.1).

time data for the ion migration experiments*. It is seen that after an initial rapid decline the leakage current through the ash bed relaxes to a steady value. A similar observation has been made by McLean (M2).**

The variations of current during the length of an experiment is indicated by vertical bars in the plots of Figures 5.6, 5.7 and 5.8. The current value at which the voltage drop ΔV is assumed (Experiment No. 1, Figure 5.6) is obtained as a time weighted average from the current-time data of Appendix K. This average current as well as its maximum and minimum values (after an initial period of decrease) are shown in Table 5.5.

The initial period (of stabilization) referred to earlier is obtained from the current-time data in Table K.1 (Appendix K). This period designates the time (after switching on the power supply) required for the leakage current to fall to its lowest value. The minimum value is determined by the criterion that at least one current measurement, after this time period, is equal to or higher than this value†. The stabilizing period ranges from about 5 minutes for

*The current-time data for the ion migration experiments are presented in Appendix K.

**That the current drops from an initial high value immediately after switching on the power supply.

†This criterion, however, is partly subject to the error that the current measurement may be made during a (current) fluctuation due to the equipment. This minimum current is not the same as I_{min} (Table 5.5) in every case.

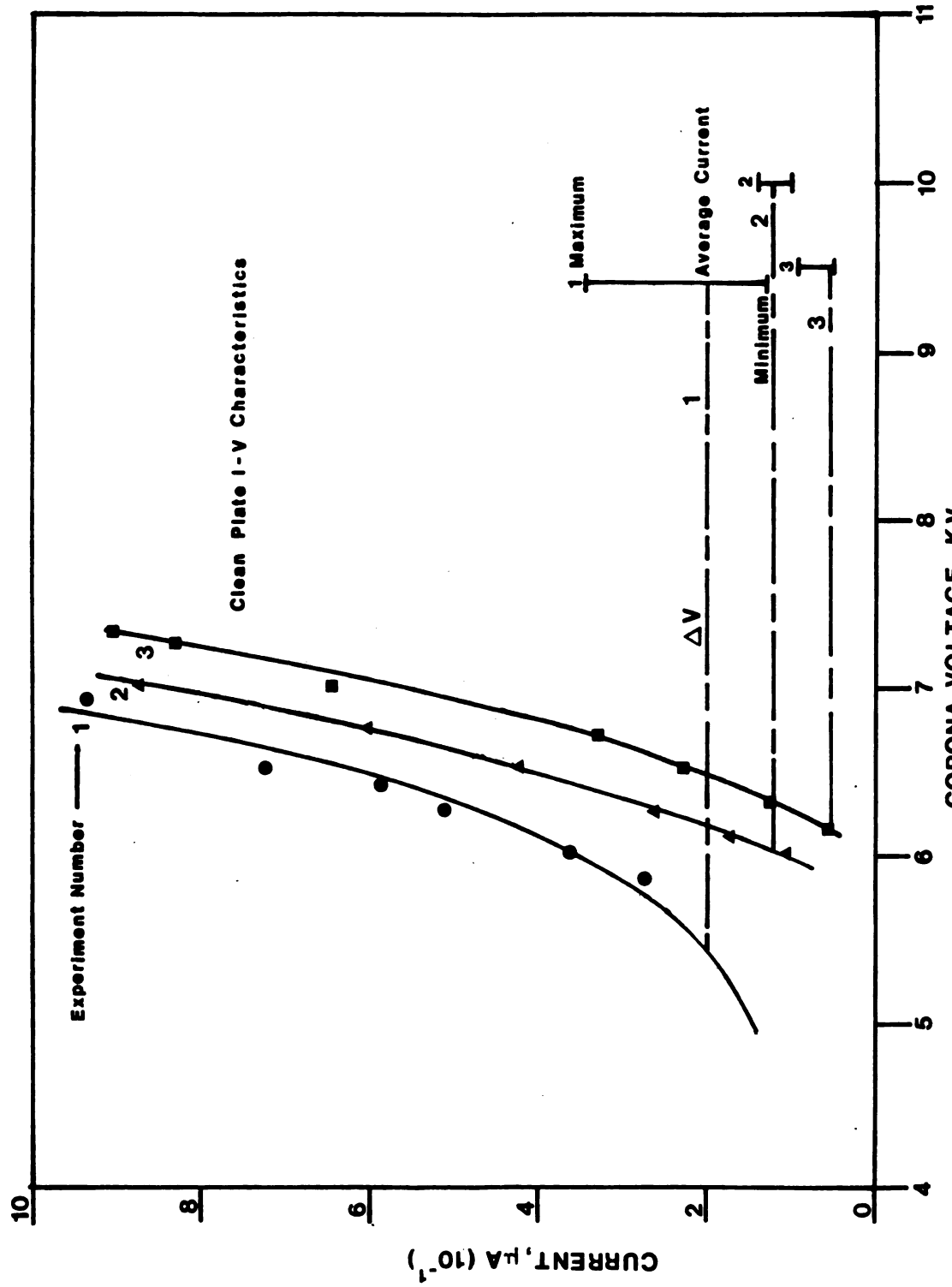

Figure 5.6. Time average voltage drops across the particulate bed.

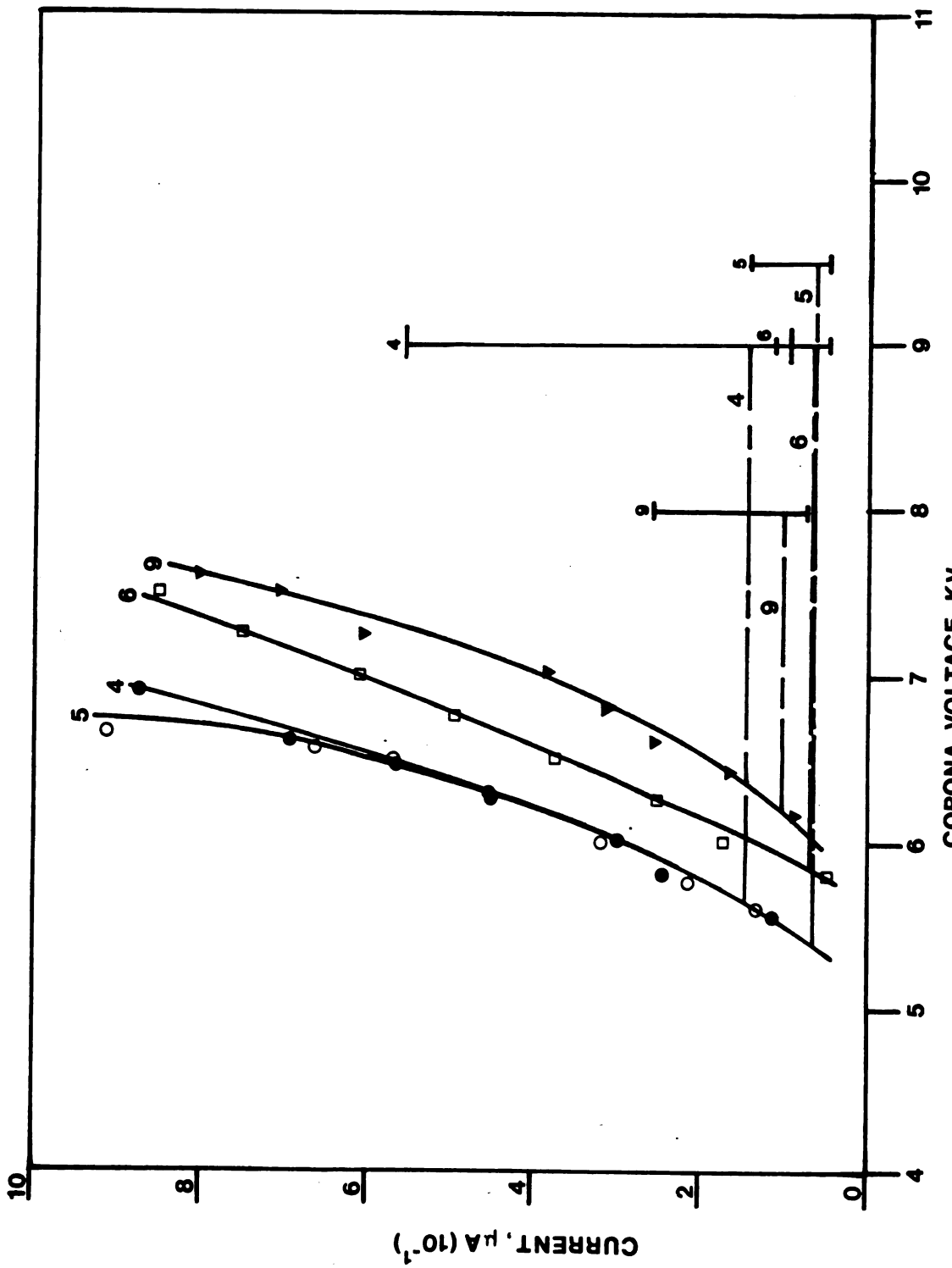

Figure 5.7. Time average voltage drops across the particulate bed.

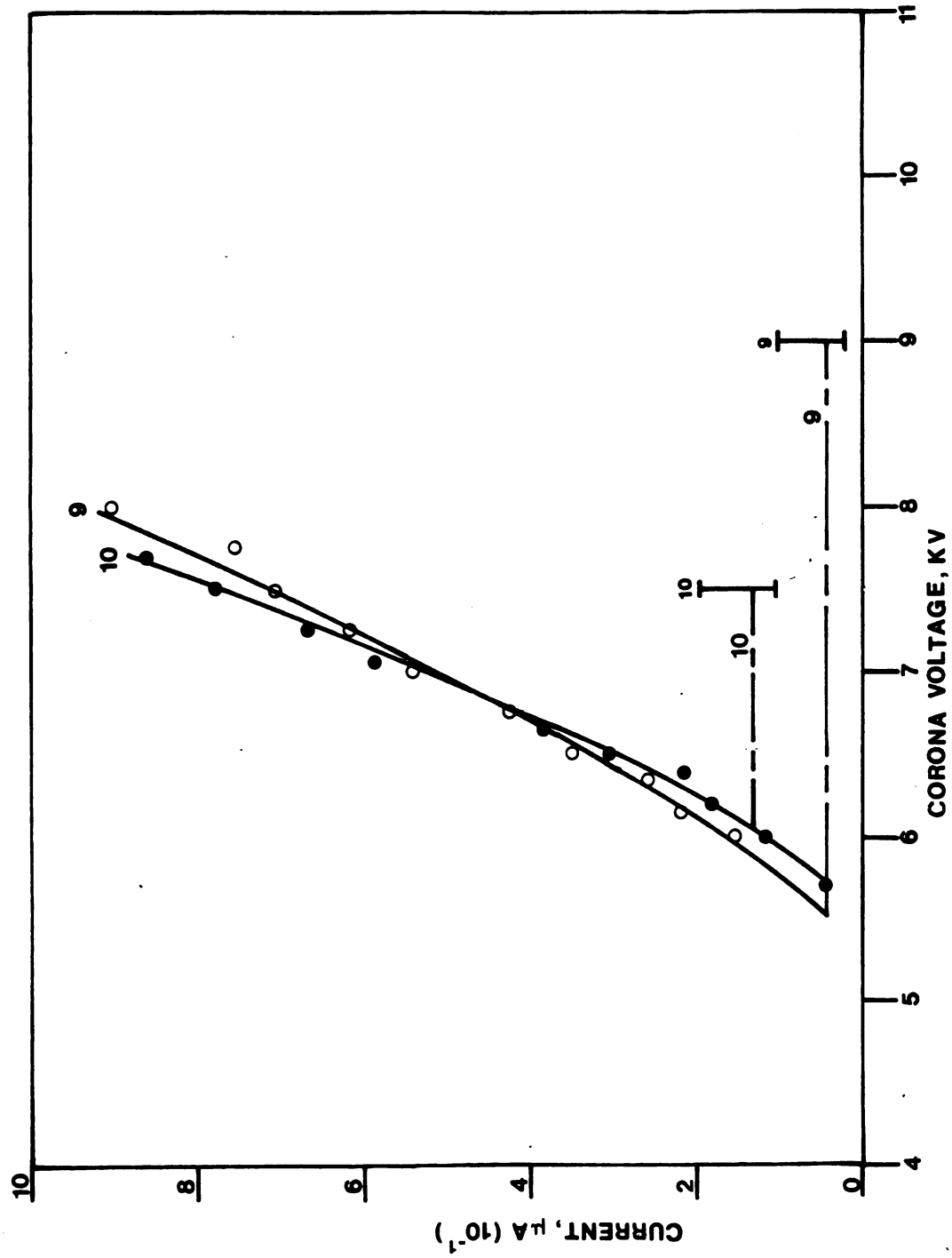

Figure 5.8. Time average voltage drops across the particulate bed.

Table 5.5. Maximum, minimum and average currents through the ash layer.

Expt. No.	Corona Voltage (Kv)	Bed Thickness (cm)	$I^{\dagger}_{max}$(μA)	I_{min}(μA)	I_{ave}(μA)
1	9.40	0.4367	3.470	1.320	2.010
2	10.00	0.4862	1.430	1.020	1.230
3	9.50	0.3175	0.945	0.540	0.559
4	9.00	0.3175	5.560	0.980	1.458
5	9.50	0.3175	1.485	0.500	0.678
6	9.00	0.2580	1.150	0.490	0.685
7	9.00	0.3175	1.010	0.210	0.409
8	7.50	0.3175	1.970	1.030	1.304
9	8.00	0.3175	2.600	0.760	1.023

†I is the current.

Experiment 5 to over an hour for Experiment 8. This, of course, depends on the magnitude of the current at zero time and one expects that a higher initial current would lead to a longer stabilizing period. The data in Table K.1 shows that the initial current in Experiment 8 is significantly higher than in Experiment 5.

Table K.1 also indicates that the leakage current, in general, decreases with time. However, in all of the cases the corona-ash layer system relaxes to a final current value which is more stable (relative to the variations at the end of the initial stabilizing period). This is suggested by comparing the underscored I_{min} and I_{ave} values in Table 5.5. The current-time data for the other cases (1, 2, 4, and 9) indicate that the I_{min} was measured during short lived current fluctuations (due either to the equipment or the variations in the line voltage). In fact the I_{min} for each of these cases is not the final "relaxed" value of the current. The final current values (I_{final}) for experiments 1, 2, 4 and 9 are shown in Table 6.

Table 5.6. End currents for experiments 1, 2, 4 and 9.

Experiment No.	I_{final} (μA)
1	1.565
2	1.300
4	1.200
9	1.270

A comparison of the I_{final} values from the above table and the underscored I_{min} (from Table 5.5) with the corresponding time weighted I_{ave} indicates that the average current is more stable than is suggested by the relatively rapid decrease (of leakage current) toward the beginning of an experiment*. This is illustrated by the plots in Figures 5.6, 5.7 and 5.8. The plotting of the clean plate data in these figures permits the determination of the average voltage drop across the bed. The term "distance average" mentioned earlier refers to the fact that in the ideal case** the electric field strength is uniform along the ash layer and is obtained simply by dividing the ΔV obtained from the plots by the bed thickness. It should be noted that E_a calculated by this procedure is an approximation in the sense that E_a is not really independent of time as it is purported to be in the steady state differential equation (4.9), Chapter 4. Further discussion of this aspect is deferred until Section 5.5.

The "average" field strength E_a estimated from the plots of Figures 5.6, 5.7 and 5.8 can now be used to calculate the constriction ratio K (equal to a/2S) which appears in the expression (5.1) for the migration parameter $\bar{\alpha}$. It was mentioned in Chapter 1 (Overview) that an electric field within a fly ash layer induces an interparticle cohesive force F_z. An expression for this cohesive force is also given as a function of an average (interparticle) gap field strength E_z

---

*Since I_{max} is the current at the end of the initial (stabilization) period this conclusion is also supported by the fact that I_{ave} is closer to I_{min} than it is to I_{max}.

**Perfectly spherical and identical particles in a cubic packing.

[equation (3.101), Chapter 3]*. If the fly ash particles are assumed as being elastic (M3)**, then the radius of the interparticle contact can be estimated from the Hertz equation (M5, M1) given earlier in Chapter 3 [equation (3.1)].

$$a = \left[\frac{1.75S\ (1-\nu^2)F}{Y}\right]^{\frac{1}{3}} \qquad (3.1)$$

where

$$F = F_z = \int^A \frac{\varepsilon_o}{2}\ E_z^{\,2}\ dA \qquad (3.101)$$

For a simple cubic packing the total number of particles in a plane of unit area is $1/4S^2$. The total cohesive force per unit area is F_T where

$$F_T = 0.25\ F_z/S^2 \qquad (5.2)$$

McLean (M3) has proposed a semi-empirical correlation between F_T and the applied electric field strength as follows,

$$F_T = AE_a^{\ \delta} \qquad (5.3)$$

where A and δ are constants and $\delta = 1.54$ for Y (Young's Modulus) = 7.5×10^{10} Newtons/m and ν (Poisson's ratio) = 0.25. The constant A varies between 90×10^{-6} and 150×10^{-6}. In this case an average

---

*See also reference D2.

**See Section 2.2, Chapter 2.

value of A is selected; $A = 120 \times 10^{-6}$.

Substitution of F_T from equation (5.3) into (5.2) yields an expression for F_z in terms of the particle radius S. This expression replaces F in equation (3.1) to give the following relation for the constriction ratio:

$$K = \frac{a}{2S} = \left[\frac{9\times10^{-5}}{32} \cdot \frac{(1-\nu^2)}{Y} E_a^{1.54}\right]^{\frac{1}{3}} \qquad (5.4)$$

An important significance of equation (5.4) is that the constriction ratio K is independent of particle size. Hence the average interparticle gap field strength $E_z(\theta)$ [equation (3.100)] and the cohesive force F_z [equation (3.101) above] are also independent of particle size. The constriction ratio, therefore, is simply a function of the (average) applied electric field across the layer.

An alternative and a more rigorous procedure to evaluate the contact area 'a' involves the substitution of F_z (or F) in equation (3.101) into the Hertz equation (3.1). However this means that the integral expression for F_z first needs to be evaluated by replacing E_z in (3.101) with its expression (3.100) in terms of the θ variable*. The semi-empirical method is simpler to use than this integral procedure. Furthermore, the relative contribution of the term ln K to the migration parameter $\bar{\alpha}$ is smaller than that of the average field strength E_a**.

---

*The integration variable θ has $\theta = 0$ and $\theta = \pi/2$ as the lower and upper limits respectively.

**As stated earlier the assumption of an average (constant) E_a is an approximation. This is discussed in Section 5.4.

The values of the constriction ratio (a/2S) calculated from the set of equations (5.2), (5.3) and (3.1) are presented in Table 5.7.

The voltage drop (ΔV) is estimated as the difference between the operating corona voltage (during the experiment) and the clean plate corona voltage at the (time) average current level of the migration experiment. This is illustrated in Figure 5.6 for Experiment 1. The average field strength is then simply given by dividing ΔV by the layer thickness.

The interparticle cohesive force is calculated from the explicit expression obtained by combining equations (5.2) and (5.3),

$$E_z = (4.8 \times 10^{-4})\, S^2\, E_a^{1.54} \quad (5.5)$$

Two specific observations may be made with regard to this expression:

i) The dependence of the cohesive force (F_z and F_T) upon the applied electric field is less strong than that for a homogeneous dielectric where $F_T \propto E_a^2$.

ii) In an electrostatic precipitator it is the ash resistivity (ρ) that determines the cohesive force**. The average corona current J varies from 60 $\mu A/m^2$ to 250 $\mu A/m^2$ and $E_a = J\rho$ so that a large change in E_a is more likely due to a change in the bulk resistivity (ρ) which may vary over several orders of magnitude (M3).

---

*The particle radius S = 9.575 x 10^{-6}m. The results of the bulk property determinations for the fly ash are presented in Appendix J.

**This force holds the particulate layer onto the collecting plate.

Table 5.7. Values of the cohesive force (F_z), the average field strength (E_a), and the constriction ratio (a/2S) for the ion migration experiments.

Experiment No.	Voltage drop, ΔV (Kv)	Bed Thickness (cm)	$F_z \times 10^5$ (Newtons)	$E_a \times 10^{-5}$ (Vm)	$\frac{a}{2S} \times 10^3$
1	3.96	0.4367	6.579	9.069	9.439
2	3.97	0.4862	5.598	8.166	8.944
3	3.36	0.3175	8.341	10.580	10.216
4	3.35	0.3175	8.305	10.550	10.201
5	4.12	0.3175	11.428	12.980	11.346
6	3.15	0.2580	10.407	12.210	10.997
7	3.48	0.3175	8.807	10.960	10.402
8	1.45	0.3175	2.287	4.567	6.637
9	1.79	0.3175	3.164	5.638	7.395

The calculated values of the constriction ratio (K) in Table 5.7 are in agreement with those found in literature*. Referring to Figure 4.1 (Chapter 4) it is seen that when the two spheres meet at a circular contact (of radius a) the angles θ_c and θ_o must take this feature into account. This was mentioned earlier in the present section where θ_{cc} was described as the capillary ring angle, and $\theta_{cc} - \theta_{co}$ corresponds to the angle due only to the ring of capillary condensate around the interparticle contact. It follows, therefore, that $\theta_c > \theta_{cc}$ and $\theta_o > \theta_{co}$.

If the particles are assumed to be elastic then the cohesive force acts in such a way so as to deform them into (almost spherical) spheroids. Since the deformation is small, the contact between two spherical particles (at the circumference of the circle of radius a) can still be assumed to be tangential. This deformation is not significant enough so as to disturb the spherical curvature of the particle beyond the contact. Hence the liquid-vapor interface** of the condensate ring extends out (of the pore) the same distance† i.e., $x_1 - x_0$ in Figure 2.9 is assumed to be the same irrespective of whether K†† equals zero or not. Thus if $x_1 - x_0$ (Figure 2.9) and the radius of curvature $\overline{R}$ are unchanged then the length of the solid-liquid interface is the

---

*In terms of the order of magnitude. See reference M2 for example.

**This is also spherical. See Section 2.12, Chapter 2.

†As in the ideal case of point contact.

††K = a/2S in this chapter is distinguished from the same notation used for the mean curvature of the capillary condensate in Chapter 2.

same for the two cases of point and circular contact. From this it follows that the angle due to the capillary condensate is also unchanged and*

$$\theta_c = \text{arc tan } \frac{a}{S} + \theta_{cc} \qquad (5.6)$$

where θ_{cc} is the capillary angle defined earlier in this section and $\theta_{cc} - \theta_{co} = \theta_c - \theta_o$. The angle arc tan $\frac{a}{S}$ is subtended by the contact circle at the center of a sphere. Furthermore the lower limit θ_{co} (due to pore restriction) is also increased by the same amount as above, i.e.,

$$\theta_o = 0.306 + \text{arc tan}^{-1}\ a/S \qquad (5.7)$$

The equations (5.6) and (5.7) are used to evaluate to the capillary ring angles** for the real case of a finite area of (circular) contact. This is different from the ideal situation principally due to the cohesive forces which are present in a (resistive) particulate layer. The results of the calculations leading to θ_c and θ_o are presented in Table 5.8. These angles are referred to as the modified capillary angles.

---

*This is discussed in Section 5.5.

**θ_c and θ_o.

Table 5.8. Capillary ring angles θ_c and θ_o in the presence of cohesive forces within the ash layer.

Experiment No.	$E_a x 10^{-5}$ (v/cm)	arc tan $\frac{a}{S}$ (Deg)	θ_c (Deg)	θ_o (Deg)
1	9.069	1.0815	1.391	1.387
2	8.166	1.0247	1.0247*	--
3	10.580	1.1705	1.1705*	--
4	10.550	1.1688	1.1688*	--
5	12.980	1.3000	1.624	1.606
6	12.210	1.2600	1.669	1.566
7	10.960	1.1918	1.567	1.498
8	4.567	0.7605	1.342	1.066
9	5.638	0.8473	1.416	1.153

*These cases corespond to the situation where there is no capillary condensation.

It is seen from the above table that the capillary angles exceed 1^o in every case. Although θ_c (and θ_o) appears to be small its effect upon the ionic concentration profile is significant. The data in Table 5.8 are the end result of the evaluation of the effect of capillary condensation upon the particulate layer. The information regarding the experimental conditions (temperature, humidity, ash layer geometry) are sufficient to evaluate the parameters in the expression (5.1) for $\bar{\alpha}$. The term μ/D in this equation, however, is obtained from the concentration profiles over the particulate bed. As is discussed later (Section 5.4), the evaluation of the ratio of the electric mobility to the molecular diffusivity is one of the objectives of this work. In

the next section, the experimental concentration profiles are presented as plots of concentration vs. distance through the ash layer.

5.3 Experimental Concentration Profiles for the Particulate Bed

As mentioned earlier in this chapter one of the important objectives of the (sodium) ion migration experiments is to determine the (surface) concentration distribution when the transport process occurs under the coupled effect of a concentration gradient and an electric field gradient. The shape of the concentration profile along the bed leads one to conclude about the relative* importance of the ionic contribution to the (surface) leakage current. It may be recalled that such a conclusion applies only to low temperature electrostatic precipitators in which case the surface resistivity is more important than the volume resistivity.

The configuration of the fly ash bed with respect to the corona point was described in the experimental procedure (Section 5.2). The sodium hydroxide solution is deposited on the plane (Figure 5.1) prior to filling the hollow space of the cup (formed by the support) with the fly ash. This sodium hydroxide therefore provides the "pool" of sodium ions** at the lower boundary of the ash layer. As in the case of an electrostatic precipitator a negative corona is used in this instance. As a result the positive ions migrate up through the ash bed†.

---

*Relative to the electronic current.

**This was referred to earlier in Section 4.1, Chapter 4.

†Hence it must be assured that the inside surface of the (teflon) support is entirely free of sodium (as NaOH) at the beginning of the experiment.

It was stated in Section 5.2 that the sodium ion concentration of the fly ash samples is determined by neutron activation analysis of the irradiated samples*. The (gamma) count data are generated by a computer based analyzer** and these are compared with the standard counts to give the desired concentration by means of the following formula:

$$\text{Na. Concentration} = \frac{A\ (\text{sample})}{A\ (\text{standard})} \cdot \frac{M_{Na}\ (\text{standard})}{M\ (\text{sample})} \cdot 100\%$$

where

A - activity (area under sodium - 24 peak), counts.

M - mass, gm.

The ion concentration calculated above is assigned to a sample of known thickness which in turn, is estimated from the corresponding rotation of the turn screw attached to the plane of the resistivity probe (Figure 5.1)†. From this the location of the sample in the original ash layer (in the probe) is also determined.

The foregoing calculations were performed for all of the nine cases and the results for one typical case (Experiment No. 3) are shown in Table 5.9. As mentioned before†† the minimum rotation of

---

*This also includes one standard sample with a known concentration of sodium.

**See Section 5.1 and Appendix L.

†This is described in the experimental procedure, Section 5.1.

††See also Appendix K and Appendix L.

the turn screw corresponds to a vertical motion of the plane by 0.009922 cm; hence all distances in the ash bed are multiples of this number and are given as δ_2 in the table. The distances are measured from the plane, i.e., from the bottom of the ash layer in each case.

Table 5.9. Typical laboratory data for the sodium ion concentration distribution within the fly ash layer*.

Sample No.**	Distance (cm)	δ_2	Na Concentration, c (% wt.)	c/c_o
19	0.0198	2	2.5673	1.0000
18	0.0298	3	0.3422	0.1333
17	0.0397	4	0.2847	0.1109
16	0.0496	5	0.2832	0.1103
15	0.0595	6	0.2846	0.1109
14	0.0794	8	0.3062	0.1193
13	0.0992	10	0.3017	0.1175
12	0.1191	12	0.2860	0.1114
11	0.1389	14	0.2855	0.1112
10	0.1588	16	0.3156	0.1229
9	0.1786	18	0.2781	0.1083
8	0.1984	20	0.2974	0.1158
7	0.2183	22	0.3128	0.1218
6	0.2381	24	0.3072	0.1197
5	0.2580	26	0.2682	0.1045
4	0.2778	28	0.2892	0.1126
3	0.2977	30	0.2685	0.1046
1 & 2†	0.3175	32	0.2602	0.1014

*These data are for Experiment No. 3.

**The samples are numbered in the order that they are withdrawn from the ash bed in the probe chamber (Figure 5.1).

†Sample numbers 1 and 2, in this experiment, were lumped together and treated as a single sample.

The last column in the foregoing table is the dimensionless sodium concentration where c_o is the concentration of the first sample (in this case Sample No. 19). It is seen that for $\delta_2 > 3$ the sodium concentration does not decrease any further but varies about a mean value {c/c_o (mean) = 0.1127}. This abrupt drop in concentration from a high value at the bottom of the ash layer* (Sample No. 19) is typical for all of the ion migration experiments conducted in the laboratory**.

The variation of the surface ion concentration with distance (δ_2) from the plane is shown in Figures 5.9 through 5.15. The concentration-distance data for each of the laboratory experiments are presented in these figures†. The term "concentration-distance" refers to the sodium (ion) concentration of the fly ash sample which is located at a known distance from the bottom of the particulate bed in Figure 5.1. The sample (in the irradiation vial) in its "original"†† state represents a thin layer in the bed which has a uniform ion concentration. Additionally, the voltage at all points on the top surface of this layer is constant*†

---

*This refers to the fly ash bed within the cylindrical (teflon) support inside the probe chamber (see Figure 5.1).

**See Appendix L.

†The data for Experiment No. 7 are not shown for reasons discussed later.

††This term is used to imply the fact that the sample is present as a thin layer during the experiment, i.e., before it is removed from the bed for subsequent analysis.

*†This suggests that the voltage drop in the portion of the bed above this layer is constant at all points.

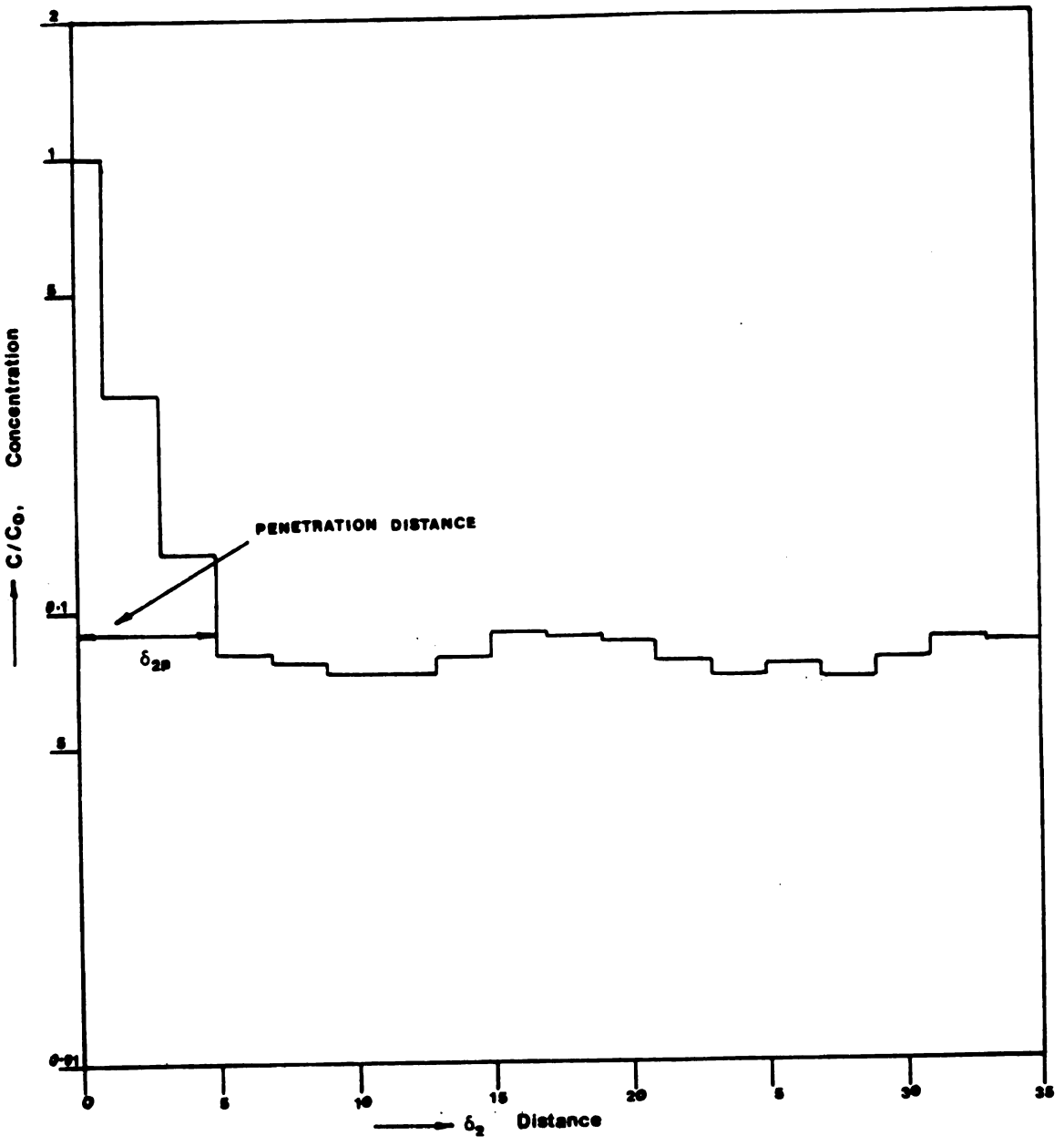

Figure 5.9. Experimental ion concentration profile [2]

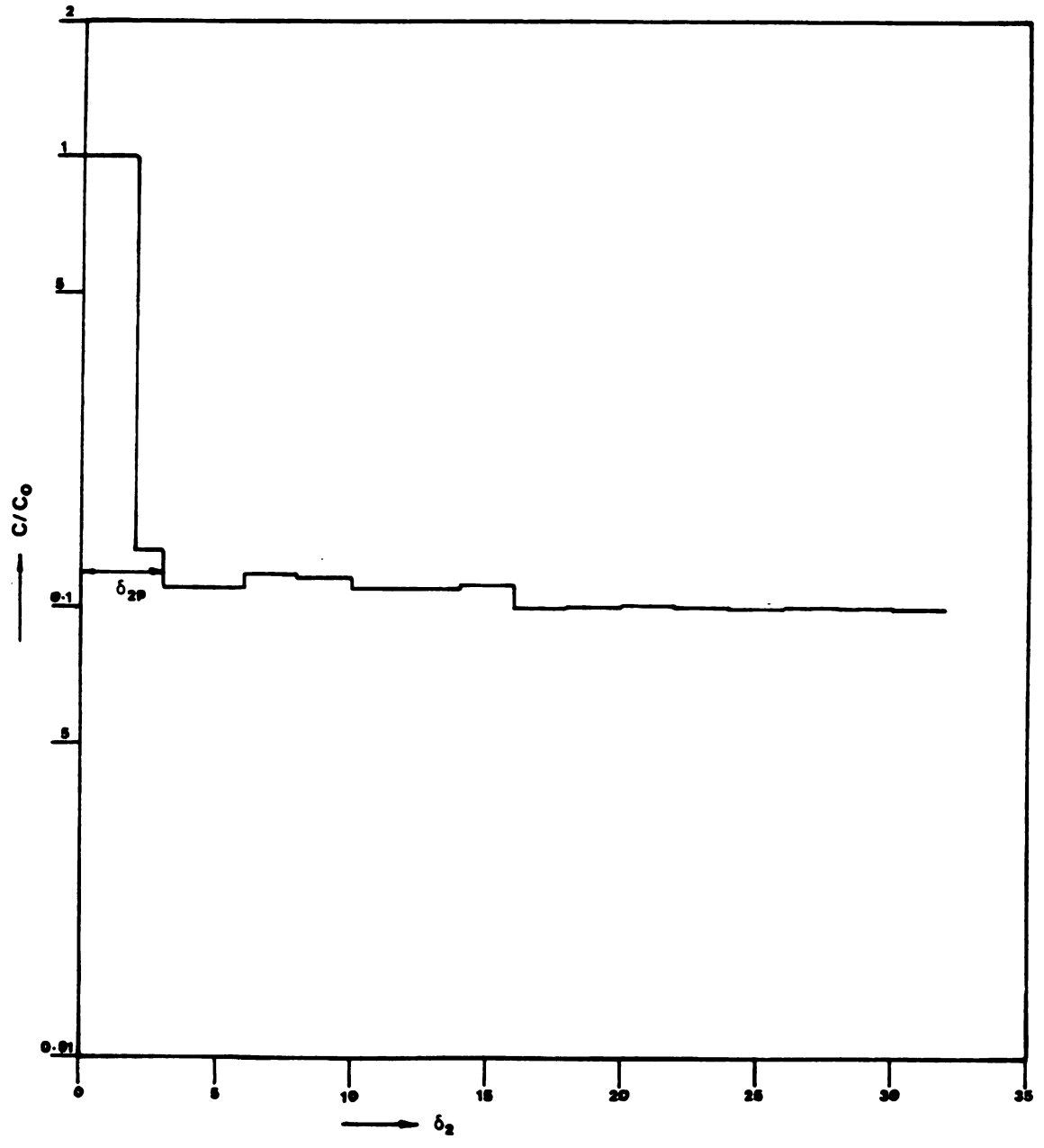

Figure 5.10. Experimental ion concentration profile [3]

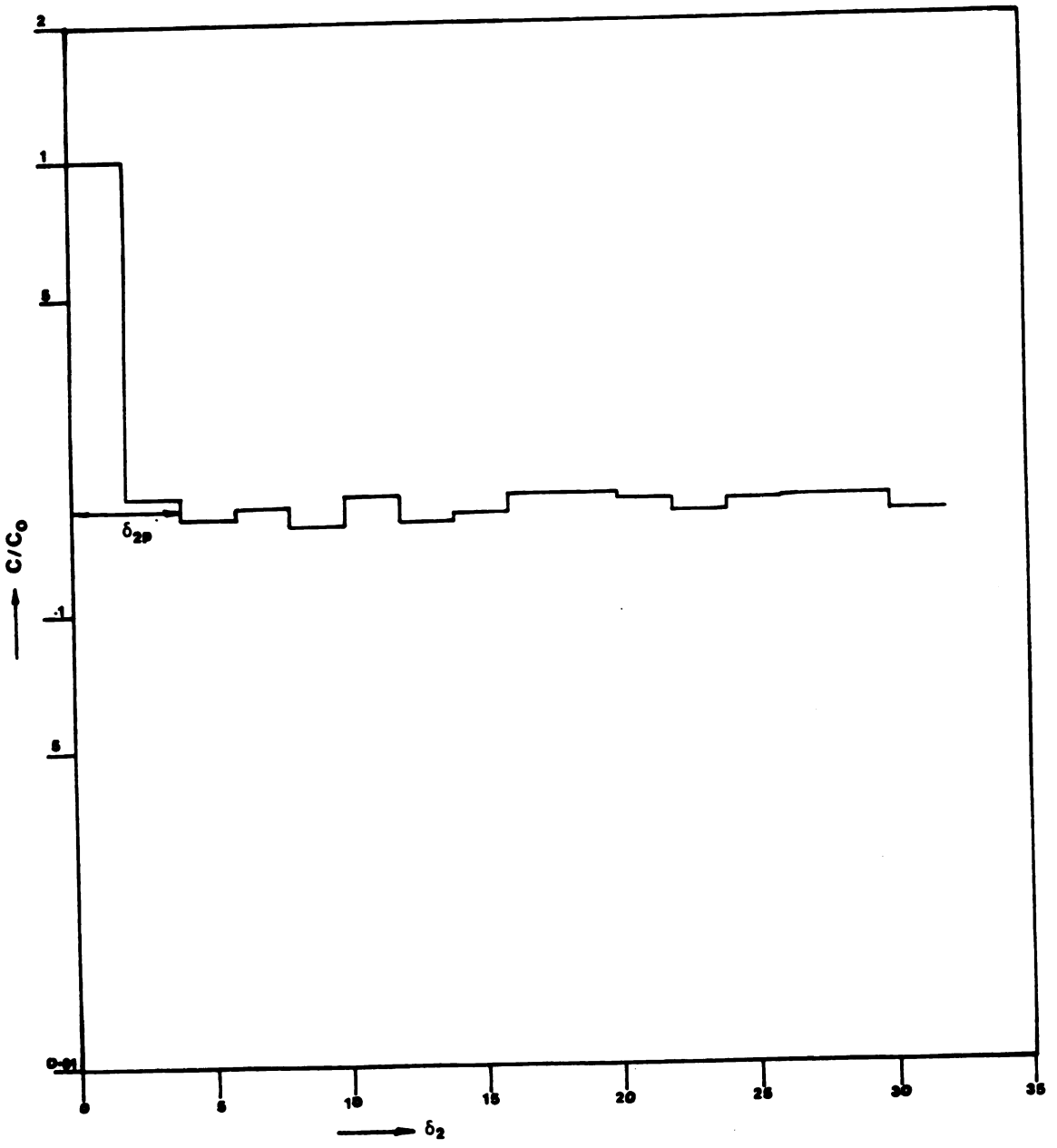

Figure 5.11. Experimental ion concentration profile [4]

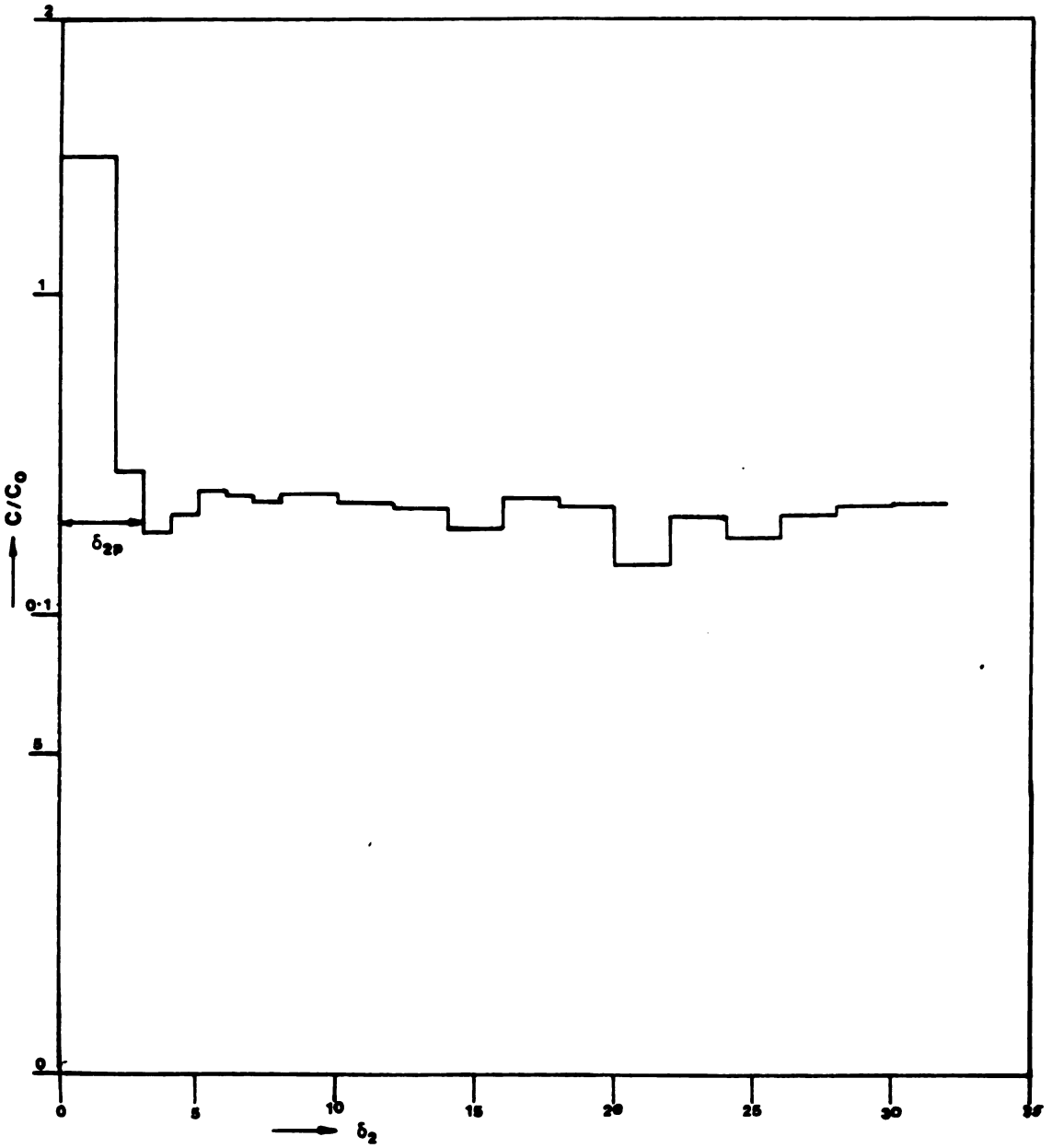

Figure 5.12. Experimental ion concentration profile [5]

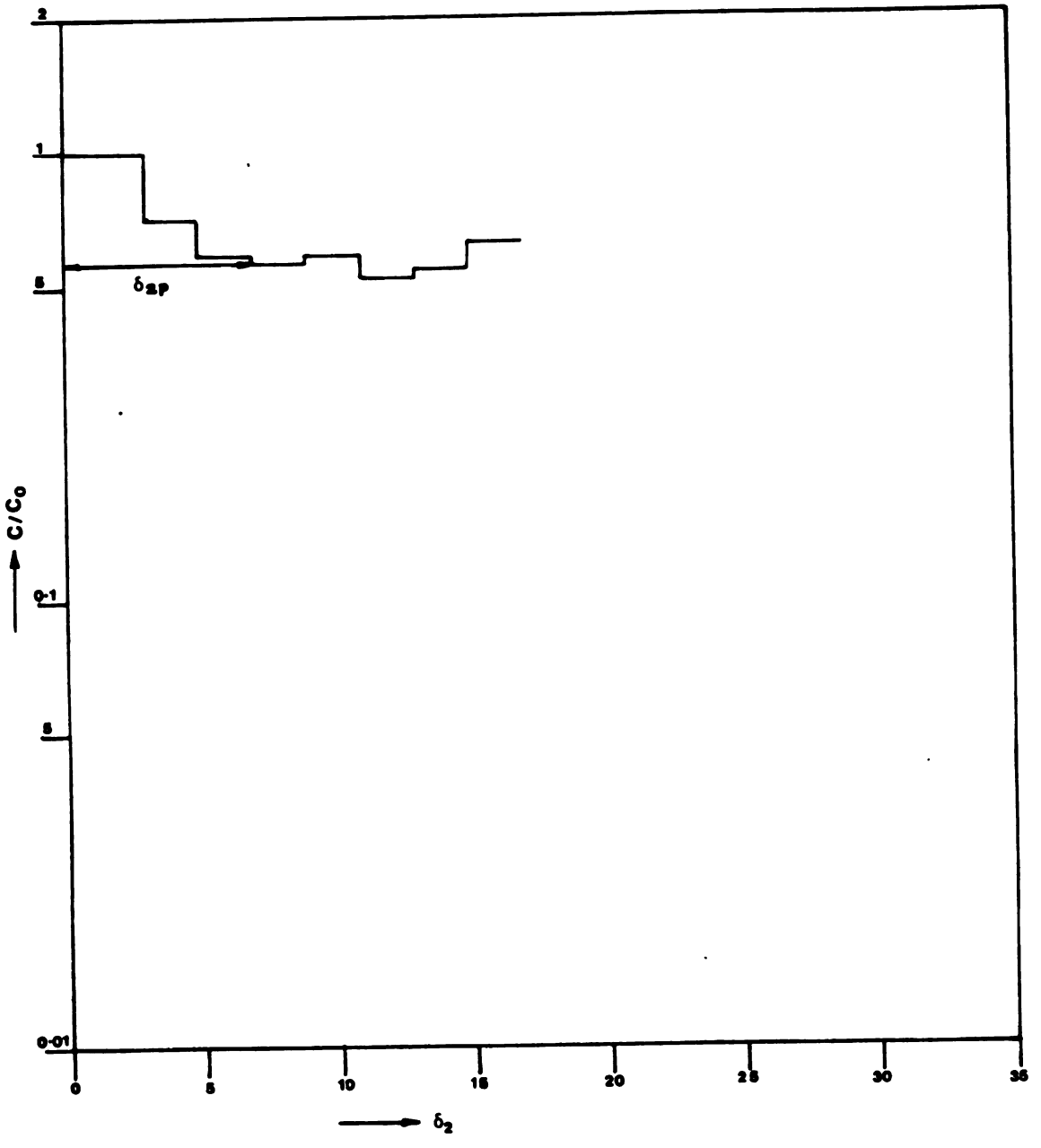

Figure 5.13. Experimental ion concentration profile [6]

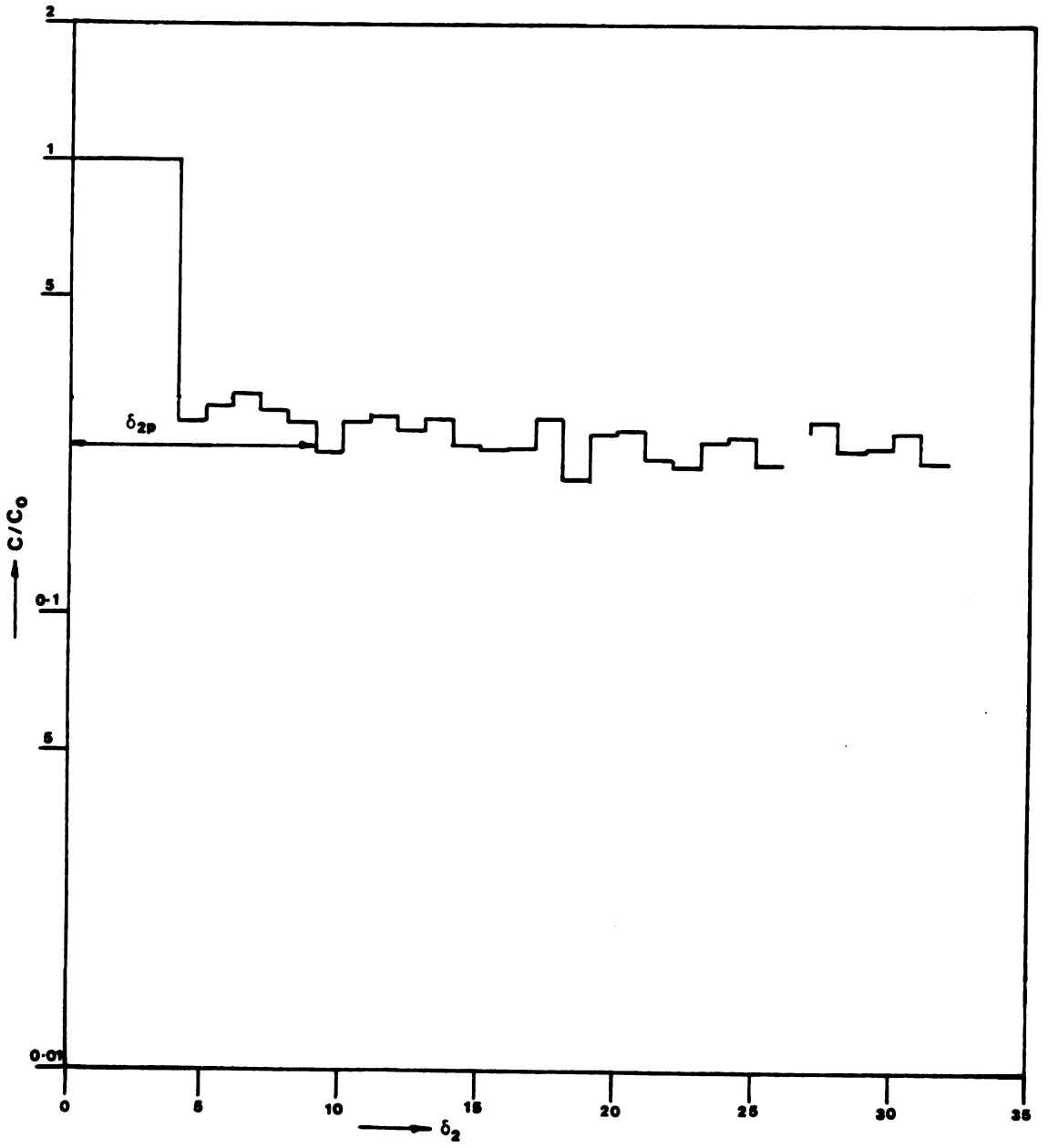

Figure 5.14. Experimental ion concentration profile [8]

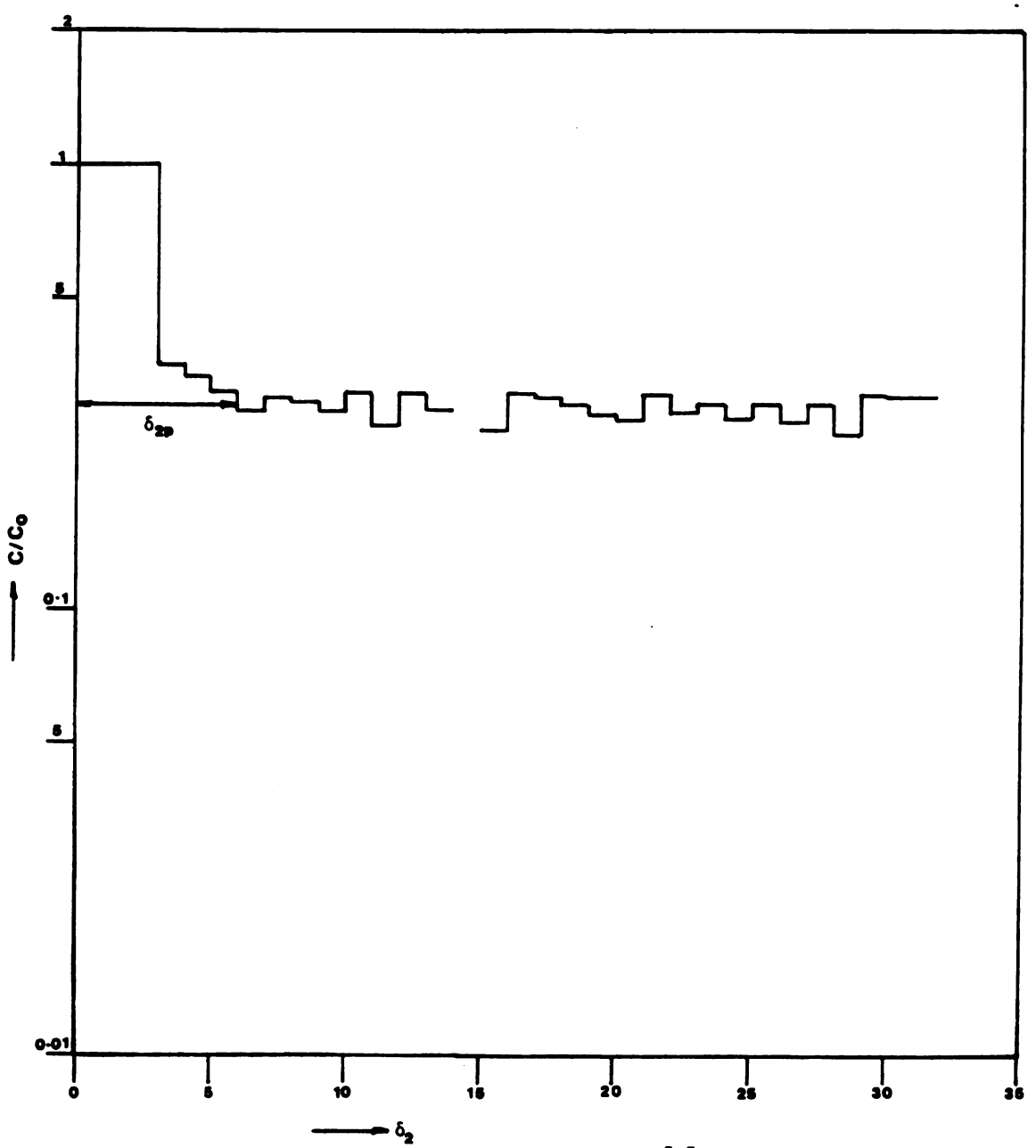

Figure 5.15. Experimental ion concentration profile [9]

as well.

As stated above the drop in the ion concentration near the bottom of the ash layer occurs for all of the experiments. The concentration falls from a high value at the lower boundary to the mean sodium concentration of the fly ash matrix itself.* This rate of fall (with respect to distance) is a function of several factors and for this particular case (the experimental conditions in the laboratory) these factors are:

i) Bed temperature, T

ii) Radius of curvature of the capillary condensate, $\overline{R}$

iii) Thickness of the bed

iv) Corona voltage

v) Sodium ion concentration at the lower boundary (of the ash layer), and

vi) Time duration of the experiment.

The radius of curvature $\overline{R}$ is directly related to the amount of capillary condensate in the bed macropores and factors iii) and iv) above determine the magnitude of the average layer field strength E_a (Section 5.2). These factors, in effect, constitute the variables which determine the distance of penetration** of an alkali ion through the particulate layer. In this work the effect of some of the variables above were accounted for in the dimensionless migration parameter $\overline{\alpha}$ in equation (5.1)

*The concentration units are normalized with respect to the Na concentration of the lowest layer. See Appendix L.

**The penetration distance is taken to mean the distance (from the plane of the probe) over which the ion concentration falls to a mean value.

$$\bar{\alpha} = \mu S E_a / D \ln K \qquad (5.1)$$

The dimensionless constriction ratio K is itself a function of E_a as given by equation (5.4).

In light of the material presented earlier (Chapter 2, 4 and this chapter) one would expect the penetration distance, δ_{2p}, to increase with the amount of liquid present in the macropores. This is observed in the results of experiment numbers 8 and 9* (Figures 5.14 and 5.15) where the value of δ_{2p} is 8 in one case (Experiment No. 8, Figure 5.14) and 5 in the other. The relative amounts of condensate for these two cases is reflected by the values for the capillary ring angles given in Table 5.4. The dimensionless penetration distances, δ_{2p}, for the laboratory experiments are shown in Table 5.10.

It is observed from the figures (5.9 through 5.16) that δ_{2p} is fairly small relative to the bed thickness. The effect of the ash layer thickness appears to be significant only with respect to the average field strength E_a and (hence) to the constriction ratio K.

Finally, it is noted that the shape of the concentration-distance plots for all of the experiments are consistent. The significance of this feature needs to be interpreted in light of the method of dominant balance solution (MDB) of Chapter 4, and this is presented in the next section.

---

*The results of these two experiments are compared to each other because the other experimental conditions (except for the water bath temperature) are similar for the two cases.

Table 5.10. Ion penetration distance through the particulate layer.

Experiment	T^{*} (^{o}C)	θ_{cc}^{**} (Degrees)	$E_a \times 10^{-5}$ (v/m)	δ_{2p} (dimensionless)
1	146.67	0.310	9.069	2
2	174.69	--	8.166	5
3	154.44	--	10.580	3
4	157.22	--	10.550	2
5	156.67	0.324	12.980	3
6	98.89	0.409	12.210	5
7	126.67	0.375	10.960	-
8	65.56	0.582	4.567	8
9	65.56	0.568	5.638	5

*T is the temperature of the particulate bed (assumed equal to the probe temperature.

**θ_{cc} is the capillary ring angle in degrees (see Table 5.4).

5.4 Significance of the Profile Shape with Respect to the MDB Solution

It is evident from the results of the previous section (Figures 5.9 through 5.16) that the sodium ion migration through the particulate layer is restricted to fairly small values of the penetration distance, δ_{2p} (Table 5.10). As a result the ion concentration falls sharply from the lower boundary to the layer (Figure 5.1). The number of particles over which the concentration falls to its mean* value may be estimated from the ion penetration distance. For a value of δ_{2p} equal to three the corresponding number of (spherical) particles is approximately equal to 16.** In an ash layer of thickness equal to 0.3175 cm (Table 5.7) the total number of particles in one vertical stack of cubic packing is equal to $0.3175/19.15 \times 10^{-4}$ or 166 (approximately). Hence the penetration distance in this case is about 9.6% of the thickness of the ash layer.

The relatively short ion penetration distances such as the above indicate correspondingly large concentration gradients over the surface of a particle near the end of the lower boundary layer. Furthermore, the (semi-logarithmic) plots also show that the slope decreases with increase in distance and approaches zero at the end of the penetration thickness (δ_{2p}) within the ash bed. As seen later in this section, this feature is also indicated by the theoretical model.

---

*As stated earlier in this chapter the mean value refers to the intrinsic concentration of sodium in the fly ash. The sodium occurs primarily as sodium oxide.

**Equal to ($\delta_{2p} \times 0.009922$) cm $\div$ 19.15×10^{-4} cm (particle diameter).

One of the objectives of the following analysis is the determination of an "average" concentration gradient. The term average refers to the (linear) gradient obtained from the concentrations at the two boundaries* of a particle, where the particle is within the distance δ_{2p}. This does not imply, however, that the local concentration gradient (at a point, on the surface) is linear. The solution equation to the mathematical model of Chapter 4 does indeed predict that the local concentration gradient is non linear. The formal solution obtained in Chapter 4 is given as

$$c(\theta) \simeq c_1 \exp(\bar{\alpha} \cot\theta)\{1 - a_o \beta^2 [\sum_{k=0}^{3} \psi_k \quad (k+2)\ \theta^{k+4} + \sum_{k+4}^{\infty} \phi_k\ \theta^{K=4}]\} + c_2 \sin\theta \cdot \mu(\theta) \qquad (4.40)$$

$$\theta \to 0, \pi^{**}$$

where the functions ψ_k and θ_k have been defined in connection with equation (4.32) and the function $\omega(\theta)$ is given as:

$$\omega(\theta) = 1 - a_o \beta^2 [\sum_{k=0}^{3} \psi_k \quad (k+2)\ \theta^{k+4} + \sum_{k=4}^{\infty} \phi_k\ \theta^{K+4}] \quad k=4 \qquad (4.32)$$

---

*The upper and lower boundaries refer to the neighbourhood of the two "longitudinal" contacts of a particle. (See footnote in Section 3.8, Chapter 3).

**For the case $\Theta \to \pi$, the series expansion is in terms of $(\pi-\theta)$ and $\mu(\theta)$ is given as $\mu_\pi(\pi-\theta)$. See equation (4.43).

Both $\omega(\theta)$ and $\mu(\theta)$ behave asymptotically like a constant as θ approaches the irregular singularities. Differentiating equation (4.40) above with respect to θ one obtains:

$$\frac{\partial \bar{c}}{\partial \theta} \simeq -\bar{\alpha} \csc^2 \theta \exp(\bar{\alpha} \cot \theta)\, w(\theta) + \exp(\bar{\alpha} \cot \theta)\, w'(\theta) + \frac{c_2}{c_1} \cos \theta\, \mu(\theta) + \frac{c_2}{c_1} \sin(\theta)\, \mu'(\theta) \qquad (5.8)$$

$$\theta \to 0$$

where $\bar{c}$ is the normalized c oncentration with respect to the constant c_1. As $\theta \to 0^*$, $w'(\theta)$ and $\mu'(\theta) \to 0$ so that the asymptotic approximation to the first derivative of the concentration is given as,

$$\frac{\partial \bar{c}}{\partial \theta} \simeq -\bar{\alpha} \csc^2 \theta \exp(\bar{\alpha} \cot \theta)\, w(\theta) + \frac{c_2}{c_1} \cos \theta\, \mu(\theta) \qquad (5.9)$$

$$\theta \to 0, \pi$$

It may be observed from this equation that the first term dominates as θ approaches zero. Similarly as θ approaches π (at the upper boundary)**

---

*Or as $\theta \to \pi$, in which case $\mu = \mu_\pi$ and w and μ are series expansions about $(\pi-\theta)$.

**In this context the upper and lower boundaries of any particle are taken to represent the neighborhoods of $\theta \to \pi$ and $\theta \to 0$ respectively. See Figure 4.1

the second term is the dominant part of the approximation for the first derivative. At $\theta = \frac{\pi}{2}$, however, the second term vanishes and

$$\frac{\partial \bar{c}}{\partial \theta} \simeq -\bar{\alpha} \cdot w(\theta) \tag{5.10}$$

It is seen from equations (5.9) and (5.10) that the slope $(\partial \bar{c}/\partial \theta)$ is negative in all of the three cases, $\theta < \pi$, $\theta = \pi$ and $\theta > \pi$. Hence the ion concentration decreases from $\theta = \theta_c$ to $\theta = \pi - \theta_c$ in a manner specified by equation (4.40). Furthermore, the migration parameter $\bar{\alpha}$ may be estimated from equation (5.10) since an approximation to $w(\theta)$ is already given by equation (4.32).

One way to ascertain the nature of the concentration profile (over one particle) is to determine the relative magnitudes of $\frac{\partial \bar{c}}{\partial \theta}$ as θ increases from θ_c* to $\pi - \theta_c$. The modified asymptotic approximations for the first derivative may be obtained for the three cases as follows:

$$\frac{\partial \bar{c}}{\partial \theta} \simeq -\bar{\alpha} \csc^2 \theta \exp(\bar{\alpha} \cot \theta)\, w(\theta) \tag{5.11}$$

$$\theta \to 0$$

$$\frac{\partial \bar{c}}{\partial \theta} \simeq -\bar{\alpha} \cdot w(\theta), \quad \theta = \frac{\pi}{2} \tag{5.10}$$

---

*The modified capillary angle (see Section 5.2)

and

$$\frac{\partial \bar{c}}{\partial \theta} \simeq \frac{c_2}{c_1} \cos\theta \, \mu(\theta) \qquad (5.12)$$
$$\theta \to \pi - \theta_c$$

Upon comparing equations (5.11) and (5.10) it is immediately evident that $|\frac{\partial \bar{c}}{\partial \theta}|_{\theta \to 0} > |\frac{\partial \bar{c}}{\partial \theta}|_{\theta=\pi/2}$. Hence the slope falls from a very high value* near the end of the lower contact to a magnitude which is approximately given by $\bar{\alpha} \cdot w(\theta)$. Since $w(\theta)$ is an asymptotic series whose first term is 1 it may be expected that the first derivative near $\theta = \pi/2$ has an order of magnitude similar to that of the migration parameter $\bar{\alpha}$. It is emphasized, however, that the accuracy of this conclusion depends upon how close $w(\theta)$ is to one. This, in turn, reflects upon the accuracy of the solution (4.40) itself.

From equation (5.12) above it is seen that the ion concentration falls near the upper boundary $(\pi-\theta_c)$. However, this rate of decrease $(\partial\bar{c}/\partial\theta)$ can be compared to that in the region $\theta = \pi/2$ from equation (5.12) as follows:

$$\frac{\frac{\partial \bar{c}}{\partial \theta}|_{\theta=\pi/2}}{\frac{\partial \bar{c}}{\partial \theta}|_{\theta=\pi-\theta_c}} = \frac{-\bar{\alpha} \cdot w(\theta)}{\frac{c_2}{c_1} \cos\theta \cdot \mu(\theta)} \qquad (5.13)$$

*Due mainly to the controlling factor $\exp(\bar{\alpha} \cot\theta)$. As is indicated later the migration parameter $\bar{\alpha}$ is positive.

The ratio of the derivatives in equation (5.13) depends upon the relative magnitudes of $\bar{\alpha}$ and the ratio of the solution constants c_2/c_1. It is, therefore, necessary to evaluate the magnitudes of $\bar{\alpha}$ (from the experimental data) and to determine the nature of the ratio c_2/c_1 as well.

One method to estimate the migration parameter $\bar{\alpha}$ is provided by the Nernst-Einstein* equation (E1, D4)

$$\frac{\mu}{D} = \frac{e}{kT} \tag{5.14}$$

where

μ = electric mobility

D = diffusivity

e = electronic charge (1.6022×10^{-19} coulombs)

k = Boltzmann's constant

= 1.3805×10^{-23} joules/molecule/^{o} K

T = absolute temperature, ^{o} K

This equation is obtained for the case of ion transport in the solid state where the diffusion occurs under the effects of a concentration driving force and an electric field driving force. From the condition of electroneutrality the mass fluxes due to these two forces are equated to yield the number of ions per unit volume at a any point within the solid*. This is also obtained, independently,

---

*See, for example, reference M6.

from the Boltzmann's law and upon equating the two expressions for the ion (volume) concentration one gets the Nernst-Einstein equation (5.14).

The equation indicates that the ratio of electric mobility to the molecular diffusivity μ/D is only a function of the absolute temperature T. The underlying assumption is that the ionic migration occurs through the solid matrix*. The validity of the Nernst-Einstein equation, therefore, establishes a mechanism of migration. The ratio μ/D was calculated from equation (5.14) for each of the laboratory experiments and the results are shown in Table 5.11.

---

*Charles (C4) has, for example, postulated a migration mechanism on the basis of the fact that there are a number of equivalent positions of stability, for an alkali ion, within a glassy matrix. These positions occur around a non-bridging oxygen ion in the glass. Fly ash can be considered to be a glassy material (B3) in terms of its principal constituents which are metal oxides. Besides its chemical composition, a glass must also confirm to a non-crystalline structure given in terms of network formers and network modifiers. This terminology occurs in the context of the random network theory or the Warren-Zachariasen theory (02).

Table 5.11 The ratio of the electric mobility to molecular diffusivity (μ/D) from the Nernst-Einstein equation.

Experiment No.	Bed Temperature (^{o}K)	μ/D (couls/joule)*
1	419.83	27.644
2	447.85	25.915
3	427.60	27.142
4	430.38	26.967
5	429.83	27.001
6	372.60	31.149
7	399.83	29.027
8	338.72	34.264
9	338.72	34.264

The foregoing estimates of the μ/D ratio may now be used to evaluate the migration parameter $\bar{\alpha}$. The other terms lumped in this parameter have been evaluated earlier in Section 5.2 (Table 5.7).

$$\bar{\alpha} = \mu S E_a/D \ln K^{**} \qquad (5.1)$$

The values of $\bar{\alpha}$, from equation (5.1), are shown in Table 5.12.

*1 Volt = 1 joule/coulomb

**The units are as follows: $[\frac{\mu}{D}]$ = $Volt^{-1}$, [S] = m, $[E_a]$ = Volts/m, [K] = dimensionless.

Table 5.12. Values of the migration parameter $\bar{\alpha}$ from the Nernst-Einstein equation (5.14).

Experiment No.	Temperature (^{o}C)	$\vec{E}_a \times 10^{-5}$ * (V/m)	$K \times 10^{3}$	$\bar{\alpha}$
1	419.83	9.069	9.439	51.481
2	447.85	8.166	8.944	42.959
3	427.60	10.580	10.216	59.985
4	430.38	10.550	10.201	59.410
5	429.83	12.980	11.346	74.927
6	372.60	12.210	10.997	80.743
7	399.83	10.960	10.402	66.717
8	338.72	4.567	6.637	29.876
9	338.72	5.638	7.395	37.696

The nature of the variation of $\bar{\alpha}$ with the experimental parameters is already indicated by equation (5.1). However, the results of Table 5.12 indicate that $\bar{\alpha}$ is sensitive to changes in the average layer field strength E_a and bed temperature T than it is to variations in the constriction ratio. Furthermore, as explained subsequently it is also significant that the value of $\bar{\alpha}$ estimated above is much greater than unity.

* The average layer field strength E_a actually has a negative sign since both the negative voltage (due to the corona) and distance (from the plane) increase in the same direction. Hence $\bar{\alpha}$ is positive.

The (weighted) average slope $\frac{\partial \bar{c}}{\partial \theta}$ (ave) of the concentration profile over the surface of a single particle may be evaluated from equation (5.9) as follows:

$$\frac{\partial \bar{c}}{\partial \theta}\ (\text{ave}) = \int_{\theta_c}^{\pi-\theta_c} \frac{\partial \bar{c}}{\partial \theta} \cdot d\theta \Big/ \int_{\theta_c}^{\pi-\theta_c} d\theta \qquad (5.15)$$

where θ_c is the modified capillary angle.

Substituting for $\partial \bar{c}/\partial \theta$ and integrating the expression, one gets

$$\frac{\partial \bar{c}}{\partial \theta}^{*}\ (\text{ave}) \simeq \frac{1}{\pi-2\theta_c} \{\exp\ (\bar{\alpha}\ \cot\theta) + f_1 \sin\theta\}\Big|_{\theta_c}^{\pi-\theta_c}$$

$$\text{where } f_1 = c_2/c_1$$

This can be simplified to

$$\frac{\partial \bar{c}}{\partial \theta}\ (\text{ave}) \simeq -\frac{1}{\pi-2\theta_c}\{\exp\ (\bar{\alpha}\ \cot\ \theta_c)\} \qquad (5.16)$$

The magnitudes of the capillary angle θ_c for the laboratory experiments were shown earlier in Table 5.8. It is seen that θ_c is small enough in each case so that the above simplification is possible. An alternative method for obtaining an approximation to an average first derivative is to determine the ion concentrations

*In this case the asymptotic functions are treated as constants and equal to unity. This feature distinguishes equation (5.15) is view of the fact that it appears to be a linear derivative (see equation 5.19).

at $\theta = \theta_c$ and $\theta = \pi - \theta_c$. In the solution equation (4.40), the first term is dominant near the lower boundary, hence,

$$\bar{c}\ (\theta_c) \simeq \exp\ (\bar{\alpha}\ \cot\ \theta_c) \cdot w(\theta) \tag{5.17}$$

Similarly the second term dominates near upper boundary at $\theta = \pi - \theta_c$.

$$\bar{c}\ (\pi-\theta_c) \simeq f_1\ \sin\ (\pi-\theta_c) \cdot \mu_\pi\ (\pi-\theta_c) \tag{5.18}$$

Since both solutions (5.17) and (5.18) are near the regions of irregular singularity the asymptotic functions w and μ_π may be dropped* from the above. Additionally, $\sin\ (\pi-\theta_c) \ll \exp\ (\bar{\alpha}\ \cot\theta_c)$, so that the magnitude of (linear) concentration gradient is given by

$$\frac{d\bar{c}}{d\theta}\ (\text{linear})^{**} \simeq -\ \frac{\exp\ (\bar{\alpha}\ \cot\ \theta_c)}{\pi-2\theta_c} \tag{5.19}$$

Hence, by using the set of approximations applicable to this problem, one arrives at identical expressions for the two derivatives, $\frac{\partial\bar{c}}{\partial\theta}$ (ave) in equation (5.16 and $\frac{d\bar{c}}{d\theta}$ (linear) in equation (5.19). More significant is the fact that the effect of the second solution of

---

*As explained in Chapter 4, both $w(\theta)$ and $\mu_\pi\ (\tau-\theta) \to 1$ as $\theta \to 0$ and $\theta \to \pi-\theta_c$ respectively.

**It may be noted here that f_1 is not mentioned in this case. For the approximation [$\sin\ (\pi-\theta_c \ll \exp(\bar{\alpha}\ \cot\ \theta_c)$] not to hold, the value of the ratio of the solution constants, f_1, has to be extremely large. This is discussed later.

equation (4.40) is ignored in both cases. The average slope of the concentration profile is therefore almost completely determined by the magnitudes of the migration parameter $\bar{\alpha}$ and the modified capillary angle θ_c. This also follows from equations (5.10) and (5.11) in that the first term in equation (4.40) not only dominates in the region $\theta_c < \theta \leq \pi/2$ but it is also very large compared to the second term*. This assumption is used to obtain the expression for the "average" linear derivative, however, it may also be viewed as a corollary to the result:

$$\frac{\partial \bar{c}}{\partial \theta} \text{ (ave)} \simeq \frac{d\bar{c}}{d\theta} \text{ (linear)} \qquad (5.20)$$

It was stated in the footnote to equation (5.19) that the expression for the linear derivative is not valid in the event that the ratio of the solution constants is very large. For this to occur the magnitude of f_1 is of the order of $\exp(\bar{\alpha} \cot \theta_c)/\sin(\pi-\theta_c)$. In such a case the assumptions leading to the conclusion associated with equation (5.20) are not valid. In particular, the first and second terms in equation (4.40) cannot be ignored (relative to each other) except in the immediate neighborhood of the singularities. This aspect is further investigated on the basis of the following:

i) The nature of the variation of the local (first) derivative**.

---

*The value of $\bar{\alpha}$ is assumed to be given by the Nernst-Einstein equation (Table 5.12).

**Or, equivalently, the second derivative, $\partial^2\bar{c}/\partial\theta^2$.

ii) The experimental concentration profiles.

The set of equations (5.10) and (5.11) which are derived from equation (5.9) indicate that the absolute value of the first derivative decreases in the region of the lower boundary. Furthermore, irrespective of the value of c_2/c_1 (or f_1), equation (5.12) indicates that the slope increases in magnitude as the upper boundary is approached ($\theta \to \pi - \theta_c$). Then if f_1 is of the high order of magnitude indicated above i.e., $O^*\{\exp \bar{\alpha} \cot \theta_c/\sin(\pi-\theta_c)\}$ one can obtain an estimate of the average derivative by substituting this expression for c_2/c_1, into equation (5.9).

$$O\left\{\frac{\partial \bar{c}}{\partial \theta}\right\} \simeq -\bar{\alpha} \csc^2 \theta \exp(\bar{\alpha} \cot \theta) \cdot w(\theta) + \exp(\bar{\alpha} \cot \theta_c) \csc(\pi-\theta_c) \cos\theta \cdot \mu(\theta) \tag{5.21}$$

In a manner similar to equation (5.15) the weighted average can be obtained. The result is,

$$O\left\{\frac{\partial \bar{c}}{\partial \theta}\right\}(\text{ave}) \simeq \frac{1}{\pi-2\theta_c}\{\exp(\bar{\alpha} \cot \theta) + f_1 \sin\theta\}\Big|_{\theta_c}^{\pi-\theta_c} \tag{5.22}$$

This expression simplifies to the following,

$$\text{L.H.S.} \simeq \frac{1}{\pi-2\theta_c}[\exp\{\bar{\alpha} \cot(\pi-\theta_c)\} + \exp\{\bar{\alpha} \cot \theta_c\} \cdot \csc^2(\pi-\theta_c) - \exp\{\bar{\alpha} \cot \theta_c\} - \exp\{\bar{\alpha} \cot \theta_c\} \csc^2(\pi-\theta_c)]$$

*Order of magnitude.

or, upon neglecting the term exp $\{\bar{\alpha} \cot (\pi-\theta_c)\}$, one gets,

$$0 \left\{\frac{\partial \bar{c}}{\partial \theta}\right\} \text{(ave)} \simeq - \frac{\exp (\bar{\alpha} \cot \theta_c)}{\pi-2\theta_c} \qquad (5.23)$$

This result is the same as that obtained earlier in equations (5.16) and (5.19). However, it is observed that the numerator in the above equation has a minimum value of 1. This is suggested by the criterion that the concentration at the upper boundary ($\theta = \pi-\theta_c$) of the particle* cannot be zero or negative. Furthermore, this is in contrast to the experimental results in Table 2.10 where the penetration distances δ_{2p}, are shown to have real values.

The apparent disagreement with the experimental results stems from the (implicit) assumption of the order of magnitude of the migration parameter, $\bar{\alpha}$, from the Nernst-Einstein equation. The expressions for the average derivative [equations (5.16), (5.19) and (5.23)] are valid for the case where $\bar{\alpha}$ ranges from 30 to (approximately) 80 as in Table 5.12. However, this leads to extremely large (negative) values for the derivative in these equations. The existence of such (infinitely) large concentration gradients <u>within</u> the first (particulate) layer is not possible in view of the experimental observation referred to earlier.

The assumption of the values of $\bar{\alpha}$ (from Table 5.12) leads the approximation exp $(\bar{\alpha} \cot \theta_c) >>$ exp $\{\bar{\alpha} \cot (\pi-\theta_c)\}$. This inequality is used in all of the three cases resulting in the expressions (5.16), (5.19) and (5.23). It therefore follows that neither one of the terms is negligible

*This refers to a particle in the first layer (of particles in the ash bed) contacting the (probe) plane.

compared to the other and the "average" slope for all of three cases is given as:

$$\left.\frac{\partial \bar{c}}{\partial \theta}\right|_{mean} = \frac{1}{\pi - 2\theta_c} \left[\exp\{\bar{\alpha} \cot (\pi - \theta_c)\} - \exp (\bar{\alpha} \cot \theta_c)\right] \qquad (5.24)$$

Thus, for a non-zero value of δ_{2p} to exist, it is observed that the numerator of this expression cannot be greater than 1. This, therefore, is the cut-off value and may be used to estimate the maximum value of the migration parameter, $\bar{\alpha}_{max}$. The results of this evaluation are presented in Table 5.13.

Table 5.13. Estimates of the maximum values of the migration parameter, $\bar{\alpha}_{max}$, for the laboratory experiments.

Experiment No.	Modified Capillary angle, θ_c (from Table 5.8)	$\bar{\alpha}_{max}$
1	1.3910	1.220×10^{-2}
2	1.0247	8.600×10^{-3}
3	1.1705	9.830×10^{-3}
4	1.1688	9.800×10^{-3}
5	1.6240	3.710×10^{-2}
6	1.6690	3.810×10^{-2}
7	1.5670	3.590×10^{-2}
8	1.3420	1.150×10^{-2}
9	1.4160	1.200×10^{-2}

The significance of the results in Table 5.13 lies in the fact that the variations in the magnitude of the modified capillary angle influence the migration parameter $\bar{\alpha}$ and, hence, the penetration distance (δ_{2p}) as well. Additionally, the nature of the effect of the capillary angle upon $\bar{\alpha}$ is also indicated. It is seen by comparing cases 8 and 9* (in the table) that an increase in the value of θ_c corresponds to an increase in the maximum permissible value of $\bar{\alpha}$. Thus, for a fixed $\bar{\alpha}$, it is seen from equation (5.24) that $\frac{\partial \bar{c}}{\partial \theta}\Big|_{mean}$ decreases with increasing θ_c. This implies a larger penetration distance and hence an increase in the extent of migration of the alkali ion.

The Nernst-Einstein values of the migration parameter exceed the corresponding $\bar{\alpha}_{max}$ by several orders of magnitude (Tables 5.12 and 5.13). As discussed in the next section, this is an important conclusion since it suggests that the ion migration mechanism mentioned earlier (in this section) may not be operative. Finally, as was mentioned in the overview (to this chapter), the objective of the analysis based on the Nernst-Einstein theory was to substantiate the above speculation.

The next section deals with a discussion of the various estimates and analyses conducted in this chapter so far. The important assumptions, made in this connection, are mentioned and the effects of departures from the idealized model are discussed.

---

*The experimental conditions for these two cases are similar. See Section 5.2.

5.5 Discussion

In Section 5.1 the laboratory apparatus which was used for the ion migration experiments and the humidity measurements, is described. The procedures used for both of these experiments are not free from the usual measurement errors. It was also mentioned earlier that the moisture content (B_{wo}) determination needs to be made under conditions (water bath temperature, air flow rate) identical to the corresponding ion migration experiment. The two important sources of error in this regard are:

i) Moisture condensation in the (initially cold) line leading to the ice bath impinger. This is significant because the volumes of (humid) air sampled were low (less than 10 cu. ft).

ii) Water level in the (bubbler) impingers. During the migration experiments* the glass impingers were periodically opened to be refilled. The average water level may not be the same as that during the relatively short (≃ 2 hours) humidity experiments and this affects the degree of saturation of the air.

Both of these sources of error have a direct bearing upon the calculated value of B_{wo}.

The ion migration experiments presented two significant procedural problems. One of these involves the scraping method used to remove the samples from the ash bed in the probe chamber. With few exceptions, almost all of the samples were carefully removed by

*Which ran over a period of 100 hours (typically).

scraping over the bed just once; however, during this process, there is a strong likelihood of some degree of mixing between vertical layers of particles. This is particularly significant in view of the small* penetration distances for particle layers within the thickness δ_{2p} from the plane of the resistivity probe.

The second procedural problem deals with the analytical technique** after (neutron) irradiation of the individual samples. It is essential that the geometry (location of the samples) with respect to the Ge-Li detector be identical for all of the samples of the experiment. However, during the transfer of fly ash into the plastic vial** some material adheres to the side of the vial and this affects the counting data.

The minimum measureable thickness of the ash layer depends upon the pitch of the turn screw, and this value (thickness) is equal to 0.009922 cm. Since the mean particle diameter is 19.15 μm, this minimum thickness corresponds to a (layer) sample which is approximately "5 particles" thick. Hence the measured sodium concentration for such a sample is averaged over 5 particles which were originally in one vertical stack in the ash bed. In the plots of Figures 5.9 through 5.15 the sample concentration, for an "original"† layer, is indicated by a horizontal line where the length of the line is proportional to the layer thickness.†† The penetration thickness,

---

*The penetration distances are small relative to the thickness of ash bed. For example, δ_{2p} is 9.6% of the bed thickness in experiment no. 3 (Table 5.9).

**From the ash bed.

δ_{2p}, is estimated as the distance from the bottom of the ash bed (where c/c_o equals unity) to the position of the first layer that exhibits a (mean) matrix sodium ion concentration. As mentioned in the previous section, the value of δ_{2p} is dependent upon the magnitude of the migration parameter $\bar{\alpha}$.

The dimensionless parameter $\bar{\alpha}$ is constituted by the fundamental parameters [equation (5.1)] of the model and these are evaluated in Section 5.2.* The extent of capillary condensation is determined by the magnitude of the capillary angle θ_{cc}. This, in turn, depends upon the radius of curvature, $\bar{R}$, of the capillary condensate. The evaluation of $\bar{R}$, from the exact thermodynamic equation (2.67), is based on the material of Chapter 2. A detailed discussion pertaining to the validity of this equation has been presented in Appendices C, D and E. In order to evaluate $\bar{R}$ the relative saturation α must be known. The relative saturation $\bar{\alpha}$ is obtained from the moisture content B_{wo} (determined from the humidity experiments) and the probe temperature T. In Table 5.3 the (pore) dimensional restriction is used to conclude that capillary condensation cannot occur for the conditions of Experiment Nos. 2, 3 and 4. The data in Tables 5.2 and 5.3 indicate that for Experiment 2 the probe temperature

---

†This term was explained in Section 5.3.

††In Experiment numbers 1 and 7, the porous ash bed collapsed near the plane yielding a concentration profile with a maximum value for the lowest layer and a mean (matrix) composition for every subsequent sample. An evaluation of the penetration distance, δ_{2p}, is not possible in such cases and hence these data are not presented.

*Except for the ratio μ/D.

is too high (to permit capillary condensation) relative to a water bath temperature of 146° F. Increasing the water bath temperature raises the mositure content, B_{wo}, of the air and the likelihood of capillary condensation is greater. The explanation given above for Experiment 2 is also valid for the other two cases (3 and 4). A comparison of the data (results) for Experiments 4 and 5 indicates that at a (probe) temperature of about 157° C the water bath temperature must be at least between 160° C and 175° C for capillary condensation to occur.

The magnitude of the capillary ring angle, θ_{cc} does not identify the location of the outer ring of the condensate for the case of an "area"* contact. This type of contact occurs due to the presence of a cohesive force acting on particles (which are assumed to be elastic). This force occurs when an electric field is applied across a resistive body of particulates. In Section 5.2, the empirical relation of McLean (M3) is used to evaluate this force, F_T [equation (5.3)]. It is seen that F_T is entirely given by the average ash bed field strength E_a (with the exception of constants A and δ). This force, F_T, is then substituted into the Hertz equation to evaluate the area of contact** or the constriction ratio. McLean's empirical equation is simple to use and the effect of errors in the resulting estimate are mitigated by the

---

*As opposed to a point contact between the solid spheres.

**In the analysis of Section (5.4) this area is assumed to be circular in agreement with the assumption made in Section 3.4, Chapter 3.

fact that the logarithm of this term is used in the expression for the migration parameter $\bar{\alpha}$.

The evaluation of the constriction ratio K presupposes the determination of E_a. In the development of the model in Chapter 4, E_a is isolated as a constant. Since the average field strength is given by the voltage drop across the bed (ΔV) divided by its thickness, the assumption of a constant E_a is tantamount to the assumption that ΔV is constant over the time duration of the experiment. This, in turn, implies that the bulk resistivity of the ash bed is a constant* and one concludes that the leakage current must have a steady state value. Since the leakage current is comprised of both the electronic and ionic flow, a steady state current implies that the ionic migration also occurs at steady state. Hence it is seen that the assumption of constant $\vec{E}_a$ also stipulates that no local concentration changes (with respect to time) occur in the ash bed. This is in agreement with the steady state differential equation (4.9), Chapter 4. However, it has been noted in Section 5.2 that the current-time do not strictly confirm to the steady state assumption. In any case the I_{ave} values (Table 5.5) are closer to the (final) relaxed current and the steady state assumption is used to evaluate a (time weighted) mean value of E_a from the plots in Figures 5.6, 5.7 and 5.8.

The existence of a non zero area of contact** (or the constriction ratio K) implies that the outer edge of the capillary ring is "pushed"

---

*This conclusion follows from Section 1.2, Chapter 1.

**Or a point contact.

out of the pore by the amount of the angle* corresponding to the contact radius 'a' (Figure 4.1). Hence, to determine the "dry" resistance path along the surface, the capillary ring angle θ_{cc} must be increased by the amount arc tan a/s [equation (5.6)]. This yields the modified capillary angle θ_c. It is noted here that θ_c depends ultimately, in part, upon the magnitude of the average layer field strength E_a.

The calculations of Section 5.2 enable one to determine all of the model parameters with the exception of the electric mobility-molecular diffusivity ratio, μ/D. This being the only unknown (in the expression for $\bar{\alpha}$), it was determined appropriate to examine the shape of the concentration profiles before evaluating μ/D (or $\bar{\alpha}$). The experimental ion concentration profiles are shown as plots in Section 5.3. The key observation here is that the plots are characterized by penetration distances, δ_{2p}. Although relatively small in magnitude a non zero value of δ_{2p} indicates the existence of finite (negative) concentration gradients within the thickness δ_{2p} from the lower boundary of the ash layer. It would be expected that an increase in θ_{cc} (or the amount of capillary condensate) results in an increase in the penetration distance. This was implicitly suggested in the speculations in Chapters 2 and 3.

In Section 5.4 the nature of the experimental plots (Figures 5.9 through 5.15) is interpreted in terms of the solution [for the ion concentration, equation (4.40)] to the theoretical model

---

* The angle subtended at the center of a particulate sphere.

of Chapter 4. The basis of such a comparison lies in the magnitude of the average (first) derivative for the concentration. The Nernst-Einstein equation (5.14), which gives μ/D only in terms of the absolute temperature, is used to estimate the migration parameter $\bar{\alpha}$. This equation presupposes a mechanism of ion migration through the solid matrix* of the fly ash. The results are shown in Table 5.12.

The order of magnitudes of $\bar{\alpha}$ in Table 5.12 is implicitly assumed in the analysis following the table. The key assumption made in the evaluation of an average derivative (for the concentration) is:

$$\exp\{\bar{\alpha}\cot(\pi-\theta_c)\} \ll \exp(\bar{\alpha}\cot\theta_c) \qquad (5.25)$$

This inequality is valid for the first layer of particles at the bottom of the experimental ash bed. Such a criterion translates into an infinitely large (negative) concentration gradient over a particle. This has been discussed in the previous section where it is also noted that this feature is in contrast to the plots of Figures 5.9 through 5.15. It is therefore concluded that such high values of $\bar{\alpha}$ are not possible in view of the observed penetration distances.**

Hence, in the analysis following this conclusion, it is recognized that inequality (5.25) is not valid anywhere in the

---

*This migration occurs on the surface of the particulates.

**Although δ_{2p} is relatively small, it is not negligible.

region $\theta_c \leq \theta \leq \pi-\theta_c$. This results in a modified expression for the average (or mean) derivative in equation (5.24) which is used to evaluate new values of $\bar{\alpha}$. The assumption made here is that the maximum (negative) value of the derivative corresponds to an ion concentration of zero at the upper boundary of a particle ($\theta = \pi-\theta_c$). This enables one to estimate the maximum value of the migration parameter, $\bar{\alpha}_{max}$, for each of the experiments. The results of these calculations are shown in Table 5.13. There are two important observations that may be made with regard to Table 5.13.

i) The influence of the modified capillary angle upon the migration parameter, $\bar{\alpha}_{max}$.*

ii) The difference in the magnitudes of $\bar{\alpha}_{max}$ and the $\bar{\alpha}$ obtained from the Nernst-Einstein equation.

This latter observation indicates the wide discrepancy between the prediction (for the value of $\bar{\alpha}$) of the Nernst Einstein equation and the $\bar{\alpha}_{max}$ obtained in Table (5.13). This discrepancy leads one to the speculation that the ionic migration does not proceed through the particulate matrix.

One of the conclusions that follows from this is that the migration parameter for the laboratory experiments is indeed much lower than that predicted by the Nernst-Einstein equation. Furthermore, in view of the (relatively) lower values of $\bar{\alpha}$, the ionic migration on the fly ash surface is perhaps facilitated by an additional phenomenon not accounted for in this work.

---

*This has been discussed in the previous section.

In this connection it may be recalled that the effect of micropore adsorption* has not been considered in this work. This was stated earlier in the overview to Chapter 2. Micropore adsorption refers to the (multilayer) adsorption upon the particle surface. It is expected that the effect of this phenomenon would be to increase the penetration thickness and hence to enhance the "extent of the ionic migration". As stated earlier, this effect would be in agreement with the lower values of the migration parameter $\bar{\alpha}$,

As observed in Table 5.13, the influence of capillary condensation is demonstrated by the dependence of $\bar{\alpha}_{max}$ upon θ_c. This is not apparent from equation (5.1) where $\bar{\alpha}$ appears to be independent of θ_c. Hence the coupling of the phenomena of capillary condensation with the other parameters in equation (5.1) is established.

Finally, it may be noted that the results of the laboratory experiments are used to interpret the phenomenon of (alkali) ion migration in terms of two important quantities viz., θ_c and $\bar{\alpha}$. The shape of the concentration profiles permits one to evaluate the relative effects of both these terms. In essence, the theoretical bases behind the development of θ_c and α^* were presented in Chapters 2 and 3 respectively.

---

*Of moisture.

CHAPTER 6

CONCLUSIONS

The major implications of the results of the theoretical and the experimental portions of this research are presented in this Chapter. From the perspective of the mathematical model formulated in Chapter 4 it is seen that the effects* of the two important physical factors of capillary condensation and the (applied) electric field are examined in this work. The quantitative effects of these factors are individually evaluated (in Chapters 2 and 3) from the corresponding thermodynamic and the electric contact theories.

The results of the analyses of Chapter 2 and 3 are incorporated into the model (of Chapter 4) for the surface migration of alkali ions. As mentioned at the end of Chapter 5, the objective in this case is to determine the extent of the ionic migration within the particulate bed. It is assumed, a priori, that the total leakage current through the bed is comprised of an electronic current and an ionic current. For a fixed value of the voltage drop across the bed, the leakage current is inversely proportional to the bulk resistivity of the fly ash. Hence, if the (alkali) ion concentration of the particulate bed is artifically increased (by chemical conditioning) then the leakage current is also expected to increase. As a result of this, the bulk resistivity decreases.

---

*Upon a particulate bed.

The term bulk resistivity refers to the overall resistivity of the particulate bed, irrespective of the nature of conduction*. A new method for the determination of this property is proposed in Chapter 1**, and the advantages of this (point-plane) technique are underscored in light of the experimental results obtained from power-plant measurements. Furthermore, the influence of the experimental variables upon the bulk resistivity is also indicated in this chapter. This, therefore, provides a convenient starting point in view of the overall problem that provided the motivation for this work.

In Chapter 2 (Section 2.14) the uncertainties involved in the use of the Kelvin equation are discussed. It is shown that the "uncertainties" increase with decreasing volumes of the capillary condensate (as the gas-liquid interface recedes into the macropore). The magnitudes of the pertinent thermodynamic variables ($\Delta\mu_l$, $\Delta\mu^c{}_l$, and χ_l)*† are estimated for small (molecular) volumes of the capillary condensate (Appendices C, D and E). The liquid (condensate) is under tension† and its physical property values†† depart from

---

*Either surface or volume conduction. The bulk resistivity has units of ohm-cm.

**See also Appendix A.

*†Liquid phase chemical potential, $\Delta\mu_l$ correction term, and the isothermal susceptibility.

†Negative pressures.

††Freezing point and latent heat of vaporization, for example.

those normally attributed to it (C1). It is concluded that, under these circumstances, the compressibility equation of state for the liquid cannot be used in the region of tension. This, in turn, suggests the non-linear variation of the isothermal susceptibility, χ_1, with the liquid density. This inference is contrary to the assumption made by Melrose (M4) in his paper.

As discussed in Section 2.14, there exists a lower limit to the radius of curvature, $\overline{R}$, of the capillary condensate. This limit is specified by one of the following criteria:

i) Size of the liquid molecule (pore dimensional restriction)

ii) Rupture of the liquid, at which point $\chi_1 = 0$ (mechanical instability criterion).

It is observed that the first criterion is the limiting one in the temperature range of the ion migration experiments. It is also shown that the modified liquid potential correction term $\Delta\mu^c{}_{11}{}^*$ < $\Delta\mu^c{}_1$, and the net effect of this inequality is such that the use of the thermodynamic equation (2.67) is favored.

In Chapter 3, the electric fields $\vec{E}_1$ and $\vec{E}_s(\theta)$ near the region of the interparticle contact (or macropore) are examined. This chapter begins with a description of the electric contact between two (spherical) particles. A generalized expression for the contact resistance is formulated** and it is seen that this resistance induces

*This term is based upon the inclusion of additional contributions to the total change in the liquid potential (from the reference state), $\Delta\mu^c{}_1$.

**This expression is analogous to that derived for the case of heat flow (C3).

electric field strengths which assume near breakdown values near the immediate neighborhood of the contact. This is true for the case where the externally applied voltage gradient $\vec{E}_a$ is of the same order of magnitude as that commonly encountered in resistivity measurements. As a result of this, the gap (near the contact) experiences an electric breakdown and hence a gap discharge. It is observed that this phenomenon is largely responsible for the non linear I-V characteristics of the particulate layer (Chapter 1).

The expression for the surface field strength E_s (θ) is derived in Section 3.8* and its variation with position on the particle surface is obtained. It is observed that E_s (θ) behaves in the same way as $\vec{E}_1$** (with respect to position), however the regions of electrical breakdown for the two cases are different (Figure 3.12). The effect of the constriction ratio $\frac{a}{S}$ (or $\frac{a}{2S}$) upon the fields E_1 and E_s (θ) is noted viz., while E_s (θ) varies in the same direction as $\frac{a}{S}$, the expression for E_1 indicates an inverse dependence (upon $\frac{a}{S}$).

The ion migration problem (for the configuration of the experimental set up) is mathematically represented in Chapter 4. The method of dominant balance solution for the first order differential equation (4.9) is an approximation to the unknown exact solution and is derived near the regions of the (irregular) singularities of the equation ($\theta = 0, \pi$). These two regions "coincide" with the boundaries (of a particle) for the diffusion problem, as indicated by the magnitudes of the modified capillary angle, θ_c, in

---

*This derivation is based of the surface current.

**The axial field strength.

Chapter 5. This is a fortuitous circumstance and thus provides a stronger basis for the validity of the MDB solution.

The identification and subsequent evaluation of the model parameters in Chapter 5 constitute an important part of this work. The electric mobility and the diffusion coefficient D, the particle diameter S and the constriction ratio K are all lumped into a dimensionless migration parameter $\bar{\alpha}$. The significance of this parameter with regard to the ion penetration distance, δ_{2p}, is elucidated in Section 5.4. A higher value of $\bar{\alpha}$ suggests a smaller penetration distance and vice versa. Hence it is evident [from equation (5.1)] that as the particle diameter increases the penetration distance decreases.** If the ionic current is assumed to contribute to the leakage current one would expect the bulk (surface) resistivity to increase with increasing particle size. This conclusion concurs with the results of McLean's semi-empirical analysis (M1). However this analysis (M1) recognizes the presence of electronic conduction only. Since both are charge carriers* it is expected that their qualitative response to a change in any model parameter to be similar. Hence, an increase in the leakage current should occur due to an increase in both the electronic

---

*Electrons and alkali ions have different electrical mobility.

**It is observed that the upper boundary of the ash bed does not affect the value of δ_{2p}. Hence a smaller thickness of the fly ash corresponds to a larger value of δ_{2p} (relative to the bed thickness) and when δ_{2p} is equal to the bed thickness the flow of the ionic charge carriers through the bed is possible.

and ionic currents although smaller). As indicated in plot for the power plant data in Figure 1.3, a higher leakage current implies a lower resistivity (ρ_b). It is seen (in the same plot) that the voltage drop (and hence E_a) across the ash bed increases as ρ_b decreases. However, this is contrary to the suggestion in equation (5.1)*. In a more realistic model, therefore, one would expect the influence of E_a to be opposite to that suggested in the expression for $\bar{\alpha}$. In effect, the power plant resistivity data suggest that the migration parameter does not fully account for the (overall) influence of E_a and hence the expression (5.1) lacks in (certain) qualitative features.

The quantitative features of $\bar{\alpha}$ are observed with regard to the Nernst-Einstein equation (5.14) in Section 5.4, Chapter 5. The laboratory experimental results indicate that the values of $\bar{\alpha}$ (and hence the concentration gradients) predicted by the above equation are far too high. Hence it is co ncluded that the ion (surface) migration does not occur through the solid matrix of the particulate and the possibility of the occurence of other** physical phenomena is strong.

In this context, the assumption of the "dry" resistance path ($\theta_c \leq \theta \leq \pi-\theta_c$), on the particle surface, is significant. The results of Table 5.13 establish the fact that an increase in the volume of capillary condensate (increase in θ_c) corresponds to an increase in the penetration thickness. Hence, if the resistance path $\theta_c \leq \theta \leq \pi-\theta_c$ is not assumed to be dry, i.e., if multilayer adsorption occurs, one

---

*An increase in E_a increases the cohesive force F_z [equation (5.5)] and hence the constriction ratio K (< 1.0).

**Not included in this work.

expects a penetration distance of 100% (of the ash bed thickness). Equivalently, this suggests the possibility of ionic current.

The phenomenon of multilayer adsorption on oxide* surfaces has been investigated by several authors (Z1). The structure of the bonded adsorbate molecule is different (from water) and therefore the ionic conductivity is not the same as that for water. Furthermore, it has also been observed that the conductivity (which is related to the dielectric constant) changes as the number of (adsorbed) layers upon the surface changes. This indicates that the degree of adsorption affects the (extent of) ion migration.

On the basis of fly ash resistivity (conditioning) tests conducted in the power plant, it was determined that the amount of adsorption (capillary condensation and surface adsorption) does indeed affect the resistivity. That the correlation between these two variables is negative is indicated by the results in Table 6.1.

The apparatus for the conditioning experiments in the power plant is shown in Figure A.4. The resistivity probe and the stack sampler were used in these experiments and these are described in Appendices A and I respectively. The conditioning equipment comprises of a race track unit and a jet sprayer arrangement for moisture injection. Water is fed, at a predetermined rate, into the flue gas entering the race track unit. The resistivity measurements are conducted upon the gas exiting this unit.

The surface resitivity values in Table 6.1 indicate the coupled

*Fly ash is principally composed of alkali and other metal oxides.

Table 6.1. Power Plant Conditioning Data

Date	Probe Temperature (^{o}F)	B_{wo} %	ρ_b† ohm-cm
2/12	225	4.207	2.921×10^{11}
2/13	198	3.220	2.381×10^{11}
2/14	220	4.965	1.667×10^{11}
5/2	223	5.242	9.886×10^{10}
5/2	227	4.382	1.069×10^{11}
5/8	230	4.006*	**R - 9.811×10^{11}
			**C - 4.230×10^{11}
5/9	230	7.345*	R - 5.586×10^{11}
			C - 1.620×10^{11}
6/24	218	5.587*	R - 1.199×10^{11}
			C - 8.946×10^{9}
6/26	235	7.536*	R - 4.061×10^{11}
			C - 7.119×10^{10}
6/30	224	7.535*	R - 1.521×10^{11}
			C - 8.657×10^{9}

*These values refer to the (moisture) content during conditioning.

**Terms R and C are the raw and conditioned fly resistivities.

†As measured by technique in Appendix A.

effects of temperature (Figure I.1) and moisture content, B_{WO}. It is clearly evident from the last five results (5/8 - 6/30) that the effect of the addition of moisture (conditioning), into the flue gas, is demonstrated by a lowering of the ash resistivity.

Hence, in the context of ionic migration, it may be concluded that both surface (multilayer) adsorption and capillary condensation are important factors. The lowering of the ash resistivity is accompanied by an increase in both the electronic and ionic currents in the presence of capillary condensate and the adsorbate in the ash bed. This is contrary to the suggestion of Bickelhaupt (B1) that resistivity is a function of the alkali ion content of the fly ash. The author's (B1) correlation of resistivity with the alkali ion content is at odds with the conclusions of this work, since the effect of moisture condensation is ignored. It is important to recognize that a key feature of the conclusions of this work is based upon a migration mechanism that is different from the one suggested for volume conduction through glassy materials.*

The effect of enhanced adsorption of water vapor due to the presence of hygroscopic (chemical) conditioning agents is pertinent to the above conclusion. It may be speculated that multilayer adsorption is perhaps increased due to the presence of the conditioning agent.

Finally, it may be noted that the results of this work provide a theoretical basis for the speculations and conclusions in this chapter. These conclusions may be used to develop a model at least

---

*This mode of conduction agrees with the Nernst-Einstein equation.

to the extent where the effects of surface adsorption is included. This development may lead to an estimate of the relative magnitudes of the ionic and electronic currents and thus resolve the present controversy (M7) regarding the sensitivity of resistivity (ρ_b) to the chemical composition of the fly ash.

APPENDIX A

A.1. The Resistivity Probe

The operating manual for the SRI resistivity probe used in all of the field tests has been presented in reference S2. Briefly, the probe consists of a movable disk mounted coaxially with a tapering needle, the tip of which (corona point) is at a fixed distance away from a symmetrically situated plane (Figures A.1,A.2). A perforated sheet metal shroud protects the deposited layer from outside turbulence (Figure A.3).

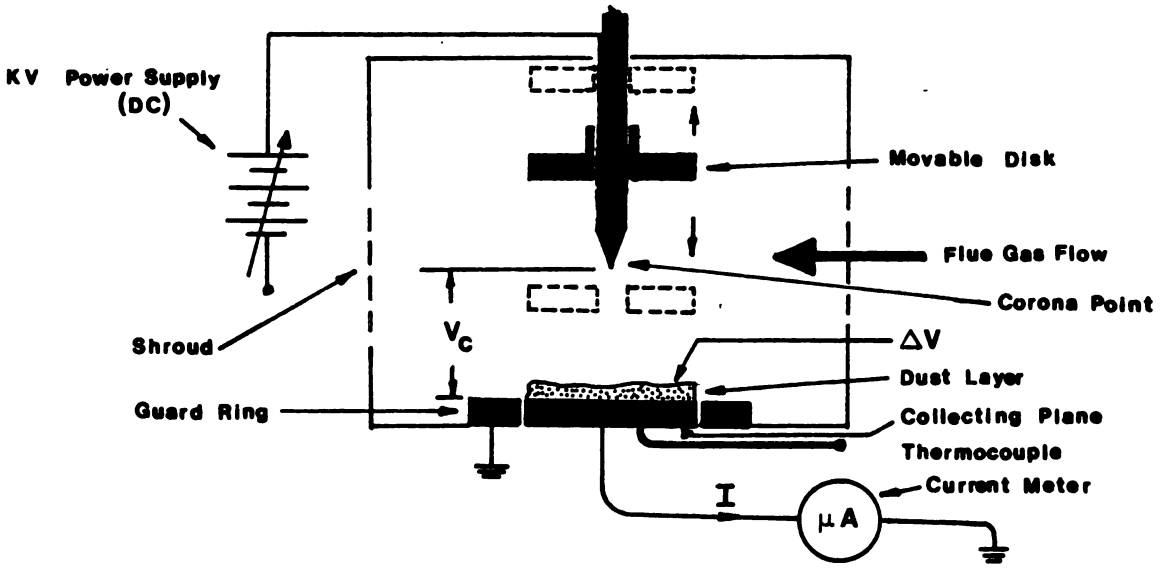

Figure A.1 Schematic illustration of the probe collection chamber.

A.2. Experimental Procedures

In either of two measurement techniques, herein referred to as the

APPENDIX A

Figure A.2. Detail of disk, point-plate arrangement.

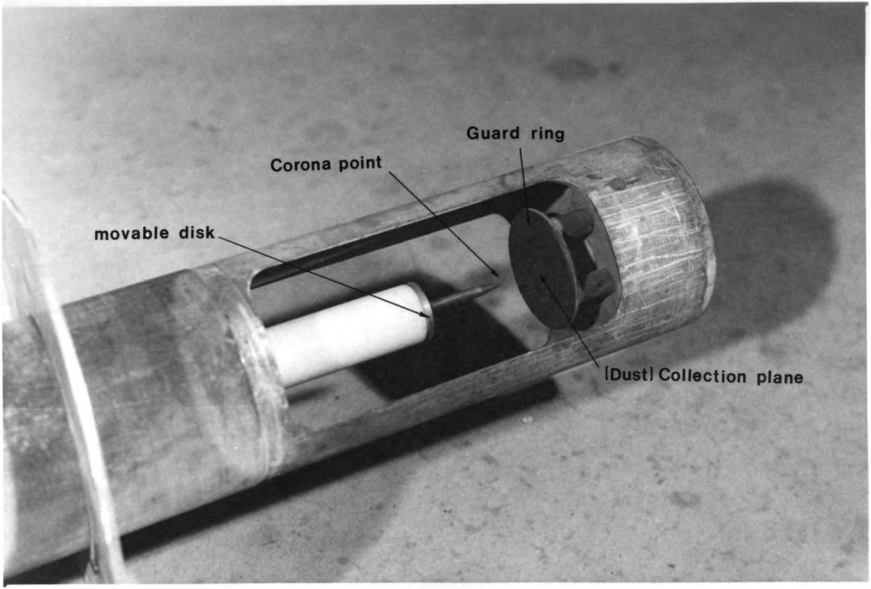
Guard ring
Corona point
movable disk
[Dust] Collection plane

Figure A.3. (SRI) Resistivity probe and shroud.

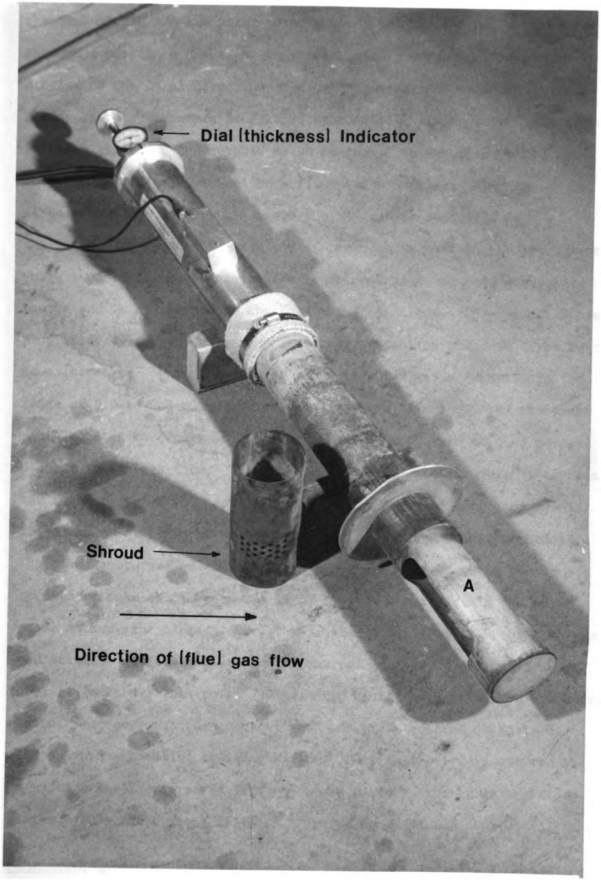
Dial [thickness] Indicator
Shroud
A
Direction of [flue] gas flow

the disk method and the point plane method, the clean probe is inserted through a port into the flue gas stream, with shroud openings perpendicular to the local direction of flow to prevent deposition. After a steady state temperature is reached, the initial clean plate dial reading is taken and the probe rotated by 90 degrees. In the disk method the collection voltage V_c is set to a fixed value depending upon the point plane distance. During this stage the fly ash is deposited on the plane. The principle involved is the same as that in the precipitator where a particle upon entering the charging region acquires a negative charge and is driven toward the collecting electrode. The current decreases progressively (due to corona current suppression) as the dust layer thickness increases. When the current drops to a low value (usually in the range of 0.0 to 0.5 microamperes), the voltage is cut off and the probe again rotated carefully so that the shroud openings are aligned perpendicular to the gas flow. The disk is gradually lowered until it touches the top surface of the particulate layer and the dial indicator needle ceases to move. This gives the final dial reading and dust thickness. The power is turned on and the leakage current corresponding to the applied voltage ΔV, is measured until sparkover occurs. In the point plane method, the clean plate I-V characteristics (actually the flue gas characteristics) are measured after thermal equilibration, until sparkover is reached. This point is indicated by the sudden jump in the current value. The power is then shut off and the probe rotated so that the slots are now parallel to the gas flow. Dust collection is started at a voltage level determined from the clean plate sparkover as explained later. When the current falls to a low value as in the disk method, the

probe is rotated carefully to its initial position and the particulate layer I-V characteristics measured until breakdown. The layer thickness is measured at this time. Knowing the independent variables in Equation 1.1 the ash resistivity can be calculated.

$$P_b = (\Delta V)\ (A)\ /\ (I)\ (d) \qquad (1.1)$$

(see Chapter 1)

In both of these methods, care should be taken so that the flue gas temperature does not change appreciably during the test. The general experimental set up is shown in Figure A.4.

A.3. Comparison of Procedures

The initial resistivity tests were conducted by the disk method, however this was later discarded in favor of the point plane technique owing to several inherent problems. In principle, though, both procedures are equally valid and should yield identical results. The disk method suffers from the severe disadvantage that the leakage current can only be measured when the movable disk touches the upper surface of the initially uncompacted particulate layer. This disturbs the structural integrity of the dust deposit and (particularly in cases of high thicknesses) it was found that a portion of the dust was dislodged. A physical compression of the dust is unavoidable and causes a change in the resistivity due to rearrangement of the layer (M1). Furthermore, there exists a strong likelihood (as was discovered in numerous instances) that all of the disk surface may not uniformly contact the surface of the layer. This results in air gaps at some points. This fact therefore introduced a serious error in the reported value of the ash resistivity.

Figure A.4. Power plant experimental set up.

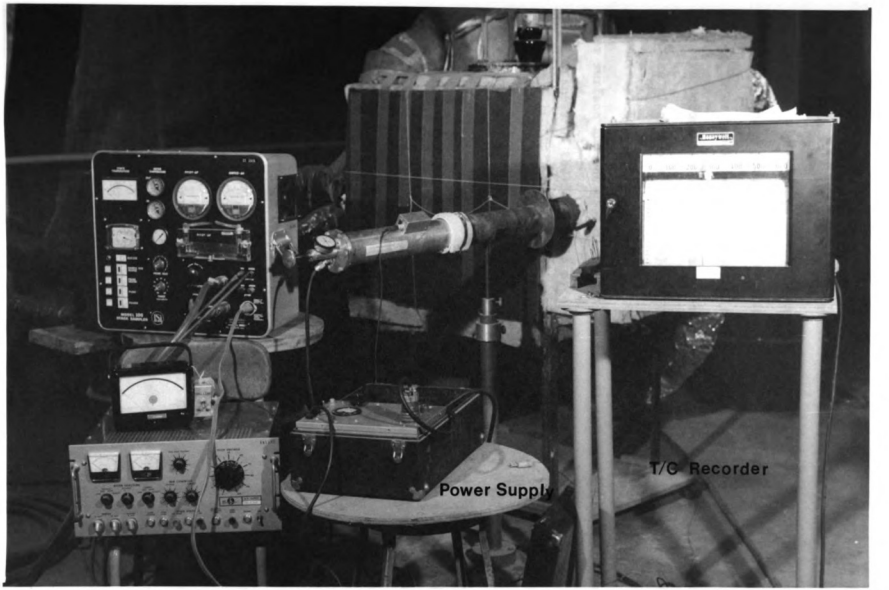
Power Supply
T/C Recorder

The measurement of leakage current by the disk method was especially difficult with ashes of high resistivity. When the value exceeded 5.0 x 10^{11} ohm-cm, wide current fluctuations (in the microampere range) were observed. These progressively worsened as the applied voltage (corresponding to layer breakdown) was approached. In the point plane method, the negative corona is used to obtain the current voltage characteristics for both the clean plate (gas only) and the particulate layer (gas plus dust). In contrast to the disk method, there is no external contact with the layer surface and the disk is lowered to contact the surface to determine the thickness of the layer only after all current voltage measurements are completed. In the disk method, the reported value of the resistivity corresponds to the last set of recorded current-voltage values just prior to total breakdown. However, in the neighborhood of the breakdown region, fluctuations of current are very strong. The resistivity value reported is quite possibly inconsistent and would vary from experiment to experiment with the same fly ash. This is particularly true for high resistivity dusts of thicknesses exceeding 0.5 mm and for non uniform deposits, as explained earlier. Hence this method establishes a value for the ash resistivity in a voltage region where it is likely to be most suspect. Further, the suggestion of reporting resistivity just prior to sparkover is non-specific since the last set of I-V data partially depends upon the judgement of the personnel involved. It is noteworthy at this point that once a small spark goes through the dust even before total breakdown is encountered, the dust layer characteristics change.

The procedure the disk method permits evaluation of the resistivity at all field strengths below sparkover. However, as indicated

earlier only the final value is useful. The point plane technique also enables one to calculate the same at arbitrarily small current increments (Chapter 1). Since no voltage is applied "directly" on the upper surface of the fragile dust layer, the problems associated with the disk method do not arise. It is also difficult to identify the incipient spark point M (Figure 1.3) in the disk technique particularly where the first spark is weak and is immediately followed by a succession of sparks.

A.4. Optimal Layer Thickness

As mentioned in Chapter 1 the sparkover voltage for negative corona drops with increasing values of the resistivity for the ash layer upon the plane. That point M (Figure A.5) lies to the left of the clean plate sparkover indicates incipient sparking at that point. This is illustrated in Figure A.5 where HD, IE, JF and KG are the "dirty" plate characteristics for dust layers of different thicknesses, and D, E, F and G are the corresponding spark points. The higher the value of the constant voltage (V_c) during collection, and the longer the collection time, the higher will be the corresponding layer thickness.

As the thickness of the dust layer of a given resistivity increases upon the plane, the corona initiation voltage, V_{ID}, also increases due to the "insulating" effect of the ash. Curves HD, IE, JF and KG represent layers of increasing thicknesses and lie below each other due to the increasing corona current suppression. The net result of increasing the thickness of a particulate layer upon the plane is that the incipient sparking voltage is shifted to lower current values. By the same token a low dust layer thickness will move the dust layer I-V curve close to the clean plate characteristics and incipient sparking will be close to

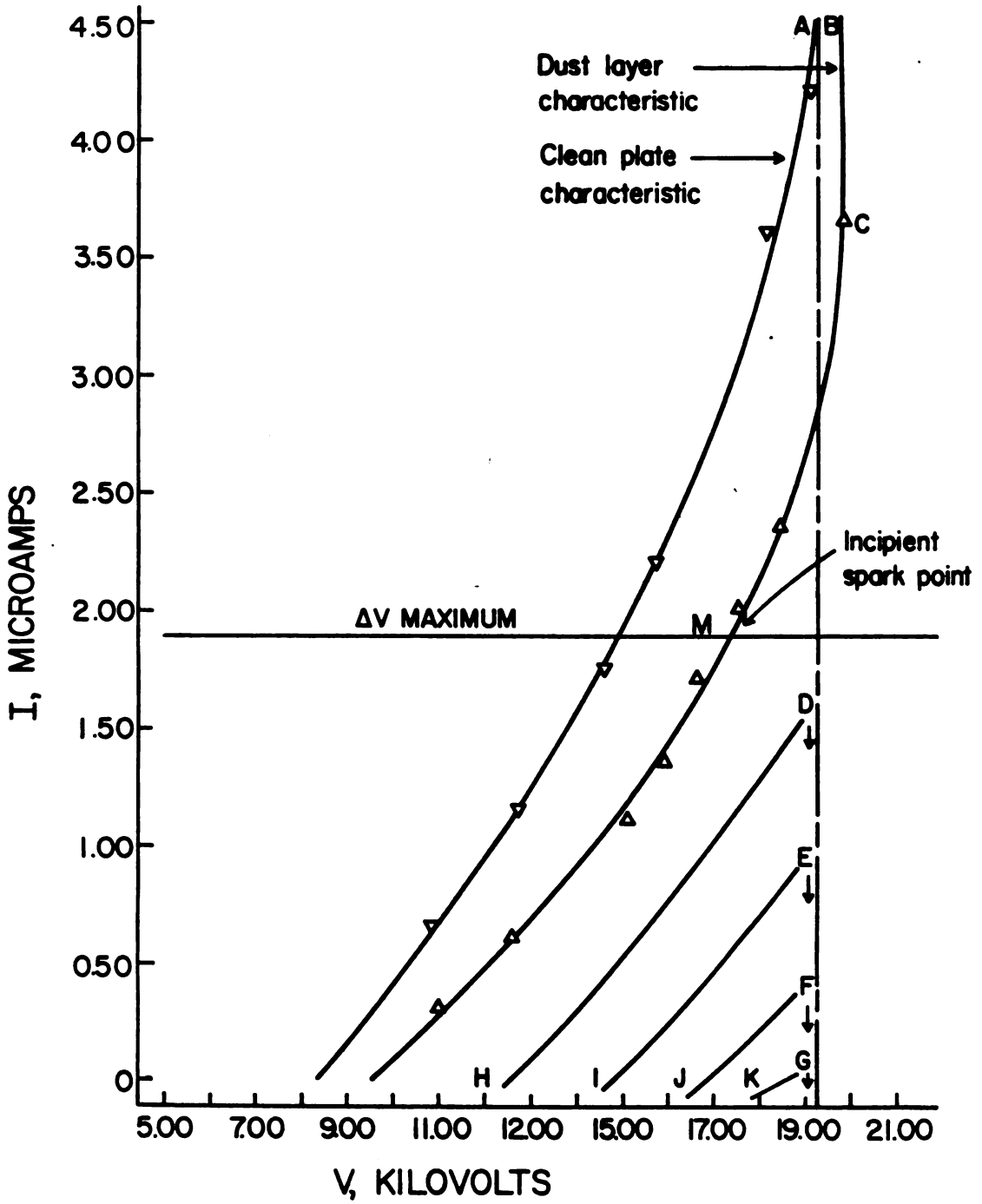

Figure A.5. Points D, E, F, and G on the dust layer curves correspond to total breakdown. H, I, J and K are the corona initiation points.

the clean plate sparkover. Therefore, a good experiment corresponds to a layer thickness which yields the incipient spark point M midway between these two extremes. Since the dust layer thickness is controlled by V_c and the collection time, a high collection voltage (for a given collection time) implies a high corona initiation voltage, while at low V_c, longer time is required for a reasonably thick layer. It is not possible to specify these parameters universally, since they depend upon the conditions of power plant operation, port location, ambient temperature, flue gas composition, point to plane distance, and resistivity of the fly ash. For the same thickness, fly ashes of increasing resistivity will correspond to lower sparkover voltages. Long collection times are also required for low end current values of less than 0.5 μA, particularly for flue gases with low particulate concentration. Some preliminary runs help establish the value of V_c and length of time required. It is suggested that V_c be set at approximately 75% of the observed clean plate sparkover voltage, V_{STC}. The collection time is suggested by the criterion that V_{ID} should be about 30% of the clean plate range V_{STC}-V_{IC} in excess of V_{IC}.

$$V_{ID} \simeq V_{IC} + 0.3\ (V_{STC}-V_{IC})$$

$$V_e \simeq 0.75\ V_{STC}$$

where

V_C = collection voltage

V_{IC} = clean plate corona initiation voltage

V_{ID} = dust layer corona initiation voltage

V_{STC} = clean plate sparkover voltage

It is emphasized that the above values are suggested for a point plane distance of 1" and dust thickness between 0.3 mm and 0.5 mm. In order to achieve the desired layer thickness, it is necessary to determine the final collection current (and hence the collection time) experimentally for each situation.

A.5. Sources of Error

Measurement errors in the variables of the resistivity equation contribute to errors in the calculated value. Some of these are associated with the experimental problems. The resistivity is sensitive to the clean plate dust thickness (if any) because any significant accumulation of dust during clean plate measurements will shift the clean plate I-V curve to the right (Figure A.5), giving a lower value of ΔV. The thickness of the layer will be more than that corresponding to the true ΔV resulting in a lower value of resistivity. An order of magnitude estimate of the error on one set of data gave an average resistivity value of 25% lower than the true resistivity. The range of variation was from 0.0% to 31.6%. The actual measurement (instrument) errors in thickness, voltage and current values contribute proportionally to the resistivity.

The ash layer temperature also varied in a few cases by as much as 12^{o} F in one test as indicated in Table A.1. Since all of the experiments were conducted on low temperature precipitators, the sensitivity of resistivity to temperature depends upon the location of the experimental point on the left leg of the hump shaped (see Introduction) resistivity temperature curve. Calculations made on the data showed the variability to range from 4.7% to 70.0% for different coals. Hence, it is important to assure that the gas temperature is stable and no more than up to 5^{o} F variation

should be tolerated.

Based on these sources of error equipment modifications and a field resistivity data format have been suggested (S1,S2).

A.6 Conclusions

Of the two techniques for determining the resistivity of fly ash (with the SRI probe), the point plane method is preferable primarily because it does not involve contacting the particulate layer surface before or during I-V measurements. Furthermore, this procedure is conceptually similar to the actual situation inside a precipitator when compared to the operation of other resistivity cells (N1).

The point plane method gives a point (M) on the I-V plots defined as incipient sparkover, on which the resistivity is based. This definition meets the criteria stated at the end of Chapter 1. The resistivity as it relates to an operating precipitator is the value that belongs to an ash layer deposited on the collecting electrode. The calculated values should represent this "operational" resistivity. Furthermore, repeated measurements (ideally) should be made at the same field strength across the layer. Figure A.5 shows that ΔV increases with layer thickness so that the incipient spark point moves to lower current values. Hence the resistivity is reported at lower current values. However, both ΔV and d change in the same direction so that within a "good experimental range" (as explained earlier), the field strengths at the different incipient spark points should be approximately equal.

Referring to results in Table A.1 for 4/5, 4/24, 5/17, and 5/19 it is seen that the duplicate sets of results for each case are comparable. The effect of the changes of temperature is inhibited in some cases since

Table A.1. Experimental Data - Power Plant

Date	Dust Thickness (mm)	Resistivity x 10^{-11} (ohm - cm)	$T_1(^oF)$	$T_2(^oF)$
4/5	0.81	0.811	290	289
4/5	0.50	1.269	289	280
4/10	0.28	2.460	280	285
4/10	0.46	1.540	285	286
4/24	0.71	1.520	348	360
4/24	0.28	1.200	350	360
4/27	0.76	0.940	320	315
4/27	0.44	2.330	314	310
5/15	0.25	1.180	276	286
5/15	1.34	0.713	309	305
5/16	1.13	0.856	287	289
5/16	0.72	1.580	280	280
5/17	0.53	2.380	305	312
5/17	0.41	2.180	297	310
5/19	1.32	0.676	305	300
5/19	1.15	0.649	301	307
5/26	0.57	1.720	285	280
5/26	1.11	3.230	280	283

T_1 and T_2 are temperatures at the beginning and end of each experiment.

it is expected that the operating points are near the peak of the ρ_b-T (temperature) curve.

The variables that need to be studied before conducting tests to yield reliable values have been indicated. From the discussion it is evident that these parameters need to be ascertained during trial tests. There is an optimum region within which a dust layer (thickness) ought to lie for a good experiment.

APPENDIX B

APPENDIX B

Appendix B is a listing of the Fortran (IV) programs associated with the computations of Chapter 1. Program CURFIT (Section B.1) is the final version of the working program used to evaluate the data from the power plant (sodium sulfate) conditioning tests*. As described in Chapter 1** this program evaluates the incipient spark point resistivity as well as the sparking voltage. Subroutines GOSELM and BACKSO (S2) are used with program CURFIT and are presented in Section B.2. Subrouting FETCH (Section B.3) is a STAT4 plot routine which traces the clean plate and dust layer V-I characteristic curves. This subroutine utilizes the coefficients of the (power plant data) fitting polynomial to plot the experimental curves.

---

*This program evaluates the bulk resistivity for both the raw and conditioned fly ashes at the same temperature.

**See also Appendix A. Even though this listing was used for conditioning tests it is equally applicable to the situation where no chemical conditioning is used.

B.1.

```
      PROGRAM CURFIT(INPUT,OUTPUT)
C     ****************************************************************************
C     *                                                                          *
C     *                                                                          *
C     *                    RESULTS   OF   THE   SODIUM   SULFATE                 *
C     *                                                                          *
C     *                    CONDITIONING   TESTS   AT   THE                       *
C     *                                                                          *
C     *                   M S U    POWER   PLANT   DURING                       *
C     *                                                                          *
C     *                    JANUARY   THRU   APRIL    1979                       *
C     *                                                                          *
C     ****************************************************************************
      DIMENSION X(2,26),Y(2,26),A(3,4),Z(3),V(2),P(2,4),NC(26),ND(26),DE
     1LX(26),CL(26),CU(26),E(26),TC(26),TD(26),RO(26),RE(26),VS(26)
      INTEGER TD,TC
C     X,Y, ARE THE CURRENT,VOLTAGE VALUES. A(3,4) ARE THE COEFFICIENTS OF
C     THE NORMAL EQUTIONS MATRIX. Z(3) ARE THE PARAMETERS OF THE POLYNOMIAL
C     Y=Z(1)+Z(2)**Z(3)*X**2.V,C ARE THE FITTED POLYNOMIAL VOLTAGE AND
C     AND CURRENT VALUES.
C        NC AND ND ARE THE TOTAL NUMBER OF CLEAN AND DIRTY PLATE
C        EXPERIMENTS. DELX IS THE DUST LAYER THICKNESS. CL AND CU ARE THE
C     SMALLEST AND LARGEST CURRENT VALUES FOR THE DIRTY PLATE READINGS.
C     TC,TD ARE THE INITIAL AND FINAL TEMPERATURES OF THE DUST LAYER.
C     VS IS THE ESTIMATED SPARKOVER VOLTAGE.
C        RO AND RE ARE THE RESISTIVITY AND RESISTANCE (RO * DELX)
C        RESPECTIVELY. D IS THE DATE OF THE EXPERIMENT.
      READ*,N,(D(I),DELX(I),NC(I),ND(I),CL(I),CU(I),TC(I),TD(I),I=1,N)
    4 FORMAT(7X,*N*,10X,*DATE*,5X,*NC*,5X,*ND*,7X,*CL(I)*,9X,*CU(I)*,7X,
     1*DELX*,9X,*TE-I*,8X,*TEMP-F*,//)
    6 FORMAT (6X,I2,12X,F4.2,5X,I2,5X,I2,5X,F4.2,5X,F5.2,5X,F5.3,10X,I3,
     15X,I3,/)
   10 FORMAT(16F5.2)
   21 FORMAT (40X,*CONDITIONED TEST DATA*,/)
   23 FORMAT (40X,*RAW TEST DATA*,/)
   25 FORMAT((2X,15(F5.2,1X)),/)
   90  FORMAT(5X,*PARAMETERS OF POLYNOMIAL*,/)
  100 FORMAT(10X,* *3(*Z(*I2*)= *,F8.5,3X)/)
  110 FORMAT(7X,*FICS*,6X,*DELV*,10X,*RES*,7X,*V(1)*,8X,*V(2)*,/)
  120 FORMAT(6X,F5.2,5X,F5.3,4X,E12.5,3X,F5.2,7X,F5.2,/)
  140 FORMAT(10X,*INFLECTION OF VOLTAGE ACROSS DUST AT SPARKOVER*,/)
  180 FORMAT(40X,*SPARKING CHARACTERISTICS*,/)
  190 FORMAT(10X,*DATE      RESISTIVITY      SPARK VOLTAGE      RESISTANCE
     6    DUST THICKNESS      TSTART      TEND      COMMENTS*//)
  200 FORMAT(10X,F4.2,5X,E11.5,9X,F5.2,8X,F11.5,10X,F4.2,10X,I3,5X,I3,//
     1/)
  205 FORMAT(1H1,20X,*SUMMARY OF RESULTS*,//)
```

```
      PRINT 4
      PRINT 6,(I,E(I),NC(I),ND(I),CL(I),CU(I),DELX(I),TC(I),TD(I),I=1,N)
      DO 10000 M=1,26
      IF (MOD(M,2).EQ.0) GO TO 20
      IF (MOD(M,2).EQ.1) GO TO 22
   20 PRINT 21
      GO TO 11
   22 PRINT 23
      CONTINUE
   11 KC=NC(M) $ KD=ND(M)
      READ 10,(Y(1,J),J=1,KC)
      READ 10,(X(1,J),J=1,KC)
      READ 10,(Y(2,J),J=1,KD)
      READ 10,(X(2,J),J=1,KD)
      C=CL(M) $ D=CU(M)
C     DELV EVALUATED AT STEP INCREASES OF CURRENT DC. SETTING DC.
      IF((D-C).LE.0.75) DC=0.15
      IF((D-C).GT.0.75.AND.(D-C).LE.1.75) DC=0.20
      IF((D-C).GT.1.75) DC=0.25
      DO 1000 I=1,2
C     IF I.EQ.1 (LEAD PLATE DATA FITTING
C     IF I.EQ.2 (DIRTY PLATE DATA FITTING
      IF (I.EQ.1) N=NC(M)
      IF (I.EQ.2) N=ND(M)
      PRINT 25,(Y(I,J),J=1,N)
      PRINT 25,(X(I,J),J=1,N)
      DO 30 J=1,3
      DO 40 K=1,4
   40 A(J,K)=0.0
      DO 50 L=1,N
C     EVALUATING NORMAL EQUATIONS MATRIX COEFFICIENTS
      A(J,1)=A(J,1)+X(I,L)**(J-1)
      A(J,2)=A(J,2)+X(I,L)**J
      A(J,3)=A(J,3)+X(I,L)**(J+1)
      A(J,4)=A(J,4)+X(I,L)**(J-1)*Y(I,L)
   50 CONTINUE
   30 CONTINUE
      NROW=3 $ NCOL=4
      CALL GAUELM(A,NROW,NCOL)
      CALL BACKSO(A,NROW,NCOL,Z)
      PRINT 90
      PRINT 100,(J,Z(J),J=1,3)
      DO 105 L=1,3
  105 P(I,L)=Z(L)
 1000 CONTINUE
      PRINT 110
      IREC=0 $ DELV=0.0
  111 DO 125 I=1,2
```

```
C  NOTE. C HAS BEEN INITIALISED TO CL(M)
  125 V(I)=P(I,1)+P(I,2)*C+P(I,3)*C**2.
      F=DELV
      DELV=V(2)-V(1)
C  IF IREC.EQ.1  INFLEXION HAS OCCURRED
      IF(IREC.EQ.1) GO TO 115
      IF(F.GE.DELV) GO TO 150
  115 RES=DELV*5.0*10.**10/(C*DELX(M))
      PRINT 120,(C,DELV,RES,V(1),V(2))
      VSPK=V(2)
      C=C+DC
      IF(C.GT.(D+.1)) GO TO 130
      GO TO 111
C  IF IREC REMAINS AS ZERO NO INFLEXION HAS OCCURRED
  130 IF(IREC.EQ.0) GO TO 160
C  DEFINING CURRENT RANGE FOR ZEROING IN ON THE INFLEXION POINT
      D=CINF+0.15
      C=CINF-.21
      PRINT 140
      PRINT 110
      DELV=0.0
C  RECALCULATE DELV AND RESISTIVITY AROUND POINT OF INFLEXION
  141 DO 142 I=1,2
  142 V(I)=P(I,1)+P(I,2)*C+P(I,3)*C**2.
       F=DELV
      DELV=V(2)-V(1)
      IF(F.GE.DELV) GO TO 160
      VSPK=V(2)
      RES=DELV*5.0*10.**10/(C*DELX(M))
      PRINT 120,(C,DELV,RES,V(1),V(2))
      C=C+0.03
      IF(C.GT.D) GO TO 160
      GO TO 141
  150 IREC=1
C  RECORD APPROXIMATE CURRENT AT INFLEXION OF DELV VS RO
      CINF=C-DC
      GO TO 115
  160 R=RES*DELX(M)
      RO(M)=R $ RES(M)=RES $ VS(M)=VSPK
      PRINT 180
      PRINT 190
      PRINT 200,(I(M),RES,VSPK,R,DELX(M),TC(M),TD(M))
10000 CONTINUE
      PRINT 205
      PRINT 190
      K=25
      DO 210 M=1,K
      PRINT 200,(I(M),RO(M),VS(M),RES(M),DELX(M),TC(M),TD(M))
  210 CONTINUE
      END
```

B.2.

```
      SUBROUTINE GOSELM(A,NROW,NCOL)
C     REDUCE THE NORMAL EQUATIONS MATRIX TO THE UPPER TRIANGULAR FORM BY
C     THE  "GAUSS ELIMINATION" TECHNIQUE.
      DIMENSION A(3,4)
C     INITIALISING PIVOTS
      K=0 $N=NROW-1
   10 CONTINUE
      K=K+1 $ INDIC =K
      PIV=ABS(A(K,K))
C     SCAN FOR PIVOT ELEMENTS
      DO 20 I=K,NROW
      IF(PIV.LT.ABS(A(I,K))) 30,20
   30 PIV = ABS (A(I,K))
      INDIC =I
   20 CONTINUE
      IF(INDIC.EQ.K) 55,40
C     SWITCHING ROWS
   40 DO 50 J=1,NCOL
      D=A(INDIC,J)
      A(INDIC,J)=A(K,J)
      A(K,J)=D
   50 CONTINUE
C     ROW OPERATIONS
   55 PIV = A(K,K)
      DO 60 I = K,NCOL
   60 A(K,I) = A(K,I)/PIV
      KM = K+1
      DO 80 J = KM,NROW
      FM = A(J,K)
      DO 70 L = K, NCOL
   70 A(J,L) = A(J,L)-FM*A(K,L)
   80 CONTINUE
      IF (K.EQ.N) 90,10
   90 IF(A(NROW,NROW).NE.1.0) 100,110
  100 A(NROW,NCOL)=A(NROW,NCOL)/A(NROW,NROW)
      A(NROW,NROW)=1.
  110 RETURN
      END
```

```
      SUBROUTINE BACKSO (A,NROW,NCOL,Z)
C     BACKSOLUTION METHOD TO SOLVE THE UPPER TRIANGULAR MATRIX FOR Z
      DIMENSION A(3,4),Z(3)
      Z(NROW)=A(NROW,NCOL)
      N=NROW-1
      DO 80 I=1,N
      J=NROW-I
      SUM=0.0
      DO 90 K=J,N
   90 SUM=SUM+A(J,K+1)*Z(K+1)
      Z(J)=A(J,NCOL)-SUM
   80 CONTINUE
      RETURN
      END
```

B.3.

```
      SUBROUTINE FETCH(X,NR,IDR,IS,JP,DUM1,LABEL,DUM2,NTOT)
C     THIS PROGRAM TRACES THE POLYNOMIAL CURVE AND PLOTS EXPERIMENTAL
C     POINTS INDEPENDENTLY USING THE STAT4 ROUTINE.
C     SUBROUTINE FETCH PLOTS THE SECOND ORDER POLYNOMIAL GIVEN BY THE
C     CLEAN AND DIRTY PLATE COEFFICIENTS ESTIMATED BY PROGRAM CURFIT.
      DIMENSION X(2),A(2),B(2),C(2),D(2),HSPK(2),ZSPK(2),DV(200)
      IF (JP.EQ.2) GO TO 30
      IF (JP.EQ.3) GO TO 40
C     A(1),B(1),C(1),D(1) ARE THE COEFFICIENTS OF THE CLEAN PLATE
C     POLYNOMIAL.
      DATA A(1),B(1),C(1),D(1)/6.90494,4.61227,-0.57106,0.00/
C     A(2),B(2),C(2),D(2) ARE THE COEFFICIENTS OF THE DIRTY PLATE
C     POLYNOMIAL.
      DATA A(2),B(2),C(2),D(2)/8.08837,5.95710,-0.99542,0.00/
      DATA I,J/1,2/
      HMAX=15.00
C     X(1) IS THE APPLIED VOLTAGE. X(2) IS THE MEASURED CURRENT.
      X(1)=A(1)+B(1)*X(2)+C(1)*X(2)**2
C     X(C) AND X(D) ARE THE CLEAN AND DIRTY PLATE VOLTAGES.
      XC=A(1)+B(1)*X(2)+C(1)*X(2)**2
      XD=A(2)+B(2)*X(2)+C(2)*X(2)**2
      DV(1)=0.0
C     DV(J) IS THE DIFFERENCE BETWEEN DIRTY AND CLEAN PLATE VOLTAGES
C     CORRESPONDING TO THE SAME CURRENT - DELTA-V.
      DV(J)=XD-XC
      IF (DV(J).GT.DV(J-1)) I=J
C     COMPARISON OF DELTA-V WITH NEW DELTA-V.
      IF (.NOT.DV(J).LT.DV(J-1))DVMAX=DV(I)
      IF (I.EQ.J) XMAX=X(2)
      J=J+1
C     DETERMINATION OF CURRENT AT POINT OF TANGENCY.
C     BY POLYNOMIAL DIFFERENTIATION.
      ZSPK(1)=-B(1)/(C(1)*2.0)
      HSPK(1)=A(1)+B(1)*ZSPK(1)+C(1)*ZSPK(1)**2
C     IF CURRENT EQUALS INCIPIENT SPARK CURRENT SET CORRESPONDING
C     VOLTAGE AS INCIPIENT SPARKOVER VOLTAGE.
      IF(X(2).GE.ZSPK(1)) X(1)=HSPK(1)
C     WHEN BOTH CURVES ATTAIN A SLOPE OF 90 DEGREES A VERTICAL LINE IS
C     DRAWN AT POINT OF TANGENCY. IF THIS IS NOT ACHIEVED PLOTTING
C     TERMINATES.
      IF(HSPK(1).GE.HMAX) IS=1
      RETURN
```

```
C       SAME OPERATION WITH DUST LAYER CHARACTERISTICS.
   30   X(1)=A(2)+B(2)*X(2)+C(2)*X(2)**2
        ZSPK(2)=-B(2)/(C(2)*2.0)
        HSPK(2)=A(2)+B(2)*ZSPK(2)+C(2)*ZSPK(2)**2
        IF(X(2).GE.ZSPK(2)) X(1)=HSPK(2)
C       IF ESTIMATED SPARK VOLTAGE EXCEEDS THE MAXIMUM APPLIED VOLTAGE
C       - TERMINATE PLOT.
        IF(HSPK(2).GE.HMAX) IS=1
        RETURN
   40   X(2)=XMAX
        RETURN
        END
TITLEV-I PLOTS 4/1[illegible] 7
FILEBUILD
MV1...4=BLANK
L1=VOLTAGE,CURRENT,VOLTAGE,CURRENT
PLOT(1,2)INVT,HSIZE=8.5,VSIZE=11,HMIN=4,HMAX=15,VMIN=0,VMAX=8,HS=1,VS=0.5,
HUNITS=KILOVOLTS,VUNITS=MICROAMPS,SPECIAL15,QUEUE=5
PLOT(3,4)TRT,SAME
DRAW,JP=1,SAME,VRANGE
DRAW,JP=2,SAME,VRANGE
DRAW,JP=3,SAME
FORMAT(2F5.2/2F5.2)
7.50  0.15
[illegible].40  0.45
8.00  0.3
12.00  0.70
9.30  0.45
14.20  1.30
11.40  1.15
14.60  1.45
12.80  1.65
15.50  1.85
14.50  2.25
16.50  2.20
16.10  3.60
```

APPENDIX C

APPENDIX C

The capillary condensate ring is under a state of tension for values of ΔP_1 (equal to $P_g^o - P_1$) exceeding the water vapor saturation pressure at a particular temperature. As indicated in Section 2.14 (Chapter 2) this follows from equation (2.72) when numerical values of the relative saturation α are substituted to evaluate the equilibrium liquid phase properties.

$$BP_g^o (1-\alpha) - RT \ln\alpha = \int_{\eta}^{1} \chi_1 \, d\ln \eta \qquad (2.72)$$

The fact that the compressibility equation of state for the liquid ceases to be valid for low water vapor partial pressures was discussed in the same section. In particular, the empirical linear relationship between the isothermal susceptibility χ_1 and liquid relative density, equation (2.64), does not hold. It may be recalled that compressibility data are determined for positive pressures only and using equation (2.64) for liquids in this case amounts to extending its region of applicability to negative* pressures.

$$\chi_1 = K_1\eta - K_2 \qquad (2.64)$$

C.1. The van der Waals Approximation to the Equation of State

In light of the above argument it is evident that an alternative, perhaps a semi-empirical equation of state for the capillary condensate

*This term implies the tensile stress in a liquid.

is required. An obvious, semi-empirical equation of state is the van der Waals equation or an expression similar to it. It is known that most simple molecular models incorporating almost any law of force yield expressions very similar to the van der Waals equation as a first approximation (T3, B5). It has been applied with considerable success in the prediction of liquid behaviour for non-associating liquids.

The following phase P-$\hat{V}$ diagram (Figure C.1) shows the typical isotherms for a van der Waals gas.

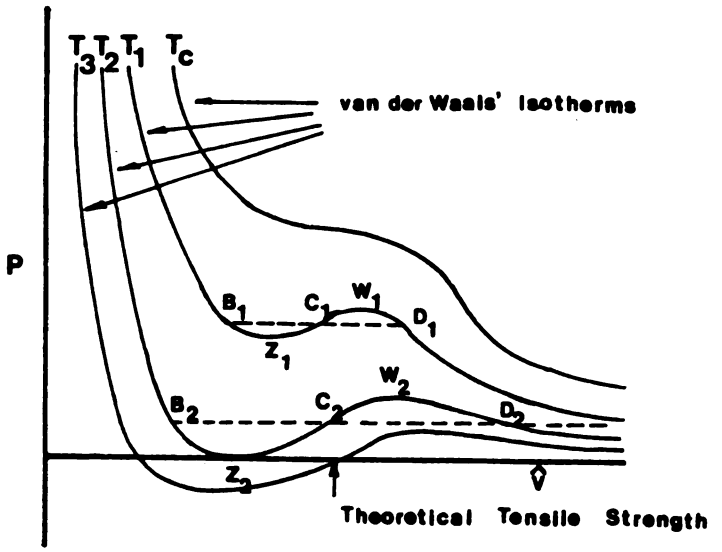

Figure C.1. Illustration of the tensile strength of a liquid.

The isotherms indicated are those for the critical temperature T_c and for other temperatures less than T_c. As seen from the figure the solution for the cubic van der Waals equation (C.1) has three roots in V at a fixed pressure for a given isotherm within the

two-phase region.

$$(P + \frac{a}{\hat{V}^2})\ (\hat{V} - b) = RT \qquad (C.1)$$

and

$$\hat{V}^3 - \hat{V}^2\ (b + \frac{RT}{P}) + \hat{V}\ \frac{a}{P} - \frac{ab}{P} = 0 \qquad (C.2)$$

In the figure the points B_1, C_1, D_1 and B_2, C_2,D_2 represent the roots of equation (C.2). The curves $B_1Z_1C_1W_1D_1$ and $B_2Z_2C_2W_2D_2$ represent regions of metastability for the gas and liquid phases. For example on the T_1 isotherm, the point Z_1 implies that the liquid has a vapor pressure which is lower than the equilibrium vapor pressure at the temperature (T_1), or equivalently that the liquid is superheated. This is evidently a metastable condition and the points Z_1 and Z_2 represent the limit for this kind of metastability from the van der Waals isotherm. In contrast to the representation by the curve $B_1Z_1C_1W_1D_1$ for example, the liquid to vapor transition, in reality, is not continous, and the points Z_1 and W_1 may be approached under carefully controlled conditions from the liquid and vapor sides respectively. Ordinarily, the isotherm follows the straight line B_1D_1;

The usual definition of compressibility implies decreasing volumes of liquid as the pressure increases upon it. However, as shown in the figure (C.1), the rising portion of the isotherm Z_1C_1 within the two phase region indicates a positive slope $(\partial P/\partial \hat{V})_T$. This is a physical inconsistency and obviously not realized in practice. It may be noted that along the labeled curves within the two phase region the value of the thermodynamic potential is stationary. The limits of metastability indicated by Z_1, W_1, Z_2 and W_2 on the isotherms are approached from

the negative slope side of the curves in practice. These limits are then given by the vanishing of $(\partial P/\partial \hat{V})_T$

$$(P - \frac{a}{\hat{V}^2} + 2ab/v\ (3/\ (\hat{V}-b) = 0 \qquad (C.3)$$

$$\therefore \quad P - \frac{a}{\hat{V}^2}\{1 - \frac{2b}{\hat{V}}\} = 0 \qquad (C.4)$$

Thus P is positive for $\hat{V} > 2b$ and negative for $\hat{V} < 2b$.

For a liquid at conditions corresponding to Z_2 (zero pressure)

$$\hat{V} = 2b \qquad (C.5)$$

from equation (C.4).

From the criteria at the critical point

$$(\partial P/\partial \hat{V})_T = (\partial P^2/\partial \hat{V}^2)_T = 0 \qquad (C.6)$$

one gets

$$T_c = 8a/17Rb \qquad (C.7)$$

Substituting P = 0 and equation (C.5) into the van der Waals equation

$$\frac{T_2}{T_c} = \frac{27}{32} \qquad (C.8)$$

for water $T_2 \simeq 270^{o}$ C.

It should be noted that (C.8) is a universal relationship. The validity of this relationship was verified by Kenrick, Gilbert and Wismer (see Reference T3) who obtained a good correlation with experimental results for various liquids. This evidence indicates, qualitatively at least, the appropriateness of the use of the van der Waals

equation to examine the tensile strength of liquids.

From equation (C.1) at the limiting case for T = 0

$$\hat{V} = b \tag{C.9}$$

Below zero pressure the liquid is in a state of tensions (negative pressure); hence the entire range of tension is covered by the criterion

$$b \leq \hat{V} \leq 2b \tag{C.10}$$

At T = 0, equation (C.4) gives

$$P_T = \frac{a}{\hat{V}^2}\left(1-\frac{2b}{\hat{V}}\right) = -\frac{a}{b^2} \tag{C.11}$$

Since $P_c = a/27b^2$, equation (C.11) states that the tensile strength at T = 0 is 27 times the critical pressure P_c (217.7 atm for water).

As temperature increases the volume of the liquid increases as well (V goes from b to 2b), and the tensile strength* is given by

$$P_T \simeq -\frac{a}{V^2} \tag{C.12}$$

The extremely large value of the tensile strength for water at absolute zero reflects the crude approximation by the van der Waals of the liquid state in such an extreme case. Further, the variation of the constants a and b with temperature has been neglected. The effect of temperature on the excluded volume is related to the "softness" of the molecules which reduces the tensile strength below the value predicted by equation (C.11). This "softness" favors the formation of "holes" in the liquid (T3).

*This tensile strength is the pressure necessary to rupture the fluid and is also known as the intrinsic pressure.

Finally, using P_T as the criterion of mechanical instability of the capillary condensate, it is seen that the likelihood of rupture for low values of the relative saturation α is far greater at the higher experimental temperatures than at the low values of T.

C.2. Temperature Variation of the Tensile Strength of Water.

As was discussed in Section C.1 the validity of the van der Waals equation for estimating the tensile strength and its variation with temperature is justified. As will be evident later, this procedure will also yield estimates for the orders of magnitude of the terms $\Delta\mu_1$ and $\Delta\mu_1{}^{c*}$ for the capillary condensate.

The reduced form of equation (C.1) is

$$P_R = \frac{8T_R}{(3\hat{V}_R - 1)} - \frac{3}{\hat{V}_R{}^2} \qquad (C.13)$$

where

$$P_R,\ \hat{V}_R,\ T_R = P/P_c,\ \hat{V}/\hat{V}_c \text{ and } T/T_c \text{ respectively.}$$

Differentiating (C.13) with respect to V_R and setting the derivative to zero

$$\left(\frac{\partial P_R}{\partial \hat{V}_R}\right)_{T_R} = \frac{-24T_R}{(3\hat{V}_R - 1)^2} + \frac{6}{\hat{V}_R{}^3} = 0 \qquad (C.14)$$

It may be observed that the derivative $(\partial P_R/\partial \hat{V}_R)$ is independent

---

*$\Delta\mu_1$ = Liquid phase thermodynamic potential departure from the reference state ($P = P_g{}^o$)

$\Delta\mu_1{}^c$ = Correction to $\Delta\mu_1$.

of the gas constant R, so that any alternate P-V relationship of the van der Waals type containing some other thermodynamic constant in place of R is also valid in this derivation.

It was mentioned in Section C.1 that the vanishing of the derivative $(\partial P/\partial \hat{V})_T$ corresponds to the limit of metastability at a given temperature and pressure. This is equivalent to the condition for mechanical instability of the liquid at which $\chi_1 \to 0$ or $\beta^* \to \infty$.

The cubic in $\hat{V}_R$ from equation (C.14) yields three roots of which one value of $\hat{V}_R$ is relevant for the region of tension**

$$\left.\begin{array}{l} \frac{1}{3} \leq \hat{V}_R \leq \frac{2}{3} \\ T_R < 27/32 \end{array}\right] \qquad \text{(C.15)}$$

[see equation (C.8)]

From equations (C.13) and (C.14) the following expressions are obtained

$$P_R = 3/\hat{V}_R^2 - 2/\hat{V}_R^3 \qquad \text{(C.16)}$$

and

$$T_R = \frac{1}{4}\left[\frac{(3\hat{V}_R - 1)^2}{\hat{V}_R^3}\right] \qquad \text{(C.17)}$$

---

*β = Liquid compressibility $[-\frac{1}{V}(\partial V/\partial P)_T]$.

**Of the other two roots one corresponds to the region of the isotherm where P_R is always negative and hence is meaningless, while the third root represents the gas phase metastability at the maximum of the isotherm, for example point W_1 on Figure C.1 (D3).

It should be noted that P_R is the maximum reduced tension a body of liquid can sustain, without rupture, at a particular temperature T_R given by equation (C.17) while at thermodynamic equilibrium with its vapor. Benson and Gerjouy (B5) have obtained P_R at various values of T_R ($T_R \leq 27/32$) from equations (C.16) and (C.17) and the results are shown in Figure C.2. The sensitivity of the tensile strength is evident due to the steep descent of the curve especially at the lower temperatures. The curve intersects the x-axis at 270° C which is the maximum superheating temperature at zero atmosphere pressure [see equation (C.8)].

The values of the maximum tensile strengths at the experimental temperatures were deduced from Figure C.2 and these are shown in Table C.1. In the third column of the table are presented values of the ideal case (incompressible) liquid chemical potential departures, $\Delta\mu_1$ (approximately equal to $\Delta P_1/\rho_1^{o}$) obtained from the compressibility equation of state.

Table C.1. Tensile strength and approximate values of $\Delta\mu_1$ (ideal) at experimental temperatures.

Temperature (°C)	Tensile strength (atm)	$\Delta\mu_1 \simeq \frac{\Delta P_1}{\rho_1^{o}}$ (cc-atm/g-mole)
65.56	791	1.456×10^4
98.89	626	1.176×10^4
126.67	500	9.656×10^3
143.33	434	8.549×10^3
157.22	378	7.592×10^3
176.67	306	6.372×10^3

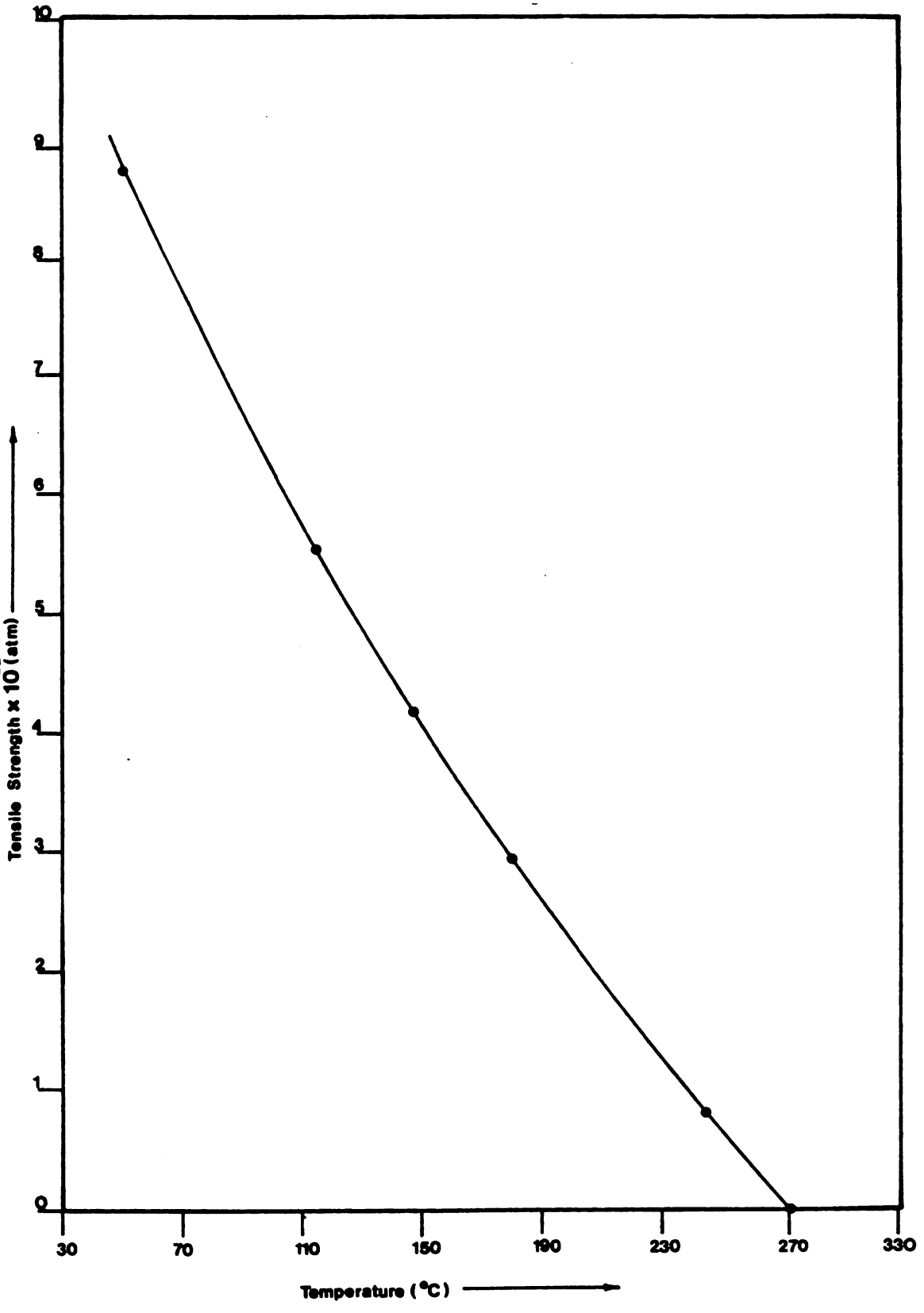

Figure C.2. Variation of the maximum tensile strength of water with temperature.

A physical interpretation of the magnitudes of $\Delta\mu_1$ from the above table is possible as follows:

At 126.67^{o} C, for $\Delta\mu_g^{c} << \Delta\mu_g^{id}$

$$- RT \ln\alpha \simeq \Delta\mu_1 \qquad (C.18)$$

[from equations (2.37) and (2.38)]

For $\alpha = 0.75$, $\Delta\mu_1 \simeq 9.44 \times 10^3$

From the results of the computer program (to evaluate $\Delta\mu_1$ at negative pressures using the procedure of Section 2.9), the value of the isothermal susceptibility χ_1 at -500 atm (maximum tension) is 2.987×10^5 cc - atm/g-mole. From the foregoing discussion it is obvious that this is an inconsistency, since χ_1 is expected to vanish at this pressure. The value of 0.75 for the relative saturation α appears to be too high for the liquid to exhibit instability.

Furthermore

$$\Delta\mu_1 = \Delta\mu_1^{id} + \Delta\mu_1^{c} \qquad (C.19)$$

and

$$\Delta\mu_1^{id} = \Delta P_1/\rho_1^{o} \qquad (C.20)$$

and it is seen by comparing the value of $\Delta\mu_1$ calculated above with the corresponding value in Table C.1 that

$$|\Delta\mu_1^{c}| << |\Delta\mu_1^{id}| \qquad (C.21)$$

Inequality (C.21) implies that the capillary condensate is still fairly ideal at this high tension. For the liquid to demonstrate ideal behaviour (approximately), χ_1 should be large, corresponding to a low value for the compressibility β.

However, as stated earlier, the physics of the situation requires the vanishing of χ_1, instead, the compressibility equation of state [equation (2.56)] predicts relatively small departures of ideality resulting in large values for the susceptibility. These values, which are obtained from the above equation, are shown in Table C.2.

Table C.2. Isothermal susceptibilities from the compressibility equation at the point of liquid rupture.

Temperature (^{o}C)	Tensile strength (atm)	$(\chi_1)_T \times 10^{-5}$ (cc-atm/g-mole)
65.56	791	3.4412
98.89	626	3.2480
126.67	500	2.9852
143.33	434	2.7936
157.22	378	2.6372
176.67	306	2.4447

The magnitudes of χ_1 from the table are obviously inconsistent with the conditions that require mechanical instability within the capillary condensate. This discrepancy is partly resolved by disregarding the compressibility equation for the liquid phase and resorting to the van der Waals equation of state in this region of tension. It is apparent that if χ_1 approaches zero [from

O(M)* of 10^5], the liquid is no longer ideal and an expression for the correction to the chemical potential departure $\Delta\mu_1^c$ from the reference state is needed. Such an expression has been derived in Appendix D where this analysis continued with the objective of arriving at a quantitative basis to support the above arguments.

---

*O(M) = Order of Magnitude

APPENDIX D

APPENDIX D

The analysis in Appendix C resulted in the estimation of the liquid (water) tensile strength at various temperatures. The discussion presented at the end of Section C-2 demonstrated the contrasting assertions made, regarding liquid behaviour, by the compressibility and the van der Waals equations of state. These assertions (for the liquid under tension) lend themselves to further scrutiny when the values for the liquid chemical potential ($\Delta\mu_l$) and the potential correction ($\Delta\mu_l^c$) terms, from the two equations of state, are compared with each other. The expression for $\Delta\mu_l$ based on the van der Waals equation is derived in this Appendix. The resulting magnitudes of $\Delta\mu_l$ as well as the values from Table C.1 and $\Delta\mu_l{}^c$ from equation (2.65) yield a quantitative basis for discriminating between the two equations of state. In as much as the results of this section are required to complete the analysis, two specific comments may be made with reference to the computations involving liquid state parameters in Chapter 2:

i) The compressibility equation is valid for the region of tension. This assumption has been made by Melrose (M4), however, as is shown in this Appendix, such an "extrapolation" is not true for water.

ii) The degree of uncertainty associated with these calculations is reduced when the change in the total (Gibbs) free energy, accompanying a (liquid) volume change, is

examined. This uncertainty arises due to the variation in the liquid phase bulk properties (C1, H3).

D.1. Variation of Liquid Chemical Potential ($\Delta\mu_1$) with Temperature for States of Tension.

The dimensionless van der Waals equation is used to formulate an expression for $(\Delta\mu_1)_T$.

The isothermal departure $(\Delta\mu_1)_T$ was given in Chapter 2 as

$$(\Delta\mu_1)_T = \int_{p_g}^{p_1^o} (\hat{v}\, dP)_T \qquad (D.1)$$

$$= \int_{\hat{v}_{1\,mim}}^{\hat{v}_1} \hat{v}_1 \left(\frac{\partial P}{\partial \hat{v}_1}\right)_T d\hat{v}_1$$

Introducing critical constants into the integral above

$$(\Delta\mu_1)_T = P_c \hat{v}_c \int_{\hat{v}_{R\,min}}^{\hat{v}_R^o} \hat{v}_R \left(\frac{\partial P_R}{\partial \hat{v}_R}\right)_T d\hat{v}_R \qquad (D.2)$$

where $\hat{v}_R^{\,o}$ is the reduced molar volume at saturation. Substituting for the derivative inside the integral from equation (C.14)

$$(\Delta\mu_1) = P_c \hat{v}_c \int_{\hat{v}_{R\,mim}}^{\hat{v}_R^o} \hat{v}_R \left[- \frac{24T_R}{(3\hat{v}_R - 1)^2} + \frac{6}{\hat{v}_p^3} \right] d\hat{v}_R \qquad (D.3)$$

Integration (T2) of expression (D.3) yields:

$$(\Delta\mu_1)_T = [M(T_R)\{\ln(9\hat{v}_R^2 - 6\hat{v}_R + 1) + \frac{2}{1-3\hat{v}_R}\} - \frac{6}{\hat{v}_R}]_{\hat{v}_{R\,min}}^{\hat{v}_R^o} \qquad (D.4)$$

where, $M(T_R) = -24T_R$

The lower limit $\hat{v}_{R\,min}$ is the minimum liquid volume corresponding to the point of rupture at which $\chi_1 = 0$. It is estimated from equations (C.16) and (C.17) for given values of P_R and T_R. Benson and Gerjuoy (B5) have determined the reduced volume by this method and their data are shown on the plot of $\hat{v}_{R\,min}$ versus temperature (Fig. D.1). The values of $\hat{v}_{R\,min}$ for the experimental temperatures are deduced from this figure and are shown in Table D.1 below.

Table D.1 Minimum and Saturation Reduced Volumes at the Experimental Temperatures.

Temperature (^oC)	$\hat{v}_{R\,min}$	$\hat{v}_R^o$
65.56	0.5080	0.3251*
98.80	0.5265	0.3319*
126.67	0.5427	0.3400**
143.33	0.5530	0.3453**
157.22	0.5630	0.3503**
176.67	0.5770	0.3580**

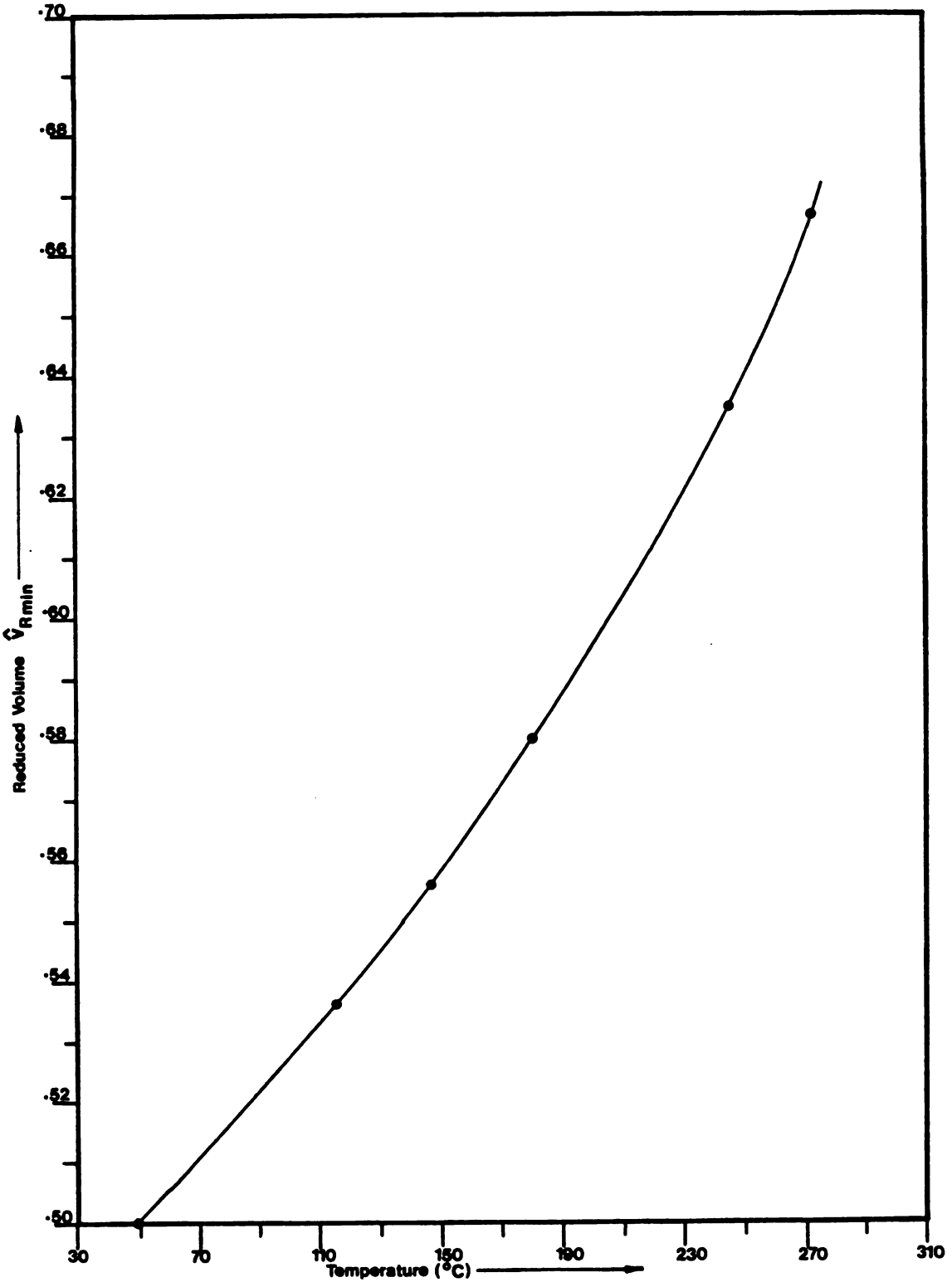

Figure D.1. Variation of the minimum reduced volume with temperature.

*From equation (D.3) it is seen that the integrand has a point of discontinuity at $\hat{v}_R^o = 1/3$. For $\hat{v}_R^o \leq 1/3$ equation (D.4) gives values of $(\Delta\mu_1)_T$ which are negative. This corresponds to one of the two roots described in the footnote on page representing the portion of the isotherm for which P_R is always negative. In the present context, this circumstance arises due to the choice of a specific equation of state, (in this case the van der Waals equation) where the critical constants are so defined in terms of the van der Waals constanta a and b that the expression for the reduced pressure P_R in equation (C.13) contains the term $(3\hat{v}_R-1)$ in the denominator. This situation could be circumvented by using some other simple P - V relationship; however, as shown later it does not detract from the objective of this analysis.

**These values of the liquid volume are calculated for a ΔP_1 of 25 atm. Since all of the saturation vapor pressures are less than 25 atm, the upper limit of the definite integral [equation (D.4)] corresponds to negative liquid pressures. Hence the van der Waals equation is used to calculate $\Delta\mu_1$ only in the region of liquid tension. A complete computation would require the summation of this value and the liquid potential departure $\Delta\mu_1$ in the positive pressure region (P^o_R - 0 atm) and the region of tension up to $\Delta P_1 \leq 25$ atm utilizing the compressibility equation of state [equation (2.55)] for positive pressures. This latter calculation assumes that equation (2.55) is valid up to $\Delta P_1 \leq 25$ atmospheres. Table C.1 shows that this region of negative pressure represents a small fraction of the entire range of tension for all of the experimental temperatures, and as indicated

Footnote continued

by the order of magnitudes of $\Delta\mu_1$ in Table D.2, the approximation does not introduce any significant error.

The upper limit $\hat{v}^o_R$ [in equation (C.25] is given by

$$\hat{v}^o_R = \frac{\hat{v}^o}{\hat{v}_c} = \frac{1}{(\rho^o)\ (56.6)}$$

where $\hat{v}_c$ = 0.0566 lit/mole

The value of the (thermodynamic) potential departure for the capillary condensate in tension is calculated from equation (D.4) upon substituting the limits from Table D.1. These values for $(\Delta\mu_1)_T$ are presented in Table D.2.

Table D.2 Values of the Liquid Potential Departures From Saturation up to Point of Rupture of the Capillary Condensate (from the van der Waals equation of state)

Temperature (^oC)	$\Delta\mu_1$ (cc-atm/g-mole)
65.56	$>1.000 \times 10^7$
98.80	$>1.000 \times 10^7$
126.67	1.111×10^7
143.33	6.152×10^6
157.22	4.285×10^6
176.67	2.873×10^6

The immediate observation to be made here is that of the large differences in the magnitudes of $\Delta\mu_1$ in Tables C.1 and D.2. The former values were estimated using the compressibility equation of state

[equation (2.55), Chapter 2]

$$\Delta\mu_1 = \int_1^{\eta} \chi_1 \, d\ln \eta \qquad (2.55)$$

The apparent failure of the above equation to relate liquid state variables for large negative pressures was demonstrated in Section C.2. In addition, far from being ideal, the capillary condensate shows "large"* departures from the ideal incompressible case since,

$$\Delta\mu_{1_{v.d.V}}^{**} \text{ (from Table D.2)} >> \Delta\mu_1 \text{ (equal to } \frac{\Delta P_1}{\rho^o_1}\text{, from Table C.1)} \qquad (D.5)$$

---

*The description of "large" departures is used tentatively in the present context. This is directly inferred from equations (D.5) and (D.6) only if the total change in $\Delta\mu_1^{id}$ is completely accounted for by the condensate pressure which is given in terms of ΔP_1. As discussed in Appendix E, the change in liquid potential for small volumes is, in addition to the above, given by terms which were neglected in the analysis in Chapter 2 beginning with the expression for the H lmholtz free energy change [equation (2.1)]. It was also mentioned in Chapter 2 that the assumption of invariance of the intensive properties of the liquid starts to break down with decreasing volumes and the changes in $\Delta\mu_1$ would, therefore, partly result from some of these properties.

**Subscript v.d.V = van der Waals.

and

$$\Delta\mu_1 = \Delta\mu_1^{id} + \Delta\mu_1^{c}$$

$$\Delta\mu_1^{id} = \Delta P_1/\rho^{o}{}_1 \qquad (D.6)$$

It must be mentioned here that the representation of $\Delta\mu_1$, in the third column of Table C.1, only by liquid pressure ($\Delta P_1/\rho^{o}{}_1$) implicitly asserts that the correction term $\Delta\mu^{c}{}_1$ is negligible compared to the total potential change $\Delta\mu_1$. Furthermore, in the computations resulting in Table 2.3, $\Delta\mu^{c}{}_1$ was neglected. While the magnitudes of the numbers for $\Delta\mu^{c}{}_1$ in this latter case (shown in Table 2.5) justify the above assumption for relatively small departures from the reference state, the validity of the inequality, $\Delta\mu^{c}{}_1 \ll \Delta\mu_1$, needs to be verified for the liquid in the region of high tension. The values given in the fourth column of Table D.3 have been calculated from the following equations [(2.59) and (2.65)] which were derived from the integral form of the compressibility equation of state [equation (2.56)].

$$\Delta\mu^{c}{}_1 = \int_{\eta}^{1} \chi_1 \left(\frac{1}{\eta} - 1\right) d\eta \qquad (2.59)$$

$$\Delta\mu^{c*}{}_1 = K_1\{0.5 - \eta + 0.5\eta^2\} + K_2\{1-\eta+\ln \eta\} \qquad (2.65)$$

---

*K_1 and K_2 are the constants relating the isothermal susceptibility χ_1 to the relative density η [see equation (2.64)].

Table D.3. Magnitudes of the Liquid Potential Correction Term (at the estimated point of rupture) Using the Compressibility Equation of State.

Temperature ^{o}C	Relative density η	Tensile Strength, P (atm)	$\lvert\Delta\mu^{c}_{1}\rvert$ (cc-atm/g-mole)
65.56	0.9607	791	2.799×10^{2}
126.67	0.9699	500	1.423×10^{2}
176.67	0.9754	306	7.712×10^{1}

It may be noted that even though the dimensionless van der Waals equation was used in this region of tension (Section C-1), the compressibility equation (2.56) has been assumed to apply as indicated in Table D.3. In the light of this substitution of the equations of state and magnitudes of $\Delta\mu^{c}_{1}$ in Table D.3, the following two pertinent observations may be made:

1) The compressibility equation has been used to compute $\Delta\mu^{c}_{1}$ [from from equation (2.65)] at tensile strengths estimated from equation (C.16). This latter equation was derived from the van der Waals equation. Equation (2.56) cannot be used to estimate tensile strengths, indeed it can only be used in the present context, to estimate parameters that define a given liquid state which is not far removed from the region of positive pressures (Section 2.14, Chapter 2).

2) A comparison of the values of $\Delta\mu^{c}_{1}$ for the three temperatures in Table D.3 with the corresponding entries for $\Delta\mu^{1}$ (approximated by $\Delta\mu^{id}_{1}$) in Table C.1 justifies the validity of the following assumption stated earlier:

$$\Delta\mu^c_1 \ll \Delta\mu_1 \text{ (from compressibility equation)}$$

The liquid potential correction term is approximately two order of magnitudes lower than $\Delta\mu_1$ ($\simeq \Delta P_1/\rho^o_1$).

These two conclusions do not confirm the assumptions made by Melrose (M4) in the estimation of $\Delta\mu^c_1$ for liquid Argon at negative pressures. The values of the liquid potential, given by $\Delta\mu_1$ in Table D.2, are far too large (for $\alpha \ll 0.01$) so that one might expect large deviations from ideality for large departures from the reference state. Furthermore $\Delta\mu^1$ increases (as α decreases) at a rate much higher than $\Delta P_1/\rho^o_1$ (equal to $\Delta\mu^{id}_1$). This, in turn implies one or more of the following:

i) The potential correction term $\Delta\mu^c_1$ takes up the slack in $\Delta\mu^{id}_1$ to account for the total change $\Delta\mu_1$ [see equation (2.58)] accompanying a decreasing volume of liquid.

ii) The representation of $\Delta\mu^{id}_1$ by the condensate pressure change $\Delta P_1/\rho^o_1$ only [as given by equation (D.6)] is essentially incomplete, and, as stated earlier in this section, additional terms involving liquid property changes need to be included.

In any case, the compressibility equation is not valid for the liquid at negative pressures, and a further examination of observations (i) and (ii) is required in order to complete the present analysis. Contrary to a possible speculation earlier, that the compressibility equation would at least yield order of magnitude results comparable with those from the van der Waals equation, it has been shown that $\Delta\mu^c_1$ is still $\ll \Delta\mu_1$ [Table D.3] with the associated implication that

the liquid demonstrates near ideal behaviour even when under high tension. This speculation would be legitimate if based solely on the results tabulated in Section 2.9 (Chapter 2), and, were it to be true, at least the first of the two observations made above would be inappropriate. A discussion of these observations has been presented in Appendix E, which, again is based upon the a priori assumption that the van der Waals equation approximates the equation of state for water under tension.

APPENDIX E

APPENDIX E

The inappropriateness of the extension of the compressibility equation of state [Equation (2.56), Chapter 2] to high negative pressures in the capillary condensate was discussed in Appendices C and D. This is largely due to the fact that the isothermal susceptibility χ_1 was fairly high* at the point of mechanical instability of the liquid where instead it is required to vanish. Furthermore, the results from this equation did not show the expected large deviations from ideality, indeed in this region (of tension) $\Delta\mu^c_1 \ll \Delta\mu_1$.

In order to circumvent this problem, the van der Waals relationship was invoked with some justification. This equation was used to estimate tensile strengths of the liquid at different temperatures, and the liquid phase chemical potentials as well. The large values of $\Delta\mu_1$ obtained by this method in Table D.2 did not agree with those obtained from the compressibility equation. As far as the degree of departure, from ideality, of the liquid phase was concerned, it was concluded at the end of Appendix D that two distinct possibilities arise as a result of such magnitudes of $\Delta\mu_1$.

In this Appendix, therefore, these two alternatives are investigated in order to ascertain the nature of the uncertainty in equation

---

*Table C.2 (Appendix C) shows that χ_1 changes by less than one order of magnitude over the entire pressure range $P_{saturation} - P_{Tensile\ strength}$. The values of χ_1 near saturation are shown in Table 2.3, Chapter 2.

(2.58), as well as to present the analysis of the phenomena of capillary condensation in as complete a form as possible.

E.1. Estimation of the Liquid Potential Correction Term $\Delta\mu^c_1$ in the Region of Tension.

It was established in Appendices C and D (see Tables C.1, D.2) that for large negative pressures within the capillary condensate

$$\Delta\mu_1 \not\approx \Delta P_1/\rho^o_1 \tag{E.1}$$

where $\Delta\mu_1$ is the liquid phase potential term estimated from the van der Waals equation.

Thus referring to the set of equations (D.6), it is seen that $\Delta\mu^c_1$ is not small any more but assumes orders of magnitudes comparable to $\Delta\mu_1$.

For example, from Table D.2 at 126.67^o C

$$\Delta\mu_1 \simeq 0^*\{10^7\} \tag{E.2}$$

and from Table C.1

$$\Delta P_1/\rho^o_1 \simeq 0\{10^4\} \tag{E.3}$$

$$\Delta\mu^c_1 = \Delta\mu_1 - \Delta P_1/\rho^o_1$$

$$\simeq 0\{10^7\} \tag{E.4}$$

---

*Order of magnitude

It may be recalled at this stage that $\Delta\mu^c_1$ is, by virtue of its definition in equation (2.60), a correction term to account for non ideal liquid behaviour. It is employed in equation (2.58) to account for the real case where the specific molar volume is a function of the liquid pressure:

$$\rho^o_1 \Delta\mu_1 = \Delta P_1 + \rho^o_1 \Delta\mu^c_1 \qquad (2.58)$$

$$\Delta\mu^c_1 = \int_{p_1}^{p^o_1} \hat{v}\, d\rho_1 - \hat{v}^o_1 \int_{p}^{p^o_1} dP_1 \qquad (2.60)$$

This functional dependence of $\hat{v}$ upon P_1 is relatively weak for small departures from the reference state, or equivalently

$$\frac{\partial P_1}{\partial \rho} = \chi_1 \neq f(P_1) \qquad (E.5)$$

For α (= P_g/P_g^o) close to unity, χ_1 is large and approximately invariant with liquid pressure.

For large departures equation (E.5) does not hold and ρ_1 (or $\hat{v}$) is strongly dependent on P_1. Hence, as the liquid meniscus (in the interparticle region of contact) receded into the pore, the susceptibility decreases. Referring to Figure C.1 (Appendix C) it is seen that this rate of decrease of χ_1 is slow at the beginning (starting with positive pressures, P^o_g, close to the P = 0 line) and then rises subsequently until the limit of metastability is reached where $\frac{\partial P}{\partial \hat{v}}$

and χ_1 become zero*. As mentioned in Section C.2 (Appendix C), this limit of metastability (for example, the point Z_2 on Figure C.1) is approached from the direction where $\partial P/\partial v$ is negative and represents the vanishing of the isothermal susceptibility χ_1.

It has been established up to this point that the van der Waals approximation to the thermodynamic state (of tension) representation of the liquid confirms the anticipated deviation from ideality. In the present context, ideal behaviour is not taken to imply that χ_1 is infinite, but instead that it is finitely large {0 (10^5) for water} and constant. In each case $\Delta\mu^c{}_{1\ vdV}$ exceeds $\Delta P_1/\rho^o{}_1$ (Table C.1), where $\Delta P_1/\rho^o 1$ is the ideal case potential (departure from reference) with constant susceptibility. Furthermore, the van der Waals potentials ($\Delta\mu_1$), in Table D.2, which vary from approximately 3×10^6 to 1.0×10^7 (or greater) are associated with free energy changes associated only with a pressure - volume type of energy term.

$$(d\mu_1)_T = (v_1 d\rho_1)_T \qquad (E.6)$$

If equation E.6 is valid and complete for large negative pressures within the liquid, then the van der Waals equation, in effect, states that the liquid is (very) non ideal and that this non ideality arises due to the liquid demonstrating (gas like) compressible behaviour. However, an equation such as (E.6) is a "macroscopic" relationship

---

$$(\partial P/\partial\hat{v})_T = \partial P/\partial(\frac{1}{\rho_1}) = -(\rho^2{}_1\ \partial P/\partial\rho_1)_T = (-\rho^2{}_1\ \chi_1)_T$$

$$\{(\partial P/\partial\hat{v})_T \to 0\} \Rightarrow \{(\chi_1)_T \to 0\} \qquad (E.5)$$

involving thermodynamic properties and (state) parameters which are defined for the bulk phase. Though there is no sudden transition from "maccroscopic" bulk to molecular volumes, it is evident that equation (E.6) cannot be applied with equal rigor in the latter case. This is further complicated by the fact that the total free energy changes, in this case, are not only of the pressure-volume type, but also include surface energy changes which become increasingly important as the mean radius of curvature $\overline{R}$ (Figure 2.7) decreases. The surface (free) energy contributions are due to the (relatively)* rapidly varying dimensions of the liquid-vapor and solid-liquid interfaces and the associated interfacial tensions. These contributions are described qualitatively in the next section.

E.2. Additional Contributions to the Change in Liquid Phase Potential (from the reference state) - Applicability of the Thermodynamic Equation (2.62) to Molecular Dimensions.

It has been emphasized so far (Appendix D and Section E.1) that the application of the van der Waals equation to the expression for $d\mu_1$ (equation E.6) leads one to the conclusion that the liquid is extremely non ideal. This conclusion is valid for $\overline{R}$ (the mean radius of curvature) approaching molecular dimensions.

The following material provides the necessary contrinuity to the discussion presented in the foregoing section, since it is an extension of the second of the two observations made at the end of Appendix D.

---

*In other words, the proportional contribution of the surface (free) energy changes to the total free energy change is small when $\overline{R}$ is large, unlike the case above.

The hydrostatic balance for the capillary condensate {equation 2.17} which led to the Laplace and Young equations {(2.19), (2.20)} of capillarity in Chapter 2 is written as

$$KdV_l + d\Omega_{lg} = \cos\theta_{sl}\, d\,\Omega_{sl} \qquad (2.17)$$

$$P_g - P_l = \sigma_{lg} K \qquad (2.19$$

Laplace and Young equations.

and

$$\sigma_{sl} - \sigma_{sg} = \sigma_{lg} \qquad (2.21)$$

for an angle of contact of zero.

For macroscopic volumes of liquid where large numbers of molecules are present, the meniscus curvature K is assumed to be constant, as stated in Chapter 2. It is seen that this is also implied by the first of the Laplace and Young equations above, provided, of course, that the liquid-vapor interfacial tension σ_{lg} is constant. Thus, for small curvatures, the following numerical criterion is valid:

$$|V_l dK| \ll |KdV_l| \qquad (E.7)$$

As molecular volumes of the condensate are approached, with decreasing α (relative saturation, $P_g/P^o{}_g$), the curvature increases typically, for all of the experimental temperatures, by about two orders of magnitude. This is indicated in Figure E.1 which is a plot of K versus α. For instance, at 143.33^o C

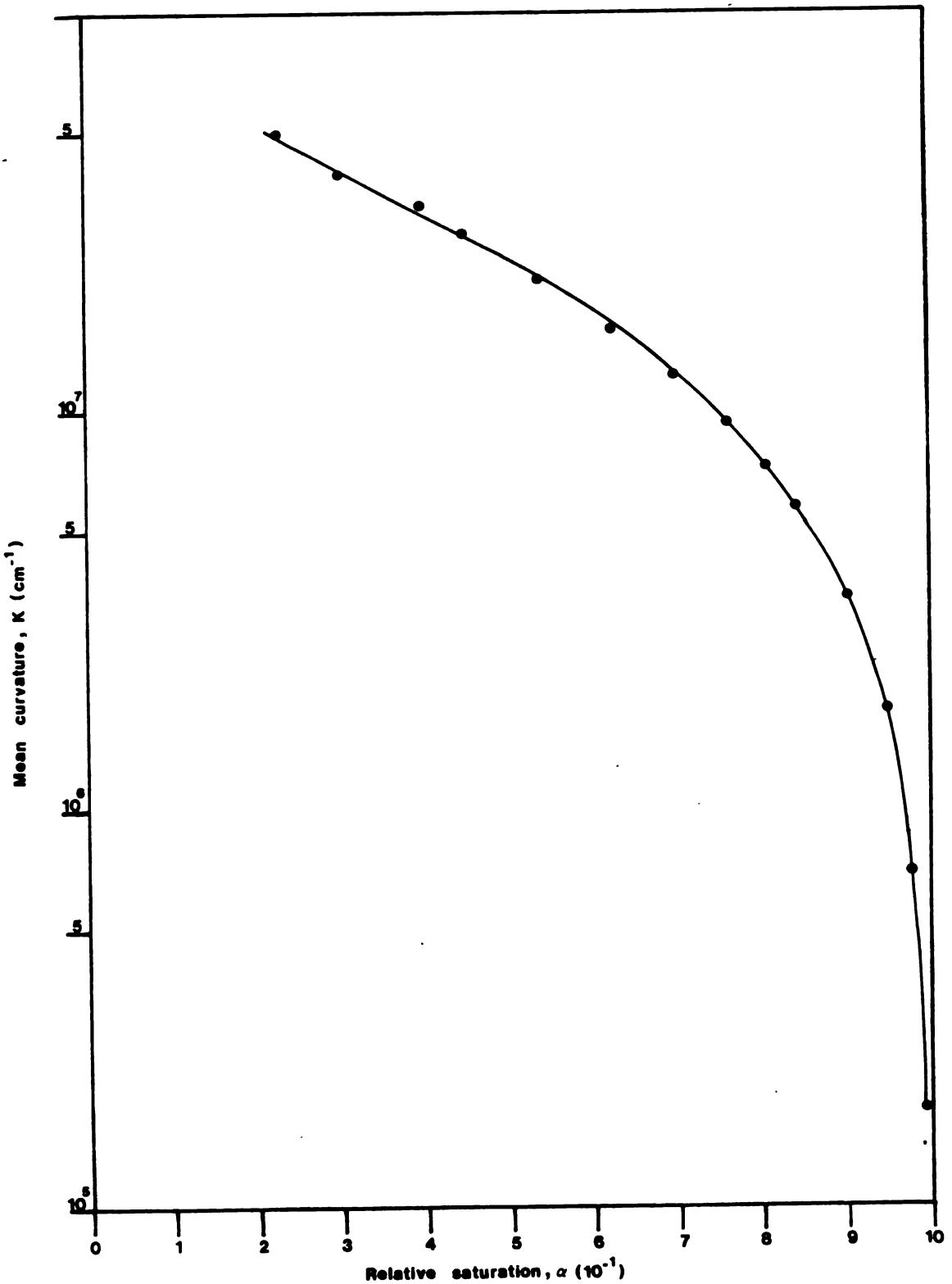

Figure E.1. Plot of the mean curvature K versus relative saturation α at T = 143.33° C.

α	$K\ (cm^{-1})$
0.9872	4.353×10^{5}
0.3899	3.246×10^{7}

Thus the change in the meniscus curvature K is relatively larger at the smaller values of α. Additionally, low values of α correspond to molecular volumes of the liquid so that inequality (E.7) does not hold in this region and the two terms are of comparable magnitude. The hydrostatic balance equation is then appropriately given by

$$K\, dV_1 + V_1\, dK + d\Omega_{1g} = \cos\theta_{s1}\, d\Omega_{s1} \qquad (E.8)$$

It may be noted here that the Laplace and Young equations do not immediately follow by matching the coefficients of equation (E.8) with those of the expression for the total (Helmholtz) free energy change, as was done in Chapter 2.

One of the restrictions imposed upon the thermodynamic system described in Section 2.3 (Chapter 2) was that the surface tension is invariant with curvature K (or condensate volume). This assumption breaks down under the present situation where the liquid-vapor interface id highly curved (large K) with respect to a plane surface. Buff and Kirkwood (B6, 1950) have commented on the dependance of the surface tension σ_{1g}. Hill's (H4, 1950) extension of Fowler's (approximate) theory of surface tension for plane surfaces also leads to the same qualitative conclusion that surface tension decreases with increasing curvature. The underlying assumption made by Hill in his thermodynamic

model is that the liquid phase is incompressible, however he specifically notes that "this becomes serious at large curvatures owing to accompanying large internal pressures" (within the liquid). One representation of the variation of σ_{lg} with K is given by the Gibbs - Tolman - Koenig equation (E.9), (H3):

$$\ln \frac{\sigma_{lg}}{\sigma_{lg0}} = - \int_r^\infty \frac{\frac{2Z_0}{r^2}\left[1 + \frac{Z_0}{r} + \frac{1}{3}\left(\frac{Z_0}{r}\right)^2\right]}{1 + 2\frac{Z_0}{r}\left[1 + \frac{Z_0}{r} + \frac{1}{3}\left(\frac{Z_0}{r}\right)^2\right]} dr \qquad (E.9)$$

where

r = radius of curvature

σ_{lg} = surface tension corresponding to r

σ_{lg0} = surface tension at $r = \infty$

Z_0 = displacement of the surface toward the body of the liquid.

Once again, there are uncertainties associated with the variation of the physical properties of liquid in the model that led to the derivation of equation (E.9). It is noteworthy, as the authors themselves point out, that an equation such as the above should be applied with caution.

The emphasis, in the context of this discussion, is not so much on the numerical values of the surface tension as on the fact that it decreases with increase in curvature. In fact the calculations resulting from Hills' (liquid incompressibility) model show a surprisingly small effect, as the author notes, of the curvature on surface

tension. However, both the rates of change of surface tension and surface energy increase with increase of curvature.

The physical model as pictured in Figure 2.3 is different from the liquid drop (or bubble) model of either Hill or Buff and Kirkwood (B6). In addition to the liquid-vapor interface, surface energy (contribution to $d\mu_1$) is also associated with the solid-liquid interface as the liquid meniscus moves within the pore. It follows from Figure 2.3 that for tensile stresses within the liquid, the spherical particles would experience deformation forces within the circle of contact with the liquid. In the present analysis, the adsorbent particles were assumed to be incompressible (Section 2.2). The general case of dimensional changes within the nonrigid solid particles has been given by Flood and Farhan (F6).

It was not the objective of this work to formulate a thermodynamically "complete" (mathematical) model which would enable a prediction of changes of pertinent liquid phase properties. As mentioned in Section 2.14, at the end of Chapter 2, such an endeavour would need to abandon the approach (of the problem) that leads to a Kelvin type equation. A formal approach would at least require that the expression for the total (Helmholtz) free energy change be modified to incorporate surface energy terms involving variable interfacial tension. The variation in the liquid-vapor tension σ_{lg} would then be given by meniscus curvature under the assumption that the liquid is not incompressible. The mathematical problem would be formidable, especially with this restriction in force, and at this point one needs to speculate upon the relevance of the results of such

a rigorous approach. At the very least, it would clarify the integrity of the simplifying assumptions which have been stated earlier and in Appendices C and D as well. The discussion pertaining to this aspect of the capillary condensation model has been presented in Section 2.14, Chapter 2.

APPENDIX F

APPENDIX F

This appendix lists the FORTRAN (IV) programs to evaluate the parameters associated with capillary condensation in the macropores. The results of the computations are presented in Chapter 2. Sections F.1 and F.2 are essentially the same programs, however program LIQUID (F.2) was written to study the variation of liquid properties at high states of tension.* Program CAPILL (Section F.3) uses a modified version of the Kelvin equation to evaluate the radius of curvature of the capillary condensate.

---

*See Appendices C, D and E.

```
F.1.    PROGRAM LIQUID (INPUT,OUTPUT)
C
C     .....
C     .THIS PROGRAM CALCULATES THE RELATIVE LIQUID PHASE DENSITIES AND
C      THE ISOTHERMAL SUSCEPTIBILITY
C     .....
      DIMENSION A(6),B(6),P(65),T(6),PSTAR(6),VBAR1(6),VBAR(65),FMU(60)
     1,ALPHA(60),DELP(60),ETA(60),VRATIO(60),RHO1(6),CHI(60),T1(6),BC(6)
     1,CURVE(60),DMUDID(60),DRUST(60),ST(6),PSTAR1(6),ST1(6),RAD(60),PS
     U(60),BETA(60),FMUL(60)
C     A(I) AND B(J) ARE THE TEMPERATURE AND PRESSURE COEFFICIENTS IN THE
C     KELL - SHALLEY EMPIRICAL EQUATION.
      REAL INT
      DATA (A(I),I=1,6)/1.,.1,.1E-1,1.0E-3,1.0E-5,1.0E-7,1.0E-10/
      DATA (B(J),J=1,18)/-.2769,.2427,-.1067,.71969,-1.3704,2.1264,-2.
     1.1760,3.4432,-2.913,6.0227,-3.6432,11.467,-3.9041,2.0836,-7.102
     1,5.9341,-4.1744,14.841/
C     BC(I) ARE THE SECOND VIRIAL COEFFICIENTS FOR THE VARIOUS TEMPS.
C     CURVE(K) IS THE CURVATURE, ST IS THE SURFACE TENSION.
      DATA (ST(I),I=1,6)/65.20,59.26,53.52,49.93,46.73,42.14/
      DATA (BC(I),I=1,6)/-626.83,-569.487,-429.544,-387.485,-355.122,-3
     113.718/
      PRINT 3
      PRINT 4,(BC(I),I=1,6)
C     DMUL IS THE LIQUID PHASE CHEMICAL POTENTIAL.
    5 FORMAT(//,1X,*TEMP*,3X,*PRESSURE*,5X,*VBAR*,7X,*DENSITY*,9X,*ETA*
     1,9X,*BETA*,5X,*DEL-P*,7X,*CHI*,12X,*DMUL*,//)
    6 FORMAT (9X,F6.2,2X,F7.5,4X,F9.7,3X,F9.7,5X,F9.7,5X,F6.4,2X,F9.7,2X
     1,E15.8,3X,F11.4,/)
    7 FORMAT (1X,*TEMPERATURE COEFFICIENTS A(I)*,//)
    8 FORMAT (15X,E7.1,/)
    9 FORMAT (1X,*PRESSURE COEFFICIENTS B(I)*,//)
   10 FORMAT (15X,F9.5,/)
   13 FORMAT  (1X,F6.2,*A*,F7.5,5X,F6.4 ,5X,F10.5,4X,F10.5,5X,F9.7,10X,E1
     1.5,14X,F9.5 ,/)
   20 FORMAT (1X,*TEMP*,9X,*PSAT*,6X,*VBAR1*,6X,*SURFACE TENSION (DYNES
     1/CM)*,//)
   25 FORMAT (9X,F6.2,5X,F7.4,5X,F7.4,11X,F5.2,/)
   30 FORMAT (20X,*VALUES OF THE SECOND VIRIAL COEFFICIENT*,//)
   32 FORMAT (3X,F5.3,/)
    5 FORMAT (2X,*THE FOLLOWING VALUES OF PSATM AND SPECIFIC VOLUME
     1 ARE OBTAINED FROM LITERATURE*,//)
  550 FORMAT (2X,*PSATM OR PSTAR IS IN BARS AND VBAR IS IN CC/G-MOL*,
     1//)
  575 FORMAT(/,5X,*TEMP(DEG-C)*,3X,*PRESSURE(ATM)*,3X,*VBAR(CC/G-MOL)*,
     13X,*DENSITY(G/CC)*,3X,*BETA(ATM)*,7X,*CHI(CC-ATM/G-MOL)*,3X,*
     DMUL(CC-ATM/G-MOL)*,//)
```

```
  6   FORMAT(//,2X,'THE WELL AND CHALLEY COEFFICIENTS APPEAR QUITE',/)
  7   FORMAT(2X,'ACCURATE AS CAN BE SEEN BY COMPARING APPROPRIATE',/)
800   FORMAT(2X,'VBAR VALUES WITH VBAR1 VALUES FROM LITERATURE',//)
      PRINT
      PRINT 6,(A(I),I=1,4)
      PRINT
      PRINT 10,(B(J),J=1,10)
C     T(I) IS THE TEMPERATURE OF THE AMBIENT VAPOR IN EQUILIBRIUM WITH
C     THE CAPILLARY CONDENSATE (DEG.C).
C     PSTAR(I) IS THE SATURATION VAPOR PRESSURE CORRESPONDING TO EACH
C     OF THE TEMPERATURES...BARS. A(I) AND B(I) ARE THE WELL AND CHALLEY
C     TEMPERATURE AND PRESSURE COEFFICIENTS IN THE GENERALIZED
C     EXPRESSION FOR THE SPECIFIC VOLUME OF WATER.
C     PSTAR(I) IS THE STARTING VALUE USED FOR THE LIQUID PRESSURE FOR
C     EACH TEMPERATURE. THESE CALCULATIONS ASSUME THAT THE LIQUID
C     PRESSURES ARE NEAR ATMOSPHERIC.
      READ*,(T(I),PSTAR(I),VBAR1(I),I=1,6)
      PRINT
      PRINT 55
      PRINT
      PRINT 25,(T(I),PSTAR(I),VBAR1(I),ST(I),I=1,6)
      PA=1.1317                PA1=1.
      PRINT 75
      DO 10 I = 1,4
      PRINT
C     PSTAR1 AND PA1 ARE IN ATMOSPHERE UNITS.
      R=82.057
      T1(J)=T(J)+273.16
      PSTAR1(J)=PSTAR(J)*.967
      CHI(1)=
      F(1)=PSTAR1(J)   K=1
C     PB(K) IS IN BARS
 3    PB(K) = P(K)/1.967
      Z = PB(K)*PA1
C     C,D,E,F,G,AND H ALL ARE INDIVIDUAL TERMS IN THE WELL - CHALLEY
C     EMPIRICAL EQUATION.
      C=A(1)*(1.+B(1)*Z+1.E-6*B(2)*Z*Z+1.E-9*B(3)*Z**3*1.E-13)
      D = A(2)*T(J)*(B(4)*Z*1.E-6+B(5)*(Z*Z)*1.E-9+B(6)*(Z**3)*1.E-13
     1)
      E = A(3)*(T(J)**2)*(B(7)*Z*1.E-6+B(8)*(Z*Z)*1.E-9*B(9)*(Z**3)*1.
     1 E-13)
      F= A(4)*(T(J)**3)*(B(10)*Z*1.E-6+B(11)*(Z*Z)*1.E-9+B(12)*(Z**3)*
     11.E-13)
      G= A(5)*(T(J)**4)*(B(13)*Z*1.E-6+B(14)*(Z*Z)*1.E-9+B(15)*(Z**3)*
     11.E-13)
      H= A(6)*(T(J)**5)*(B(16)*Z*1.E-6+B(17)*(Z*Z)*1.E-9+B(18)*(Z**3)*
     11.E-13)
```

```
C       VRATI  IS VBAR/VBAR(T,1 AT )
        VRATIO(K) = C+D*L+E*G+F
        VBAR(K) = VRATIO(K)*VBAR1(J)
C       RHO(K) IS THE MOLAR DENSITY OF WATER UNDER THESE CONDITIONS
        RHO(K) = 1./(VBAR(K)*18.016)
C       DELP(K) IS THE REDUCTION IN LIQUID PRESSURE AND IS USED TO
C       EVALUATE CHI AT VARIOUS PRESSURES. IT IS  THE    SAME AS DELTA-P
C       FOR THE LIQUID PHASE WHICH IS DEFINED AS THE DIFFERENCE BETWEEN
C       THE REFERENCE PRESSURE PL(J) AND THE EXISTING PRESSURE PL.
C       BETA (K) IS AN INTERNAL PARAMETER USED TO EVALUATE DELP.
        BETA(K) = P(K)/PSTAR1(J)
        DELP(K) = PSTAR1(J)*(1.00-BETA(K))
        RHO1(J)=1./(VBAR(1)*18.016)
        ETA(K) = RHO(K)/RHO1(J)
C       CHI(K) IS THE ISOTHERMAL SUSCEPTIBILITY.
        IF (K.EQ.1) GO TO 20
        CHI(K)=(P(K)-PO)/(RHO(K)-R1)
        IF (CHI(K).LE..0) GO TO 1
        AVCHI = (CHI(K) + CHI(K-1))/2.0
        DX = ALOG(ETA(K)/ETA(K-1))
        INT = AVCHI * DX
        DPUL1 = ABS(INT)
        DPUL(K) = DPUL(K-1) + DPUL1
   30   DPUL(1) = 0.0
    4   PRINT 40,T(J),P(K),VBAR(K),RHO(K),ETA(K),DETA(K),DELP(K),CHI(K),DP
       UL(K)
        IF (J.EQ.1.OR.J.EQ.2) P(K+1)=P(K)-.2
        IF (J.GT.3.AND.J.LE.5) P(K+1)=P(K)-.3
        IF (J.EQ.6) P(K+1)=P(K)-.5
        IP=P(K)
        K1=RHO(K)
        K = K+1
        IF (P(K).LE.0.0) GO TO 1
        GO TO 3
    1   CONTINUE
        PRINT 60
        PRINT 70
        PRINT 80
        END
65.56,0.2561,1.0217,95.89,.9743,1.4261,126.67,0.4425,1.667,143.33,
3.9692,1.8451,157.52,5.7566,1.6856,176.67,9.2834,1.1534
```

F.2.

```
      PROGRAM LIQUID (TAPE6,OUTPUT)
C     ******************************************************************
C     THIS PROGRAM CALCULATES THE RELATIVE LIQUID PHASE DENSITIES AND
C     THE ISOTHERMAL SUSCEPTIBILITY UPTO A TENSION OF 1000 ATMOSPHERES.
C     ******************************************************************
      DIMENSION A(6),B(10),P(600),T(6),PSTAR(6),VRAP1(6),VRAM(600),RHO(6
     1,6),ALPHA(6,6),DELI(6,6),ETA(6,6),VRATIO(6,6),RHO1(600),CHI(600),T
     L1(6),PC(6),PSTAR1(6),ST1(6),ST(6),PP(600),PETA(600),PMUL(600)
C     A(I) AND B(J) ARE THE TEMPERATURE AND PRESSURE COEFFICIENTS IN THE
C     KELL - WHALLEY EMPIRICAL EQUATION.
      REAL INT
      DATA (A(I),I=1,6)/1.0,1.0E-1,1.0E-3,1.0E-5,1.0E-7,1.0E-10/
      DATA(B(J),J=1,10)/-.9769,.2627,-5.1E-2,7.7199E-3,-1.3704E-4,2.426E-7,
     1-.1761,3.432E-2,-.9136,.9227,-3.6432,11.467,-3.1941,2.836,-7.102
     1,5.9316,-4.1744,14.241/
C     PC(I) ARE THE SECOND VIRIAL COEFFICIENTS FOR THE VARIOUS TEMPS.
C     CURVE(Y) IS THE CURVATURE. ST IS THE SURFACE TENSION.
      DATA (ST(J),I=1,6)/65.2,59.6,53.52,49.93,46.73,42.14/
      DATA (PC(I),I=1,6)/-726.8,-509.487,-429.644,-387.485,-355.122,-3
     113.718/
      PRINT 30
      PRINT 52,(PC(I),I=1,6)
C     PMUL IS THE LIQUID PHASE CHEMICAL POTENTIAL.
   5  FORMAT(///,10X,*TEMP*,5X,*PRESSURE*,5X,*VRAP*,7X,*DENSITY*,9X,*ETA*
     1,17X,*BETA*,5X,*DELI-P*,6X,*CHI*,17X,*PMUL*,//)
   6  FORMAT (9X,F6.2,2X,F6.2,4X,F9.7,3X,F9.7,5X,F9.7,5X,F8.2,2X,F8.2,2X
     1,E15.8,3X,F11.4,/)
   7  FORMAT (10X,*TEMPERATURE COEFFICIENTS A(I)*,//)
   8  FORMAT (15X,E7.1,/)
   9  FORMAT (10X,*PRESSURE COEFFICIENTS B(I)*,//)
  10  FORMAT (15X,E9.5,/)
  11  FORMAT  (1X,F6.2,4X,F7.5,5X,F6.4 ,3X,E11.5,4X,E10.5,5X,F9.7,10X,E1
     1.5,14X,F9.5  /)
  20  FORMAT (1 X,*TEMP*,6X,*PSAT*,6X,*VRAP1*,6X,*SURFACE TENSION (DYNES
     1/CM)*,//)
  25  FORMAT (4X,F6.2,5X,F7.4,5X,F7.4,11X,F5.2,/)
  30  FORMAT (2 X,*VALUES OF THE SECOND VIRIAL COEFFICIENT*,//)
  32  FORMAT (3 X,E9.3,/)
  50  FORMAT (20X,*THE FOLLOWING VALUES OF PSAT. AND SPECIFIC VOLUME
     1 ARE DRAWN FROM LITERATURE*,//)
  55  FORMAT (2 X,*PSATS. OR PSTAR IS IN BARS AND VRAP IS IN CC/GM-MOL*,
     1//)
  57  FORMAT(//,5X,*TIME(SEC-C )*,3X,*PRESSURE(ATM)*,3X,*VRAP(CC/GM-MOL)*,
     13X,*DENSITY(GM-MOL/CC)*,3X,*BETA(ATM)*,3X,*CHI(CC-ATM/GM-MOL)*,3X,*
     2DELMUL(CC-ATM/GM-MOL)*,//)
  60  FORMAT(//,2 X,*THE KELL AND WHALLEY COEFFICIENTS APPEAR QUITE*,/)
  70  FORMAT(2 X,*ACCURATE AS CAN BE SEEN BY COMPARING APPROPRIATE*,//)
  80  FORMAT(2 X,*VRAP VALUES WITH VRAP1 VALUES FROM LITERATURE*,///)
```

```
      PRINT 6
      PRINT 55,(A(I),I=1,6)
      PRINT 66
      PRINT 100, (B(J),J=1,12)
C     T(I) IS THE TEMPERATURE OF THE ASBIENT VAPOR IN EQUILIBRIUM WITH
C     THE CAPILLARY CONDENSATE (DEG.C).
C     PSTAR(I) IS THE SATURATION VAPOR PRESSURE CORRESPONDING TO EACH
C     OF THE TEMPERATURES...PARS. A(I) AND B(I) ARE THE KELL AND SHALLEY
C     TEMPERATURE AND PRESSURE COEFFICIENTS IN THE GENERALIZED
C     EXPRESSION FOR THE SPECIFIC VOLUME OF WATER.
C     PSTAR(I) IS THE STARTING VALUE USED FOR THE LIQUID PRESSURE FOR
C     EACH TEMPERATURE. THESE CALCULATIONS ASSUME THAT THE FITTING
C     POLYNOMIAL FOR THE LIQUID VOLUME IS VALID FOR THE STATE OF TENSION
      READ*,(T(I),PSTAR(I),VPAR1(I),I=1,6)
      PRINT 666
      PRINT 55,(A(I),I=1,6)
      PRINT 2 ,(B(I),I=1,12)
      PRINT 25,(T(I),PSTAR(I),VPAR1(I),ST(I),I=1,6)
      PA=1.1317                 PA1=1.
      PRINT 575
      DO 1  J = 1,
      PRINT
C     PSTAR AND PA1 ARE IN ATMOSPHERE UNITS.
      I=82.57
      T1(J)=T(J)+273.16
      PSTAR1(J)=PSTAR(J)*.987
      CPI(1)=
      P(1)=PSTAR1(J)    I=1
C     PR(K) IS IN BARS
    3 PR(K) = P(K)/.987
      Z = PR(K)-PA
C     C,D,E,F,G,AND H ARE THE INDIVIDUAL TERMS IN THE KELL - SHALLEY
C     EMPIRICAL EQUATION.
      C=A(1)*(1. +B(1)*Z*1.0E-6+B(2)*Z*Z*1.0E-9+B(3)*Z**3*1.0E-13)
      D = A(2)*T(J)*(B(4)*Z*1.0E-6+B(5)*(Z*Z)*1.0E-9+B(6)*(Z**3)*1.0E-13
     1)
      E = A(3)*(T(J)**2)*(B(7)*Z*1.0E-6+B(8)*(Z*Z)*1.0E-9+B(9)*(Z**3)*1.
     10E-13)
      F= A(4)*(T(J)**3)*(B(10)*Z*1.0E-6+B(11)*(Z*Z)*1.0E-9+B(12)*(Z**3)*
     11.0E-13)
      G= A(5)*(T(J)**4)*(B(13)*Z*1.0E-6+B(14)*(Z*Z)*1.0E-9+B(15)*(Z**3)*
     11.0E-13)
      H= A(6)*(T(J)**5)*(B(16)*Z*1.0E-6+B(17)*(Z*Z)*1.0E-9+B(18)*(Z**3)*
     11.0E-13)
```

```
C       VRATIO IS VBAR/VBAR1(T,1 ATM)
        VRATIO(K) = C+D*E+F*G+H
        VBAR(K) = VRATIO(K)*VBAR1(J)
C       RHO(K) IS THE MOLAR DENSITY OF WATER UNDER THESE CONDITIONS
        RHO(K) = 1.0/(VBAR(K)*18.016)
C       DELP(K) IS THE REDUCTION IN LIQUID PRESSURE AND IS USED TO
C       EVALUATE CHI AT VARIOUS PRESSURES. IT IS THE SAME AS DELTA-P
C       FOR THE LIQUID PHASE WHICH IS DEFINED AS THE DIFFERENCE BETWEEN
C       THE REFERENCE PRESSURE PL(J) AND THE EXISTING PRESSURE PL.
C       BETA(K) IS AN INTERNAL PARAMETER USED TO EVALUATE DELP.
        BETA(K) = RHO(K)/RSTAR1(J)
        DELP(K) = PSTAR1(J)*(1.00-BETA(K))
        RHO1(J)=1.0/(VBAR(1)*18.016)
        ETA(K) = RHO(K)/RHO1(J)
C       CHI(K) IS THE ISOTHERMAL SUSCEPTIBILITY.
        IF (K.EQ.1) GO TO 30
        CHI(K)=(P(K)-P(1))/(RHO(K)-R1)
        IF (CHI(K).LE.0.0) GO TO 1
        AVCHI = (CHI(K) + CHI(K-1))/2.0
        DX = ALOG(ETA(K)/ETA(K-1))
        INT = AVCHI * DX
        DMUL1 = ABS(INT)
        DMUL(K) = DMUL(K-1) + DMUL1
   30   DMUL(1) = 0.00
   40   PRINT 60,T(J),P(K),VBAR(K),RHO(K),ETA(K),BETA(K),DELP(K),CHI(K),DM
       1UL(K)
        P(K+1) = P(K)-25.
        P0=P(K)
        R1=RHO(K)
        K = K+1
        IF (ABS(P(K)).GE.1.0 ) GO TO 1
        GO TO 7
    1   CONTINUE
        PRINT 7
        PRINT 70
        PRINT 80
        END
55.56,.2563,1.1213,55.89,.9743,1.4261,136.67,2.4425,1.0667,143.33,
3.9682,1.0561,157.22,5.7560,1.0856,176.67,9.2824,1.1534
```

F.3.

```
      PROGRAM CAPILL (INPUT,OUTPUT)
C     ******************************************************************
C     THIS PROGRAM CALCULATES THE PROPERTIES OF THE CAPILLARY CONDENSATE
C     IN TERMS OF ITS DEVIATION FROM IDEALITY.THE CURVATURE CORRESPON-
C     DING TO EACH RELATIVE VAPOR PRESSURE IS CALCULATED.
C     ******************************************************************
      DIMENSION A(6),B(18),P(600),T(6),PSTAR(6),VBAR(600),VBAR1(6),RHO(6
     100),ALPHA(600),DELP(600),ETA(600),VRATIO(600),RHO1(6),T1(6),BC(6),
     1CURVE(600),DMUGID(600),DMUGST(600),ST(6),PSTAR1(6),ST1(6),RAD(600)
     1,PB(600)
C     A(I) AND B(J) ARE THE TEMPERATURE AND PRESSURE COEFFICIENTS IN THE
C     KELL - WHALLEY EMPIRICAL EQUATION.
      DATA (A(I),I=1,6)/1.0,1.0E-1,1.0E-3,1.0E-5,1.0E-7,1.0E-10/
      DATA(B(J),J=1,18)/-50.9769,8.2627,-9.109,3.71999,-1.3794,2.626,-7.
     101760,3.4032,-8.913,6.00227,-3.6432 ,11.467,-3.09041,2.0836,-7.102
     1,5.93416,-4.1744,14.841/
C     BC(I) ARE THE SECOND VIRIAL COEFFICIENTS FOR THE VARIOUS TEMPS.
C     CURVE(K) IS THE CURVATURE. ST IS THE SURFACE TENSION.
      DATA (ST(I),I=1,6)/65.20,59.06,53.52,49.93,46.73,42.14/
      DATA (BC(I),I=1,6)/-626.603,-509.487,-429.544,-387.485,-355.122,-3
     113.718/
      PRINT 300
      PRINT 320,(BC(I),I=1,6)
   70 FORMAT (10X,*TEMPERATURE COEFFICIENTS A(I)*,//)
   80 FORMAT (15X,E7.1,/)
   90 FORMAT (10X,*PRESSURE COEFFICIENTS B(I)*,//)
  100 FORMAT (15X,F9.5,/)
  120 FORMAT(/,1X,*TEMP*,8X,*PRESSURE*,4X,*ALPHA*,4X,*DELTA-MUID*,4X,*DE
     1LTA-MUST*,6X,*DELTA-P*,10X,*CURVATURE(INV.CM)*, 8X,*RADIUS OF CURV
     2ATURE (ANGS)*,//)
  130 FORMAT  (1X,F6.2,6X,F7.5,5X,F6.4 ,3X,E10.5,4X,E10.5,5X,F9.7,10X,E1
     10.5,14X,F11.5,/)
  200 FORMAT (10X,*TEMP*,6X,*PSAT*,6X,*VBAR1*,6X,*SURFACE TENSION (DYNES
     1/CM)*,//)
  250 FORMAT (9X,F6.2,5X,F7.4,5X,F7.4,11X,F5.2,/)
  300 FORMAT (20X,*VALUES OF THE SECOND VIRIAL COEFFICIENT*,//)
  320 FORMAT (30X,F8.3,/)
  500 FORMAT (20X,*THE FOLLOWING VALUES OF PSATN. AND SPECIFIC VOLUME
     1 ARE DRAWN FROM LITERATURE*,//)
  550 FORMAT (20X,*PSATN. OR PSTAR IS IN BARS AND VBAR IS IN CC/GM-MOL*,
     1//)
  900 FORMAT(10X,*TEMP(DEG.C),PRESSURE(ATM),DELTA-MUID(ATM-CC/G-MOLE),DE
     1LTA-MUST(ATM-CC/G-MOLE),DELTA-P(ATM)*,//)
      PRINT 70
      PRINT 80,(A(I),I=1,6)
      PRINT 90
```

```
      PRINT 160, (B(J),J=1,18)
C     T(I) IS THE TEMPERATURE OF THE AMBIENT VAPOR IN EQUILIBRIUM WITH
C     THE CAPILLARY CONDENSATE (DEG.C).
C     PSTAR(I) IS THE SATURATION VAPOR PRESSURE CORRESPONDING TO EACH
C     OF THE TEMPERATURES...BARS. A(I) AND B(I) ARE THE KELL AND WHALLEY
C     TEMPERATURE AND PRESSURE COEFFICIENTS IN THE GENERALIZED
C     EXPRESSION FOR THE SPECIFIC VOLUME OF WATER.
      READ*,(T(I),PSTAR(I),VBAR1(I),I=1,6)
      PRINT 500
      PRINT 550
      PRINT 200
      PRINT 250,(T(I),PSTAR(I),VBAR1(I),ST(I),I=1,6)
      PA=1.01317       $       PA1=1.000
      PRINT 900
      DO 10 J = 1,6
C     PSTAR1 AND PA1 ARE IN ATMOSPHERE UNITS.
      PRINT 120
      ST1(J)=9.8687E-7*ST(J)
      R=82.057
      T1(J)=T(J)+273.16
      PSTAR1(J)=PSTAR(J)*0.987
      P(1)=PSTAR1(J)   $   K=1
C     PB(K) IS IN BARS.
   30 PB(K) = P(K)/0.987
      Z = PB(K)-PA1
C     C,D,E,F,G,AND H ARE THE INDIVIDUAL TERMS IN THE KELL - WHALLEY
C     EMPIRICAL EQUATION.
      C=A(1)*(1.0+B(1)*Z*1.0E-6+B(2)*Z*Z*1.0E-9+B(3)*Z**3*1.0E-13)
      D = A(2)*T(J)*(B(4)*Z*1.0E-6+B(5)*(Z*Z)*1.0E-9+B(6)*(Z**3)*1.0E-13
     1)
      E = A(3)*(T(J)**2)*(B(7)*Z*1.0E-6+B(8)*(Z*Z)*1.0E-9+B(9)*(Z**3)*1.
     10E-13)
      F= A(4)*(T(J)**3)*(B(10)*Z*1.0E-6+B(11)*(Z*Z)*1.0E-9+B(12)*(Z**3)*
     11.0E-13)
      G= A(5)*(T(J)**4)*(B(13)*Z*1.0E-6+B(14)*(Z*Z)*1.0E-9+B(15)*(Z**3)*
```

```
     11.0E-13)
      H= A(6)*(T(J)**5)*(B(16)*Z*1.0E-6+B(17)*(Z*Z)*1.0E-9+B(18)*(Z**3)*
     11.0E-13)
C     VRATIO IS VBAR/VBAR(T,1 ATM)
      VRATIO(K) = C+D+E+F+G+H
      VBAR(K) = VRATIO(K)*VBAR1(J)
C     RHO(K) IS THE MOLAR DENSITY OF WATER UNDER THESE CONDITIONS
      RHO(K) = 1.0/(VBAR(K)*18.016)
C     ALPHA(K) IS THE RELATIVE VAPOR PRESSURE P(I)/PSTAR1(J)
      ALPHA(K)=P(K)/PSTAR1(J)
      DELP(K) = PSTAR1(J)*(1.00-ALPHA(K))
      RHO1(J)=1.0/(VBAR(1)*18.016)
      ETA(K) = RHO(K)/RHO1(J)
      IF (K.EQ.1) GO TO 40
C     DMUGST IS THE GAS PHASE CHEMICAL POTENTIAL DEVIATION FROM
C     IDEALITY. DMUGID IS THE IDEAL CASE CHEMICAL POTENTIAL FOR THE
C     GAS PHASE.
      DMUGST(K) = -BC(J)*PSTAR1(J)*(1.0-ALPHA(K))
      DMUGID(K)=-R*T1(J)*ALOG(ALPHA(K))
C     CURVE(K) IS THE MEAN CURVATURE (INVERSE CM.)
      CURVE(K)=(RHO1(J)*(DMUGID(K)-DMUGST(K))-DELP(K))/ST1(J)
C     RAD(K) IS THE RADIUS OF CURVATURE(ANGSTROMS).
      RAD(K) = (2.0*1.0E+08)/CURVE(K)
      DMUGID(1) = 0.00
      DMUGST(1) = 0.00
      CURVE(1) = 0.00
      RAD(1)=0.00
   40 PRINT 130,T(J),P(K),ALPHA(K),DMUGID(K),DMUGST(K),DELP(K),CURVE(K),
     URAD(K)
      IF (J.EQ.1.OR.J.EQ.2) P(K+1)=P(K)-0.002
      IF (J.GE.3.AND.J.LE.5) P(K+1)=P(K)-0.01
      IF (J.EQ.6) P(K+1)=P(K)-0.02
      PO=P(K)
      R1=RHO(K)
      K = K+1
      IF (P(K).LE.0.0) GO TO 10
      GO TO 30
   10 CONTINUE
      END
65.56,0.2563,1.0213,98.89,0.9743,1.04261,126.67,2.4425,1.0667,143.33,
3.9692,1.08351,157.22,5.7569,1.09856,176.67,9.2824,1.1234
```

APPENDIX G

APPENDIX G

When two resistive bodies contact each other, and a voltage is impressed across them, the lines of current flow are constricted in the small conducting spots where the contacting members meet. The bulk of the measured resistance is due to this contact resistance. Equation 3.68 (Section 3.3, Chapter 3) gives the expression for the contact resistance, where the contact spot is a circle of radius a and is formed by two solid spherical particles.

$$R_{\mu} = \frac{\rho}{2\pi a} \tan^{-1} \frac{\sqrt{\mu}}{a} \qquad (3.68)$$

However, when this contact resistance needs to be incorporated into a model that has a larger scope*, some assumptions could perhaps be made that would enable a simplification of the mathematical model. Furthermore, to complete the description of the contact resistance, beyond the expression given in (3.68), a qualitative examination of the contact resistance is required. This is accomplished in the next section.

G.1 The Contact or Constriction Resistance

The constriction resistance is (simplistically) defined in this section. In contrast to a rigorous mathematical representation, the

*Such as in the present case of determining the resistivity of a (spherical) particulate layer .

emphasis here is on the physical significance behind the narrowing of the lines of current flow near the contact.

Figure G.1 shows two cylinders, A_1 and A_2, (contacting members) joined at a contact which has an area less than the cylindrical cross section. This (electrical) contact is indicated by A_c in the diagram.

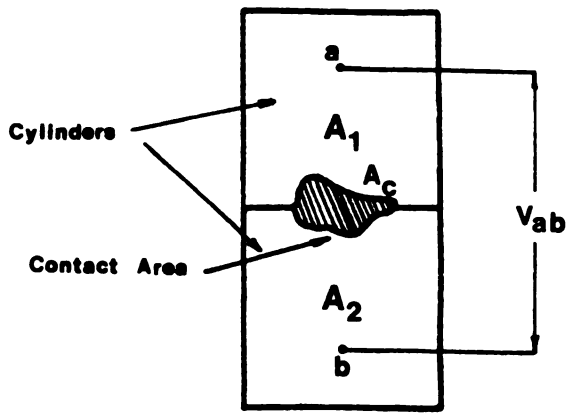

Figure G.1. Electrical contact between two identical cylinders.

If an external voltage V_{ab} is applied as shown, then the effective resistance R between points a and b is given by*

$$R_{ab} = V_{ab} I \qquad (G.1)$$

where I is the (measured) current resulting from the impressed voltage.

Let a new resistance $\overline{R}_{ab}$ be measured for the case where the contact area is equal to the cylindrical cross section, i.e., A_1 and A_2 are now parts of a single solid cylinder. In this instance, there is no constriction of the current flow (lines). Then, by definition, the constriction resistance is

---

*Due to Holm. See reference H1.

$$R_c = R_{ab} - \bar{R}_{ab} \qquad (G.2)$$

The "constriction" voltage is similarly defined as

$$V_c = R_c I \qquad (G.3)$$

where the quantities V_c, R_c and I are terms due to the constriction only. Having defined these parameters associated with a constriction, it is appropriate, at this stage, to look into the types of constrictions. This is investigated in Section G.2.

G.2. Types of Constrictions

To enable an understanding of the constriction of the lines of current flow (hence also the magnitude of the resistance), these are classified into two types; namely, short and long constrictions. The constriction region refers to that region within the contacting members where the lines of current flow deviate from their straight path. This is illustrated by Figure G.2.

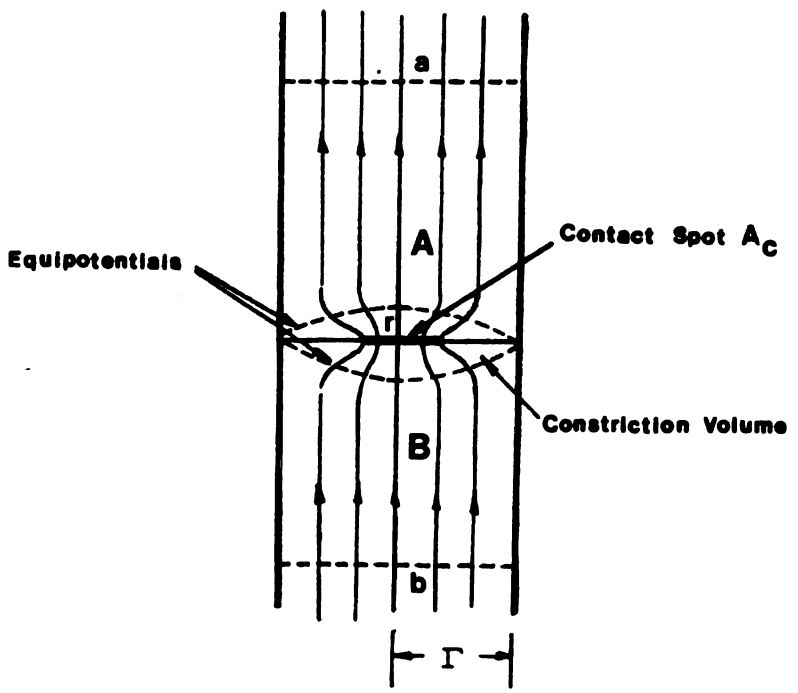

Figure G.2. The constriction region in a contact.

The figure shows lines of current flow and equipotential surfaces for the two members, A and B, in contact. A and B are of the same material. The constriction is indicated near the contact, and it is the region beyond which the lines of force are straight. The distance of the equipotentials from the line of contact is of the same order of magnitude as the radius Γ so that the approximate resistance (between

the equipotentials) $\overline{R}$, in the absence of a contact*, is

$$\overline{R} = O(M) \left\{\frac{\rho\Gamma}{\pi\Gamma^2}\right\}^{**} \qquad (G.4)$$

(see also equation (3.2), Chapter 3)

where,

ρ = material resistivity, ohm-cm

Γ = radius of cylinder (Figure G.2)

Let R be the resistance measured for the configuration of Figure G.2. This resistance is also measured between the equipotentials as before. This resistance then comprises of two separate contributions:

1) The resistance R_c due to the constriction, where r (in the figure) is the radius of the contact A_c.
2) The resistance between the equipotentials, due to the material itself.

For the case where $\Gamma >> r$, the constriction volume is small relative to the volume $\pi\Gamma^3$, across which $\overline{R}$ [in equation (G.4)] is measured. Hence if $\pi\Gamma^3 >> r^3$, $\overline{R}$ is negligible compared to R. This is the criterion for a long constriction. When, instead, a constriction is limited to a distance comparable with the radius r, $\overline{R}$ is not negligible, and the constriction is called short.

---

*That is, if A and B are parts of a single solid cylinder [see equation (G.2)] obviously, the equipotentials are not as shown, for this particular case.

**O(M) = order of magnitude. Also see footnote to equation (3.2), Chapter 3.

APPENDIX H

APPENDIX H

The relation between electrostatic field strength and charge density (which is the source of the field) is one of Maxwell's (electrostatic) field equation. These are developed beginning the familiar Coulomb's law for the interaction between two point charges. The first field equation is derived in Section H.1.

H.1. Relation Between the Electrostatic Field Strength and the Charge Density in Vacuum.

The force between two stationary point charges q, and q_2 is given by Coulombs law as

$$\vec{f}_{12} = K \frac{q_1 q_2}{|\vec{r}_1 - \vec{r}_2|} \hat{n} \qquad \text{(H.1)}$$

where

$\vec{f}_{12}$ = force on q_1 due to q_2

$|\vec{r}_1 - \vec{r}_2|$ = shortest distance between q_1 and q_2

$\hat{n}$ = unit vector from q_2 to q_1.

The force $\vec{f}_{12}$ is collinear with $\hat{n}$ and $\hat{n}$ is given as

$$\hat{n} = \vec{r}_1 - \vec{r}_2 / |\vec{r}_1 - \vec{r}_2| \qquad \text{(H.2)}$$

K is a proportionality constant given by,

$$K = \frac{1}{4\pi\varepsilon_0} \text{ in MKS units}$$

ε_0 = permittivity of free space

$= \frac{1}{36\pi} \times 10^{-9}$ (farads/meter)

The force $\vec{f}$ due to a fixed ensemble of charges on a charge q is

$$\vec{f} = \frac{1}{4\pi\varepsilon_0} q \sum_{j=1}^{n} \{q_j/(\vec{r}-\vec{r}_j)^2\} \hat{n}_j \qquad (H.3)$$

$$= q \vec{E}(\vec{r}) \qquad (H.4)$$

where

$\vec{E}(\vec{r})$ is the electrostatic field strength, and is given as

$$\vec{E}(\vec{r}) = \frac{\vec{f}}{q} = \sum_{j=1}^{n} \{q_j/(\vec{r}-\vec{r}_j)^2\} \hat{n}_j \qquad (H.5)$$

The foregoing expression is for a discrete charge distribution. If, instead, the charge distribution is continuous and specified by a density $\sigma(\vec{r})$ on a surface of area dS', the following holds:

$$d\vec{E} = \frac{1}{4\pi\varepsilon_0} \frac{\sigma(\vec{r}')dS'}{|\vec{r}-\vec{r}'|^2} \hat{n} \qquad (H.6)$$

where

$$\sigma(\vec{r})\, dS' = dq$$

and

$$\hat{n} = \frac{\vec{r}-\vec{r}'}{|\vec{r}-\vec{r}'|} \qquad (H.7)$$

Substituting for the unit vector $\hat{n}$ into (H.6), from above

$$d\vec{E} = \frac{1}{4\pi\varepsilon_0} \frac{\vec{r}-\vec{r}'}{|\vec{r}-\vec{r}'|^3} \sigma(\vec{r}')\, dS'$$

Taking limits as $\Delta S' \to 0$

$$\vec{E}(\vec{r}) = \frac{1}{4\pi\varepsilon_0} \lim_{\Delta S' \to 0} \Sigma \frac{\vec{r}-\vec{r}'}{|\vec{r}-\vec{r}'|^3} \sigma(\vec{r}')\, dS'$$

or

$$\vec{E}(\vec{r}) = \frac{1}{4\pi\varepsilon_0} \int_S \frac{\vec{r}-\vec{r}'}{|\vec{r}-\vec{r}'|^3} \sigma(\vec{r}')\, dS' \qquad \text{(H.8)}$$

Similarly, for a volume charge distribution,

$$\vec{E}(\vec{r}) = \frac{1}{4\pi\varepsilon_0} \int_{\hat{V}} \frac{\vec{r}-\vec{r}'}{|\vec{r}-\vec{r}'|^3} \rho(\vec{r}')\, d\hat{V}' \qquad \text{(H.9)}$$

where

$\rho(\vec{r}')$ = volume charge density

$\hat{V}, \hat{V}'$ = volume.

From vector algebra it can be shown that

$$\nabla \left[\frac{1}{|\vec{r}-\vec{r}'|}\right] = -\frac{\vec{r}-\vec{r}'}{|\vec{r}-\vec{r}'|^3} \qquad \text{(H.10)}$$

Using the substitution from (H.10) into the expression for the field strength, equation (H.9), one gets

$$\vec{E}(\vec{r}) = -\nabla \left[\frac{1}{4\pi\varepsilon_0} \int_{\hat{V}} \frac{\rho(\vec{r}')d\hat{V}'}{|\vec{r}-\vec{r}'|}\right] \tag{H.11}$$

The above transposition is possible since the ∇ operator is in dependent of the $\vec{r}'$ vector.

If the scalar potential ϕ is defined by the term within the parenthesis in (H.11), the more familiar expression for the field strength is obtained.

$$\vec{E}(\vec{r}) = -\nabla\phi \tag{H.12}$$

Thus the field is equal to the spatial gradient of the scalar potential.

From equation (H.11), the divergence of the electric field strength $\nabla\cdot\vec{E}(\vec{r})$ is

$$\nabla\cdot\vec{E}(\vec{r}) = -\frac{1}{4\pi\varepsilon_0} \int_V \nabla^2 \left[\frac{1}{|\vec{r}-\vec{r}'|}\right] \rho(\vec{r}')\, dV' \tag{H.13}$$

Using the divergence theorem it can be shown that

$$\int_V \nabla^2 \left(\frac{1}{R}\right) dV' = \begin{cases} -4\pi; & R \text{ in } V \\ 0; & R \text{ not in } V \end{cases}$$

where

$$R = |\vec{r}-\vec{r}'|$$

also

$$\nabla^2 \left(\frac{1}{R}\right) = -4\pi\delta(\vec{r}-\vec{r}') \tag{H.14}$$

where δ is the Dirac delta function having the following properties,

i) $$\delta(\vec{r}-\vec{r}') = \begin{cases} \infty \text{ for } R = 0 \\ 0 \text{ for } R \neq 0 \end{cases}$$

ii) $$\int_{\infty} \delta(\vec{r}-\vec{r})\, dV' = 1$$

so that

$$\int_V f(\vec{r}')\, \delta(\vec{r}-\vec{r}')\, dV' = f(\vec{r}) \tag{H.15}$$

Using the substitution (H.14) into equation (H.13)

$$\nabla\cdot\vec{E}(\vec{r}) = -\frac{1}{4\pi\varepsilon_0} \int_{\hat{V}'} -4\pi\delta(\vec{r}-\vec{r}')\, \rho(\vec{r})\, d\hat{V}'$$

hence

$$\nabla\cdot\vec{E}(\vec{r}) = \rho(\vec{r})/\varepsilon_0 \tag{H.16}$$

Equation (H.16) is Maxwell's first relation. Applying the divergence theorem to this equation, the following useful relationship are obtained,

$$\int_{\hat{V}'} \nabla\cdot\vec{E}\, d\hat{V}^1 = \int_S n\cdot\vec{E}\, dS = \frac{1}{\varepsilon_0}\int_V \rho\, d\hat{V}$$

or

$$\int_{\hat{V}} \nabla\cdot\vec{E}\, d\hat{V} = \frac{Q}{\varepsilon_0} \qquad \text{(H.17)}$$

This last equation is the Gauss's law for $\vec{E}$ field.

APPENDIX I

APPENDIX I

I.1 The Stack Sampler

The determination of the moisture content (of air and flue gas) in the laboratory and the power plant involved the use of a stack sampler.* The equipment comes with a control unit and a sampling train unit. The sampling train unit comprises of a pitot tube probe, a filter (to remove particulates) and a set of four (ice bath) impingers. The control unit houses all the electrical and mechanical controls needed for operation and provides all readouts for directly obtainable data (see Figure 5.4).** Some of these are:

1. Meter Temperature: Two temperature gauges designated OUT and IN measure the respective gas (or air) temperatures. The sample temperature at the gas meter (see below) is the arithmetic average of these two temperatures.
2. Gas Meter: This measures the volume of sample gas drawn through the instrument.
3. Sample Box Heater: This switch controls the heater in the sampling train unit which also encloses the (gas) filtering assembly. The heater prevents any moisture condensation in this housing.

---

*Lear Siegler, PM100 Manual Stack Sampler.

**This was also used in the power plant experiments as indicated by Figure A.4.

4. Probe Heater: This on/off rocker switch controls the sampling (pitot-tube) probe heater.
5. Pump: The vacuum pump inside the control unit is used to draw the flue gas (or air) into the sampling train. Attached to this are two coarse/fine valves which provide the desired control of the sample flow through the instrument.
6. Pitot - ΔH Gauge: These instruments provide the velocity and flow pressure differentials respectively.

In the laboratory ion migration experiments only one silica gel impinger was used.* The outlet from this impinger is connected to the control unit. The length of the line leading to the impinger from valve B (Figure 5.1) is made as small as possible in order to prevent condensation in this line. The glass impinger containing silica gel is weighed on an ordinary pan balance before and after an experiment. The difference between these two weights is the amount of moisture condensed. Barring any errors involved with an experimental run and subsequent measurements, this weight difference can be assumed to be equal to the moisture content of the air sampled through the instrument. A typical set of data for a humidity experiment is given below.

---

*This is generally appropriate for low volumes of samples gas (less than 10 cu. ft.).

Humidity Measurement Data for Experiment No. 2

1.

Volume of air sampled (cu. ft)	Meter Temperature (^{o}F) In	Out
838.558	83.5	83.0
838.900	102.0	84.0
838.200	106.5	86.0
839.480	110.0	88.0
840.200	117.5	94.0
841.850	119.0	98.0
842.600	120.0	98.0
845.550	120.0	98.0
845.720	120.0	98.0

2. Water Bath Temperature - 147.46^{o} F.

3. Weight of moisture condensed in impinger - 9.60 gms.

4. Total volume (of air) sampled - 7.162 cu. ft.

5. (Air) Flow Rate - 142 cu. in/min.

To evaluate the moisture content (B_{wo}) both the gas and water volumes are needed at standard conditions (70^{o} F, 29.92 in Hg). These are given as,

$$V_m = (V'_m) \cdot 17.71 \frac{^{o}R}{\text{in. Hg}} \cdot \frac{P_{bar}}{T_m} \qquad (I.1)$$

and

$$V_w = 0.0474 \frac{\text{cu. ft}}{\text{ml}} \quad (V_w') \qquad \text{(I.2)}$$

where

V_m = sample volume through dry gas meter at standard conditions, cu. ft.

V_m' = sample volume at meter conditions, cu. ft.

T_m = average meter temperature, ^oR.

P_{bar} = barometric pressure, in. Hg.

V_w = volume of water vapor in the air (or gas) sample at standard conditions cu. ft.

V_w' = volume of liquid collected in impinger(s), ml.

The mean temperature T_m is evaluated as the weighted mean of the average temperatures. The average temperature (equal to $\frac{T_{in} + T_{out}}{2}$) is weighted by the volume (of air) sampled between two consecutive readings.

Hence, $T_m = 106.87^o$ F and from equations (I.1) and (I.2) one gets the following values for V_m and V_w,

V_m = 6.712 cu. ft. ($P_{bar} \simeq 30$ in. Hg)

V_w = 0.455 cu. ft

Hence, the (volumetric) moisture content is

$$B_{wo} = 0.455/(0.455 + 6.712) \times 100\%$$
$$= 6.349\%$$

The relative saturation α (Chapter 2) is obtained from B_{wO} if the saturation pressure corresponding to the resistivity probe (or ash layer) temperature is known.

$$\alpha = \frac{B_{wO}}{100P_{sat}} \qquad (I.3)$$

This assumes, of course, that the probe chamber is at 1 atmosphere pressure. Furthermore, the value of the relative saturation calculated applies to the region in the probe chamber.

This completes the description of the stack sampler and of the computations associated with the humidity measurements.

APPENDIX J

APPENDIX J

This appendix presents the results of tests* conducted to physically characterize the fly ash used in the ion migration experiments. Two separate samples** of the fly ash were used for the analyses. The samples were extracted by repeated halvings of the entire original bulk which was well mixed. The results of these tests are as follows:

Sample No.	Bet Specific Surface (m^2/gm)	Density (gm/cc)	Bulk Porosity (% Void Volume) Loose	Tapped
1	3.31	2.20	73.0	59.5
2	3.28	2.23	75.8	57.3

Specific surface area was determined using the classic BET method with nitrogen gas as the adsorbent. The density was determined with a gas (He) pycnometer. The bulk porosity was measured volumetrically after pouring into a calibrated cylinder and after tapping to maximum density.

The particle size distribution was determined with precision sieves using a Sonic-Sifter. The results are listed below.

---

*This work was conducted by W.A. Hockings at the Institute of Mineral Research, Michigan Technological University.

**The samples weighed approximately 50 grams each.

SIZE ANALYSIS*
(Micro-Mesh Sieves, Weight %)

Size (μm)	Sample No. 1	Sample No. 2
+ 37	33.9	31.1
- 37 + 20	16.3	15.7
- 20 + 10	17.6	20.8
- 10 + 5	27.2	23.9
- 5	5.0	8.5
Median size (μm)	20.0	18.3

The arithmetic average of the values for the two test samples are as follows:

1. Density - 2.215 gm/cc.
2. Bulk Porosity (loose) - 74.4% void volume.
3. Bulk Porosity (tapped) - 58.4% void volume at maximum density.
4. BET Specific surface area - 3.295 m^2/gm.
5. Geometric mean diameter (2S) - 19.15 μm.
6. Standard deviation (size analysis) - 0.33115.

*The fly ash sample was obtained from the power plant combustion of 0.75% sulfur coal. The sample was withdrawn from the precipitator hopper.

APPENDIX K

APPENDIX K

This appendix contains the current time data for all of the nine laboratory ion migration experiments. As mentioned in Section 5.1, Chapter 5, these data are obtained on a strip chart recorder. The pen movement on the recorder is calibrated to correspond to a scale of 0 - 10 μA across the chart. The recorder is coupled with microammeter* which is used to monitor the initial rapid decline in the leakage current through the fly ash bed (Table K.1). The data obtained is presented in Section K.1.

K.1. Current-Time Data and Clean Plate Characteristics

The current-time data** obtained in Table K.1 are used to evaluate the time average field strength E_a across the ash layer (Section 5.2, Chapter 5). This also involves the determination of the clean plate characteristics (I-V plots) for each set of experimental conditions (moisture content and probe temperature). In this instance the probe geometry (corona point-plane distance) is identical to that corresponding to the ion migration experiments with the exception of the ash layer. It may be recalled with that clean plate I-V data are also

*Simpson Model 269, Series 3, scale 0 - 16 μA. The power supply used with the resistivity probe was part of an MSA (Mining Safety Appliance), Electrostatic Sampler (115 V, 60 Hz, 0 - 20 Kv, F.S. - 150 μA).

**The data presented in Table K.1 are a summarized form of the complete laboratory data.

required in the ash layer resistivity determinations of Chapter 1.

The clean plate current-voltage data for the laboratory experiments are shown in the plots of Figures 5.6, 5.7 and 5.8, Chapter 5. A typical I-V data set for one experiment is presented in Table K.2.

The specifications for the resistivity probe are given in Section K.2. The specifications apply to the modified probe (see Section 5.1, Chapter 5) used in the laboratory ion migration experiments.

K.2. Specifications for the Modified Resistivity Probe

As described in Section 5.1, Chapter 5, the probe was slightly modified for the migration experiments. The (corona) point-plane distance is constant for all of the experiments and the surface of the ash layer is flush with the top edge of the cylindrical (teflon) support in each case.

1. Plane diameter - 4.997 sq. cm.
2. Point-Plane distance - 2.6797 cm.
3. Height of support - 1.619 cm.
4. Distance between corona point to the (top) surface of ash layer (or support) - 1.061 cm.
5. Pitch of Turn Screw - 0.079375 cm.

The bottom face of the screw is subdivided into eight divisions so that the minimum thickness of the fly ash layer is equal to $\frac{\text{Pitch}}{8}$ (equal to 0.009922 cm).

Table K.1. Current-time data for the ion migration experiments.

Experiment No. 1 9.40 Kv+		Experiment No. 2 10.00 Kv		Experiment No. 3 9.50 Kv	
Time (hrs)	Current (μA)	Time (hrs)	Current (μA)	Time (hrs)	Current (μA)
0.000	6.500	0.000	4.700	0.034	1.300
0.050	4.560	0.250	1.900	0.169	1.030
0.217	2.640	0.317	1.670	0.253	0.850
0.317	3.470	0.450	1.330	0.506	0.945
0.583	2.450	0.667	1.430	0.708	0.720
0.883	1.830	1.533	1.220	4.170	0.625
41.433	2.130	2.400	1.120	12.520	0.625
59.190	1.690	23.373	1.220	20.110	0.625
71.028	1.830	31.265	1.170	23.900	0.560
74.974	1.830	41.129	1.280	31.490	0.550
78.920	1.950	47.049	1.190	44.570	0.540
92.731	1.800	54.940	1.210	66.270	0.540
106.542	1.720	78.616	0.920*	86.720	0.540
118.380	1.560	88.481	1.190	103.130	0.540
124.299	1.020	90.455	1.210		
130.218	1.565	92.427	1.300		

+Constant corona voltage for the experiment.

*The corona voltage dropped from 10 Kv to 9 Kv at this time.

Table K.1. Continued

Experiment No. 4 9.00 Kv		Experiment No. 5 9.50 Kv		Experiment No.6 9.00 Kv	
Time (hrs)	Current (μA)	Time (hrs)	Current (μA)	Time (hrs)	Current (μA)
0.000	7.220	0.000	1.850	0.000	1.760
0.337	7.030	0.034	1.580	0.017	1.520
0.675	7.220	3.795	1.485	0.051	1.340
0.810	6.660	6.520	1.125	0.118	1.250
0.995	5.800	6.820	1.275	0.236	1.050
1.434	5.560	7.130	0.900	0.538	0.980
1.687	5.520	8.650	1.080	9.250	1.150
2.243	4.750	12.900	1.150	14.190	1.125
3.172	3.570	16.240	1.030	18.175	1.010
6.325	2.580	18.360	0.875	23.610	0.980
14.220	1.600	31.800	0.760	30.170	0.600
26.921	1.675	40.910	0.800	41.760	0.850
35.370	1.180	66.700	0.580	60.380	0.550
48.040	1.375	120.460	0.500	78.670	0.500
55.920	1.140			95.330	0.490
120.570	1.200				

Table K.1. Continued

Experiment No. 7 9.00 Kv		Experiment No. 8 7.50 Kv		Experiment No. 9 8.00 Kv	
Time (hrs)	Current (μA)	Time (hrs)	Current (μA)	Time (hrs)	Current (μA)
0.000	1.970	0.000	7.410	0.000	8.550
0.034	1.625	0.008	7.360	0.017	7.260
0.067	1.485	0.017	6.100	0.051	6.570
0.101	1.370	0.051	5.475	0.084	5.800
0.169	1.125	0.084	4.990	0.118	5.080
0.236	0.978	0.118	4.650	0.152	4.630
0.422	0.720	0.152	4.160	0.186	4.325
0.692	0.650	0.186	3.810	0.219	4.070
8.890	0.670	0.270	3.780	0.270	3.730
15.090	0.520	0.793	2.870	0.573	3.010
23.270	0.425	1.400	2.225	0.894	1.720
24.050	0.375	3.373	1.900	1.000	2.600
36.080	0.230	6.527	1.970	4.167	1.600
62.580	0.400	11.417	1.750	7.134	0.990
111.28	0.380	34.577	1.730	23.200	0.830
120.82	0.210	41.930	1.575	35.384	0.790
		64.860	0.940	56.517	0.900
		74.120	1.260	90.184	1.180
		95.650	1.030	103.067	1.270

Table K.2. Clean plate current voltage data for Experiment No. 5 (Probe temperature - 314° F).

Corona Voltage (Kv)	Recorder Current (μA)
5.60	1.30
5.75	2.16
6.00	3.20
6.30	4.56
6.50	5.66
6.55	6.63
6.65	9.14

Figure 5.7 (Chapter 5) shows the I-V curve for the above data.

APPENDIX L

APPENDIX L

The information regarding the specific quantities of materials used in the migration experiments is presented in this appendix. As stated in Chapter 5 the sodium ions migrate upward from the lower boundary of the vertical fly ash bed towards the negative corona (Figure 5.1). The (ion) concentration gradient and the overall voltage gradient* therefore superimpose each other with respect to the direction of the ion migration.

The ions "available for migration" are provided by the sodium hydroxide deposited on the plane of the probe. The amounts of sodium hydroxide used in each of the experimental cases is indicated in Table L.1.

Table L.1. Quantities of NaOH deposited on probe plane.

Experiment No.	NaOH (1.824 g/l) (ml)
1	2.490
2	1.680
3	3.010
4	3.020
5	3.025
6	1.700
7	1.510
8	1.490
9	1.505

*This is the voltage drop across the bed divided by its thickness.

After the completion of an experiment the samples are withdrawn beginning from the top of the ash bed. The turn screw (attached to the plane) is rotated by the requisite number of divisions (one-eighth or one-fourth of the pitch) so that the ash bed rises above the top surface of the support. The amount of fly ash equivalent to this thickness is carefully removed by means of a sharp edged scraper. This removal is facilitated by the use of a protruding (teflon) lip which is inserted over the support and is flush with its top edge. The (ash) sample is then transferred to an irradiation vial. The vial is heat sealed, washed and rinsed with double distilled water and stored in an environment free from any contamination (especially sodium).

Each set of samples for an experiment are irradiated with a (sodium) standard. The standard is prepared with the same NaOH solution* as used for the experiments (Table L.1). Approximately 1.5 ml of NaOH solution is used as standard in each case. The standard is evaporated (in a vial) prior to irradiation.** Finally, during the counting process, care is taken that the irradiated vials are in a geometrically identical position with respect to the detector.

---

*The concentration of the irradiation standard was 0.1824 g/l

**This was not done for the first five experiments. For these cases the liquid standard was irradiated instead.

BIBLIOGRAPHY

BIBLIOGRAPHY

A1 Attar, A., "Bubble Nucleation in Viscous Material Due to Gas Formation by a Chemical Reaction: Application to Coal Pyrolysis", AI CHE Journal, 24, 1, Jan., 1978.

A2 Awakuni, Y., and Calderwood, J.H., "Water Vapour Adsorption and Surface Conductivity in Solids", J. of Physics, D; Applied Physics, 5, (1972), p. 1038.

B1 Bickelhaupt, R.E., "Surface Resistivity and the Chemical Composition of Fly Ash", J. of the Air Pollution Control Association, 25, 2, Feb 1975.

B2 Bickelhaupt, R.E., "Volume Resistivity - Fly Ash Composition Relationship", Environmental Science and Technology, 9, 4, Apr 1975.

B3 Bickelhaupt, R.E., "Electrical Volume Conduction in Fly Ash", J. of Air Pollution Control Association, 24, 3, Mar 1974.

B4 Black, C., "Vapor Phase Imperfections in Vapor-Liquid Equilibria", Industrial and Engineering Chemistry, 50, 3, Mar., 1958.

B5 Benson, S.W., and Gerjuoy, E., "The Tensile Strengths of Liquids. I. Thermodynamic Considerations", The Journal of Chemical Physics, 17, 10, Oct., 1949.

B6 Buff, F.P., and Kirkwood, J.G., "Remarks on the Surface Tension of Small Droplets", J. of Chemical Physics, 18, (1950), p. 991.

B7 Bender, C.M., and Orszag, S.A., "Advanced Mathematical Methods for Scientists and Engineers", McGraw-Hill, 1978.

B8 Bird, R.B., Stewart, W.E., and Lightfoot, E.N., "Transport Phenomena:, J. Wiley and Sons, 1960.

B9 Brenchley, D.L., Turley, C.D., and Yarmac, R.F., "Industrial Source Sampling", Ann Arbor Science Publishers, Inc., 1974.

C1 Carman, P.C., "Properties of Capillary - Held Liquids", Journal of Physical Chemistry, 57, Jan., 1953, p. 56.

C2 Coughlin, R.W., "Physicochemical Aspects of Sampling Particulates", Recent Advances in Pollution Control, AIChE Symposium Series, 70, 137, p. 273.

C3 Carslaw, H.S., and Jaeger, J.C., "Conduction of Heat in Solids", Clarendon Press, Second Edition,

C4 Charles, R.J., "Polarization and Diffusion in a Silicate Glass", Journal of Applied Physics, 32, 6, (1961), p. 1115.

D1 Ditl, P., and Coughlin, R.W., "Improving Efficiency of Electrostatic Precipitation by Physicochemical Modification of the Electrical Resistivity of Fly Ash", AI ChE Journal, 22, 4, July, 1976, p. 730.

D2 Dalmon, J., and Tidy, D., "The Cohesive Properties of Fly Ash in Electrostatic Precipitation", Atmospheric Environment, 6, (1972), pp. 81-92.

D3 Daniels, F., and Alberty, R.A., "Physical Chemistry", Third Edition, J. Wiley and Sons, Inc., 1966.

D4 Doremus, R., "Ion Transport in Amorphous Oxides", Journal of the Electrochemical Society: SOLID STATE SCIENCE, 115, 2, (1968), p. 181.

D5 Dalmon, J., and Tidy, D., "A Comparison of Chemical Additives as Aids to the Electrostatic Precipitation of Fly-Ash", Atmospheric Environment, 6, (1972), Pergamon Press, p. 721.

D6 Dismukes, E.B., "Conditioning of Fly Ash with Ammonia", J. of the Air Pollution Control Association, 25, 2, (1975), p. 152.

E1 Engel, J.R., and Tomozawa, M., "Nernst-Einstein Relation in Sodium Silicate Glass", Journal of the American Chemical Society, 58, 5-6, (1975), p. 183.

F1 Fisher, G.L., Chang, D.P.Y., and Brummer, M., "Fly Ash Collected from Electrostatic Precipitators: Microcrystalline Structures and the Mystery of the Spheres", Science 192, May 7, 1976.

F2 Fisher, G.L., Silberman, D., Prentice, B.A., Brummer, M., Tyler, W.S., Ondov, J.M., Ragaini, R.C., and Bierman, A.H., "Morphology and Chemistry of Fly Ash from Coal Combustion", American Chemical Society, Division of Environmental Chemistry, 172nd National Meeting, Preprints, 16, (2), 1976, pp. 204-207.

F3 Fisher, G.L., Prentice, B.A., Silberman, D., Ondov, J.M., Bierman, A.H., Ragaini, R.C., and McFarland, A.R., "Physical and Morphological Studies of Size - Classified Coal Fly Ash", Environmental Science and Technology, 12, 4, Apr., 1978.

F4 Fisher, G.L., "The Morphogenesis of Coal Fly Ash", Proceedings, Symposium on the Transfer and Utilization of Particulate Control Technology: Vol. 4. Fugitive Dusts and Sampling, Analysis and Characterization of Aerosols", Venditti, F.P., Armstrong, J.A., Durham, M., (Authors), Denver, Colorado, July, 1978. Environmental Protection Agency Report No. EPA-600/7-79-044d.

F5 Fisher, R.A., "On the Capillary Forces in an Ideal Soil, Correction of Formula Given by W.B. Haines", Journal of Agricultural Science, 16, (1926), p. 492.

F6 Flood, E.A., and Farhan, F.M., "Stresses and Strains In Adsorbent - Adsorbate Systems. V. Thermodynamic Theory of Adsorption - Extension Phenomena". Canadian Journal of Chemistry, 41, part 2, (1963), 1703.

H1 Holm, R., "Electric Contacts - Theory and Applications", Springer-Verlag, 1967, 4th edition.

H2 Hall, H.J., "Questions, Answers and Comments, Session 4", (in answer to a question by L. Collet), Proceedings of the Conference on Operation and Maintenance of Electrostatic Precipitators, Air Pollution Control Association, Dearborn, Michigan, April, 1978, p. 141.

H3 Hirschfelder, J.O., Curtiss, C.F., and Bird, R.B., "Molecular Theory of Gases and Liquids", J. Wiley and Sons, Inc., 1964.

H4 Hill, T.L., "Concerning the Dependence of the Surface Energy and Surface Tension of Spherical Drops and Bubbles on Radius", J. of American Chemical Society, 72, Sep., 1950, p. 3923.

H5 Haines, W.B., "Studies in the Physical Properties of Soils. II. A Note on the Cohesion Developed by Capillary Forces in an Ideal Soil". J. of Agricultural Science, 15, (1950), p. 529.

H6 Harris, C.C. (Prof.) and Morrow, N.R., "Pendular Moisture in Packings of Equal Spheres", Nature, 203, August 15, 1964, p. 706.

H7 Hildebrand, F.B., "Advanced Calculus for Applications", Prentice-Hall, Inc., 1962.

I1 International Critical Tables, Vol. IV, First Ed., (1928), p. 447.

K1 Klotz, I.M., and Rosenberg, R.M., "Chemical Thermodynamics", Benjamin/Cummings Publishing Co., Third Edition, 1974, p. 241.

K2 Kell, G.S., and Whalley, E., "The PVT Properties of Water. I. Liquid Water in the Temperature Range 0 to 150° C and at Pressures up to 1 kb", Philosophical Transactions of the Royal Society, 258a, Dec., 1965, p. 565.

L1 Lynch, J.G., "A Review of Rapper System Problems Associated with Industrial Electrostatic Precipitators", Proceedings of the Conference on Operation and Maintenance of Electrostatic Precipitators, Air Pollution Control Association, Dearborn, Michigan, April, 1978.

M1 McLean, K.J., "Factors Affecting the Resistivity of a Particulate Layer in Electrostatic Precipitators", Journal of the Air Pollution Control Association, 26, 9, Sep., 1976.

M2 McLean, K.J., and Huey, E.M. (Prof)., "Influence of Electric Field on the Resistivity of a Particulate Layer", Proceedings of the IEE, 121, 1, Jan., 1974.

M3 McLean, K.J., "Cohesion of Precipitated Dust Layer in Electrostatic Precipitators", Journal of the Air Pollution Control Association, 27, 11, Nov., 1977.

M4 Melrose, J.C., "Model Calculations for Capillary Condensation", A.I. Ch. E. Journal, 12, 5, Sept., 1966.

M5 Masuda, S., "Effects of Temperture and Humidity on the Apparent Conductivity of High Resistivity Dust", Electro Technical Journal of Japan, 7, 3, (1962), p. 108.

M6 Mott, N.F., and Gurney, R.W., "Electronic Processes in Ionic Crystals", Clarendon Press, Oxford, IInd Edition, 1948.

M7 McLean, K.J., Personal Communication, 1979.

M8 Martin, A.D., and McLean, K.J., "The Effect of Adsorbed Gases on the Surface Conductivity of Quartz", J. of Applied Physics, 48, 7, (1977).

N1 Nevens, T.D., Culbertson, W.J. (Jr). and Tassicker, O.J., "A Comparative Evaluation of Cells for Ash Resistivity Measurement", Presented at the Joint Power Generation Conference, Long Beach, California, Sept., 18-21, 1977.

O1 O'Connell, J.P., and Prausnitz, J.M., "Empirical Correlation of Second Virial Coef-icients for Vapor-Liquid Equilibrium Calculations", I & EC Process Design and Development 6, 2, Apr., 1967, p. 245.

O2 Owen, A.E., "Electric Conduction and Dielectric Relaxation in Glass", Progress in Ceramic Science, 3, Pergamon Press, The Macmillan Company, New York, 1963, p. 77.

P1 Potter, E.C., "Electrostatic Precipitation Technology: A Different Viewpoint", J. of the Air Pollution Control Association, 28, 1, Jan. 1978.

P2 Pierce, C., and Nelson Smith, R., "Adsorption in Capillaries", Journal of Physical Chemistry, 57, Jan., 1953, p. 64.

P3 Prausnitz, J.M., "Molecular Thermodynamics of Fluid-Phase Equilibria", Prentice-Hall, Inc., 1969, p. 97.

P4 Perry, R.H., and Chilton, C.H., "Chemical Engineers' Handbook', Fifth Edition, McGraw-Hill Book Company.

S1 Shukla, P.N., Someshwar, A., and Wilkinson, B.W., "Reliable Fly Ash Resistivity Measurements and the Criteria for Determination and Documentation", Proceedings of the National Conference on Quality Assurance of Environmental Measurements, Denver, Colorado, 116, Nov. 1978.

S2 Someshwar, A., M.S. Thesis, Michigan State University, Department of Chemical Engineering, 1979.

S3 Smith, J.M., "Chemical Engineering Kinetics", Second Edition, McGraw-Hill, 1970.

S4 Smythe, W.R., "Static and Dynamic Electricity", McGraw-Hill, New York, 1968.

T1 Tassicker, O.J., "Some Aspects of Electrostatic Precipitator Research in Australia", J. of the Air Pollution Control Association, 25, 2, Feb., 1975.

T2. Tuma, J.J., "Engineering Mathematics Handbook", McGraw-Hill, 1979.

T3 Temperley, H.N.V., "The Behaviour of Water Under Hydrostatic Tension: III", Proceedings of the Physical Society, 59, (1947), p. 199.

V1 Van Itterbeek, A, and Verbeke, O., "Density of Liquid Nitrogen and Argon as a Function of Pressure and Temperature", Physica, 26, (1960), p. 931.

W1 White, H.J., "Resistivity Problems in Electrostatic Precipitation", Journal of the Air Pollution Control Association, 24, 4, April, 1972.

W2 Walcott, E.R., "Effects of Dielectrics on the Sparking Voltage", Physical Review, XII, Oct., 1918.

W3 White, H.J., "Electrostatic Precipitation of Fly Ash", Journal of the Air Pollution Control Association, 27, 1, Jan., 1977.

W4 White, H.J., "Industrial Electrostatic Precipitation", Addison-Wesley Pub. Co., 1963.

W5 White, H.J., "Chemical and Physical Particle Conductivity Factors in Electrostatic Precipitation", Chemical Engineering Progress, 42, pp. 244-248.

Y1 Young, G.J., and Bursh, T.P., "Immersion Calorimetry Studies of the Interaction of Water with Silica Surfaces", J. of Colloid Science, 15, (1960), pp. 361-369.

Z1 Zettlemoyer, A.C., and McCafferty, A.C., "Water on Oxide Surfaces", Croatica Chemica Acta, 45, (1978), p. 173.

Z2 Zettlemoyer, A.C., and McCafferty, A.C., "Discussion of Papers at the 44th National Colloid Symposium", J. of Colloid Science, 34, 4, (1970), p. 606.